University of Glasgow

Franco, Fabiane Fantinelli (2023) *Fabrication and characterization of electrochemical ammonia and nitrite sensors for water quality monitoring.* PhD thesis.

https://theses.gla.ac.uk/83872/

Copyright and moral rights for this work are retained by the author

A copy can be downloaded for personal non-commercial research or study, without prior permission or charge

This work cannot be reproduced or quoted extensively from without first obtaining permission from the author

The content must not be changed in any way or sold commercially in any format or medium without the formal permission of the author

When referring to this work, full bibliographic details including the author, title, awarding institution and date of the thesis must be given

Enlighten: Theses
https://theses.gla.ac.uk/
research-enlighten@glasgow.ac.uk


# Fabrication and Characterization of Electrochemical Ammonia and Nitrite Sensors for Water Quality Monitoring

Fabiane Fantinelli Franco, MSc

SUBMITTED IN FULFILMENT OF THE REQUIREMENTS FOR THE DEGREE OF

*Doctor of Philosophy*

James Watt School of Engineering

College of Science and Engineering

University of Glasgow

September 2023

# Abstract

High levels of dissolved inorganic nitrogen ($NH_3$ and $NO_2^-/NO_3^-$ ions) in water can lead to eutrophication and negatively impact human health and aquatic ecosystems, making it an important parameter to monitor. The development of affordable, continuous sensors for $NH_3$ and $NO_2^-/NO_3^-$ ion detection in water has been an ongoing challenge due to the limitations and high cost of standard monitoring techniques. Voltammetric sensors have been presented as an alternative, however, achieving high sensitivity while maintaining long-term stability and low/no signal interference remains a significant challenge. Moreover, the environmental impact of the sensor lifecycle and the materials used during the fabrication steps are crucial considerations when designing new sensors for continuous use in water bodies but are often not investigated. In this manner, printed voltametric sensors are a good alternative to standard monitoring techniques due to their versatility and cost-effective nature.

The work described here focus on two main aspects of the development of printed sensors: the electrode material choice and the synthesis of new sensing material for the detection of $NH_3$ and $NO_2^-$ ions. In the electrode material aspect, screen-printing and laser induced graphene (LIG) techniques were used to develop new sensors and to investigate the effect of silver and carbon materials on the electrode tracks. It was inferred that silver, a material that is commonly used as a conductive paste in screen-printed sensors, can interfere with the electrochemical response of the sensor. In this manner, carbon electrode tracks were explored as a more stable and sustainable alternative. To improve the conductivity of the track, LIG electrodes were developed and compared to carbon screen-printed electrodes (SPEs). The LIGs demonstrated improved stability and sensitivity compared to the SPE in the oxidation of $NO_2^-$ ions, revealing they can be an alternative to disposable carbon-based SPEs.

In the sensing material aspect, materials that are easy to incorporate with current sensor fabrication techniques were prioritised. Different metal oxides were explored to detect $NH_3$, a challenging parameter to detect due to effects of pH and temperature on the ion dissociation. From the materials synthesised, the Cu-BDC metal-organic framework presented the best performance, although further improvements on material stability and reproducibility are necessary. For the $NO_2^-$ ion monitoring, the unmodified LIGs showed enhanced sensitivity and fast detection, important parameters to achieve when detecting unstable ions such as $NO_2^-$. Furthermore, the use of unmodified LIGs facilitate the fabrication of $NO_2^-$ sensors. Overall, by researching the materials employed in both the electrode pathway and the sensing electrode, improved printed electrochemical sensors were achieved.

# Table Of Contents

# List of Tables

# List of Figures

# Acknowledgments

There are many people to whom I am grateful to have shared my time, joys, and worries these past few years. Without them, this thesis would be nothing more than an unfinished tale.

First and foremost, I want to thank my supervisors Prof Cindy Smith and Dr Caroline Gauchotte-Lindsay, the most kind and patient supervisors I could have asked for. They welcomed me during a difficult period and offered their invaluable guidance and support needed to complete this thesis. I am sincerely grateful to them.

I also want to thank Dr Libu Manjakkal, who I consider my third supervisor and friend. Without his valuable input and unwavering support, I would not have finished this thesis. I am thankful for his vast knowledge and encouragement that helped me find my own research style. I am proud to have worked alongside him.

I gratefully acknowledge the European Union's Horizon 2020 for funding the AQUASENSE project and I am fortunate to have been a part of it. I want to thank Dave Iglesias for his assistance and kindness in helping me to navigate this program. I also extend my thanks to Dr. Ali Roshanghias and Hassan for their guidance throughout my secondment in Silicon Austria Labs. Furthermore, I want to specially thank my AQUASENSE colleagues, Saoirse, Tarun, Amlan, Llewellyn, Kiranmai, João, and all the others, for making this experience much more enjoyable.

I want to thank my fellow research colleagues and friends with whom I have shared many moments of joy and sorrow – colleagues from the BEST group, Water and Environment group, and AdS. I am also grateful to Uli for his wonderful cooking and all the adventures that helped to keep me (somewhat) sane during the last years of my PhD, and to my family, who even from afar encouraged me to do my best.

Finally, I would like to dedicate this thesis to my parents. Mãe, I am especially grateful for your infinite love and encouraging words, you are the reason I achieved so much. Pai, thank you for being proud of me and trying to remember what I studied – I know it is hard to keep track of it.

Thank you to everyone who has been a part of this process. There are too many people who have supported me in innumerable ways. Although I cannot name you all individually, I will forever be grateful to each one of you.

# Declaration

I certify that the thesis presented here for examination for a PhD degree of the University of Glasgow is solely my own work other than where I have clearly indicated that it is the work of others (in which case the extent of any work carried out jointly by me and any other person is clearly identified in it) and that the thesis has not been edited by a third party beyond what is permitted by the University's PGR Code of Practice.

The copyright of this thesis rests with the author. No quotation from it is permitted without full acknowledgement.

I declare that the thesis does not include work forming part of a thesis presented successfully for another degree.

I declare that this thesis has been produced in accordance with the University of Glasgow's Code of Good Practice in Research.

I acknowledge that if any issues are raised regarding good research practice based on review of the thesis, the examination may be postponed pending the outcome of any investigation of the issues.

Name: Fabiane Fantinelli

Franco Registration Number:

# List of Abbreviations

| | |
|---|---|
| BDC | 1,4-benzenedicarboxylic acid |
| CE | Counter electrode |
| CNT | Carbon nanotube |
| CV | Cyclic voltammetry |
| DoE | Design of experiments |
| DoE-RS | Design of experiments – response surface |
| DPV | Differential pulsed voltammetry |
| *edl* | Electrochemical double layer |
| EIS | Electrochemical impedance spectroscopy |
| FeCN | Potassium hexacyanoferrate(II) trihydrate |
| GCE | Glassy-carbon electrode |
| GOx | Graphene oxide |
| G-PE | Graphite-based printed electrode |
| GS-SPE | Graphene sheet screen printed electrode |
| LIG | Laser induced graphene |
| MOF | Metal organic framework |

| | |
|---|---|
| OFAT | One-factor-at-a-time |
| PBS | Phosphate-buffered saline |
| PHB | Polyhydroxybutyrate |
| PHB/PHV | PHB 92%/PHV 8% |
| PHV | Polyhydroxyvalerate |
| PI | Polyamide |
| PPI | Pulses per inch |
| PVA | Polyvinyl alcohol |
| PVC | Polyvinyl chloride |
| RE | Reference electrode |
| $R_S$ | Sheet resistance |
| SEM | Scanning electron microscopy |
| SPE | Screen printed electrode |
| TLM | Transfer length method |
| WE | Working electrode |

# Chapter 1

# Introduction

## 1.1 General Introduction

### *1.1.1 Inorganic Nitrogen Monitoring*

Nitrogen is an important parameter in aquaculture and agriculture that can lead to environmental pollution if above a certain threshold, making it a key parameter to monitor. The nitrogen cycle (Figure 1.1a) gives an insight on which nitrogenous compounds to monitor and how they correlate to one another. Traditionally, the nitrogen cycle has been divided into three processes (dinitrate ($N_2$) fixation, nitrification, and denitrification). However, this has recently been expanded to included five nitrogen processes: ammonification, nitrification, denitrification, anammox, and nitrate-nitrate interconversion (Figure 1.1b) [1]. Mineralization and assimilation, which refer to the general processes of organic matter, complete the movement of the nitrogen cycle (Figure 1.1b). Ammonification is composed of two processes - $N_2$ fixation, performed by bacteria and archaea that have the nitrogenase enzyme, and anaerobic assimilatory and dissimilatory nitrite ($NO_2^-$) reduction to ammonium ($NH_4^+$), accomplished by bacteria and fungi. Nitrification is mediated by different groups of microorganisms that can perform nitritation, oxidation of ammonia to $NO_2^-$, nitratation, oxidiation of $NO_2^-$ to nitrate ($NO_3^-$), or completely oxidize ammonia to $NO_3^-$. Denitrification consists of the anaerobic respiration of $NO_2^-$, nitric oxide (NO), and nitrous oxide ($N_2O$) to $N_2$ from bacteria, archaea, and several eukaryotes. Anammox, short for anaerobic ammonium oxidation, transforms $NO_2^-$ and $NH_4^+$ to $N_2$ via the NO and hydrazine ($N_2H_4$) intermediates. The nitrate-nitrite process is achieved by nitrite-oxidizing or reducing bacteria [1]. In mineralization, the decomposition of organic nitrogen such as those from fertilizers or leaves into ammonia is performed by bacteria and fungi [2].

These nitrogenous compounds can have serious effects in the environment. In aquaculture, nitrogen is a significant by-product of fish rearing. For example, fin fish, commonly grown in fish farms, are fed a protein rich diet and, consequently, excrete dissolved nitrogen compounds (in

particular, ammonia) [3]. Although this is a natural process, intensive fish farming may lead to an increased concentration of dissolved nitrogen compounds. This becomes an issue as some of these compounds, such as dissolved ammonia and nitrite, when not excreted, can lead to toxic build-up in

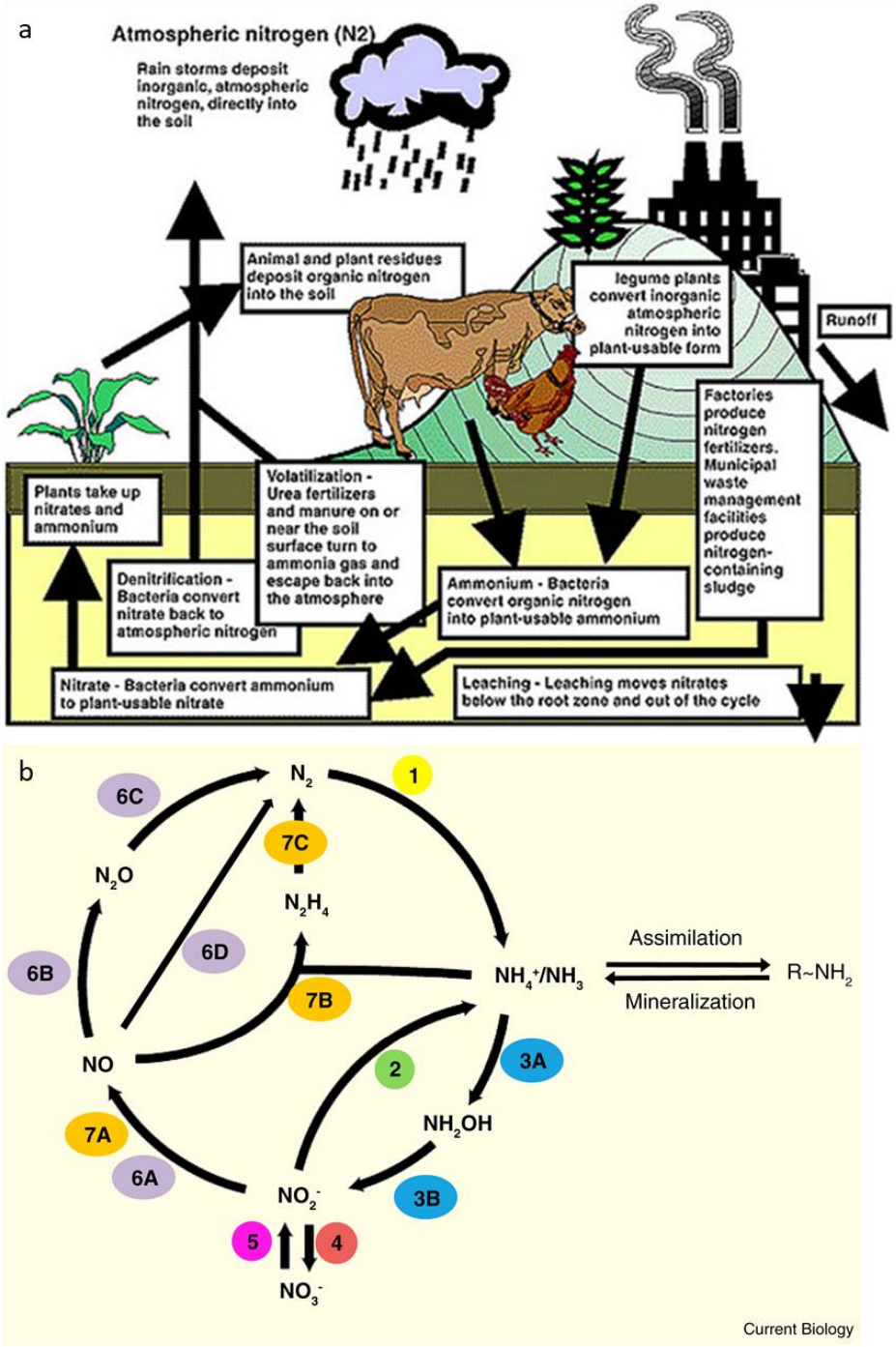


Figure 1.1. (a) Major processes of the nitrogen cycle, including nitrogen fixation, nitrification, and denitrification (*Copyright University of Missouri*) (b) Detailed scheme of the processes in the nitrogen cycle. 1 - Nitrogen fixation; 2- Dissimilatory nitrite reduction to ammonium; 3 - Nitritation; 4 – Nitratation; 5 - Reduction of nitrate to nitrite; 6 - Denitrification; 7 - Annamox [1].

tissues and blood in aquatic life [4]. Another problem is that a nitrogen-rich environment can lead to eutrophication, decreasing the amount of dissolved oxygen in water bodies which directly affects the aerobic organisms [5,6]. Similar concerns arise from agriculture runoff into water bodies. As nitrogen plays a crucial role in plant lifecycle, nitrogen-rich fertilizers are widely used, sometimes promoting overfertilization, and/or excess runoff into surrounding water bodies [7]. If this nitrogen excess reaches the water bodies, it essentially fertilises the water, causing increase plant and algal growth, which can lead to hypoxia and death of aquatic life. Therefore, constant monitoring of dissolved inorganic nitrogen (DIN), which consists of nitrate ($NO_3^-$), nitrite ($NO_2^-$) and ammonia ($NH_3$), within receiving water bodies is required to ensure the health of aquatic environments.

## 1.2 Ammonium Ion and Dissolved Ammonia

### *1.2.1 Ammonia in Aquatic Environments*

$NH_3$ is a colourless gas that can readily dissolve in water due to its trigonal pyramidal shape and ability to form hydrogen bonds. It ionizes into ammonium ion ($NH_4^+$) in a relationship governed by temperature, pH values and concentration of dissolved salts. The chemical ionization equation is shown in Equation 1.1 [8], while Equation 1.2 shows the acid dissociation constant, $K_a$, for the $NH_4^+$ ion [9].

$$NH_3 + H_2O \rightleftarrows NH_4^+ + OH^- \tag{1.1}$$

$$K_a = \frac{[NH_3][H^+]}{[NH_4^+]} \tag{1.2}$$

The $pK_a$ is temperature dependant, and can be calculated using the following revised equation, with temperature given in Celsius [10]:

$$pK_a = 0.09018 + \left(\frac{2729.92}{273.2 + T}\right) \tag{1.3}$$

And finally, the unionized fraction of $NH_3$ (also referred to as dissolved $NH_3$ throughout this thesis) can be calculated using the following equation developed by Emerson et al. using the $pK_a$ relation described on Equation 1.4 [10]:

$$Unionized\ NH_3 = \frac{100}{(1 + 10^{(pK_a - pH)})} \quad (1.4)$$

Table 1-1 expresses revised values of different unionized $NH_3$ percentages according to temperature and pH using Equation 1.3 and 1.4. At pH 7.4 and 20°C, less than 1% of $NH_3$ is present while at pH 9 and 20°C, this rises to almost 30%. Dissolved $NH_3$ is a weak base whilst the $NH_4^+$ ion is considered a weak acid, which explains why in basic pH a higher percentage of $NH_3$ is available. Salinity also affects the degree of ionization of ammonia and can be especially important in marine environments. While the percentage of unionized $NH_3$ increases with increasing temperature and pH, the opposite occurs with salinity, although it does not affect the percentage of $NH_4^+$ converted into unionized $NH_3$ as drastically as when changing the temperature and pH. Bower made a comprehensive table of $NH_3$ percentage from pH from 7.5 to 8.5 and temperatures from 0 to 25 °C in seawater with different salinities [11]. The author analysed salinity percentages from 18-22% up to 32-40% and found that at 18-22%, the $NH_3$ percentage is similar to that found in freshwater, however at 32-40%, common in seawater culture, there is up to a fifth less amount of $NH_3$ [11]. This dissociation is important because unionized $NH_3$ has been shown to be toxic to aquatic life as it is lipid soluble, while its ionized counterpart ($NH_4^+$) is mostly harmless due to its low permeability in plasma membranes [11].

Table 1-1. Percentage of unionized ammonia in aqueous solution for pH 6-9 and temperature 0-30 °C based on the calculations of Emerson et. al [10].

| Temp (°C) | pKa | pH | | | | | | | | | | | | | | | |
|---|---|---|---|---|---|---|---|---|---|---|---|---|---|---|---|---|---|
| | | 6 | 6.2 | 6.4 | 6.6 | 6.8 | 7 | 7.2 | 7.4 | 7.6 | 7.8 | 8 | 8.2 | 8.4 | 8.6 | 8.8 | 9 |
| 0 | 10.083 | 0.008 | 0.013 | 0.021 | 0.033 | 0.052 | 0.083 | 0.131 | 0.207 | 0.328 | 0.519 | 0.820 | 1.294 | 2.035 | 3.187 | 4.958 | 7.637 |
| 2 | 10.010 | 0.010 | 0.015 | 0.025 | 0.039 | 0.062 | 0.098 | 0.155 | 0.245 | 0.388 | 0.613 | 0.968 | 1.525 | 2.396 | 3.745 | 5.809 | 8.903 |
| 4 | 9.938 | 0.012 | 0.018 | 0.029 | 0.046 | 0.073 | 0.115 | 0.182 | 0.289 | 0.457 | 0.722 | 1.139 | 1.794 | 2.813 | 4.387 | 6.779 | 10.334 |
| 6 | 9.868 | 0.014 | 0.021 | 0.034 | 0.054 | 0.085 | 0.135 | 0.214 | 0.339 | 0.537 | 0.848 | 1.338 | 2.103 | 3.293 | 5.121 | 7.880 | 11.939 |
| 8 | 9.798 | 0.016 | 0.025 | 0.040 | 0.063 | 0.100 | 0.159 | 0.252 | 0.398 | 0.629 | 0.994 | 1.566 | 2.460 | 3.843 | 5.957 | 9.124 | 13.727 |
| 10 | 9.730 | 0.019 | 0.030 | 0.047 | 0.074 | 0.117 | 0.186 | 0.294 | 0.466 | 0.736 | 1.162 | 1.829 | 2.868 | 4.471 | 6.906 | 10.520 | 15.706 |
| 12 | 9.662 | 0.022 | 0.034 | 0.055 | 0.087 | 0.137 | 0.217 | 0.344 | 0.544 | 0.859 | 1.355 | 2.131 | 3.335 | 5.185 | 7.976 | 12.077 | 17.878 |
| 14 | 9.595 | 0.025 | 0.040 | 0.064 | 0.101 | 0.160 | 0.253 | 0.401 | 0.634 | 1.000 | 1.576 | 2.475 | 3.867 | 5.994 | 9.177 | 13.804 | 20.244 |
| 16 | 9.530 | 0.030 | 0.047 | 0.074 | 0.117 | 0.186 | 0.294 | 0.466 | 0.736 | 1.162 | 1.829 | 2.868 | 4.471 | 6.905 | 10.519 | 15.706 | 22.798 |
| 18 | 9.465 | 0.034 | 0.054 | 0.086 | 0.136 | 0.216 | 0.342 | 0.540 | 0.854 | 1.347 | 2.117 | 3.315 | 5.154 | 7.929 | 12.010 | 17.785 | 25.531 |
| 20 | 9.401 | 0.040 | 0.063 | 0.100 | 0.158 | 0.250 | 0.396 | 0.626 | 0.988 | 1.557 | 2.445 | 3.821 | 5.923 | 9.073 | 13.655 | 20.041 | 28.430 |
| 22 | 9.338 | 0.046 | 0.073 | 0.115 | 0.183 | 0.289 | 0.457 | 0.723 | 1.141 | 1.796 | 2.817 | 4.392 | 6.786 | 10.344 | 15.459 | 22.470 | 31.475 |
| 24 | 9.276 | 0.053 | 0.084 | 0.133 | 0.211 | 0.333 | 0.527 | 0.833 | 1.314 | 2.067 | 3.236 | 5.034 | 7.750 | 11.751 | 17.426 | 25.064 | 34.645 |
| 26 | 9.214 | 0.061 | 0.097 | 0.153 | 0.242 | 0.384 | 0.607 | 0.958 | 1.511 | 2.373 | 3.710 | 5.755 | 8.823 | 13.298 | 19.555 | 27.811 | 37.911 |
| 28 | 9.154 | 0.070 | 0.111 | 0.176 | 0.279 | 0.441 | 0.697 | 1.100 | 1.733 | 2.719 | 4.241 | 6.560 | 10.012 | 14.990 | 21.843 | 30.697 | 41.246 |
| 30 | 9.094 | 0.080 | 0.128 | 0.202 | 0.320 | 0.506 | 0.799 | 1.261 | 1.983 | 3.108 | 4.837 | 7.455 | 11.322 | 16.830 | 24.284 | 33.700 | 44.617 |

### *1.2.2 Overview of Ammonia Toxicity*

Ammonia is important in various industries, such as in the refrigeration industry and in agriculture, and is also present in different metabolic cycles in fish and humans [3,12]. Therefore, it is important to consider how ammonia affects these areas and its harmful effects. Eutrophication is an important environmental problem that can arise from high ammonia levels in water due to, for example, agriculture run-offs, intense fish farming or anthropomorphic waste. Nutrients such as ammonium, nitrate and phosphate are necessary for the growth of photosynthetic organisms, however when in excess these organisms start to consume oxygen instead of releasing it due to accelerated growth [3]. Some of the problems associated with eutrophication include increased frequency and intensity of algal blooms, which can cause red tides, foaming, and can be toxic to fish and other aquatic life forms [13]. Although $NH_3$ is naturally produced by fish, in certain conditions it can contribute to eutrophication and reach toxic levels for the aquatic life. Ammonia toxicity in fish has been widely studied and comprehensive reports of how it is produced and excreted and its toxic effects in freshwater and saltwater fish can be found in literature [12,14,15]. The degradation of α-amino group of amino acids is responsible for most of the ammonia produced in fishes. $NH_3$ can accumulate across the phospholipid bilayer of the branchial epithelium, as $NH_3$ can rapidly diffuse across thin biomembranes while $NH_4^+$ is not as permeable [12]. Recently, however, it has been found that the permeation of ammonia can also happen through transporters as $NH_4^+$ can substitute $K^+$ in ion transporters [15]. For most ammonotelic fishes, unionized $NH_3$ is excreted through the fish gills and is then dispersed in the surrounding water. However, this becomes a problem for fish exposed to high pH as the gradient for $NH_3$ diffusion is reduced which can lead to a build-up of ammonia inside the fish [16]. This could cause a dangerous rise on plasma ammonia levels or toxic levels of ammonia to accumulate in the fish body leading to the death of the specimen [12].

In humans, ammonium has been deemed as not harmful for human consumption by authorities as the WHO and the U.S. EPA [6,17], however some studies have shown that ammonium can be toxic in certain cases [18–20]. The urea cycle occurs in the liver and it converts $NH_4^+$ to urea prior to renal excretion. It also serves to maintain low levels of the $NH_4^+$ ion in the serum, as ammonia is mostly present in its ionic form in physiological conditions. The brain is particularly susceptible to the ammonia toxic effects specially during early stages of development [20]. The brain cannot convert $NH_4^+$ to urea, but it uses another route by synthesizing glutamine from glutamate and $NH_4^+$ [19]. Liver failure or urea cycle disorder can cause ammonia levels to rise, which can lead to hyperammonemia - an excess of ammonia in the blood. While in adults the toxic effects of hyperammonemia are

generally reversible, it can lead to severe cognitive impairment, seizures and cerebral palsy in infants [21]. 200 – 500 µM of $NH_4^+$ in blood during the first two years of life is enough to cause irreversible damage [19]. Restriction of proteins in the diet, dialysis or liver transplant are some of the treatments for those who suffer hyperammonemia [18,20]. It is also known that ammonia can corrode certain metals, such as brass and copper [22]. Metallic corrosion is associated with economic and safety hazards, therefore when metal parts are in close contact with high concentrations of ammonia they should be made of non-corrosive parts, such as stainless steel or aluminum [22,23].

### *1.2.3 Policies of Ammonia in Water*

The threshold concentration for ammonia differs depending on the water body and the intended application. Some countries, like the USA and the UK, have specified $NH_3$ and $NH_4^+$ quality standards in freshwater, saltwater and/or drinking water. In drinking water, the European Union (EU) directive 98/83/EC permits a maximum of 0.5 mg/L of $NH_4^+$ [24]. According to the World Health Organization (WHO), the characteristic odour of ammonia can be perceived at a concentration of more than 1.5 mg/L of $NH_3$ in water, while above 35 mg/L of $NH_4^+$ it can be tasted [6]. In this manner, the U.S. Environmental Protection Agency (EPA) classified ammonia as not classifiable as human carcinogenic with a lifetime threshold of 30 mg/L in the 2018 Drinking Water Standards and Health Advisories Tables EPA 822-F-18-001 [17]. For surface water, the WFD for England and Wales of 2015, which includes the European Directives for surface water and groundwater, present various ammonia concentrations depending on characteristics of the freshwater, such as altitude and alkalinity. For rivers and lakes, high to poor “90 percentile” standards range from 0.2 to 1.1 mg/L (types 1, 2, 4, and 6) or 0.3 to 2.5 mg/L (types 3, 5, and 7) of total ammonia nitrogen (TAN), where TAN is the total amount of nitrogen in $NH_3$ and $NH_4^+$ [25]. Types 1, 2, 4, and 6 have either low alkalinity or moderate alkalinity at high altitudes, while types 3, 5, and 7 have moderate to high alkalinity at low altitudes. The “90 percentile” standard refers to when the measured pollutant (in this case, ammonia), is greater than the standard for 10% or more of the time. For groundwater, the threshold concentration is 0.29 mg/L for total ammonia [25].

The U.S. EPA 820-F-13-013 published in 2013 a recommendation guideline for aquatic life protection of the maximum ammonia concentration at ambient freshwater at pH 7 and 20 °C, where unionised $NH_3$ accounts for approximately 0.39% of the total ammonia [5]. They have two different standards: acute, a 1-hour average of measured ammonia, and chronic, a 30-day average. Both should not be exceeded more than once every three years. The acute standard is 17 mg TAN/L and the chronic standard is 1.9 mg TAN/L [5]. Brazil also has legislations for ammonia concentrations in

different types of freshwater (type 1-3) and seawater described in the Conama Resolution 357/2005 [26]. The maximum allowed ammonia concentration is divided for different pH in freshwater, for less than 7.5 up to more to 8.5, e.g. for a freshwater body type 1 of pH < 7.5, the TAN is 3.7 mg/L and for 8.0<pH<8.5 it is 1.0 mg/L. Australian and New Zealand Environment and Conservation Council (ANZECC) & Agriculture and Resource Management Council of Australia and New Zealand (ARMCANZ) 2000 guidelines present ammonia thresholds both in freshwater and seawater, with a comprehensive table of TAN from pH 6.0 to 9.0 [27]. For freshwater, the trigger value for ammonia is 2570 µg TAN/L for pH 6.0 and 180 µg TAN/L for pH 9.0, while in seawater it is 5960 µg TAN/L for pH 6.0 and 140 µg TAN/L for pH 9.0 [27]. The U.S. EPA also has an ammonia standard for saltwater published in 1989 (EPA 440/5-88-004), where the acute standard is 0.035 mg/L of $NH_3$ and the chronic standard is 0.233 mg/L of $NH_3$ [14]. A table summarizing all the legislations for ammonia concentration in water bodies can be seen in Table 1-2. It can be observed that each legislation utilizes its own ammonia measurement unit (as $NH_3$-N, $NH_4^+$, $NH_3$, TAN), which makes it difficult to compare the threshold values.

To make it easier to compare the ammonia thresholds in different countries and regions, a bar chart with standardized unionized $NH_3$ concentration in micromolar (µM) assuming a pH range of 6.0 to 9.0 for freshwater, 6.5 to 9.5 for drinking water, 7.5 to 8.5 for seawater, and a temperature of 20°C can be seen in Figure 1.2. The percentage of $NH_3$ at different pH was calculated using the equation provided by Emmerson et al. and the molar masses used were: 14.006 mg/mmol for N, 17.031 mg/mmol for $NH_3$ and 18.039 mg/mmol for $NH_4^+$ [10]. Naturally, if there is a change in pH, temperature or salinity, the appropriate concentration should be recalculated. Furthermore, this guideline should not be taken as a substitute for the standards given by the authorities. As can be observed from Figure 1.2, the threshold varies considerably between different water bodies. Freshwater and drinking water have the highest $NH_3$ thresholds at the upper limit pH, although it is important to notice some aspects when calculating these limits. While Australia provided a comprehensive table with different TAN depending on the pH of the water body, to the best of the authors knowledge, the EU and USA guidelines did not have the exact threshold for ammonia at different pH. Therefore, the single value provided was recalculated for pH 6 to 9, making it not as reliable as the values provided by the Australia and Brazilian guidelines, which could explain the threshold difference for these countries. However, a general trend seems to be a higher upper limit of $NH_3$ in freshwater than in seawater when comparing the guidelines from the same country.

Table 1-2. Country/region legislation for threshold concentrations of ammonia as a function of the water type.

| Country/Region | Policy | Drinking Water | Freshwater | Groundwater | Seawater |
|---|---|---|---|---|---|
| **European Union** | (a) Directive 98/83/EC [24]<br>(b) WFD for England and Wales of 2015 [25] | 0.5 mg/L as $NH_4^+$ [a] | 0.2 – 1.1 mg/L as TAN (Types 1, 2, 4, 6)[b]<br>0.3 – 2.5 mg/L as TAN (Types 3, 5, 7)[b] | 0.28 mg/L as total ammonia[b] | Long term: 21 µg/L as $N\text{-}NH_3$[b] |
| **United States** | (c) U.S. EPA 822-F-18-001 [17]<br>(d) U.S EPA 820-F-13-013 [5]<br>(e) U.S. EPA 440/5-88-004 [14] | Lifetime: 30 mg/L[c] | Acute: 17 mg/L as TAN[1,d]<br>Chronic: 1.9 mg/L as TAN[1,d] | - | Acute: 0.035 mg/L as $NH_3$[e]<br>Chronic: 0.233 mg/L as $NH_3$[e] |
| **Brazil** | Resolução Conama 357/2005 [28] | - | 0.5 – 3.7 mg/L as TAN ( Types 1 and 2)<br>1.0 – 13.3 mg/L as TAN (Type 3) | - | 0.4 mg/L as TAN (Type 1)<br>0.7 mg/L as TAN (Type 2) |
| **Australia** | ANZECC & ARMCANZ (2000) [27] | - | 2570 – 180 µg/L as TAN (6 < pH < 9) | - | 5960 – 140 µg/L as TAN (6 pH < 9) |

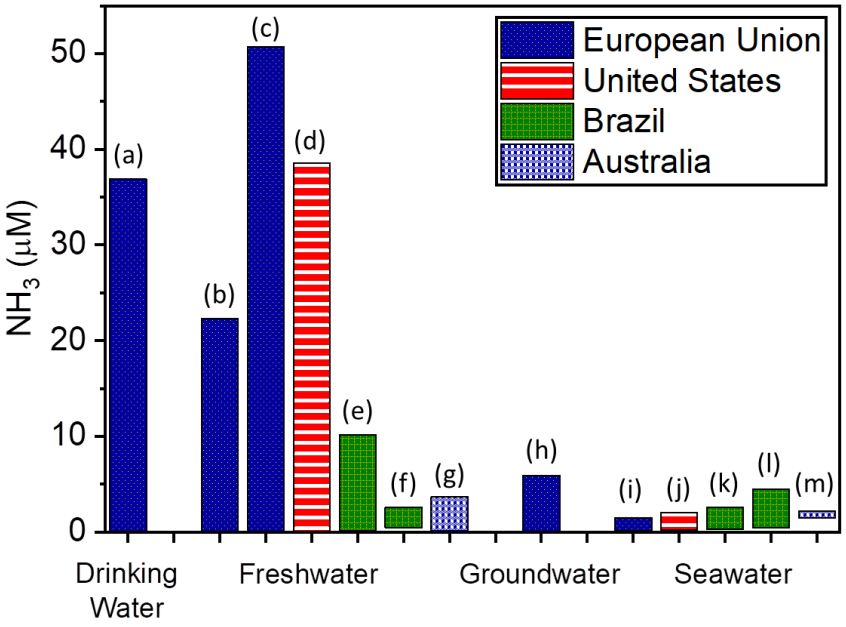


Figure 1.2. Ammonia threshold concentration range in different water bodies according to each legislation. (a) Directive 98/83/EC [24]. (b,c,h,i) WFD for England and Wales of 2015 [25]. (d) U.S EPA 820-F-13-013 [5]. (e,f,k,l) Resolução Conama 357/2005 [28]. (g,m) ANZECC & ARMCANZ (2000) [27]. (j) U.S. EPA 440/5-88-004 [14].

Considering this, an appropriate sensor needs to be able to detect the analyte in the nano and micromolar range in freshwater and drinking water if selective to unionized $NH_3$ and in the nanomolar range in seawater. If temperature and pH sensors are employed together with the ammonia sensor, and if it is sensitive to the $NH_4^+$ ion, the limit of detection (LOD) can be in the micromolar range as there is usually a higher percentage of $NH_4^+$ than $NH_3$. In seawater, other problems arise due to the high salinity level as it can often interfere with the measurement. Therefore, appropriate detection techniques need to be employed following the standard values for ammonia to monitor it in the given limit range. This makes it a tricky analyte to accurately quantify, especially when considering its dependency to temperature, pH, and salinity.

## 1.3 Nitrate and Nitrite

### *1.3.1 Nitrate in Aquatic Environments*

The World Health Organization has a detailed report on $NO_3^-$ and $NO_2^-$ in drinking water [29]. The $NO_3^-$ ion is the stable form of nitrogen for oxygenated systems and is chemically inert. When reduced by microbes, it produces the $NO_2^-$ ion, a more reactive compound due to its unstable oxidation

state, which can then be further used in the nitrogen cycle [29]. This enzymatic process is dependent on pH and temperature. Increased levels of nitrate have been detected due to the expansion of nitrogenous fertilizers, disposal of wastes from animal farm and changes in land which directly and indirectly impacts the quality of water bodies [30]. This is alarming as elevated levels of nitrate can contribute to eutrophication in freshwater and marine ecosystems. While nitrate is mostly harmless to humans, nitrite has been found to be toxic [31]. As it is considered a hazardous chemical above a certain threshold, many countries have imposed legislations on permitted levels of nitrates and nitrites making them important ions to monitor.

### *1.3.2 Overview of Nitrate Toxicity*

The excess usage of fertilisers containing nitrogenous compounds can lead to nitrate leaching, soil dentification, and volatilisation of nitrogen [7]. The volatilisation of nitrogen compounds contributes to the release of greenhouse gases such as nitric oxide and nitrous oxide [2]. Meanwhile, nitrate leaching is a major cause of eutrophication, as it contaminates groundwater, river water, and other water bodies [3,7]. Furthermore, high concentrations of the $NO_2^-$ ion can be toxic to fish. Usually, it is present at very low concentrations naturally (< 0.005 mg/L), however certain conditions such as acidity, accumulation in deep layers of lakes during stratification, and the presence of human activities can cause the accumulation of $NO_2^-$ [32]. $NO_2^-$ has an affinity for the branchial $Cl^-$ uptake route, which can lead to dangerous internal levels of $NO_2^-$ [33]. The toxicity arises mainly from the oxidation of haemoglobin to methaemoglobin by the diffusion of $NO_2^-$ into red blood cells, where it oxidises Fe to the +3 oxidation state [32]. Methaemoglobin reduces the capacity of oxygen transportation in blood. This gives the fish blood a brownish colour, which can be a visual manner of inspecting if the water body suffers from high levels of $NO_2^-$ [32,33]. Furthermore, $NO_2^-$ ions influence the $K^+$ balance, which can lead to heart failure and nerve malfunction [33].

In humans, a high nitrate diet contributes to the development of diseases such as gastric and bladder cancer, and methemoglobinemia. The toxicity is generated by the presence of $NO_2^-$ ions resulting in methemoglobinemia, which can cause cyanosis and asphyxia [29,31]. The reactive $NO_2^-$ ion can interfere with the oxygen transport system, causing irreversible conversion of hemoglobin to methemoglobin in the blood stream, much like the mechanism observed in fish. This is particularly problematic for infants and pregnant women [34]. The $NO_2^-$ ion can also form carcinogenic N-nitrosamines by reacting with secondary amines and amides in the stomach [34], as a result there are limits to the concentration of nitrate in drinking water as detailed below.

### *1.3.3 Policies of Nitrate/Nitrite in Water*

Table 1-3. Country/region legislation for threshold concentrations of nitrate and nitrite as a function of the water type.

| Country/Region | Policy | Drinking Water | Freshwater | Groundwater | Seawater |
|---|---|---|---|---|---|
| **European Union** | (a) Directive 98/83/EC [24]<br>(b) WFD for England and Wales of 2015 [25] | 50 mg/L as $NO_3^-$ [a]<br>0.50 mg/L as $NO_2^-$ [a] | - | 37.5 mg/L as $NO_3^-$ [b] | - |
| **United States** | U.S. EPA Drinking Water Regulation[35] | 10 mg/L as $NO_3^-$<br>1 mg/L as $NO_2^-$ | - | - | - |
| **Brazil** | Resolução Conama 357/2005 [28] | - | 10 mg N-$NO_3^-$/L<br>1 mg N-$NO_2^-$/L | - | 0.4 mg N-$NO_3^-$/L<br>0.07 mg N-$NO_2^-$/L |
| **Australia** | (a) Australian Drinking Water Guidelines 6 2011 [36] | 50 mg/L as $NO_3^-$ and 3 mg/L as $NO_2^-$ [a] | - | - | - |

$NO_3^-$ is usually considered toxic to humans once it has been oxidized to $NO_2^-$ [29]. As with ammonium, the nitrate/nitrite environmental threshold changes depending on the country. However, the given threshold concentration tends to be more straightforward as it is not pH and temperature dependent. The threshold concentration for drinking water in the EU according to Directive 98/83/EC is 50 mg/L for $NO_3^-$ and 0,50 mg/L for $NO_2^-$. Furthermore, the condition of $[NO_3^-]/50 + [NO_2^-] \leq 1$ in mg/L must be always ensured. For water treatment works, the threshold for $NO_2^-$ is 0,1 mg/L. In the USA, the EPA Drinking Water Regulation states that the maximum allowed concentration for $NO_3^-$ is 10 mg/L and 1 mg/L for $NO_2^-$[35]. For groundwater, the WFD for Engladn of 2015 states that the threshold concentration is 37.5 mg/L for $NO_3^-$ [25]. The Brazilian Conama Resolution 357/2005 states that a maximum quantity of 10 mg N-$NO_3^-$/L and 1 mg N-$NO_2^-$/L is permitted. The Australian Drinking Water Guidelines of 2011 indicate that a threshold concentration of 50 mg/L for $NO_3^-$ and 3 mg/L of $NO_2^-$ should be maintained to prevent nitrate toxicity in infants [36]. However, it is stated that adults can safely drink up to 100 mg/L of $NO_3^-$ [36]. In some cases, $NO_3^-$/$NO_2^-$ and $NH_4^+$ are considered as part of the DIN concentration threshold, but these policies were not included in this

chapter. Table 1-3 contains a summary of the threshold concentrations for the EU, USA, Brazil and Australia.

## 1.4 Detection Techniques for Ammonia and Nitrate/Nitrite in Water

Different techniques have been implemented for the detection of ammonia and nitrate in water, with several materials and reagents used for the selective detection of these compounds. Although there are techniques that detect the total dissolved nitrogen (TDN) or DIN, this chapter will focus on the individual detection of these nitrogenous compounds. The main detection techniques can be divided into optical and electrochemical methods, with spectrophotometry, fluorometry, and electrochemical sensors being the most researched.

***Spectrophotometry.*** In the spectrophotometer method, an electromagnetic wave from a light source irradiates the analyte, and the light amount absorbed (or transmitted) is then measured. A spectrophotometer usually is comprised of a stable light source, a sample container, a radiation detector, and a signal processor and readout unit [37]. A schematic representation of an UV-VIS spectrophotometer is given in Figure 1.3. The sample concentration is proportional to the decrease in radiation power, and it is usually given by the Beer-Lambert law:

$$A = \varepsilon C \times l \tag{1.1}$$

where $A$ is the absorbance, $\varepsilon$ is the molar absorption coefficient, $C$ is the sample concentration, and $l$ is width of the sample. $\varepsilon$ is dependent on the incident wavelength radiation, the temperature, and the solvent employed. From the Beer-Lambert law, it is observed that the molar absorptivity is constant, and the absorbance is proportional to the concentration given the same parameters.

Spectrophotometric methods have been widely employed for the detection of ammonia and nitrite in freshwater and seawater and it is the standard method advised by environmental agencies such as the U.S. EPA [38–40]. Most of the optical methods require reaction reagents and pre-treatment of the sample due to the presence of interferants commonly found in real water samples [41]. Many of these reagents are often toxic or harmful to the environment and to humans, as for example the mercury in the Nessler's reagent method or the phenol in the indophenol blue method [42]. Although the pre-treatment of samples and the use of reagents can be a hindrance for on site inspections, they are optimized to offer a higher precision and selectivity for the analyte of interest. Spectrophotometers

are usually costly, and analysis is often done in laboratories, however there are some portable spectrophotometers that can be used in routine inspections. Some other advantages of this method include a low LOD and a low volume of sample needed, but there is usually a limited working range [43]. As the reaction changes color if the analyte of interest is present, the samples can also be visually inspected for a faster qualitative analysis. Turbidity can influence the results, so natural water samples are more suited for this method [42].

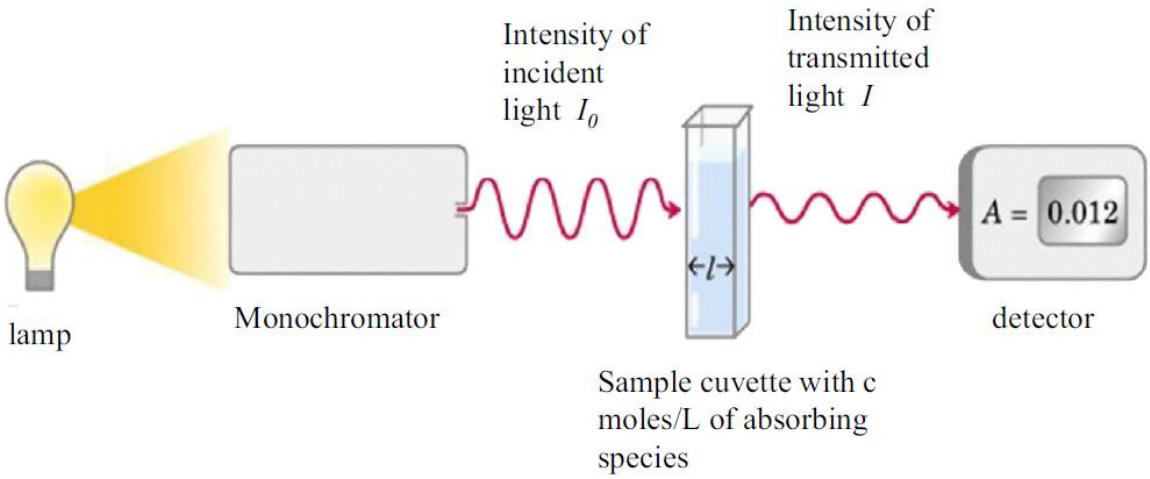


Figure 1.3. Schematic representation of an UV-Vis absorption measurement of a given sample. A light source irradiates the sample cell with an intensity $I_0$ and a transmitted light $I$ is measured by the detector [37].

***Fluorometry.*** Another method widely employed is fluorescence spectrophotometry. It is quite similar to the spectrophotometric technique however it instead analyses the fluorescence light emitted by the sample after excitation by a light source (Figure 1.4). The fluorescence is detected with photomultiplier tubes and the spectrum can be analyzed by a signal processor and readout unit [44]. As a general rule, the same fluorescence emission spectra are observed irrespective of the excitation wavelength. Unlike in spectrophotometric detection, no sample pre-treatment is needed, although the use of reagents is still necessary. Fluorometry allows for high sensitivity due to the nature of its detection. The technique can be automated with a high sample throughput and high precision by employing it together with an autonomous batch analyzer (ABA) or a flow injection analysis (FIA) [45]. However, some drawbacks are that for automated processes the sample usually needs to be analyzed in a laboratory, as the technique needs expensive equipment and trained personnel for daily calibration, routine operation and maintenance [45]. Although portable fluorometers are not

uncommon, the high reagent consumption and frequent need of calibration makes it harder for continuous *in situ* analysis.

Another important detection technique for the $NH_4^+$ and $NO_2^-/NO_3^-$ ions is electrochemistry. As it is the main technique explored throughout this thesis, it is detailed in the section below.

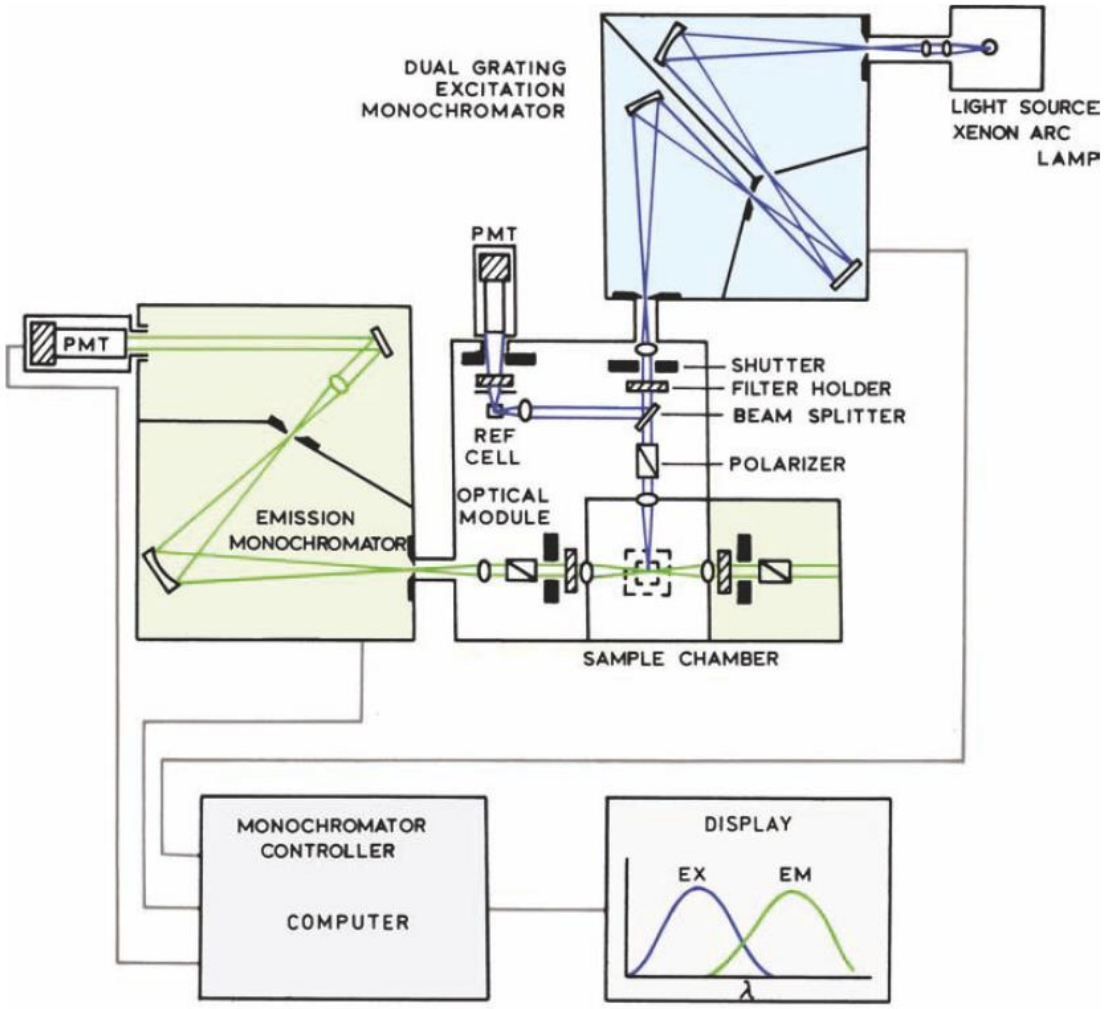


Figure 1.4. Schematic representation of a spectrofluorometer [44].

### *1.4.1 Electrochemistry*

Electrochemistry is a branch of chemistry that deals with the relationship between electrical and chemical effects. A significant part of this field focuses on the analysis of the electrical energy generated by chemical reactions when an electrical current is input in the system [46]. This is important for many fields, including analysis of corrosion, characterization of devices, e.g. electrochemical sensors, batteries, and supercapacitors, and can be used to produce different

technologies, e.g. electroplating or electrocatalysis [46]. The setup usually involves an electrochemical cell with a three-electrode setup, a supporting electrolyte solution and a potentiostat. A schematic representation of the complete setup can be seen in Figure 1.5a and that of an electrochemical cell in Figure 1.5b. The three-electrode setup consists of a working electrode (WE), where the electrochemical event of interest occurs, a counter electrode (CE), a high surface area inert electrode used to complete the circuit for current flow, and a reference electrode (RE), an electrode that has a stable potential that is used as a reference point [47]. Common WE are platinum, carbon, silver and gold, with the most important aspect being their inertness at the potential window of interest. The same aspect can be applied to the CE, where inertness plays an important role, therefore a Pt wire or disk is usually employed, although carbon-based CEs also exist [47]. REs usually have a stable equilibrium potential independent of the electrolyte used, with standard ones including the saturated calomel electrode (SCE), standard hydrogen electrode (SHE), and the AgCl/Ag electrode [47].

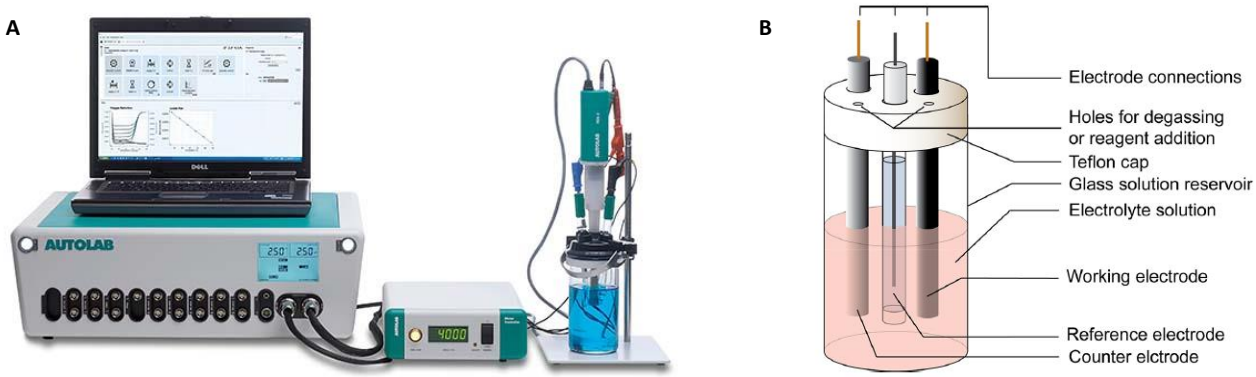


Figure 1.5. a) A three-electrode setup connected to a Methrom Autolab electrochemical workstation. b) Schematic representation of the electrochemical cell and its main components [47].

Another important aspect of the electrochemical cell is the supporting electrolyte, which consists of a salt dissolved in the solvent. Large concentrations of supporting electrolytes are needed to limit analyte migration to the electrode surface, as usually diffusion is the only type of mass transportation included in theoretical models and simulations. They are also important to maintain the conductivity of the solution, as the ions are responsible for carrying the electrons through the solution, maintaining the electron neutrality of the system [47]. After choosing the appropriate electrodes, solvent and supporting electrolyte, the experiment can begin. Usually, one or more or the following parameters can be measured: potential ($E$), current ($i$), charge ($Q$) or time($t$) [48].

Electrochemical sensors present the possibility of miniaturized, low-cost, portable sensors that do not require a variety of reagents and specialized personnel to operate it. Furthermore, the sensing material can be varied to improve the sensing range, cross-sensitivity and stability [49]. A strong advantage over other techniques is the possibility of continuous water quality measurement at a low cost. However electrochemical sensors have some drawbacks, which include higher LOD, short lifetime (although a lifetime of a year or more can be achieved in commercial sensors as long as they are regularly calibrated), and cross-sensitivity [49]. The sensitive material selection is an essential sensor fabrication factor as it dictates the sensor selectivity, sensitivity, and stability - three of the most important parameters in a sensor. Another issue is the reference electrode performance and stability, particularly for miniaturized electrochemical sensors, as this can dictate how often the sensor needs to be calibrated or replaced [50–52].

Electrochemical sensors consist of a receptor, a transducer, and a signal processor (Figure 1.5a). These sensors are usually classified by the transduction type, which consists of conductometric, impedometric, potentiometric, amperometric, and voltammetric transduction modes (Figure 1.5b) [53]. Conductometric and impedometric sensors use the change in conductivity that arises when the sensing material interacts with the analyte. While conductometric sensors are based on the migration of ions of opposite charge in the presence of an electric field between two electrodes, impedometric sensors give more characterization details on the interaction of the sensing material with the analyte solution [53]. The latter can detect the double-layer formation through the electrochemical impedance spectroscopy technique as it is sensitivity to surface phenomena and change of bulk properties [54,55]. Potentiometric and amperometric sensors choose a constant amplitude signal to measure the correlate changing concentration with the output [56,57]. For potentiometric sensors, no current passes through the system and the potential difference between the working electrode and the reference electrode is measured using a technique called open circuit potential (OCP). For amperometric sensors, a constant voltage is selected where the sensor will have a linear current response to a changing concentration of analyte [53]. Voltammetry sensors implement a voltage sweep that shows redox peaks of the analyte or substrate at a potential intrinsic to the material. Different voltammetry techniques exist, and their suitability depends on the intended outcome of the measurement. Some techniques include cyclic voltammetry (CV), linear sweep voltammetry (LSV), differential pulse voltammetry (DPV), and square wave voltammetry (SWV) [58,59]. Different techniques can be used depending on what information is wanted from the system. Of the many existing techniques, the CV, DPV, and EIS techniques are discussed in more detail below, plus the

electrochemical double-layer model, which is an important concept to understand how the analyte interacts with the electrodes.

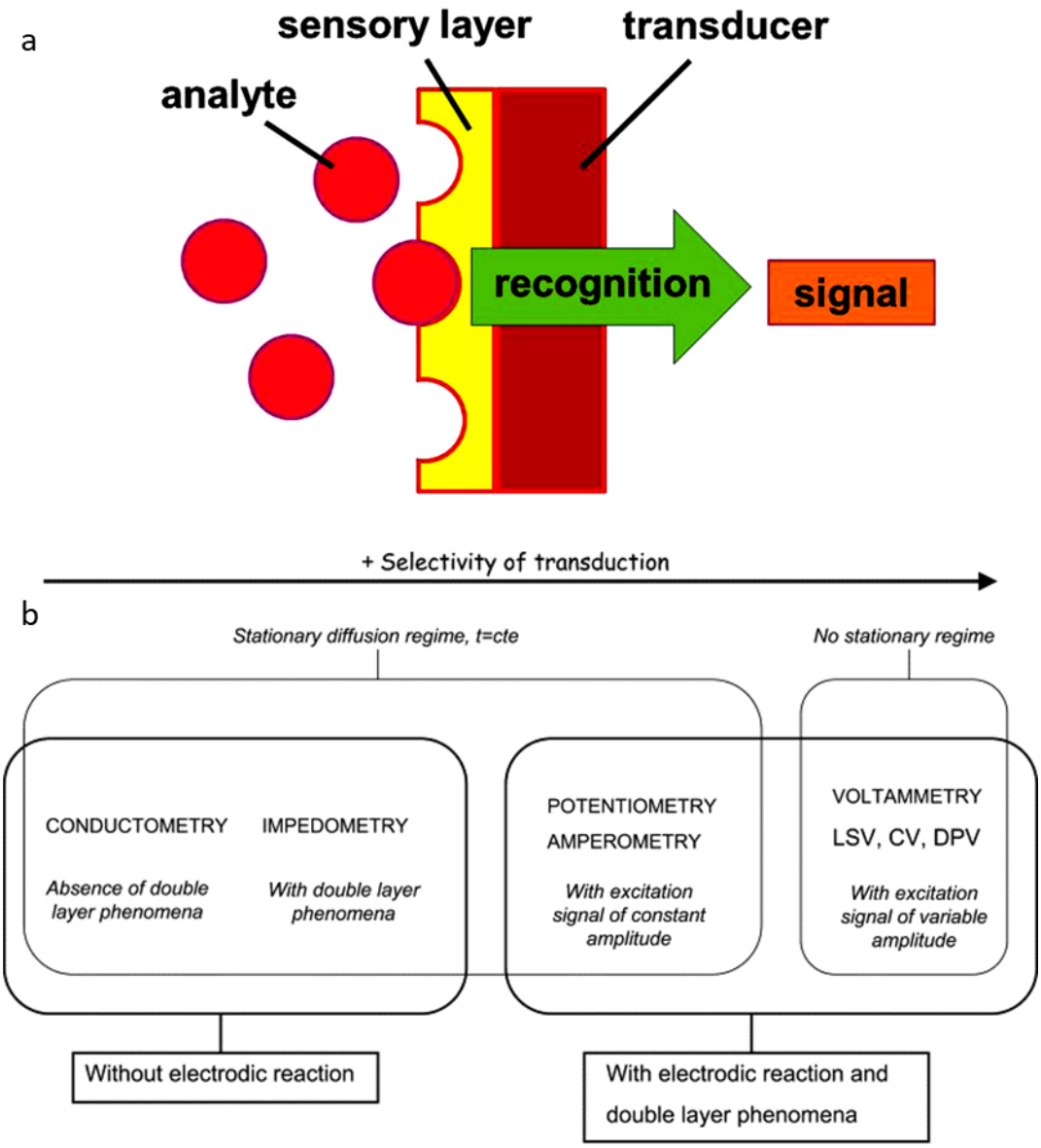


Figure 1.6.(a) Electrochemical sensors device scheme [60] and (b) transduction classification according to IUPAC classification [53].

### *1.4.1.1 The Electrochemical Double-Layer Model*

The interface region of an immersed electrode with its surrounding electrolyte solution is particularly important to understand the electrochemical double-layer occurrence. The general model is constituted of an inner layer, also called compact, Helmholtz or Stern layer, that is the closest to the electrode surface, which can contain solvent molecules, ions or other molecules specifically

adsorbed at the electrode, and a diffuse layer [46]. To better explain the interaction of each layer, the double layer is divided into two planes: the inner Helmholtz plane (IHP) and the outer Helmholtz plane (OHP), which is represented in Figure 1.7a. The IHP consists of specifically adsorbed ions up to a distance $x_1$ while at the OHP, solvated ions interact with the charged metal at a distance $x_2$ [46,61]. The diffuse layer starts from the OHP and stretches to the bulk of the solution. The reason the double layer is such an important phenomenon in electrochemistry is because it significantly affects the measurements. If the electrochemical cell is represented as a circuit, the double layer structure can be viewed as a capacitor, $C_d$ (Figure 1.7b). Therefore, to obtain the desired potential at the WE, first, the double layer must be charged, creating a capacitive current that flows in the electrical circuit. Since this current is not correlated to the reduction or oxidation of the analyte or substrate, it often interferes with the results of the electrochemical experiments [46,61]. The final current would then be the sum of the faradaic current, which corresponds to the oxidation or reduction of chemicals, and the nonfaradaic current, which comes from the capacitive behaviour of the double layer, where no charge-transfer occurs. This could be a problem when the nonfaradaic current is much larger than the faradaic current, therefore many electrochemical methods try to suppress, isolate or filter it, although other techniques might include the double layer current as a way of obtaining more information on the double layer structure [61].

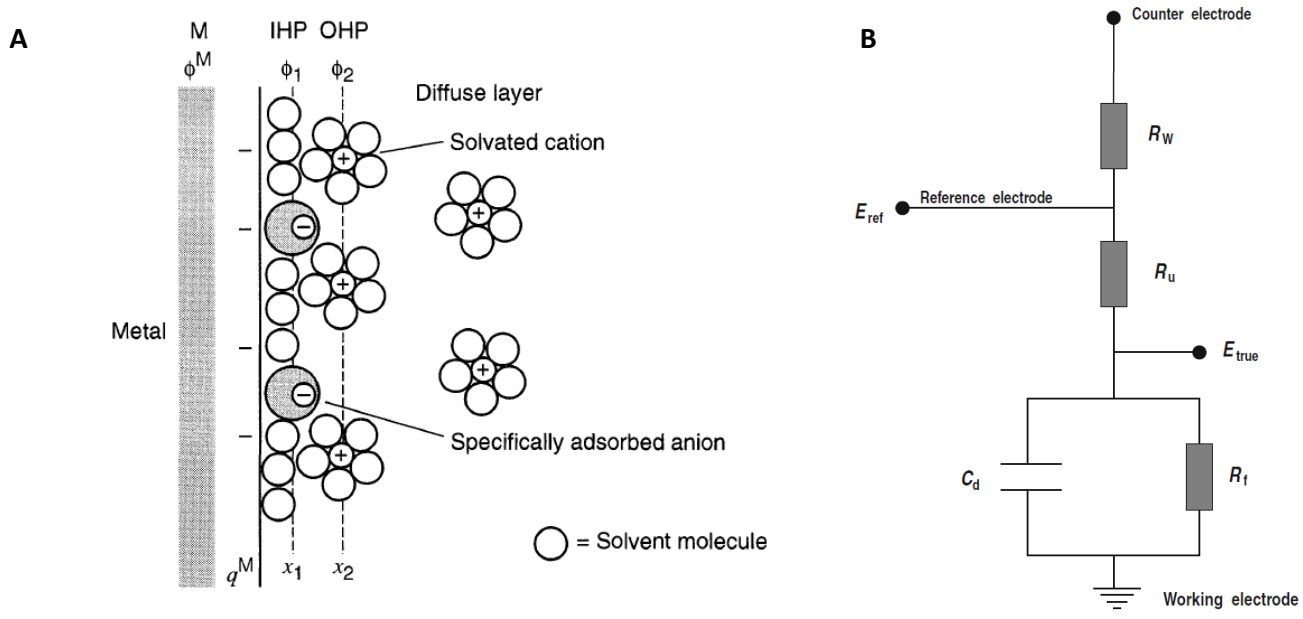


Figure 1.7. a) Double layer region where anions are specifically adsorbed at the inner layer [46]. IHP: inner Helmholtz plane. OHP: outer Helmholtz plane. b) Electrochemical cell circuit, where $R_w$ is the solution resistance, $R_u$ is the uncompensated resistance in the three-electrode system, $R_f$ is the faradaic resistance at the electrode surface and $C_d$ is the differential capacity of the double layer.

As mentioned, the double layer can greatly interfere with the experiment, causing abnormalities in the expected results. A common example is the inhibition of the electrode reaction by adsorption of electroinactive species. However, the opposite can also occur, where the double layer interacts with the analyte and may act as a crucial part of the electrochemical result [46]. This interference, be it good or bad, is highly influenced by the thickness and composition of the double layer. For ionic concentrations greater than 10 mM, the double layer thickness is ~100 Å, while its structure and capacitance depend on various parameters, including electrode material, porosity, type of solvent and supporting electrolytes, temperature, and pressure [61]. To summarize, the double layer generates the nonfaradaic current on an electrochemical experiment and can be thought of as a charge storage layer, while the faradaic current corresponds to a charge transfer reaction.

### *1.4.1.2 Cyclic Voltammetry*

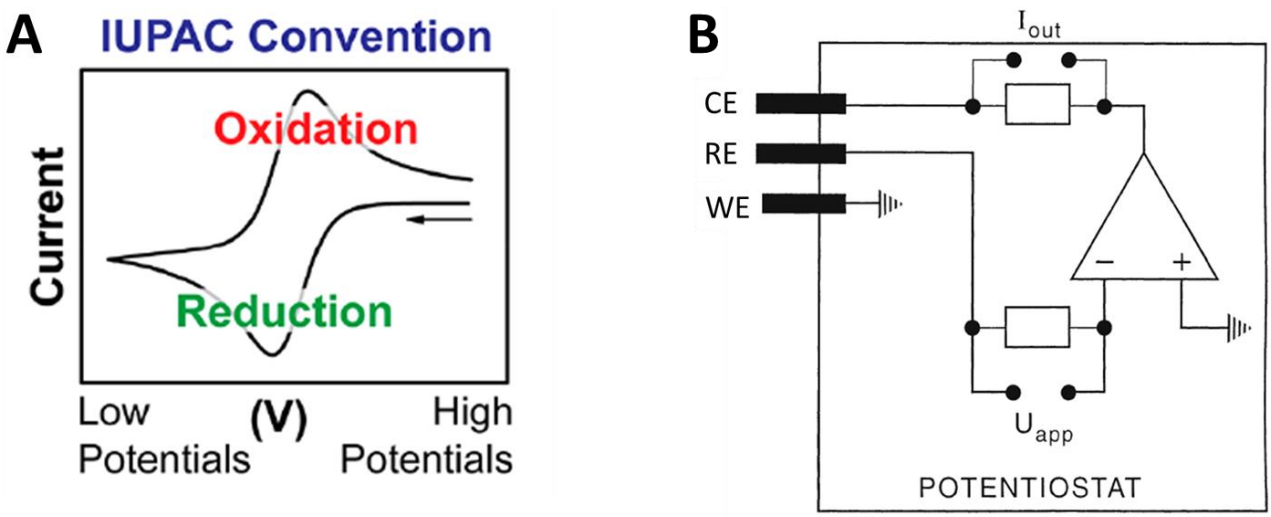


Figure 1.8. a) A cyclic voltammogram following the IUPAC convention, where *E* is swept from high to low potentials, giving rise to the reduction and oxidation peaks [47]. b) Circuit diagram of a simplified three-electrode potentiostat system [61].

CV is a popular electrochemical technique. It gives a plethora of information about the reduction and oxidation of species near the WE surface, and it can also be used to study electron-transfer initiated reactions [46,47]. CV is a technique where a potential is cycled in a stepwise manner, and the output current is measured. This results in a voltammogram (Figure 1.8a), where the redox peaks can be distinguished from the background current given the right condition [47]. A simplified potentiostat circuit is seen in Figure 1.8b, which allows minimal ohmic (*IR*) drop to interfere with the

system by controlling the potential difference between the WE and the RE. By minimising the current flowing through the RE, the potential can keep kept stable as little unwanted chemical reactions would be occurring at the RE [61].

By running multiple CV experiments, it is possible to determine a range of reaction parameters, including [48]:

- The Nerstian (reversible) or non-Nerstian behaviour of a redox couple
- If following a Nerstian behaviour, the number of electrons transferred at a redox reaction
- Reaction mechanisms
- The diffusion coefficient

Depending on the system, interpretation of the results can be quite complex, with different parameters being changed on each run to give the best performance. This could include changing the voltage window, the rate of voltage change per second, the solvent, the supporting electrolyte and the electrodes. Therefore, each experiment requires their own set of parameters, however once found, a good characterization of your system can be achieved.

### *1.4.1.3 Differential Pulsed Voltammetry*

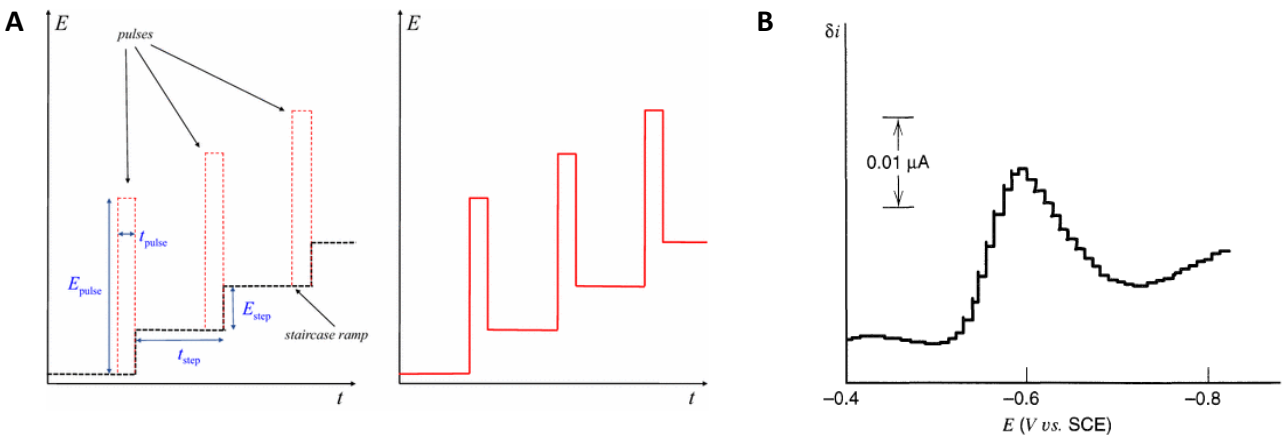


Figure 1.9. a) *Left*: Superimposition of the pulses with the potential ramp. $E_{pulse}$ and $E_{step}$ correspond to the potential of the pulse and the step, respectively and the same occurs for the time, with $t_{pulse}$ and $t_{step}$. *Right*: The resulting potential-time function [62]. b) A typical DPV voltammogram showing a clear redox peak [46].

DPV is a highly sensitive technique that improves the signal-to-noise ratio of the voltammogram. The waveform of the potential is, as the name suggests, given in pulses, with each potential pulse being fixed at small amplitudes (generally 10 to 100 mV), superimposed on a staircase potential ramp (Figure 1.9a) [62]. By sampling the current twice, at the beginning and end of each pulse, the capacitive or background current is nearly eliminated by allowing sufficient decay of the nonfaradaic current [61]. The current output is the result of the difference between the two sampled current values and it is plotted against the base potential (Figure 1.9b). DPV allows for micromolar concentrations to be accurately detected, while CV works better at higher concentrations [46,61].

#### *1.4.1.4 Electrochemical Impedance Spectroscopy*

EIS is one of the most complex techniques in electrochemistry, used to study the kinetics of charges in bulk or interfacial regions, corrosion processes, the charge transfer resistance and general electrochemical characterisation of materials and electrolytes [61]. This technique measures the impedance of the system by applying a small sinusoidal excitation AC potential and detecting the current. The impedance, *Z*, of the system can be given by the quotient of the potential-time function, *E(t)*, by the current-time function, *I(t)*, as in Equation 1.5 [63]:

$$Z = \frac{E(t)}{I(t)} = \frac{E_o \sin(\omega t)}{I_o \sin(\omega t + \varphi)} = Z' + jZ'' = \frac{1}{Y} \tag{1.5}$$

where $E_o$ and $I_o$ are the maximum potential and current signals, $\omega$ is the angular frequency, $\phi$ is the phase shift between *E(t)* and *I(t)*, *Z'* and *Z''* are the real and imaginary part of *Z* represented in the Cartesian coordinates, *j* is the imaginary unit, and *Y* is the complex conductance or admittance. *Z'* is known as resistance and *Z''* as reactance and when represented in a complex plot of -*Z*" vs Z', it is called the Nyquist plot. In this manner, the data can be analysed in terms of an equivalent electrical circuit to reflect the reality of the system as close as possible. It combines resistances, capacitances, inductances and/or other mathematical components to model the system interaction. For electrochemical cells where the electrolyte is a part of the system, four components are usually used: the ohmic resistance, *R*, the capacitance, *C*, the constant phase element, *CPE*, and the Warburg impedance, *W* [63]. More specifically, when an electrode is in contact with the electrolyte, the Randles' circuit is normally implemented. Figure 1.10 shows the schematic representation of a Nyquist plot where the Randles circuit has been used. The information that can be gathered from the model is the solution resistance, $R_S$, the charge-transfer resistance, $R_{CT}$, the double layer capacitance,

$C_{DL}$, and the Warburg impedance, *W*. $R_S$ is the resistance arising from the ions in the electrolyte solution and the electrochemical cell geometry, $R_{CT}$ results from current flow of redox reactions at the interface, and *W* is correlated to the diffusion process from the bulk solution to the interface [63]. The $C_{DL}$, which results from the charge stored in the double layer, can be calculated from the frequency at the maximum of the semicircle. Although the Randles' circuit is widely used for biosensors and electrochemical cells' models, different equivalent circuits can be used to represent other types of impedance data as long as they have a basis in the physical electrochemistry of the system studied [61]. Another way to plot the impedance data is with the Bode plot, where the magnitude of the impedance, $|Z|$, and the phase shift, $\phi$, is plotted against the measuring frequency, *f*, with $f=2\pi\omega$ [61]. In the Bode plot, all the information can be readily understood, and it is sometimes easier to visualize each electrical component. In conclusion, EIS is a powerful characterization tool that can be used in a diverse range of fields to better understand how the system is interacting with the environment.

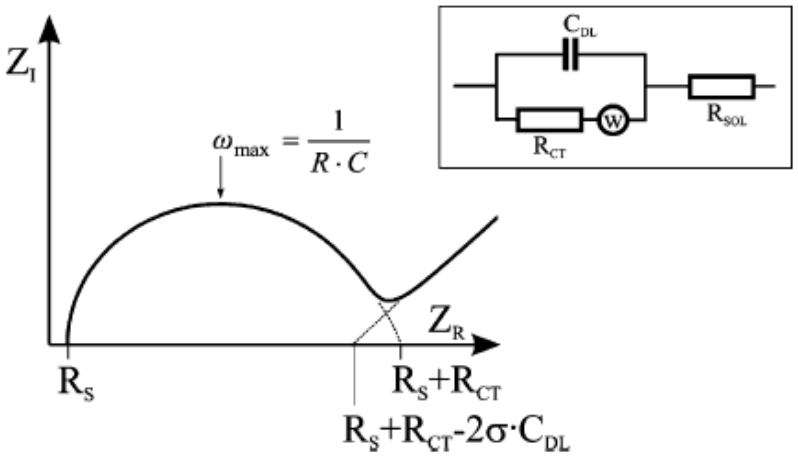


Figure 1.10. Nyquist plot of the Randles' circuit, with $R_S$ referring to the solution resistance, $R_{CT}$ the charge-transfer resistance, $C_{DL}$ the double layer capacitance, and *W* the Warburg impedance [63].

### *1.4.1.5 Printed Electrochemical Sensor Designs*

Different sensor designs are usually employed for these electrochemical techniques. To miniaturize these sensors, fabrication techniques such as screen-printing, inkjet-printing are usually employed. Figure 1.11 exemplifies the different sensor designs commonly used in printed sensors and the output technique. Potentiometric sensors (Figure 1.11a) usually have a sensing electrode covered with a selective membrane and a reference electrode to measure the electromotive force (emf) over time [64,65]. In this way, a correlation between different ion concentrations and the emf can be

done to test for pH or copper ions, for example. Unlike potentiometric sensors, where no current passes through the electrodes, voltametric sensors require a counter electrode for current collection. In this way, they normally have three electrodes: the working electrode, the reference electrode, and the counter electrode (Figure 1.11b). The techniques used rely on faradaic reactions, where electron transfer between the sensitive material in the working electrode interacts with the analyte and produces a selective redox peak [66,67]. Lastly, for impedimetric/conductimetric sensors, the spiral pattern, or an interdigitated electrode (IDE) is normally used as it increases the effective surface-to-volume ratio of the electrode, leading to a higher conductivity and ion diffusion, which influences the signal intensity [68].

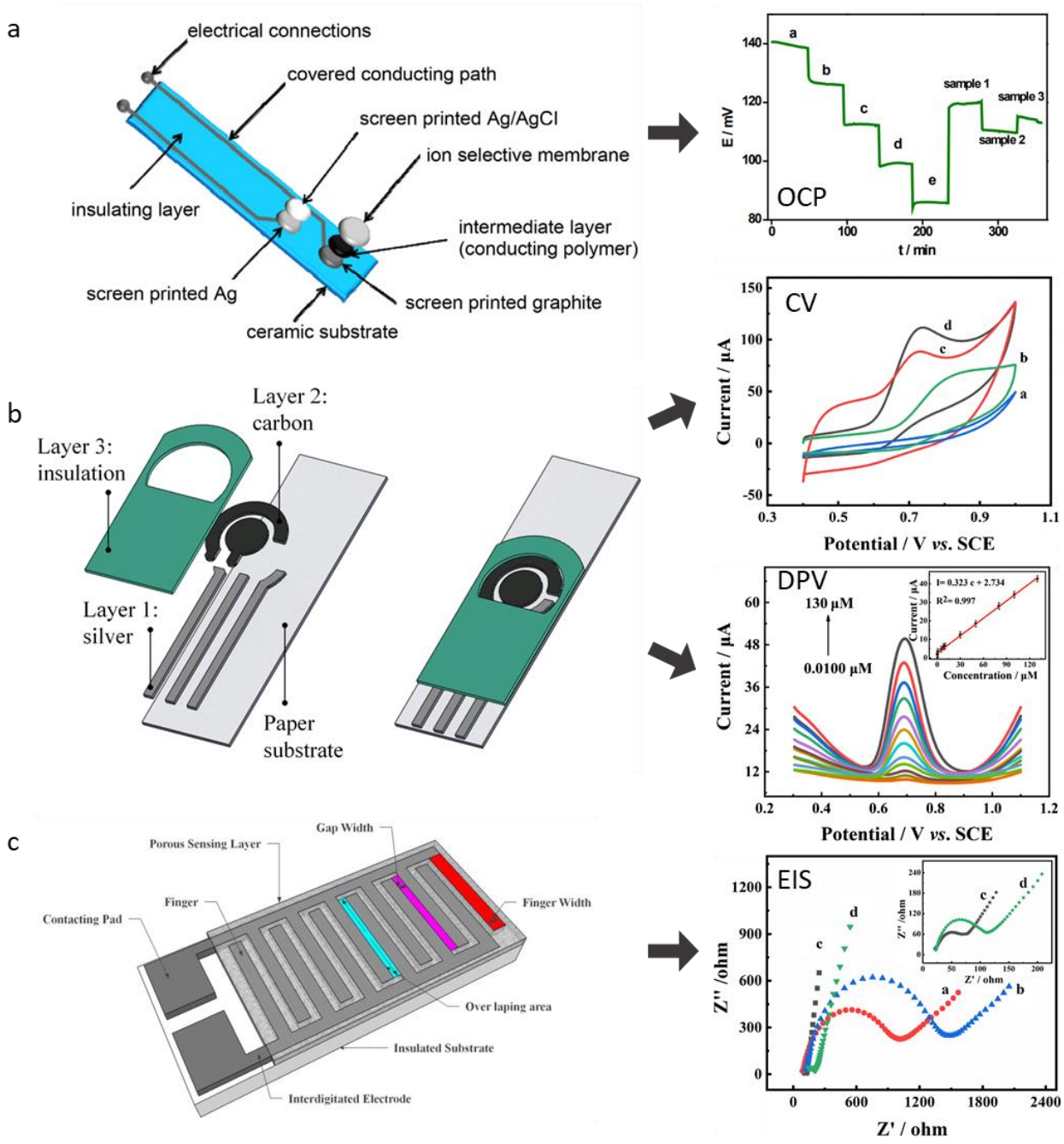


Figure 1.11. Common printed sensor designs used for the different electrochemical techniques and an illustration of the graphical output for standard techniques employed in electrochemical analyte detection. (a) Potentiometric sensor design and the signal output for OCP [65]. (b) Voltametric 3-electrode design [69] and CV and DPV output [67]. c) Impedimetric interdigitated sensor [70] and the EIS output [67].

### *1.4.2 Summary of the Detection Techniques*

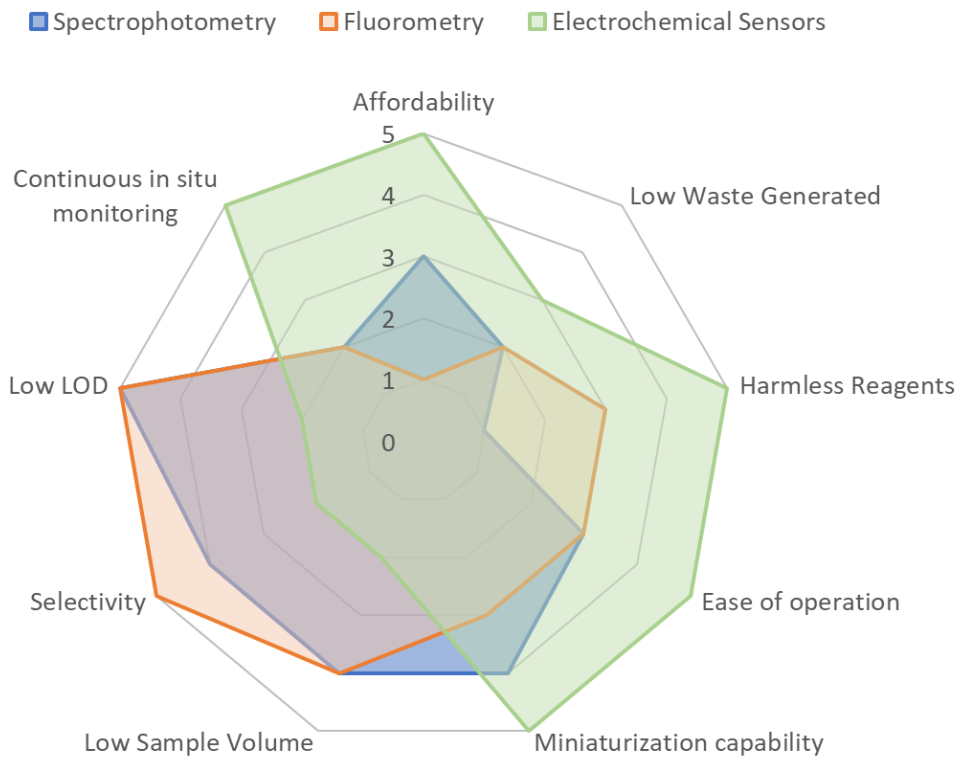


Figure 1.12. Comparison of common techniques used for the detection of $NH_4^+/NH_3$ and $NO_2^-/NO_3^-$ in water bodies.

An overview of common and upcoming methods for dissolved $NH_3$ and $NO_3^-$/ $NO_2^-$ is given in Table 1-4. Furthermore, the detection techniques can be visually summarized in Figure 1.12. It can be concluded that each technique has its advantages and disadvantages over the others. While electrochemical sensors possess the highest potential for continuous *in situ* water monitoring, the other techniques are more mature, so they can achieve higher precision and selectivity. Spectrophotometry and electrochemical sensors are usually employed in natural water, where salt interference is low, while fluorometry is the technique most often used in seawater. Considering these aspects and that electrochemical sensors are an ongoing research topic, versatile, and provide the possibility of real-time measurement coupled with good detection limits, this thesis focuses on the development of new electrochemical sensors for dissolved ammonia and nitrite detection. The next subsections cover in more detail specific examples of sensors and detection techniques used for ammonia and nitrite/nitrate.

Table 1-4. Overview of common and upcoming detection techniques for ammonia and nitrate/nitrite.

| Analyte | Method | Detection Technique | Comments |
|---|---|---|---|
| **$NH_3/NH_4^+$** | Nessler | Spectrophotometer | Classical method that uses toxic reagents. Has been dropped as a standard method. |
| | Titration | Spectrophotometer | Needs preliminary distillation. Prone to high relative error for low $NH_3$-N concentrations. |
| | Indophenol | Spectrophotometer | Good linearity from 0.02 to 2 mg $NH_3$-N/L. Sample needs to be pre-treated. Uses toxic reagents. |
| | OPA | Spectrofluorometer | Suitable for low concentrations of ammonia. High reagent consumption. |
| | ISE | Electrochemistry | Commercially available for continuous monitoring. Interference with $K^+$ ions. |
| | Metal Oxides | Electrochemistry | Possibility of system miniaturization. Can present problem with selectivity and stability. |
| **$NO_3^-$ /$NO_2^-$** | Griess Assay | Spectrophotometer | Most frequently used method. Can suffer interference from $Cu^{2+}$, $Fe^{3+}$, $S^{2-}$ and $I^-$ ions. |
| | Nitrosation | Spectrophotometer | Low standard deviation. Susceptible to $Fe^+$ influence. |
| | Catalysis | Spectrophotometer | Needs controlled reaction conditions. Interference from several ions. |
| | Carbon-based Materials or Metal Nanoparticles | Electrochemistry | Possibility of miniaturization. Detection limit in µM or mM range. Can suffer interference in complex samples. |

### *1.4.3 Ammonia Detection Techniques*

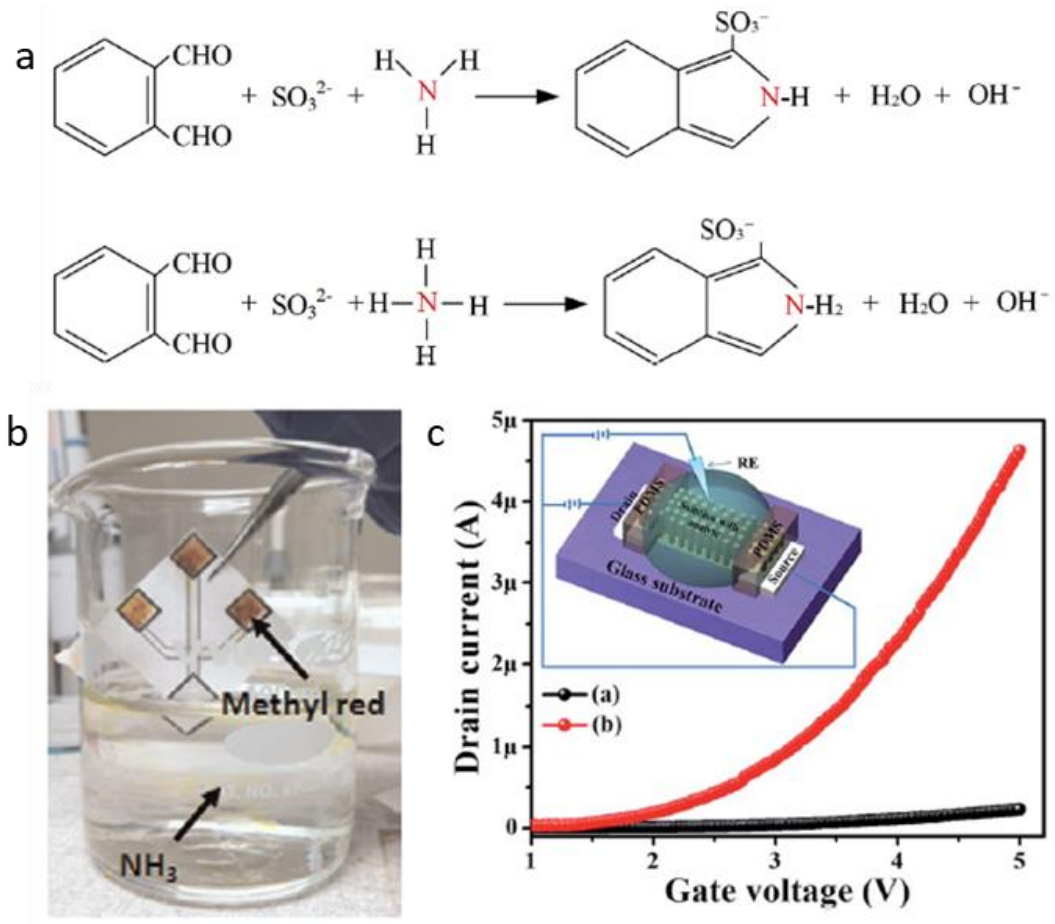


Figure 1.13. (a) Fluorometric detection of ammonia based on OPA-sulfite [41]. (b) Device for colorimetric sensing of dissolved $NH_3$ [71]. (c) ZnO-based ion sensitive field-effect transistor for the determination of dissolved $NH_3$ [8].

Ammonia in water is present as $NH_4^+$ ion and dissolved $NH_3$ and usually the $NH_4^+$ ion is determined and the $NH_3$ concentration is calculated by Equation 1.4. Some methods have been employed for ammonia detection, including spectrophotometry, fluorometry, and electrochemical sensors (Figure 1.13). Spectrophotometric analysis has been widely utilized for the detection of ammonia in freshwater and seawater, being advised by environmental agencies such as the U.S. EPA as the standard method [38–40]. Nesslerization has been considered a classical method to determine ammonia for more than a century, although it has been dropped as a standard method [72]. It consists of a pale-yellow alkaline mercury solution ($K_2HgI_4$) that becomes deep yellow in the presence of ammonia. The problem arises because of the use mercury, which is difficult to dispose of and highly toxic [72]. A standard method is the titrimetric method, where a standard solution (titrant) is prepared

and added to the analyte until a change in colour occurs. To determine $NH_3$-N, a sulfuric acid ($H_2SO_4$) titrant solution is used until a pale lavender colour is observed [72]. This method is usually employed for samples with concentration greater than 5 mg $NH_3$-N/L as the error escalates in lower concentrations and volatile amines (hydrazine and amines) can influence the result [72]. Another method is the phenate or indophenol, where the reaction between ammonia, phenol and hypochlorite, catalysed by sodium nitroprusside, produces an intense blue compound, the indophenol [73]. It can be also automated and produce a linear response from 0.02 to 2.0 mg $NH_3$-N/L [72]. These colorimetric methods require pre-treatment of the samples for an accurate measurement, which ranges from adding dechlorinating agents to distilling the water [72].

Fluorometry is a popular technique for detecting ammonia. Its low limit of detection (LOD), up to the nanomolar range, makes this technique suitable for water bodies with low concentration of ammonia, such as seawater [40]. O-phthalaldehyde (OPA) is the most used chemical for fluorometric detection of ammonia, being first developed in 1971 for amino acid detection [74]. The reaction has since been improved by some of the reagents and technologies used to minimize interference with other amines [75]. An important modification to the original method was substituting mercaptoethanol with sulfite (Figure 1.13a), which provided a more selective and sensitive method for ammonium over amino acids [76]. Different modifications to the OPA method have since been developed, including additional of methoxy groups to the benzene ring of the OPA molecule and changing the buffer solutions [40].

The selection of the sensitive material is essential for the fabrication of a successful electrochemical sensor as it influences the sensor selectivity, sensitivity, and stability. For ammonia detection, these materials include metal oxides, carbon nanotubes, metals, and ion-selective membranes, each presenting some advantages and disadvantages [41,43,77]. Some examples found in literature include ion-sensitive field-effect transistor (ISFET) ZnO-based ammonia sensors (Figure 1.13c), an amperometric dodecylbenzene sulfonate (DBSA)-doped polyaniline nanoparticles (nanoPANI)-based sensor, and ionophore-based potentiometric sensors [8,57,77,78]. The sensitivity range is usually in the micro- or millimolar range for ammonia detection, with commercial sensors usually employing ion-sensitive electrodes (ISEs) [77]. Ammonia electrochemical sensors can also be developed in flexible substrates, and research is ongoing on developing biodegradable disposable ammonia sensors. A summary of the $NH_4^+$ sensors mentioned here can be seen in Table 1-5.

Table 1-5. A summary of different sensors used for the detection of $NH_4^+$/dissolved $NH_3$.

| Detection technique | Method | Sensing material | Detection range | LOD | Ref. |
|---|---|---|---|---|---|
| Spectrophotometry | Nessler | $K_2HgI_4$ solution | 0.05 – 1 mg/L $NH_3$-N/L | - | [79] |
| Spectrophotometry | Titrimetric | $H_2SO_4$ | 5-100 mg/L $NH_3$-N/L | - | [72] |
| Spectrophotometry | Indophenol | Phenol and hypochlorite | 0.02 – 2.0 mg $NH_3$-N/L | - | [72] |
| Spectrophotometry | Fluorometric | O-phthalaldehyde | 0.2 – 60 µM | 35 nM | [40] |
| Spectrophotometry | Colorimetric | Phenolphthalein | 17-1700 ppm | 17 ppm | [71] |
| Electrochemistry | Amperometric | DBSA-doped nanoPANI | 0.02-10 mM | 3.17 µM | [57] |
| Electrochemistry | ISFET | ZnO nanorods | 10 nM -2.5 mM | 70 nM | [8] |
| Electrochemistry | I-V measurement | ZnO nanopencils | 0.05 – 500 µM | 5 nM | [78] |
| Electrochemistry | Potentiometric | Solid-sate nonactin cocktail | 7.9 µg – 1600 mg N-$NH_4^+$/L | 7.9 µg N-$NH_4^+$/L | [80] |
| Electrochemistry | Potentiometric | Gas-permeable membrane | 0.03 - 1400 mg N-$NH_3$/L | - | [72] |

### *1.4.4 Nitrate and Nitrite Detection Techniques*

Spectrometric techniques are by far the most widely employed method for the detection of $NO_3^-$ and $NO_2^-$ ions. It presents the opportunity of low detection limits in the range of 0.01 to 1 mg/L, for

example, by utilizing a continuous-flow spectrometric method that can determine both or each ion separately [29]. Nitrate absorbs UV light at 210 nm making it feasible for UV spectroscopy determination. However, components such as chlorine, nitrite, iron(III) and organic matter absorb in the same region, which can interfere with the experiment [31]. Over the years, modifications to the technique have been made for a more selective and sensitive method. Some of the spectrophotometric methods used are based on the Griess assay, nitrosation and catalytic processes [34]. The Griess assay involves a diazo-coupling procedure, where a nitrite acidified aromatic amine undergo diazotization by coupling reaction (Figure 1.14a) [31]. The reaction produces a colored azo chromophore that can be detected at 500-600 nm. The process has been modified in many aspects, including assay conditions, target amines (e.g. sulphanilic acid, nitroaniline and p-aminoacetophenone), coupling agents (phenol, 1-naphthol, 1-naphthol-4-sulfonate, 1-amino naphthalene and 1,3-diaminobenzene), among others [31]. Although this method detects only $NO_2^-$, chemical or enzymatic reduction of $NO_3^-$ to $NO_2^-$ can be employed before the diazotization process to also detect nitrates.

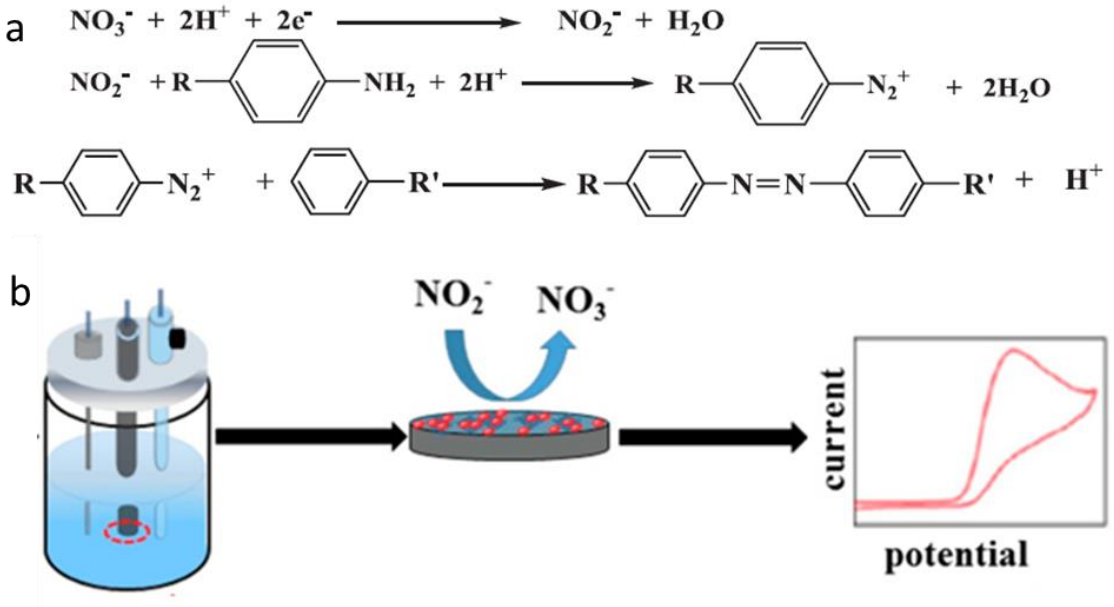


Figure 1.14. (a) The Griess assay method [31]. (b) Electrochemical detection of nitrite [81].

The nitrosation reaction is based on the reaction of several indicating species (e.g. barbituric acid, phloroglucinol (1,3,5-trihydroxybenzene)) that react with nitrite to form colored products (e.g. violuric acid) but suffers from interference from other metal ions [34]. In the catalytic-based spectrophotometric methods, the catalytic effect of nitrite on the oxidation of organic dyes or other indicating species is analyzed. For example, substituted phenothiazine derivatives, triarylmethane acidic dyes, azo dyes, quinone imide dyes, and brilliant cresyl blue have all been reported as

indicating species or organic dyes [34]. However, the determination of nitrite by catalytic-spectrophotometric methods has several drawbacks, including the need for controlled reaction conditions, such as acidity, temperature, and reagent dosage, and interference from ions as $Fe^{2+}$, $Fe^{3+}$, $Ag^{+}$, $SO_3^{2-}$, $Br^{-}$ and $I^{-}$ [34]. Recently, electrochemical detection of nitrates has been gaining attention (Figure 1.14b). Carbon-based materials such as graphene oxide, carbon-nanotubes, and carbon black have been employed as the sensitive material, but other metal nanostructures have also been used [66,81]. Many of the electrochemical sensors developed are based on glassy-carbon electrodes (GCE), which is usually employed in a laboratory setting. To bring these sensors in field, different fabrication techniques, such as screen-printing or cleanroom device fabrication, need to be employed. Other methods utilized for the determination of nitrates and nitrites include the electrochemical, chromatographic, capillary electrophoresis, and electrochemiluminescent methods [34]. Some of the techniques mentioned here are summarized in Table 1-6.

Table 1-6. A summary of different sensors used for the detection of $NO_3^-$/$NO_2^-$ ions.

| Ion | Detection technique | Method | Sensing material | Detection range | LOD | Ref. |
|---|---|---|---|---|---|---|
| $NO_2^-$ | Spectrophotometry | Griess-assay | Sulphanilamide + 1-naphthol-4-sulfonate | 2-40 ng/L | 1.4 ng/L | [82] |
| $NO_3^-$ | Spectrophotometry | Griess-assay | Sulphanilamide + 1-naphthol-4-sulfonate | 1.5-30 ng/L | 1.1 ng/L | [82] |
| $NO_2^-$ | Spectrophotometry | Nitrosation-reaction | Barbituric acid | 0 - 3.22 ppm | 1.66 µg/L | [83] |
| $NO_2^-$ | Spectrophotometry | Nitrosation-reaction | Phloroglucinol (1,3,5-trihydroxybenzene) | 0.03 – 0.30 µg $NO_2^-$-N/mL | 2.9 ng $NO_2^-$-N/mL | [84] |
| $NO_3^-$ | Spectrophotometry | Nitrosation-reaction | Phloroglucinol (1,3,5-trihydroxybenzene) | 0.1 – 1.0 µg $NO_3^-$-N/mL | 2.3 ng $NO_3^-$-N/mL | [84] |
| $NO_2^-$ | Spectrophotometry | Catalytic | Perphenazine | 0-4.5 ng/mL | 0.07 ng/mL | [85] |
| $NO_2^-$ | Spectrophotometry | Catalytic | Brilliant cresyl blue | 3.7 nM – 65 µM | 1.76 nM | [86] |
| $NO_2^-$ | Electrochemistry | Amperometric | Au-Fe(III) nanoparticles/GCE | 0.2 – 150 µM | 0.1 µM | [87] |
| $NO_2^-$ | Electrochemistry | Voltammetric | Pt-Fe(III) nanoparticles/GCE | 1.1 µM – 11 mM | 0.47 µM | [88] |
| $NO_2^-$ | Electrochemistry | Voltammetric | Reduced graphene oxide/screen-printed electrode | 20-1000 µM | 0.83 | [89] |
| $NO_3^-$ | Electrochemistry | Voltammetric | Cu nanowires | 10-1500 µ | 10 µM | [90] |

## 1.5 Aims and Objectives

From literature, it is possible to notice a gap in the fabrication of affordable, continuous sensors for $NH_3$ and $NO_2^-/NO_3^-$ in water. The standard spectroscopic techniques require regular maintenance and specialised personnel, making them costly both to purchase and maintain. Meanwhile, commercial electrochemical sensors rely on potentiometric techniques that use sensitive membranes to detect the analytes. Although this solution is more affordable and can provide continuous analyte detection, the detection time increases to several minutes at low analyte concentration. Voltammetric sensors are presented as an alternative to standard potentiometric sensors, however, achieving high sensitivity while maintaining long-term stability and low/no signal interference is extremely challenging. Moreover, considering that the aim for these sensors is to be continuously employed in water bodies, it is important to understand how the sensor lifecycle and the materials used during the fabrication step impact the environment. This has not been thoroughly considered in literature when fabricating new electrochemical sensors, with few reports currently emerging [91].

Therefore, the main aim of this thesis is to develop affordable, fast, and convenient sensors to detect dissolved inorganic nitrogen for water quality monitoring, focusing on nitrite ($NO_2^-$) and dissolved ammonia ($NH_4^+/NH_3$) sensors. Furthermore, the use of more environmentally friendly approaches to electrochemical sensor fabrication is desired. To achieve this, the study of different voltammetric techniques and printed sensor fabrication steps were performed. The specific research objectives were:

1. To investigate the potential interference of silver-based electrodes on the electrochemical performance of interdigitated electrodes (IDEs).
2. To explore more sustainable alternative materials to substitute metal-based pastes in printed electrodes. More specifically, to investigate the stability and electrochemical properties of carbon and silver pastes on the conductive tacks of printed electrodes.
3. To study different fabrication techniques for carbon-based electrodes and how they perform as $NO_2^-$ sensors. In particular, to compare the performance of laser induced graphene (LIG) electrodes to commercial screen-printed electrodes (SPEs).
4. To evaluate the electrochemical performance of Cu-based materials for dissolved $NH_3$ sensing.

## 1.6 Thesis Outline

*Chapter 1:* Thesis Introduction and Literature Review

This chapter includes the aims and objectives of this thesis, the thesis outline and a literature review of state-of-the-art methods and techniques to detect inorganic nitrogen compounds in water bodies. The review details electrochemical techniques for $NO_2^-$/$NO_3^-$ and $NH_4^+$/$NH_3$ detection as well as permitted concentrations of these analytes in water bodies.

*Chapter 2:* Influence of Silver Paste on Ammonium Interdigitated Sensors

A ZnO-based IDE for dissolved $NH_3$ sensing was studied in this chapter. The influence of the Ag electrode on the electrochemical results was investigated as a potential source of interference.

*Chapter 3:* Evaluation of Carbon Pastes on Printed Electrodes

This chapter further analyses the impact of Ag pastes as conductive tracks on voltammetric sensors and investigates the use of carbon materials as alternatives. For that, the mechanical and electrochemical performance of two commercial SPEs fabricated using commercial silver and carbon pastes and of a novel graphite printed electrode are investigated.

*Chapter 4:* Optimisation of Laser Induced Graphene Electrodes as Nitrite Sensors

The optimisation and fabrication of LIG sensors are described in this chapter as an alternative source of carbon-based electrodes. Furthermore, the LIG sensors are compared to a commercial carbon SPE to monitor $NO_2^-$ in aqueous media.

*Chapter 5:* Copper-based Dissolved Ammonia Sensors

In this chapter, a Cu metal organic framework (Cu-MOF) was explored as a new material for sensing dissolved $NH_3$. The influence of pH and Nafion were investigated on the electrochemical performance as well as material stability.

*Chapter 6:* General Conclusions and Future Perspectives

This chapter outlines the main findings of this thesis, including the substitution of silver for carbon electrodes and its application as $NO_2^-$. The findings on the Cu-MOF and how to improve its

performance for dissolved $NH_3$ voltammetric sensors are also discussed. Furthermore, the challenges and future perspectives are highlighted in this section.

# Chapter 2

# Influence of Silver Paste on Ammonium Interdigitated Sensors

*Sections 2.1, 2.2, and 2.3.1-2.3.3 are adapted with permission from: F. F. Franco, L. Manjakkal, D. Shakthivel and R. Dahiya, "ZnO based Screen Printed Aqueous Ammonia Sensor for Water Quality Monitoring," 2019 IEEE SENSORS, 2019, pp. 1-4, doi: 10.1109/SENSORS43011.2019.8956763.*

**The scanning electron microscopy (SEM) characterisation was carried out by Dr Dhayalan Shakthivel.*

## 2.1. Introduction

Continuous monitoring of water quality is needed to minimise exposure to diseases and to maintain healthy conditions for aquatic species. Among various critical parameters that need to be monitored, ammonia is especially important as a nitrogen-rich environment can lead to eutrophication, decreasing the amount of dissolved oxygen in water bodies [5,6]. Aquatic ammonia exists in equilibrium as dissolved ammonia ($NH_3$) and ammonium ion ($NH_4^+$) and the former is particularly harmful even at low concentrations [4]. Considering the harmful effects of $NH_3$, continuous online monitoring of different water types (e.g., drinking water, lake water, wastewater) with a simple, miniaturized setup is highly desirable as an alternative to time consuming laboratory techniques. In this regard, sensors with electrochemical, conductimetric, or amperometric analysis have been reported recently with different materials including conducting polymers and metal oxides [2,92]. Among these, metal oxides-based sensors, with their high surface to volume ratio, show enhanced sensitivity, selectivity, fast response and long lifetime in different environmental conditions [93].

Furthermore, the mechanical stability and miniaturization of metal oxide-based sensors make them ideal for online monitoring applications [64,94].

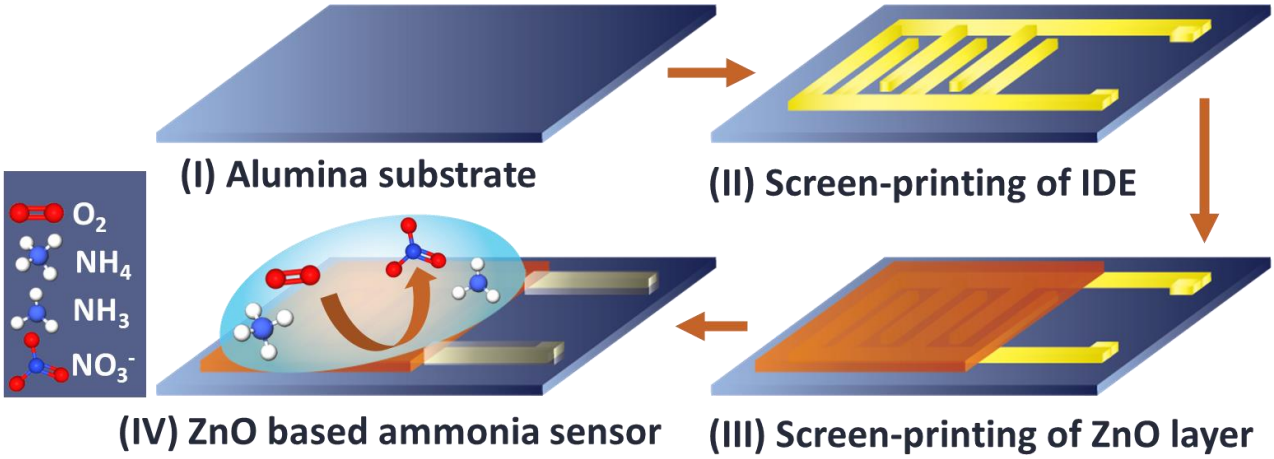


Figure 2.1. I-III) Schematic illustration of the sensor fabrication. IV) Proposed sensing mechanism of ZnO based sensor for $NH_4^+$ monitoring.

In this chapter, a ZnO thick film-based sensor was explored for $NH_4^+$ monitoring. The sensing film was screen-printed on top of a silver interdigitated electrode (IDE) structure (Figure 2.1). IDEs are microelectrodes where the working and counter electrodes form an interlaced comb structure [95]. It should be noted that the geometry of screen-printed electrodes (SPEs) can influence the sensor performance, cost, and scalability. An important element when designing a printed electrode is the uniform current distribution between the surfaces of the electrodes [96]. It has been reported that the sensing output can be enhanced by increasing the surface-to-volume ratio of the electrode [96]. Many designs exist in literature with the most usual configuration for 3-electrode SPEs being the circular geometry, consisting of a working, a reference and a counter electrode (See Section 1.4.1 for a more in-depth review). For electrochemical impedance spectroscopy (EIS), the spiral pattern or an IDE is normally used as it increases the effective surface-to-volume ratio of the electrode, leading to a higher conductivity and ion diffusion, which influences the signal intensity [68]. The IDE structure was selected as it could lead to miniaturized sensors without the need for an external reference electrode, simplifying the sensor design and possibility increasing the response due to its unique geometry.

The choice of ZnO as a sensing material was due to its high biocompatibility and chemical stability [93,97,98]. The surface oxide of the ZnO layer has been reported to react to very low concentrations of $NH_4^+$ which leads to changes in resistivity and current response [8,78]. Using this working principle, the electrochemical reaction of the ZnO film with various concentrations (0.0 to 11.0 mM)

of $NH_4^+$ was used to investigate the correlation of analyte concentration with change in current/impedance response. After further electrochemical experiments, however, it appeared that the faradaic peak was not generated only by the oxidation of $NH_4^+$. Therefore, preliminary experiments were performed to analyse the interaction of the IDE silver layer with the sulphate ions present in the solution, as silver can be oxidised to $Ag^+$ ions or interact with sulphates to form $Ag_2SO_4$ [99,100].

## 2.2. Experimental Section

### *2.1.1. Sensor Fabrication*

The first step in the fabrication of the sensor is to obtain the paste for screen printing. To this end the ZnO powder (Sigma Aldrich) was wet ball milled in isopropyl alcohol for 7 hrs in a planetary ball mill and then dried. The fine ZnO powder obtained was mixed with ethyl cellulose (40 wt.%) (Sigma Aldrich) binder and terpinol (Sigma Aldrich) solvent in agate mortar for 1hr. For the sensor fabrication, initially, a silver paste (Ag/Pd ESL 9695) was deposited on an alumina planar substrate by screen-printing to obtain the IDEs. The IDE pattern consists of 0.5 mm wide and 10 mm long fingers spaced at 0.5 mm. The metal layer was dried at 120 °C for 20 min and annealed at 850 °C for 30 min. Following this, a 13 x 17 mm ZnO sensing layer with 10 μm thickness was screen-printed on the top of IDE. The layer was dried at 120 °C for 20 min and annealed at 600 °C for 1 hr. Finally, Cu wires were soldered on the contact pad and the Ag electrodes were protected by insulative epoxy (polyurethane). The epoxy was heat treated in oven at 80 °C for 1 hr to obtain good quality of insulation. The schematic representation of the sensor fabrication is shown in Figure 2.1.

### *2.1.2. Structural and Morphological Characterisation*

The structural characterization of the film was carried out with a powder X-Ray diffractometer (XRD, P'Analytical X'Pert with Cu Kα ($\lambda = 1.541$ Å)). The morphological characterization of the film before and after the electrochemical analysis was performed by scanning electron microscopy (SEM, SU8240 Bruker at 6 kV). The ImageJ software was utilised for measuring the length of the ZnO sctructures.

### *2.1.3. Electrochemical Characterisation*

The cyclic voltammetry (CV - 0.0 to 0.8 V with a scan rate of 100 mV/s) and EIS (10 mHZ to 1 MHz) characterisation were performed using a two-electrode system on the Metrohm Autolab (PGSTAT302N) instrument. The current resolution is 0.0003% of the current range (e.g., 30 fA if a

current range of 10 nA was chosen) and the impedance resolution is 0.3% for frequencies less than 10 kHz. A concentrated dissolved ammonium solution was prepared by adding ammonium persulfate ($(NH_4)_2S_2O_8$, Merck) in milliQ water. The electrochemical evaluation of the sensors was then monitored by adding appropriate volumes of the concentrated $(NH_4)_2S_2O_8$ solution. During the measurements, the total ammonia nitrogen (nitrogen in the form of $NH_3$ plus $NH_4^+$ in water) concentration was varied from 0 to 11.0 mM by adding appropriate amounts of the concentrated ammonium solution. The pH and temperature of the system were monitored using a commercial sensor (Hanna Instruments HI-98130). The $(NH_4)_2S_2O_8$ solution gets dissociated into $NH_3$ and $NH_4^+$ ions, with the equilibrium of these constituents depending on temperature and pH. Therefore, to calculate the concentration of $NH_3$ and $NH_4^+$ ions, suitable pKa and un-ionised $NH_3$ fraction equations (Chapter 1, Equation 1.1-1.4) were employed [10]. The calculated concentration of $NH_4^+$ ions (in the range of 0-10.9 mM) was used for the calibration curves.

Additional CV and differential pulsed voltammetry (DPV) experiments were performed using concentrated liquid ammonia ($NH_4OH$) solution with the ZnO-based IDE sensor. The DPV experiments had a step size of 5 mV, a pulse time of 0.2 s, a pulse size of 50 mV, and a sample period of 0.5 s. Furthermore, CV and DPV experiments using bare Ag IDE, in which no ZnO layer was deposited on top, were also performed using concentrated ($(NH_4)_2S_2O_8$ solutions. The concentration range was from 0.1 to 3.0 mM of $NH_4OH$ or $(NH_4)_2S_2O_8$.

## 2.3. Results and Discussion

### *2.3.1. Sensing Mechanism*

The $NH_3$ gas sensing mechanism using metal oxide-based sensors, especially those based on the chemiresistance principle, is well explained in the literature [93,101]. In these sensors, the surface oxide layer adsorbs the reducing gas and alters the resistivity of the metal oxide by injecting electrons in the conduction band, and thus facilitates the flow of electrons [101]. In the case of dissolved $NH_3$ sensors, the electrochemical reaction occurs on the surface of the electrode and the aqueous $NH_3$ reacts with the surface adsorbed superoxides in an exothermic reaction [8]. Previous ZnO-based field effect transistor sensors claimed that the reaction occurring at the ZnO surface was due to the exothermic reaction of $NH_4OH$ into $NH_4^+$ ions [8,78]. These ions then react with the surface adsorbed oxygen, releasing electrons to the metal-oxide film. The equation is shown below:

$$NH_4OH_{aqueous} \rightarrow NH_4^+ + OH^- \quad (2.1)$$

Another possible mechanism for the ZnO-based sensor involves the nitrification of $NH_4^+$ into nitrate ions ($NO_3^-$) by the surface superoxides [102,103]. The energy released during the oxidation should be sufficient for the electrons to jump to the conduction band, which in turn decreases the resistance of the material. The proposed nitrification reaction is as follows:

$$NH_4^+ + 2O_2 \rightarrow NO_3^- + H_2O + 2H^+ \quad (2.2)$$

Additionally, a model for water interaction with ZnO indicates the water suffers partial dissociation at the surface and forms an ordered superstructure with (2×1) periodicity [104]. By combining these previous findings, it would be reasonable to assume that water dissociates at the surface of the presented sensor into different species and forms an ordered structure, with superoxides being the one that reacts most strongly with the ammonium ion. In addition to the redox reaction, the formation of an electrical double layer (*edl*) on the surface of the oxide was observed. When a potential is applied on the IDE, an electrochemical reaction occurs at the ZnO/electrolyte interface. The electric field generated on the IDE disturbs the electrical properties of the ZnO film, varying with the ionic ($NH_4^+$ and $(S_2O_8)^{2-}$) concentration of the solution. These electrochemical variations were initially attributed to the $NH_4^+$ ion concentration and they were investigated using CV and EIS analysis, however after further experiments (detailed in the sections below) it was discovered that the Ag IDE layer could be interfering with the CV oxidation peaks. Metallic Ag can be oxidised by the $S_2O_8^{2-}$ anions to form $Ag^+$ [99,100]. The electrochemical interaction of Ag with $S_2O_8^{2-}$ anions can be seen in Equation 2.3.

$$Ag_{(s)} \rightarrow Ag^+ + e^- \quad (2.3)$$

### *2.3.2. Structural and Morphological Characterisation*

Surface morphology of ZnO film before and after reaction with the solution are shown through SEM images in Figure 2.2a,b. The films have fine-grained microstructures and homogeneous and rectangular crystalline grains with grain sizes in the range of 60 – 200 nm. Furthermore, the absence of any change in the ZnO nanorod crystallinity before and after the measurements indicates that the

ZnO film is stable. The XRD pattern of the ZnO film in Figure 2.2c shows a highly crystalline structure with well-defined peaks. The three most intense peaks can be attributed to ZnO (100), (002) and (101). Unmarked peaks match the $Al_2O_3$ XRD pattern and are due to the presence of the alumina substrate. Although the film thickness was not analysed in this chapter, it is an important parameter to consider as thicker films can slower the diffusion of molecules, leading to lower signals [97]. Characterisation techniques such as profilometry can be used to obtain the film thickness profile.

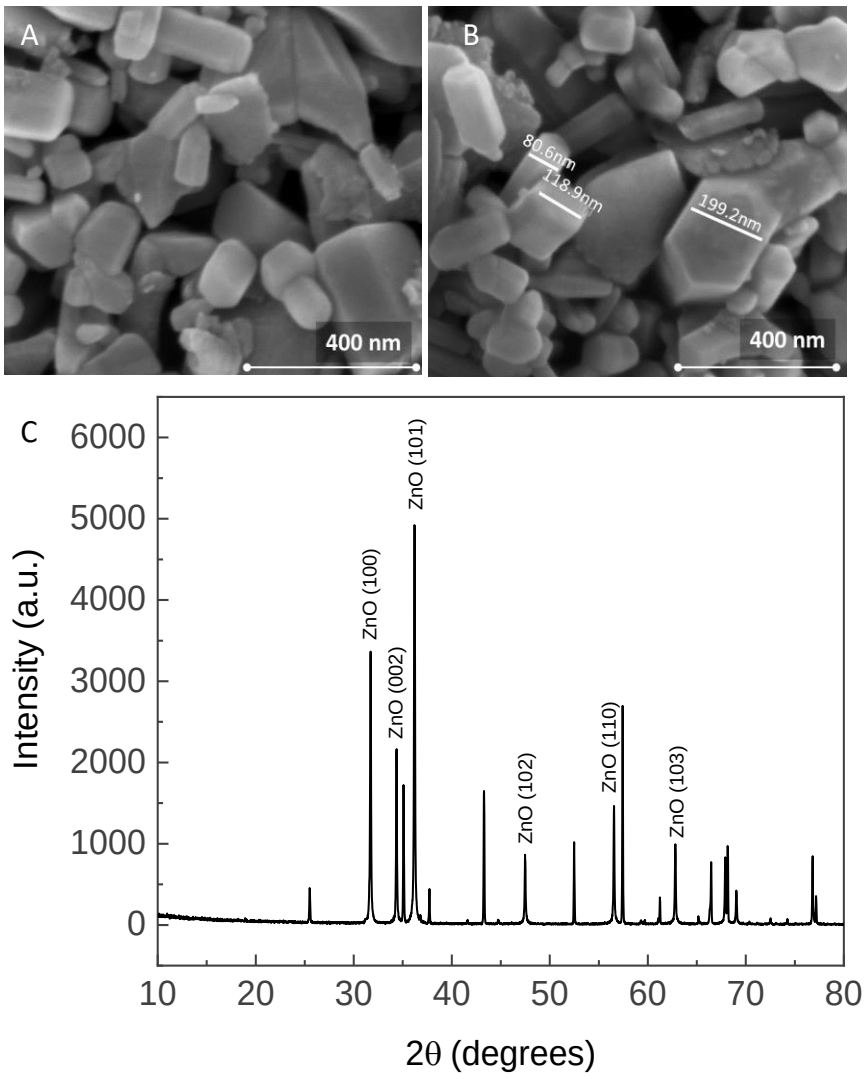


Figure 2.2. SEM images of ZnO crystals before (a) and after (b) the CV and EIS analysis. c) XRD pattern of the structure.

### *2.3.3. Initial Electrochemical Characterisation*

The CV curves for the $NH_4^+$ in the 0 to 10.9 mM range are shown in Figure 2.3a. The oxidation peaks start around the same voltage for all concentrations, with maximum current density ($J_p$) of each

oxidation peak shifting to the right as more $(NH_4)_2S_2O_8$ is added to the solution. The sensor has limited surface area, and by adding more analyte the mass transfer and the *edl* are affected [106]. In other words, the diffusion in the second layer of *edl*, which should mostly consist of $(NH_4)_2S_2O_8$ interacting with adsorbed oxygen, as described in Sensing Mechanism, is affected and increases the total energy needed for the catalysis of $NH_4^+$. The increase in the current density was observed with increasing concentration of the solution. By analysing $J_p$ vs $NH_4^+$ ion concentration (Figure 2.3b), a linear trend was observed in the range of 0.87-10.9 mM. with a sensitivity of 49.6 $\mu AmM^{-1}cm^{-2}$ and an $r^2$ value of 0.996.

The electrochemical reaction and the sensing mechanism were also investigated through EIS analysis. The Nyquist plot from the EIS analysis (Figure 2.3c) shows a spike in the high frequency range due to the influence of the solution and contact resistance ($R_S$). The large semi-circle arc in the intermediate frequency range is due to the bulk resistance and shows the charge transfer resistance ($R_{CT}$) of the electrode [63]. The total resistance ($R_T$) was obtained by $R_T = (R_S + R_{CT}) \times A$, with A being the sensing area of the ZnO layer. By plotting the $R_T$ per unit area against the $NH_4^+$ ion, a linear trend was observed from 0.39 to 10.9 mM (Figure 2.3b). The measurement reveals that the resistance decreases with increased analyte, which concurs with the hypothesized sensing mechanism for ZnO where the injection of electrons from the catalysis of the $NH_4^+$ ion in the conduction band lead to a decrease in resistance [8]. The sensitivity was found to be -1.30 $k\Omega mM^{-1}cm^{-2}$ with an $r^2$ value of 0.989. A small arc in the very low frequency range shows that the dominant reaction on the surface of the electrode is ionic adsorption [54].

Both electrochemical techniques showed a trend with increasing analyte concentration. It was initially thought that the oxidation peak shifts in the CV curves could be attributed to the oxidation of $NH_4^+$ into $NO_3^-$ ions, as Equation 2.1 does not generate an electron transfer, therefore it does not explain the faradaic peak. However, it is difficult to confirm without performing further analysis, such as using ion chromatography to quantify the ions present in the solution before and after the electrochemical experiments. As for the EIS, both Equation 2.1 and 2.2 could partake in the change of impedance, as it is a complex characterisation technique. For simplicity, CV and other voltammetry techniques are employed when characterising sensors, as it can be difficult to physically interpret the EIS graphs [61].

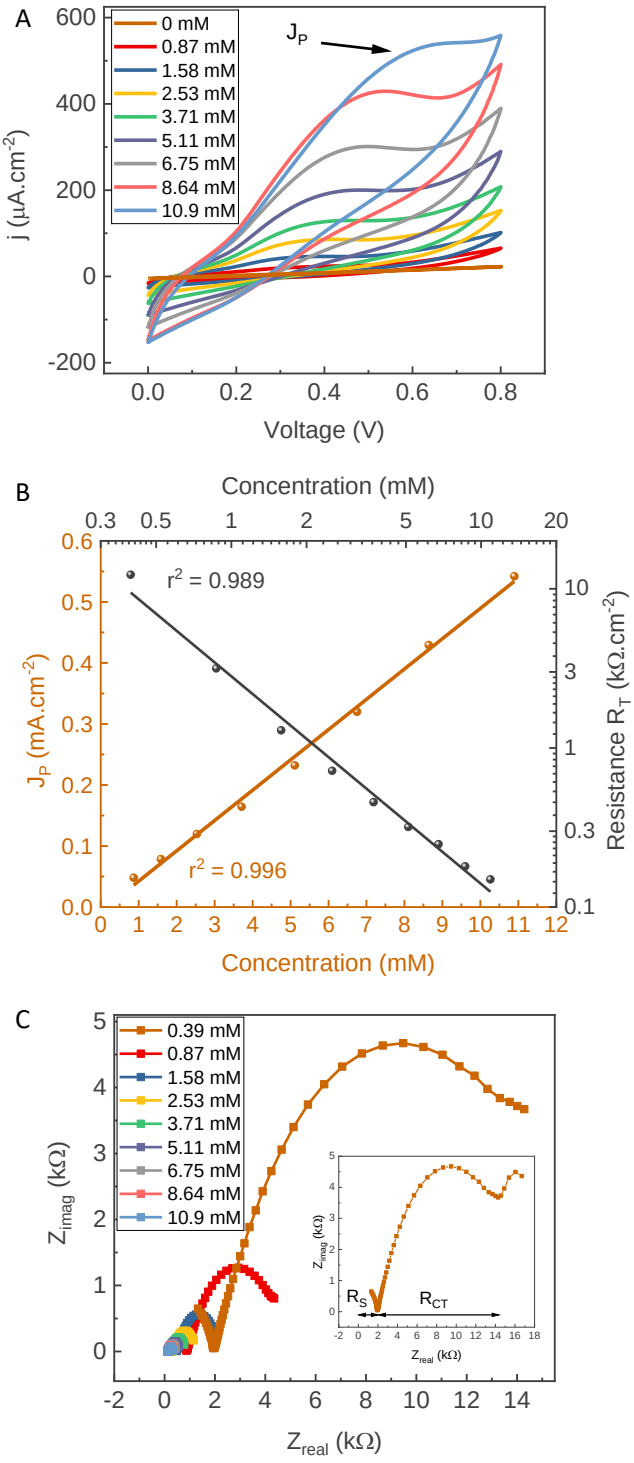


Figure 2.3. a) CV of the ZnO sensor at different concentrations of $NH_4^+$ (0 - 10.9 mM) at a scan rate of 100 mV/s in milliQ water. b) Maximum current density of CV oxidation peaks (left y-axis) and total sensor resistance (right y-axis) vs concentration of $NH_4^+$ ions. c) Nyquist plot of the sensor at different $NH_4^+$ concentrations (0.39-10.9 mM) and high frequency range. Inset shows the complete Nyquist plot for 0.39 mM, highlighting the $R_S$ and $R_{CT}$ region. This result is for one sensor, with instrument resolutions specified in Section 2.1.3.

### *2.3.4. Influence of Silver IDE on Sensing Performance*

After this initial analysis, further experiments using CV and DPV techniques were performed to better understand the oxidation process occurring at the sensor. The DPV technique was chosen as it decreases the capacitive current, facilitating the identification of the faradaic peaks [61]. A higher potential range of -0.8 to +0.8 V was used to identify if the faradaic process is reversible. Firstly, the analyte was changed from $(NH_4)_2S_2O_8$ to $NH_4OH$ to mimic the reagent used by other $NH_4^+$ ZnO-based sensors in literature. The CV and DPV of the ZnO IDE sensor did not produce strong oxidation peaks (Figure 2.4a,b). To verify that the sensor was still responsive, $(NH_4)_2S_2O_8$ was used (Figure 2.4b,c). In this case, the sensor responded as previously, with a similar CV voltammogram as in Figure 2.3a. Through the new reduction peak at -0.4V, it can be presumed that the reaction is at least partially reversible, although further analysis should be performed for quantification. In Figure 2.4d, the DPV shows the presence of various peaks, both at the negative and positive potentials. The presence of peaks with the $(NH_4)_2S_2O_8$ solution versus the absence with $NH_4OH$ indicates that the presence of $NH_4^+$ ions might not be the cause of the faradaic peaks. In this case, there are two possibilities: one is that since pH was not adjusted when using $NH_4OH$, the addition of $NH_4OH$ caused a more basic pH which interfered with the results; the other is that the Ag is interacting with the solution, more specifically to the $S_2O_8^{2-}$ anions present in the solution.

To test this hypothesis, a bare Ag IDE was produced, where no ZnO layer was printed on top of the Ag IDE. This bare Ag IDE was tested with changing concentrations of $(NH_4)_2S_2O_8$ , as observed in Figure 2.4e,d. A very similar result was observed to the one in Figure 2.4c,d. The CV peaks were not as pronounced but had a similar current output while the DPV peaks showed a few discrepancies. The difference in peaks could be due to the absence of the ZnO layer, as in the bare Ag IDE the Ag fingers were directly exposed to the solution. However, further characterisation is necessary to understand this, such as how the ZnO is bonded to the Ag electrode and how this influences the faradaic reaction. By overall comparing Figure 2.4. it is possible to infer that the Ag layer is reacting with the solution. According to Equation 2.3, it is probable that the $S_2O_8^{2-}$ ions, a strong oxidising agent, oxidise Ag into $Ag^+$ ions. This is a problematic interaction as it hinders the validity of the sensitive ZnO layer interacting with the $NH_4^+$. Even for the EIS technique, where IDE sensors are widely employed, it is difficult to verify the cause of the impedance change with increasing analyte concentration when there is no faradaic reaction supported by the CV and DPV techniques. In this regard, further studies on conductive track materials are needed to verify their influence on electrochemical sensors results.

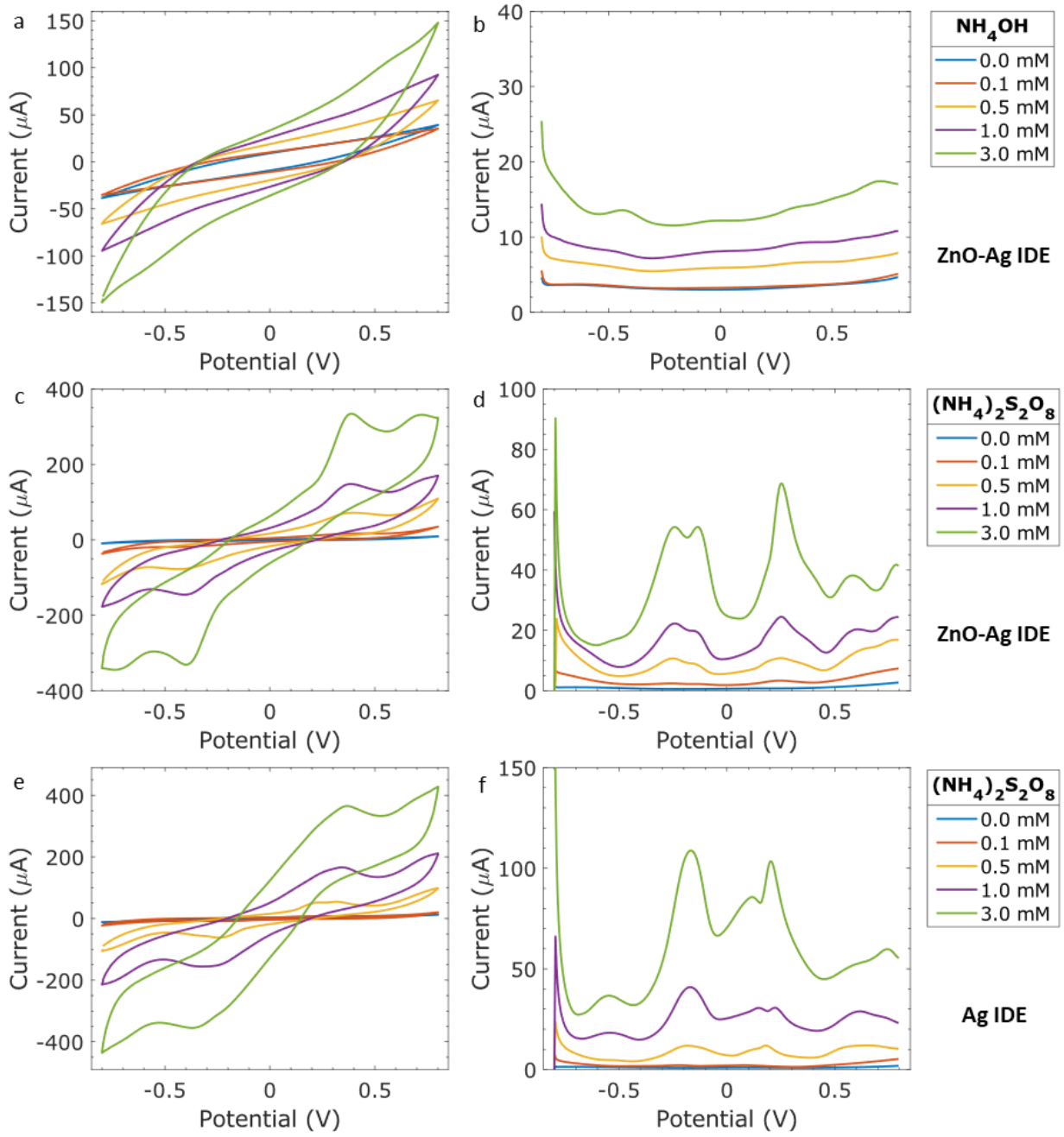


Figure 2.4. CVs at a scan rate of 100 mV/ (left) and DPVs (right) in milliQ water of the ZnO IDE sensor at different concentrations of $NH_4OH$ (0 – 3.0 mM) (first row), ZnO IDE sensor at different concentrations of $(NH_4)_2S_2O_8$ (0 – 3.0 mM) (second row), and bare Ag IDE sensor at different concentrations of $(NH_4)_2S_2O_8$ (0 – 3.0 mM) (last row).

## 2.4. Conclusions

This chapter is an introduction to how the different materials in printed sensors affect the outcome of the electrochemical measurements. ZnO was chosen as the sensitive material as it had been

previously employed for $NH_4^+$ sensing. The sensors from the literature review were field-effect transistor devices where the output current is monitored over a potential sweep, which are different than other electrochemical sensors, e.g. 3-electrode sensors and IDEs. In this sense, a similar sensor was fabricated using a ZnO layer on top of the Ag IDE, but different electrochemical techniques were used to explore its performance to detect $NH_4^+$. The ZnO later was annealed at a high temperature to produce rectangular nanostructures to increase the surface area of the electrode and to evaporate other substances present in the paste. Initial CV experiments demonstrated a faradaic peak at around +0.4 V which were attributed to the nitrification of $NH_4^+$ to $NO_3^-$. The Nyquist plot also showed a decrease in bulk resistance with addition of analyte.

Further experiments using CV and DPV were performed to better understand the oxidation process occurring. However, the voltammograms showed a poor performance for the $NH_4OH$ analyte. Further investigation comparing the Ag IDE with and without the ZnO layer demonstrated that the Ag from the IDE was interacting with the solution. This indicated that the oxidation peaks were most likely due to the formation of $Ag^+$ ions and not the nitrification of $NH_4^+$. This result revealed the importance of correctly choosing the electrode material so it does not interact with the analyte and the solution. For this, experiments with the bare electrode should be performed beforehand to verify there is no electrode/electrolyte interaction and no material degradation. Although this chapter did not result in a viable ammonia sensor, it set the motivation for the investigation of not only the sensing material but other parts of the sensors in the following chapters. In the next chapters, in experiments involving a faradaic reaction, 3-electrode systems were used for CV and DPV analysis instead of the IDE for a more comparable oxidation peak potential. In Chapter 3, the interaction of Ag with other salts commonly present in drinking water and seawater are investigated, as well as alternative materials for the electrode paste.

# Chapter 3

# Evaluation of the Electrochemical and Physicochemical Degradability of Printed Electrodes

*This chapter is adapted with permission from: F. F. Franco, S. Dervin, and L. Manjakkal, "Electrochemical and physicochemical degradability evaluation of printed flexible carbon electrodes in seawater," J. Electroanal. Chem, 2022, 920, 116592, doi: 10.1016/j.jelechem.2022.116592.*

**The scanning electron microscopy (SEM) characterisation was carried out by Dr Dhayalan Shakthivel. The pysichochemical degradability experiments were performed with the help of Saoirse Dervin.*

## 3.1. Introduction

Printed electrochemical devices have been attracting substantial attention over the past decades, becoming a well-established field. Their facile fabrication, cost-effectiveness and easy operation are some of the characteristics that allow these devices to operate in a range of different areas, such as energy storage, wearable sensors, and environmental monitoring [56,107–110]. With increasing usage and integration of sensors, it is desirable to have materials that are biodegradable and/or more sustainable to reduce the environmental impact, especially for single-use or disposable sensors. The use of non-degradable plastics and metals heavily impact the life cycle assessment of the electrode [91]. However, substitution of key components in printed electronics can negatively affect the electrode performance and stability, due to poor paste adhesion to the substrate and unexpected

chemical reactions with the conductive electrode patch. These challenges become even more prominent in electrodes employed for water monitoring. Common sustainable substrate materials, such as paper, cotton, and jute, either dissolve too quickly or have a high water intake, making their use in water difficult [71,111,112]. Furthermore, the investigation of potentially sustainable materials for the conductive pathway often does not account for other chemicals used in ink and paste preparation [91,113]. Other parts of sensor fabrication, such as the sensor disposability and the influence on the electrochemical measurements after integration of new conductive path/substrate materials, are often not investigated. In practical applications, it is important to conduct a thorough analysis of every component to reach a more sustainable production with reliable results. Therefore, a careful selection of materials for the substrate and the conductive path of disposable sensors that are economically feasible should be taken into consideration in the development of electrochemical devices.

In this regard, screen-printing is an affordable and versatile fabrication technique that allows sensors to be printed on flexible and rigid substrates [114]. Both flexible and rigid screen-printed sensors are commonly employed in routine environmental analysis, such as in pH, pesticide, heavy metal, bacteria, and inorganic nitrogen detection [64,108,115]. For these sensors, the sensitive material synthesis (e.g., metal oxides, graphite composite, carbon nanotubes, conductive polymers, etc.) and the different analyte detection methods (e.g. potentiometric, amperometric, chemiresistive) are widely discussed in literature [56,64,115]. The conductive path in printed electrodes generally uses carbon, silver, gold, and platinum pastes [115]. Gold and platinum present many of the desirable characteristics of a good conductive path material, e.g., high stability in the desired working window, low electrical resistance, and inertness in the chosen chemical environment. However, their high cost and disposability issues prevent their widespread use in printed sensors [115]. The metal of choice, in such cases, is silver, as it is highly conductive and affordable. Although more abundant and less harmful when compared to other precious metals, silver is not a long-term viable option as it still exhibits a high environmental impact [91]. Besides, silver is known to react with halides to form new components. This has been thoroughly studied in the literature for chloride, iodine, and bromide sensors [116–118]. Silver can also react with sulphates to form $Ag/Ag_2SO_4$, which has been used as an alternative to the Ag/AgCl reference electrode (RE) [99,100]. This $Ag/Ag_2SO_4$ reaction is most likely what happened with the Ag IDE in Chapter 2. Considering that silver readily reacts with components present in water bodies (e.g., NaCl, $MgSO_4$), which could rapidly deteriorate the performance and the lifetime of the sensor, and its high environmental impact, other options for the conductive path material should be explored. A metal-free alternative is carbon, as it is an

inexpensive, inert material with a broad potential window, although it is usually used in the active working electrode (WE) area and not on the entire conductive pathway due to its lower conductivity [115,119]. For electrochemical applications the carbon paste could be modified with graphene and carbon nanotubes (CNTs), for example [120–122]. Here, CNT was used to promote electron transfer reactions and enhance the stability of the printed electrodes [20]. However, to employ carbon paste electrodes as a conductive track it is essential to overcome the issue of high resistance. To further enhance the conductivity, the annealing temperature of the carbon additives and the binders also need to be investigated [123,124]. In one of the works, it was noted that to enhance the conductivity of printed carbon electrodes it is necessary to increase the size of the graphene flakes and minimize the amount of stabilizer used in the final ink formulation [123]. In another work, heat treatment was carried out to increase the conductivity by controlling the variation of the filter/matrix interaction and crystallisation of the carbon composite during the annealing [124]. Carbon electrodes also present the opportunity for a more environmentally friendly approach due to its higher biocompatibility and sustainability when compared to metal electrodes [91]. Although caution is needed when considering other materials that compose the pastes, such as the binders and the solvents, as they can be harmful to humans and/or the environment [110]. It was noticed that in screen-printed sensors for water and soil applications over the last 5 years, Ag is the main paste employed in electrodes alongside nondegradable substrates (Table 3-1).

Table 3-1. Comparison of electrodes of various screen-printed sensors.

| **Analyte Detection** | **Application** | **Substrate** | **Conductive Path** | **WE Material** | **Ref.** |
|---|---|---|---|---|---|
| $Pb^{+}$ | Seawater | Gore-Tex® fabric | Silver | Modified carbon | [125] |
| Polybrominated diphenyl ethers | Seawater, soil | Polydimethylsiloxane | Silver | Modified carbon | [126] |
| $Pb^{+}$ | Seawater | Polycarbonate sheet | - | Modified carbon | [127] |
| Pesticides | Seawater | Ceramic | Silver | Modified carbon | [128] |
| $Hg^{2+}$, $Cd^{2+}$, and $As^{3+}$ | Tap, lake, and river water | Polypropylene synthetic paper | Silver | Modified carbon | [129] |

Another important aspect to consider is the substrate, especially when developing a biodegradable and/or disposable sensor. Common substrates in printed devices include alumina, polyvinyl chloride

(PVC), and polyethylene terephthalate (PET) [80,110,130]. The flexibility of the substrate can also be an advantage in many fields, as it opens the possibility of conformable sensors. In the context of environmental monitoring, flexible sensors can be attached to the non-planar surfaces of marine animals or underwater robots, allowing for a less intrusive, more effective biologging monitoring [131,132]. Furthermore, to reduce the cost and environmental impact of electronic devices the use of eco-friendly and sustainable materials that can be reused or naturally discarded has become increasingly important [112]. Several natural biopolymers and degradable synthetic polymers, including starch, chitosan, cellulose, polylactide (PLA), and polycaprolactone (PCL), etc., have shown promise for application in a variety of flexible green electronic devices [112]. More recently, bioderived and biodegradable polyhydroxyalkanoate (PHA) polyesters, including polyhydroxybutyrate (PHB) and its copolymers with polyhydroxyvalerate (PHV) have been recognized for their far-reaching applications, including single use, disposable plastics, and packaging, as well as temporary *in vivo* biomedical technologies [133]. These sustainable and commercially available PHAs can both be produced and broken down, into water and carbon dioxide ($CO_2$) by living microorganisms in all aerobic and anaerobic environments - features that facilitate the development of biodegradable soil and marine products.

In this chapter, flexible and/or eco-friendlier screen-printed electrodes (SPEs) for environmental monitoring applications were developed based on the findings of Chapter 2, where the Ag paste seemed to interfere with the $NH_4^+$ sensor results. New carbon-based electrodes were fabricated as an alternative to Ag-SPEs. The newly prepared graphite-based printed electrodes (G-PEs) were fabricated on biodegradable PHB 92%/PHV 8% (PHB/PHV) substrates produced from renewable feedstocks. To investigate the electrodes' chemical and mechanical stability in different media, their applicability in tap water and seawater was demonstrated, as seawater is the most abundant aqueous electrolyte present in the environment [61]. To investigate the G-PEs' implementation, their performance was compared against commercial paste electrodes, silver SPEs (Ag-SPEs) and carbon SPEs (C-SPEs), which were printed on a PVC substrate. The flexible printed electrodes are shown in Figure 3.1. Cyclic voltammetry (CV) and differential pulsed voltammetry (DPV) studies were used to investigate the redox and non-faradaic reactions occurring at the electrode-analyte interface. A detailed investigation of the electrical and morphological properties of the electrodes under different bending conditions was also conducted. Finally, the physical and chemical degradability of the pastes and the substrates were examined in artificial seawater over a period of 16 weeks and by ultrasonication.

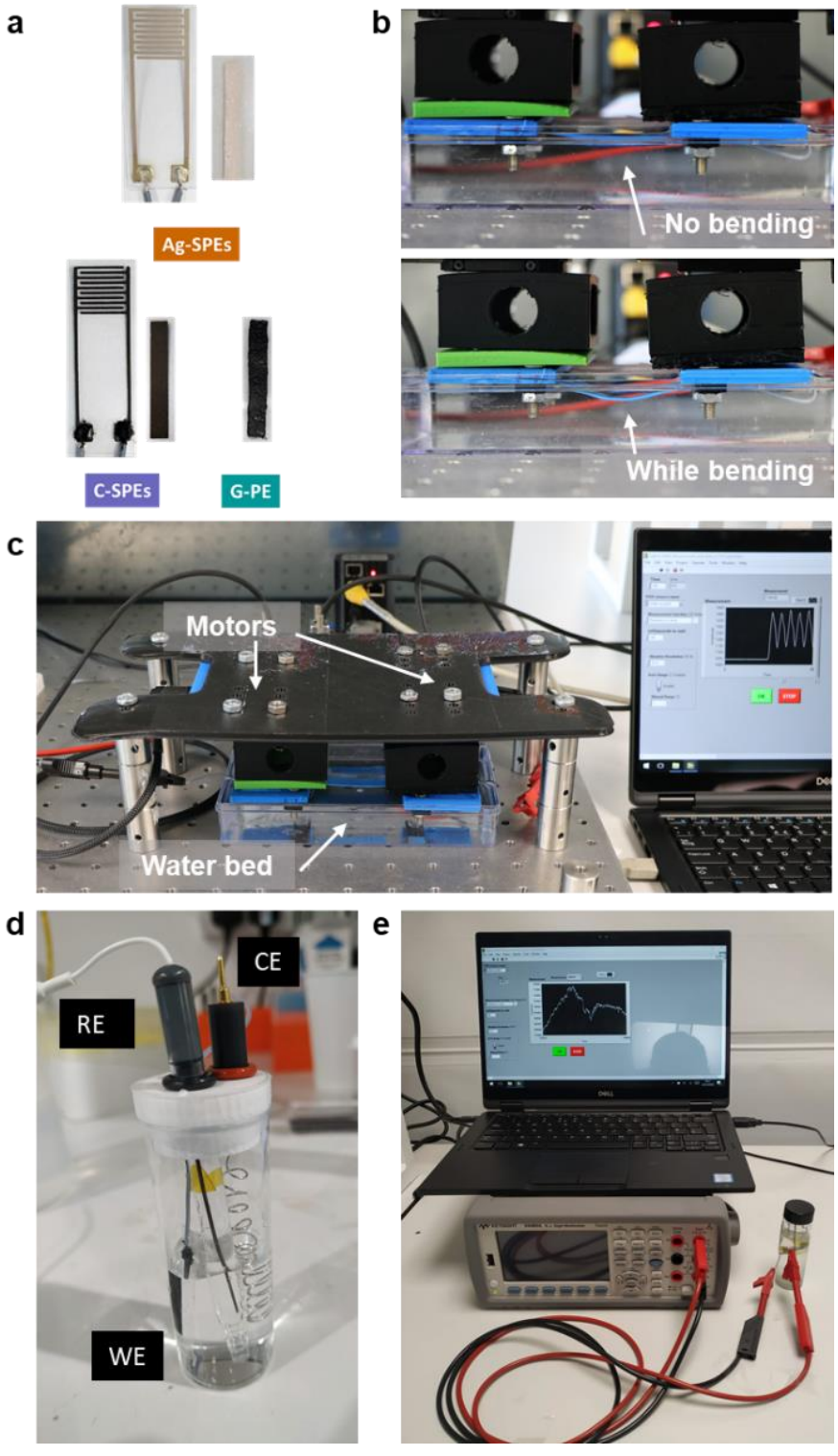


Figure 3.1. (a) Photos of the printed strips electrodes. (b) Images of the electrodes with no bending and while bending during underwater cyclic bending studies. (c) Setup of the underwater cyclic bending study. (d) Electrochemical cell setup with a Ag/AgCl reference electrode (RE), a platinum counter electrode (CE) and a Ag-SPE, C-SPE, G-PE or GCE working electrode (WE). (e) Long-term resistance study for the G-PE in seawater.

## 3.2. Experimental Section

### *3.2.1. Electrode Fabrication*

In this work, the commercial silver and carbon electrode pastes were screen printed on flexible PVC substrates while the graphite-based carbon paste electrode was printed on PHB/PHV (GoodFellow, 25µm thickness). In this way, the degradable electrode could be compared with the standard electrodes, which usually employ commercial pastes and a non-degradable plastic substrate. The G-PE was printed using a stencil mask due to the hydrophilic nature of the paste, as in screen printing, the commonly employed stainless steel stencils are sensitive to water. A 20 x 3 mm strip design was used for all CV and DPV studies while for the EIS analysis of the Ag and C-SPEs, a 0.5 mm wide and 10 mm long IDE fingers evenly spaced at 0.5 mm was utilized. The Ag-SPEs were screen printed using a low-temperature curable Ag paste (DuPont, 25 mΩ/sq at 25 µm thickness). For the C-SPEs, a conductive carbon paste (SunChemical, 21 Ω/sq at 25 µm thickness) was used. For the G-PEs, a graphite-based paste was prepared by mixing 8 g of graphite flakes (Merck, 808091) with commercially available polyvinyl alcohol (PVA) based glue (7.5 g) and water (6.7 g). After printing, the Ag-SPEs were dried at 80 °C for 10 min and the C-SPEs at 80 °C for 20 min. The G-PEs had the same drying conditions as the C-SPEs. Finally, the Cu wires were attached on the contact pads. For the Ag-SPEs, commercial Ag ink was used to glue the Cu wire on the electrode at room temperature, while the C-SPEs and G-PEs used the SunChemical carbon paste cured at 80 °C for 20 min to minimize material interference.

### *3.2.2. Material Characterization*

To evaluate the electrical characteristics of the printed electrodes, current-voltage (I-V) measurements were carried out between two voltage probes at distances of 5, 10, 15 and 20 mm for three different strips of the same material using the Omni probe station. As the printed electrodes had the same geometry, the transfer length method (TLM) was applied to obtain the sheet resistance of the screen-printed materials as described elsewhere [134]. The surface thickness of each printed electrode was investigated using a profilometer (Bruker DektakXT) with a scan range of 524 µm using the hills and valleys profile. A Savitzky–Golay filter using 1000 points was applied to the data to estimate the thickness of the samples. The morphological characterization and the cross-sectional view of the film before and after 16 weeks in artificial seawater was performed by a scanning electron microscope (SEM, Hitachi SU8240 at 8 kV) and analysed using the ImageJ software. The contact angle was estimated by using 10 µL volume of water on top the electrodes with magnified

photographed images of the drops from the same angle and direction. The contact angle was estimated using an image editor software (GIMP). To check the mechanical strength of the printed electrodes under flexible conditions underwater, the resistance of the electrodes was measured (Agilent 34461A Digital Multimeter) under 250 cycles of dynamic bending conditions. The printed electrodes were connected to two linear stage motors (from Micronix USA) and both motors were synchronized through a LabVIEW program to move along opposite directions. This motor movements leads to a cyclic bending of the electrodes at bending radius of 20° (Figure 3.1b,c). The relative resistance change ($\Delta R/R_0$) was calculated by finding the local maxima/minima ($R_M$) during the cyclic bending and subtracting and dividing each data point by the first resistance point ($R_0$). This was then multiplied by 100 to find the percentual change, with $\Delta R/R_0 = 100 \times [R_M - R_0]/R_0$. The relative resistance change ($\Delta R_C$) was calculated by subtracting the average of the last 10 points the measurement (mean($R_F$)) to the average of the first 10 points (mean($R_I$)) and diving it by $R_0$. This was then multiplied by 100 to find the relative percentage change. Therefore, $\Delta R_c = 100 \times [mean(R_F) - mean(R_I)]/R_0$. The G-PE material long-term stability in artificial seawater (10 days) was measured by monitoring the resistance of the electrode with a digital multimeter (Agilent 34461A) through a LabVIEW controlled programme (experimental setup shown in Figure 3.1e).

### *3.2.3. Electrochemical Setup*

The CV, DPV, and EIS electrochemical analysis of the printed electrodes were carried out using the Metrohm Autolab (PGSTAT302N). A 3-electrode system, with a commercial Ag/AgCl RE, a platinum counter electrode and a printed (Ag-SPE, C-SPE or G-PE) or standard (glassy-carbon electrode, GCE) WE, were employed in the CV and DPV studies (experimental setup shown in Figure 3.1d). An IDE based two-electrode system was used for the EIS analysis from 1MHz to 0.5Hz. For electrochemical measurements all reagents were used as received and all solutions were prepared in deionized (DI) water unless otherwise mentioned. Tap water was taken from the laboratory tap and immediately tested. An artificial seawater solution was prepared by mixing 38mg/mL of unrefined sea salts in DI water. 50mM of Potassium hexacyanoferrate(II) trihydrate (FeCN, Sigma) was solubilized in 0.1 M $NaNO_3$. The experiments were performed under normal ambient conditions except for the ferrocyanide studies, which were done both in ambient and nitrogen atmosphere. Ferrocyanide (FeCN) was used to compare the voltammetric behavior of the SPEs in contrast to a standard GCE. The CV and DPV static bending studies were performed by attaching the electrodes to 3D printed probes of 1.60, 1.25, 1.00, and 0.80 cm radius. The same electrode was used throughout the bending experiment. For the 10-day long-term CV and DPV study, the electrodes were left in

artificial seawater and the electrochemical voltammograms were measured on days 1, 4, and 10. For the sensor application studies, the electrodes were modified with 10 uL of 50 mg/mL graphene oxide (GOx, Graphene Supermarket) to test for nitrite ($NO_2^-$) sensing. The GOx was drop casted on top of the electrodes and dried at 80 °C for 10 min. The GOx was not optimised for sensing performance, and it was diluted without further treatment. The electrodes were tested with 3 mM of $NaNO_2^-$ in artificial seawater. A carbon pasted was added to the top of the Ag-SPE, as most sensors use carbon paste for the WE. Only the part covered with the carbon paste was submerged in the solution. The paste was dried using the same methods as in Section 2.1. The WE had an active area of 10 x 3 mm for all electrodes.

### *3.2.4. Physical and Chemical Degradability Studies*

The degradability studies were conducted by placing the printed electrodes for 16-weeks in artificial seawater at 37 °C in a $CO_2$ incubator (Thermo Scientific HERAEUS BB 15). Optical images of the G-PE before and after 16 weeks at 37 °C in artificial seawater were taken using a Nikon Eclipse LV100ND microscope connected with Leica MC170HD camera. For the ultrasound disintegration studies, the CamLab camSonix C575T ultrasonic bath was used at room temperature. The electrodes with and without the substrate, and the PHB/PHV substrate were sonicated in artificial seawater with varying times.

## 3.3. Results and Discussion

### *3.3.1. Material Characterization*

The different techniques used to characterise the electrodes' materials can be seen Figure 3.2. The sheet resistances ($R_S$) of the SPEs were calculated using TLM as given in Figure 3.2a-c and the profilometry analysis of the electrodes can be seen in Figure 3.3. The analysis reveals that the G-PE ($R_S$ =30.1 Ω/sq) and the C-SPE ($R_S$= 26.9 Ω/sq) have almost similar values which are much higher than the one for the Ag-SPE ($R_S$= 0.053 Ω/sq). To study the paste topography and thickness, the surface profilometry analysis (shown in Figure 3.3) was carried out and it shows that the G-PE presented the largest variation in electrode thickness (20-53 µm), compared to the C-SPEs (9-15 µm) and Ag-SPEs (7-12 µm). The G-PEs were about 10% less conductive than the C-SPEs, however the conductivity of the sustainable paste can be improved by using carbon additives such as graphene or CNTs [120,135]. As the conductivity of the G-PE is in the range of the C-SPEs, it should produce an adequate performance for preliminary studies. Furthermore, the observed $R_S$ values of Ag-SPE and

C-SPE were compared with commercial values (given in Table 3-2). The measured $R_S$ of Ag-SPEs is twice that of the commercial value while the measured $R_S$ for the C-SPEs was 1.3 times greater than the reported commercial $R_S$. For both SPEs, the thickness was one third or less short of 25 µm, which partially explains the difference between the measured and commercial $R_S$ as thinner layers tend to have a higher $R_S$ [136]. Difference in curing temperatures and processing times might also influence the results, as well as the material composition.

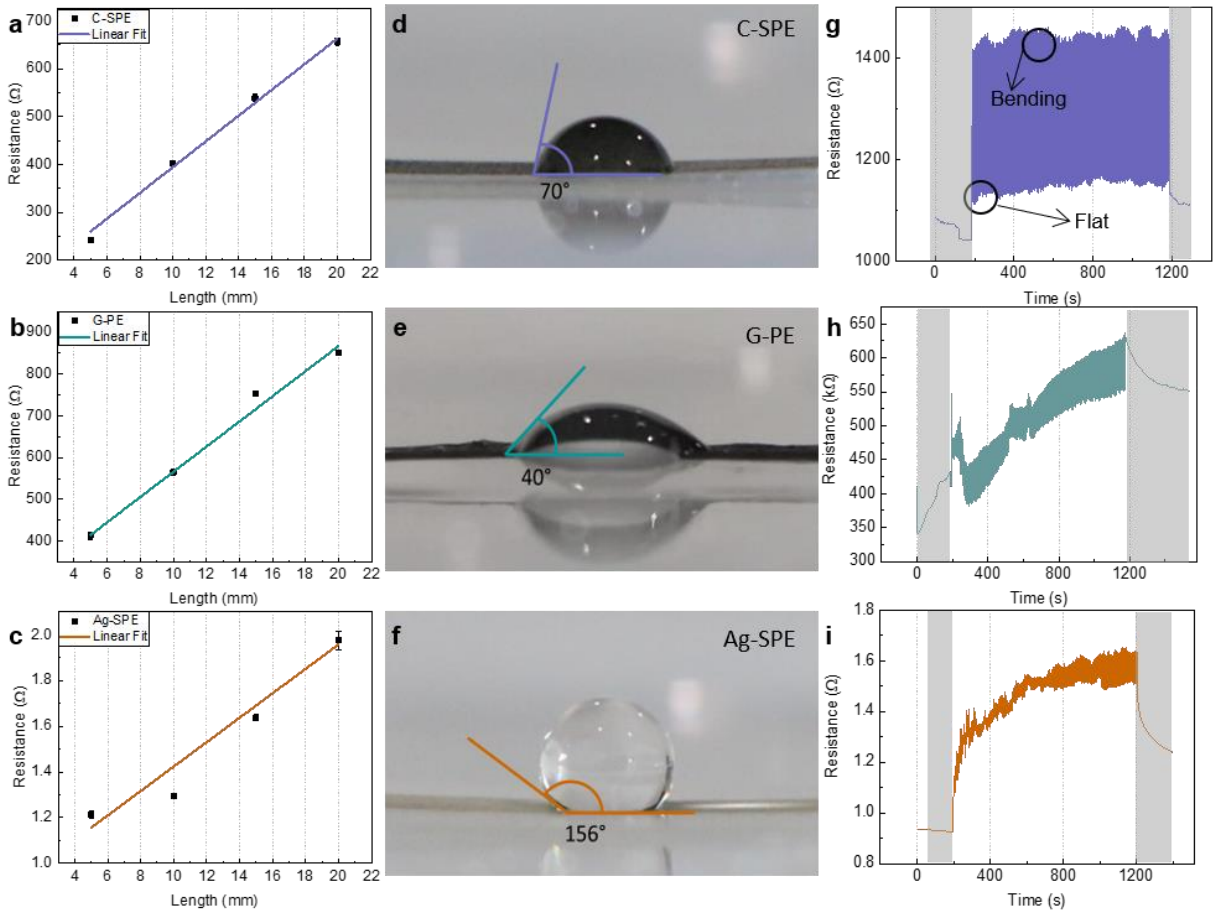


Figure 3.2. C-SPE, G-PE, and Ag-SPE: (a-c) Transfer length method for the determination of the sheet resistance. (d-f) Contact angle measurement between the electrodes and a water droplet. (g-i) Resistance monitoring before and after cyclic bending (grey rectangles) and during cyclic bending of the electrodes.

Table 3-2. Electrode thickness and measured and commercial resistivity of the printed electrodes.

| **Electrode** | **Thickness (µm)** | **$R_S$ ($\Omega$ sq$^{-1}$)** | **Error ($\Omega$ sq$^{-1}$)** | **Commercial $R_S$ ($\Omega$ sq$^{-1}$ @ 25 µm)** |
|---|---|---|---|---|
| **Ag-SPEs** | 7-12 | 0.053 | ±0.006 | 0.025 |
| **C-SPEs** | 9-15 | 26.9 | ±1.4 | 21 |
| **G-PEs** | 20-53 | 30.1 | ±1.7 | - |

The contact angle analysis showed that the sustainable graphite-based paste is more hydrophilic than the commercial pastes. The angle between the water droplet and the G-PE was of 40°, while for the Ag-SPE and the C-SPE was 156° and 70°, respectively (Figure 3.2d-f). A more hydrophilic conductive path improves the performance of electrodes in water-quality monitoring, as wettability has been shown to increase the charge transfer rate between the electrode and the electrolyte [137]. To check the adhesion and delamination of the printed layer from the substrate, cyclic bending measurements were performed. This only provides information about the mechanical properties of the electrodes during the bending cycles. Figure 3.2g-i shows the measured resistance before and after cyclic bending and during the 250 bending cycles. The C-SPE showed a very stable response during bending and quickly returned to almost the same resistance it had initially, with a relative resistance change ($\Delta R_C$) of 2.3% (after the 250 bending cycles), while for the Ag-SPE and the G-PE the values were 32.2% and 47.3%, respectively. All the resistances varied considerably during cyclic bending from the planar to the bending position (Figure 3.4) with the G-PE having the largest $\Delta R/R_0$ variation (from -7.7% to 61.0%) and the C-SPE, the lowest (from 2.5% to 35.5%), and the Ag-SPE, a $\Delta R/R_0$ variation of about 14.5% to 77.0%. This large resistance variation and steady increase of $\Delta R/R_0$ during bending for the G-PE and the Ag-SPE could indicate a breakage in the paste composite when bending. A more structural analysis (e.g., SEM before and after cyclic bending) needs to be carried out to understand the cracking of the bulk of material. This change is permanent as the resistance after cyclic bending did not return to the initial values. Even though the Ag-SPE showed a high variation in resistance, it also presented the lowest overall resistance in the $\Omega$ range while the carbon-based electrodes had resistances in the k$\Omega$ range.

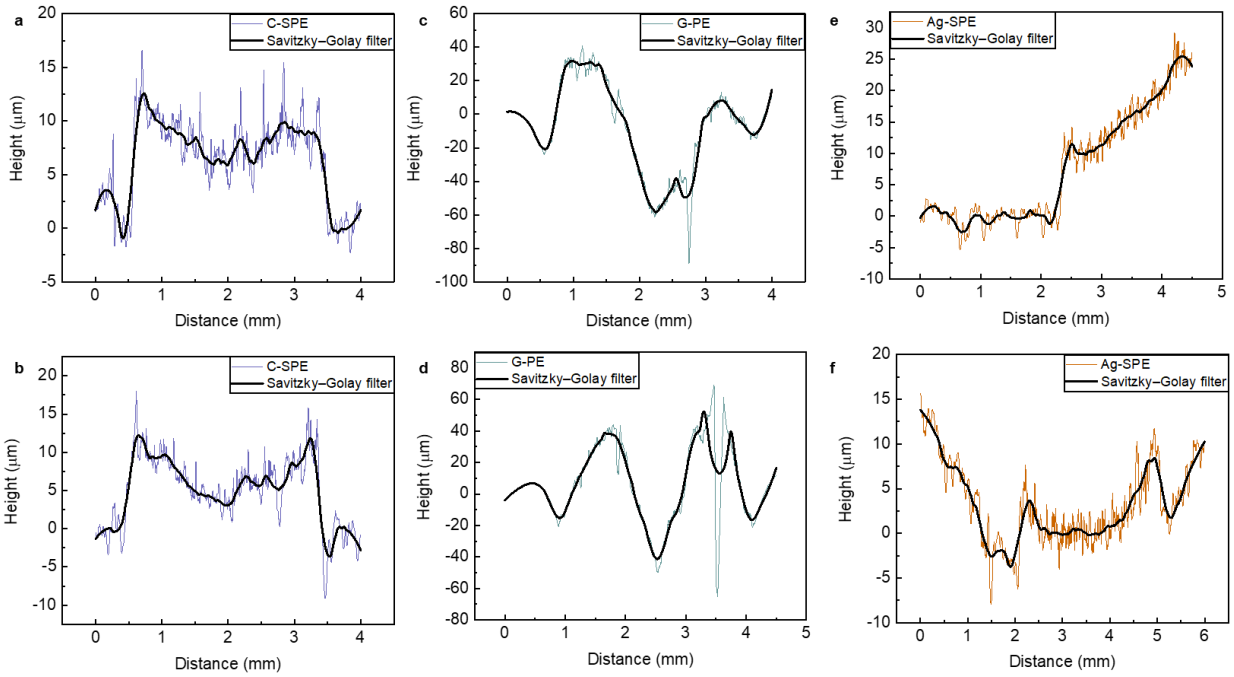


Figure 3.3. Profilometry of the (a,b) C-SPEs, (c,d) G-PE and (e,f) Ag-SPEs on two different sections of the electrodes.

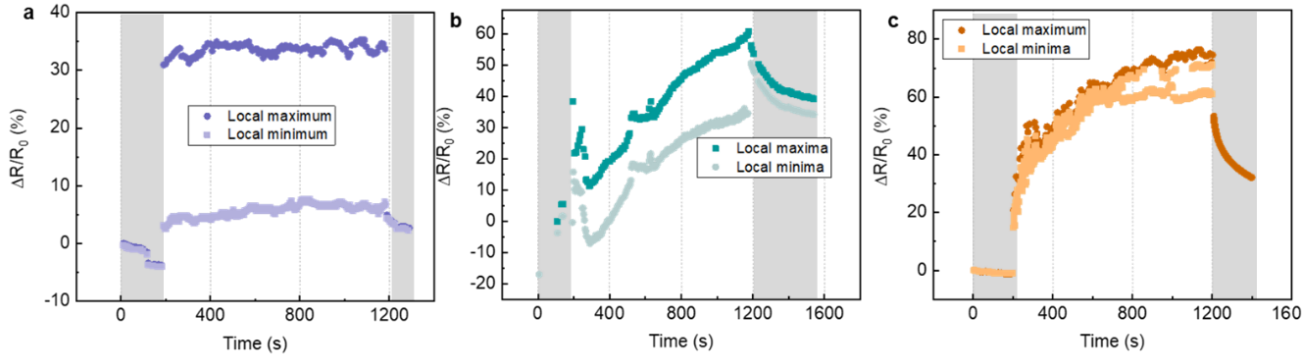


Figure 3.4. Local maxima and minima values for the relative resistance ($\Delta R/R_0$) before and after (grey rectangles) and during cyclic bending for the (a) C-SPEs, (b) G-PE and (c) Ag-SPEs.

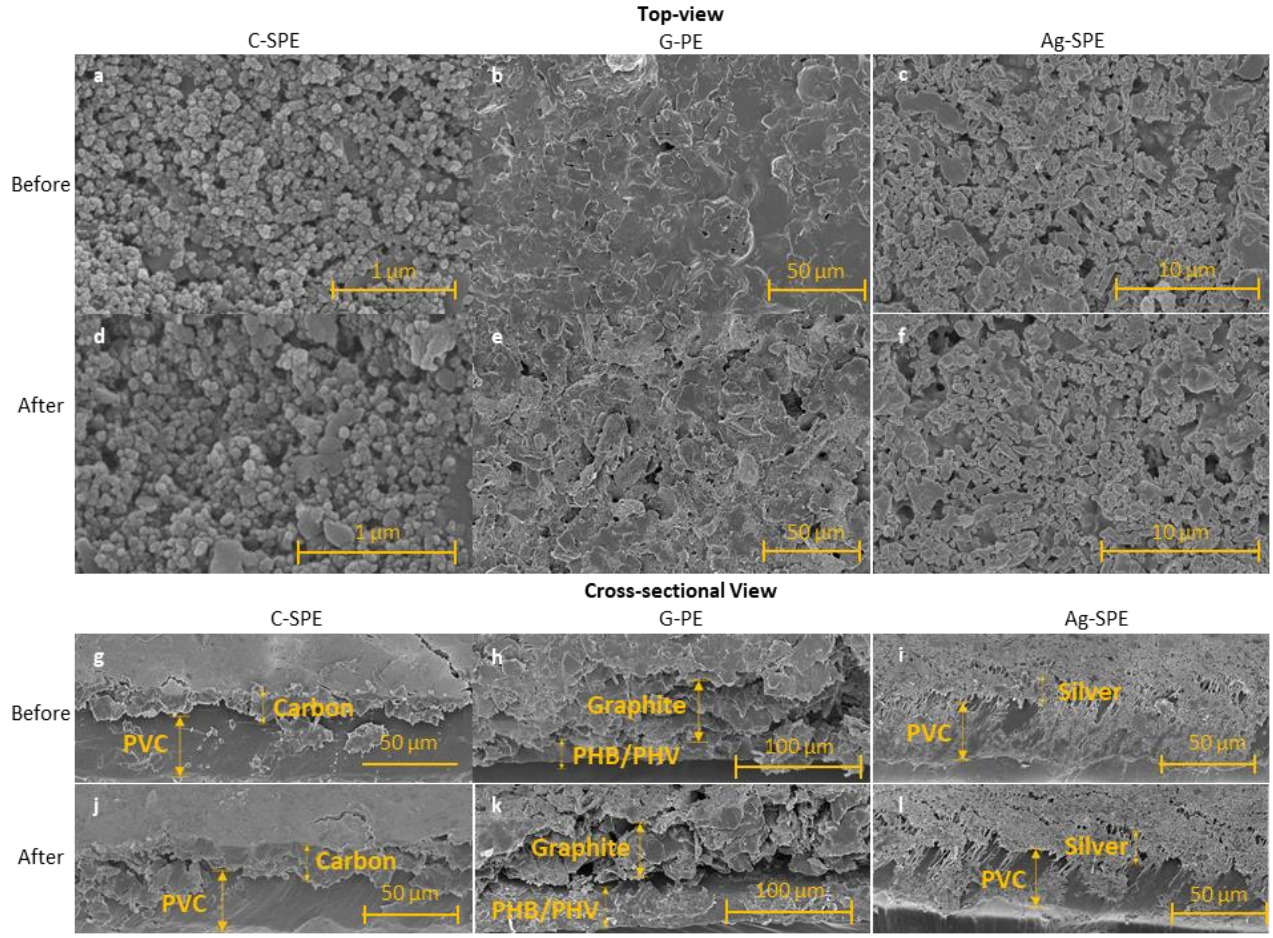


Figure 3.5. Top and cross-sectional SEM images of C-SPE, G-PE, and Ag-SPE (left to right). Surface morphology of the electrode pastes before (a-c) and after 16 weeks in artificial seawater (d-f). Cross-sectional view of the electrode pastes before (g-i) and after 16 weeks in artificial seawater (j-l).

Figure 3.5 shows the surface morphology (Figure 3.5a-f) and the cross-sectional view (Figure 3.5g-l) of the C-SPEs, G-PEs and Ag-SPEs. The porous microstructures of the C-SPEs (Figure 3.5a,d) and Ag-SPEs (Figure 3.5c,f) remains unaffected even after 16 weeks in artificial seawater while a clear difference can be seen in the before and after SEM images of the G-PE (Figure 3.5b,e), where a higher porosity is observed likely due to material degradation. From the images, one of the reasons for the higher mechanical stability of the Ag- and C-SPEs could be attributed to the fine-grained packed structure compared to the amorphous like stacked layers observed in the graphite electrode. Furthermore, the number of active sites which are capable of ionic reactions largely depends on the microstructure and crystallinity of the electrode. In this way, the fine-grained compact structure of the Ag-SPE is expected to have a less active area as compared to the loosely disordered structure of carbon flakes, but a higher mechanical stability. The film morphologies are distinct for each electrode

material, with a striking difference between the two carbon-based pastes. While the C-SPEs showed a spherical nanostructure in the sub-100nm range, the G-PEs showed stacked, smooth graphite flakes, likely due to the combination of different carbon materials, binders and solvents used in the paste preparation. The cross-sectional view of the electrodes (shown in Figure 3.5g-l) shows that the films are firmly adherent to the substrate except for the G-PE after 16 weeks in artificial seawater (Figure 3.5k), indicating that the paste is starting to detach from the substrate. The thickness of each film was measured from the cross-section view (4.7-10.5 μm for the Ag-SPE and 7-18.6 μm for the C-SPEs) without much change in thickness before and after 16 weeks in artificial seawater. The G-PEs, however, presented a wide range in paste thickness, from 40-61 μm and 49.5-87 μm before and after 16 weeks in artificial seawater, indicating paste degradation. These results are similar to the profilometer ones (Table 3-2). Another parameter that should be taken into consideration is PVA degradation. PVA is a water-soluble polymer and has been shown to accelerate degradation of polymer mixtures in seawater [138]. Therefore, PVA degradation likely contributes to the change in G-PE paste thickness seen throughout the 16 weeks by facilitating material hydrolysis.

### *3.3.2. Silver and Carbon Ionic Electrochemical Interaction*

#### *3.3.2.1. Voltammetric Analysis*

Seawater was chosen to analyse the different voltametric response of the silver and carbon materials in different chemical conditions due to its high ionic strength. Considering a seawater with salinity S = 35, the four major ions present in a standard chemical composition are chloride ($Cl^-$, 565.76 mmol/kg-$H_2O$), sodium ($Na^+$, 486.16 mmol/kg-$H_2O$), magnesium ($Mg^{2+}$, 54.75 mmol/kg-$H_2O$), and sulphate ($SO_4^{2-}$, 29.27 mmol/kg-$H_2O$) [139]. Accordingly, three different salts were chosen, NaCl, $MgCl_2$ and $MgSO_4$, to evaluate how different concentrations of these ions affect the faradaic and non-faradaic currents of the commercial SPEs. As the aim of this section is to directly compare carbon and silver in the presence of other ions, the G-PE was not included in this section. In this manner, the difference in binders and solvents would not interfere with results, as both commercial SPEs have similar paste compositions. Figure 3.6a shows the CV and DPV for the different electrodes for different NaCl concentrations (0-100 mM). The NaCl salt seems to heavily affect the voltammograms for the Ag-SPEs and considering the possible oxidation states for Ag, it is safe to assume Ag is reacting with the $Cl^-$ ion. Considering Ag NPs have been used for the detection of $Cl^-$ ions in water and sweat previously as it quickly interacts with the halide family [117,118,140], it is not surprising the Ag conductive track reacted with the $Cl^-$ ions.

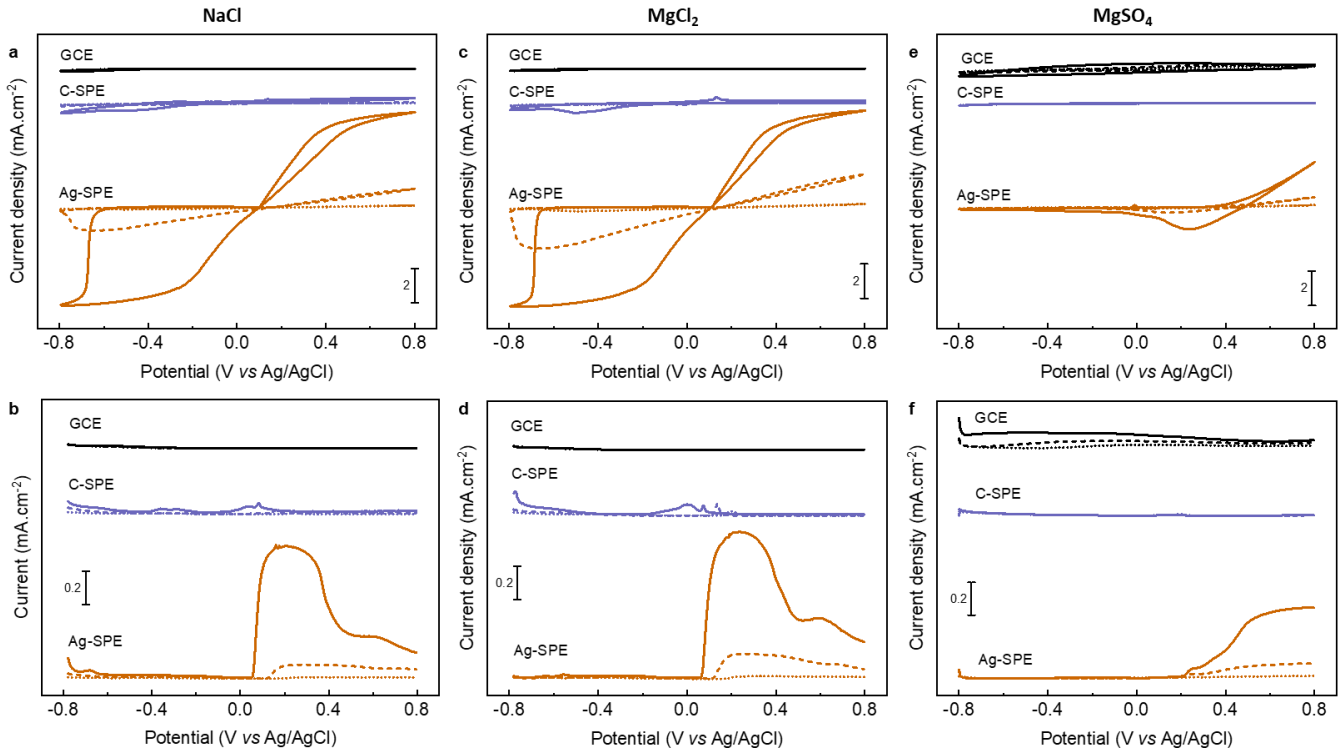


Figure 3.6. GCE, C-SPE, and Ag-SPE (top to bottom) CVs (top) and DPVs (bottom) for NaCl (a and b), $MgCl_2$ (c and d), and $MgSO_4$ (e and f) in DI water. Dotted line is for 0 mM, dashed line is for 10 mM and full line is for 100 mM of salt concentration, or half of the concentration for $MgSO_4$.

In Figure 3.6b, two broad peaks can be observed for the Ag-SPEs in the DPV, a more intense one at around +0.20 V and another at +0.60 V. This corresponds to what has been observed in literature, with the first peak matching the reaction of Ag with the $Cl^-$ ion (Equation 3.1) and the more energetic one to the one-electron oxidation of the metallic Ag to $Ag^+$ (Equation 3.2) [118]. Interestingly, the peaks cannot be distinguished in the CVs, indicating that the non-faradaic current probably dominates over the faradaic one. The formal potential of the $Ag/Ag^+$ redox pair is +0.80 V *vs* a normal hydrogen electrode (NHE), with the reaction being expected to occur at about +0.58 V when using a saturated Ag/AgCl RE [141,142]. This oxidation matches the second peak, as it seems to be centred around +0.60 V. Therefore, the more intense peak most likely corresponds to the reaction of Ag with the $Cl^-$ ion. In a previously reported work, a difference of 0.36 V between the two oxidation peaks and the results showed a difference of around 0.35 V, indicating that indeed the peak corresponds to the silver reaction with the halide [118]. Furthermore, by changing the concentration of NaCl, a clear increase in current density can be observed implying that more Ag reacts with the ions.

$$Ag_{(s)} + Cl^- \rightarrow AgCl_{(s)} + e^- \quad (3.1)$$

$$Ag_{(s)} \rightarrow Ag^+ + e^- \quad (3.2)$$

$$2Ag + SO_4^{2-} \rightarrow Ag_2SO_4 + 2e^- \quad (3.3)$$

In comparison, the carbon electrodes do not react as strongly to the presence of salts. The GCE seems to be almost inert to the changing concentration of NaCl while the C-SPE does exhibit clear peaks at about -0.50 V and +0.13 V at 100 mM NaCl. Considering the GCE did not exhibit any significant response, it could be presumed that the binders and solvents used in the C-SPEs paste influence the voltammogram. Furthermore, the source, thickness, lattice distribution, and other morphological differences of the bulk *vs* printed carbon, as observed from the SEM images in Figure 3.5, could also influence the results. As the exact composition is patented, it is difficult to analyse the interaction further. Nevertheless, the current density is quite low, so it appears that the C-SPEs can be used even in mediums with high concentration of $Cl^-$ ions. A similar result was observed for the $MgCl_2$ salt (Figure 3.6c,d), where the Ag-SPE once more seemed to strongly react with the $Cl^-$ ions. In this case, the chloride concentration was double than that of the NaCl, as the Mg salt contains two $Cl^-$ ions. Although the anion concentration was doubled, it seemed that a 100 mM of NaCl and 100 mM of $MgCl_2$ produce the same current density. However, when comparing the DPV for 10 mM of both solutions (Figure 3.7), the current density for the $MgCl_2$ is nearly double than that of the NaCl voltammogram. As the area of the Ag reacting with $Cl^-$ ion is finite, this could indicate that the reacting area reached its saturation point somewhere between 10 and 100 mM.

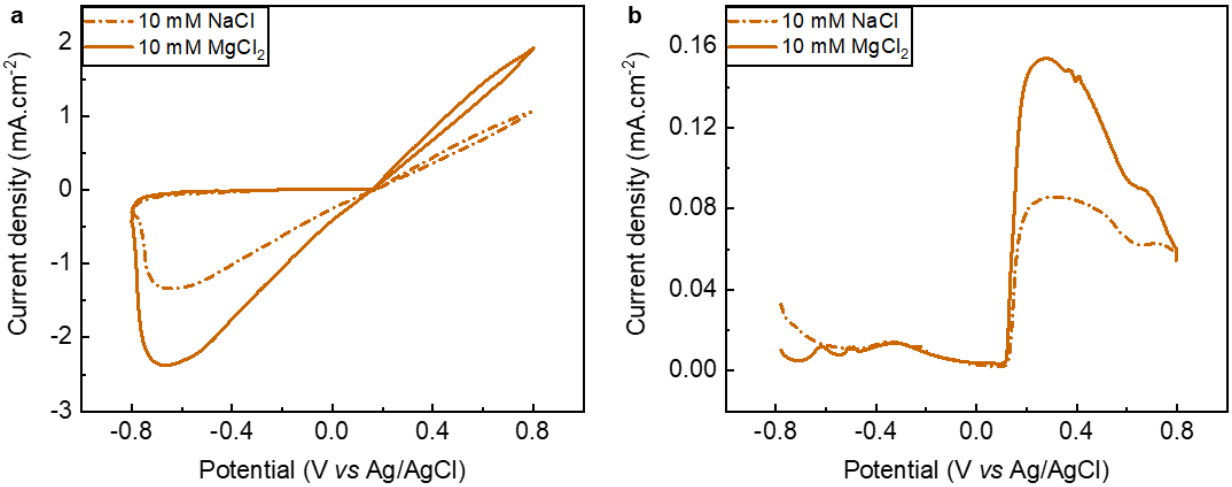


Figure 3.7. Comparison of the (a) CV and (b) DPV of the Ag-SPE in 10 mM NaCl and 10 mM $MgCl_2$.

The electrochemical interaction with the $SO_4^{2-}$ anion can be seen in Figure 3.6e,f. The interaction with the anion did not appear as strong in this potential window for neither of the electrodes even if considering half of the salt concentration was added (up to 50 mM). The redox potential for $Ag/Ag_2SO_4$ is + 0.65 V *vs.* SHE or + 0.43 V *vs.* Ag/AgCl and their reaction is described in Equation 3.3 [99]. The peak starts at around +0.2 V in the Ag-SPE DPV (Figure 3.6f) which continues to increase until +0.8V, therefore it is hard to distinguish the $Ag/Ag_2SO_4$ interaction and the Ag oxidation. It is also possible that other reactions are occurring at the electrode interface, but further studies are needed. It can be concluded that the Ag-SPEs are reacting with the $Mg_2SO_4$ solution as there is a clear increase in the faradaic peaks with increasing salt concentration while the carbon electrodes appear to be mostly inert.

#### *3.3.2.2. Electrochemical Impedance Spectroscopy Results*

The electrical results (Table 3-2), and the CV and DPV studies showed that the Ag- SPEs are highly conductive as compared to the C-SPEs. The electrode/electrolyte interaction through EIS analysis confirmed that the Ag-SPEs are more reactive to the electrolyte solution, most likely through the formation of an electrochemical double layer (*edl*, Figure 3.8a) and strong chemical interaction with the analyte ions. In artificial seawater, the observed impedance for the Ag-SPE is almost two times less than for the C-SPE (shown in Figure 3.8b). As confirmed by the CV and DPV studies, the nature of the electrolyte also strongly influences the electrode performance. Due to the high ionic conductive nature of seawater, the impedance observed for the Ag-SPE is almost 2 times less than in tap water. In contrast, the difference between impedances in tap water and artificial seawater was low for the C-SPEs. This difference in impedance between the C-SPEs and the Ag -SPEs in different electrolyte solutions could be due to the faradaic and non-faradaic reactions. For the C-SPEs, the analyte ions adsorbed on the surface of the electrode could be mainly due to the *edl* formation through non-faradaic reactions as shown in Figure 3.8a. However, for the Ag-SPEs, due to their high conductivity, both redox reactions and *edl* formation may occur due to the diffusion of ions. The diffusion of ions on the surface of the electrode was observed from the sharp decrease in impedance (as noted in Figure 3.8b) and almost linear impedance rise in the Nyquist plot (Figure 3.8c,e) both in tap water and artificial seawater. This sharp decrease in impedance for the IDEs shows a more capacitive reaction in the low frequency range. Furthermore, the negligible charge transfer resistance arising from the lack of semi-circle in the high frequency range (Figure 3.8c-f) reveals that the bulk resistance of both printed electrodes is low which is a highly advantageous feature for the conductive path of working and reference electrodes. The very low impedance value of the Ag-SPE in seawater

as compared to tap water (Figure 3.8c,e) shows the influence of conductivity of the solution on the electrode. Similarly, the influence of ions (NaCl, $MgCl_2$, and $MgSO_4$) on Ag-SPE and C-SPE was analysed. The ionic influence in the Nyquist impedance plot is shown in Figure 3.8g,h. To compare with the artificial seawater solution, 100 mM NaCl, 100 mM $MgCl_2$, and 50 mM $MgSO_4$ were used. The Ag-SPEs presented a very low resistance (Figure 3.8g), especially in NaCl and $MgCl_2$, in the order of 10-20 kΩ, while a higher resistance was seen in $MgCl_2$. The opposite trend was observed for the C-SPEs (Figure 3.8h), with a lower resistance in $MgSO_4$, although it presented a much higher overall resistance than the Ag-SPEs, in the MΩ range. The impedance values were similar to those observed for the artificial seawater solution (Figure 3.8e,f). From these results, it was observed that the Ag-SPEs presented an overall lower resistance value than the C-SPEs (Figure 3.8), however, were not as electrochemically stable when in the presence of other ions in the solution. For example, from Figure 3.6 and Figure 3.7, the $Cl^-$ seemed to strongly react with Ag, while the carbon paste remained electrochemically inert. After these initial studies on the stability of the commercial pastes, the G-PE was included in all the experiments throughout the paper to determine its performance against the SPEs.

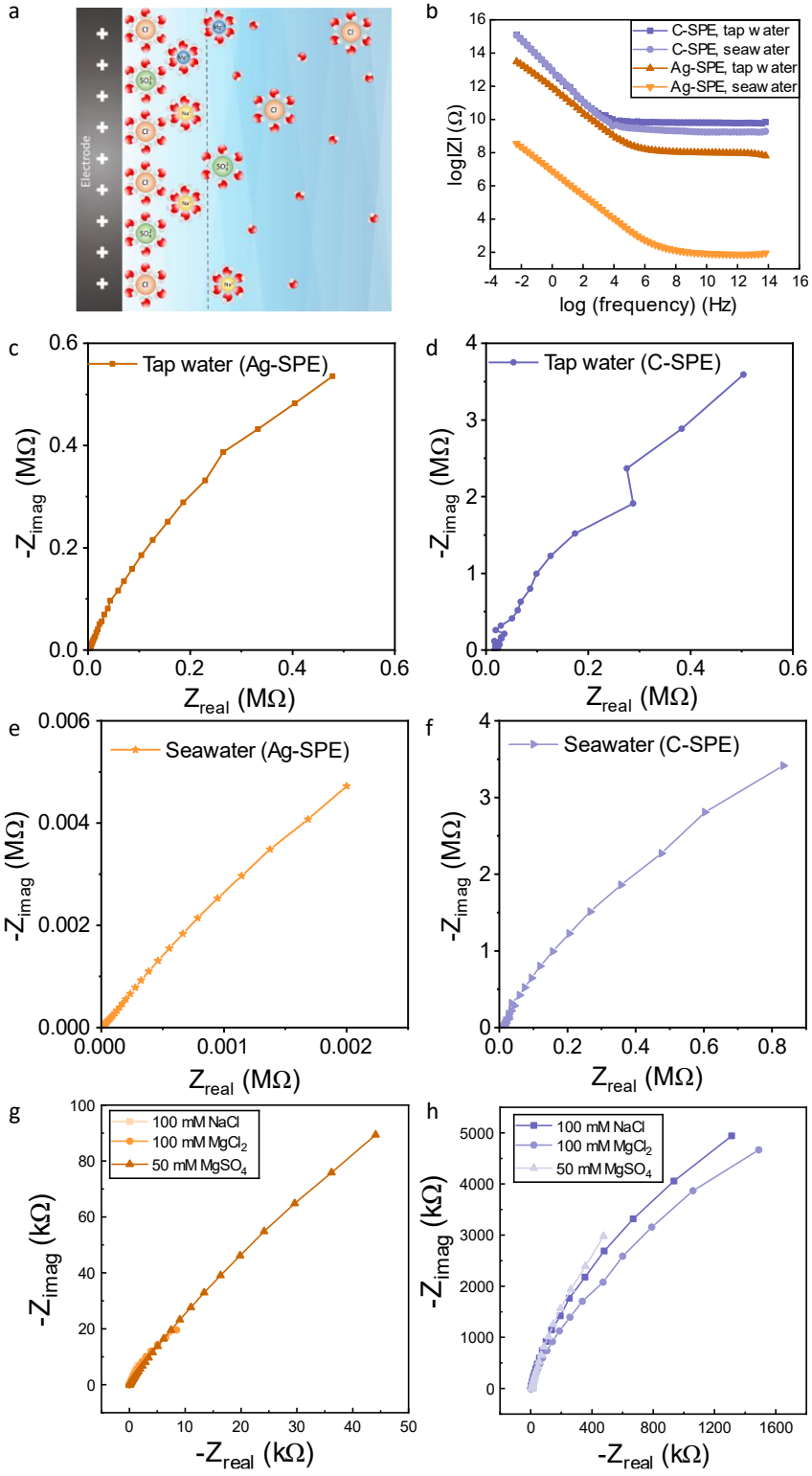


Figure 3.8. (a) Schematic representation of the *edl* on the electrode surface in artificial seawater. (b) Bode impedance plot of the Ag-SPEs and the C-SPEs in tap water and artificial seawater. Nyquist plot in tap water for (c) the Ag-SPEs and (d) the C-SPEs and in artificial seawater (e) the Ag-SPEs and (f) the C-SPEs. Nyquist plots for the (g) Ag-SPEs and (h) C-SPEs in 100 mM of NaCl, 100 mM $MgCl_2$ and 50 mM $MgSO_4$.

### *3.3.3. Electrochemical Analysis*

The CV and DPV analysis for the GCE, C-SPE, G-PE, and the Ag-SPE electrodes in FeCN were carried out and the curves are shown in Figure 3.9a,b. These electrochemical analyses show that each electrode exhibits a slightly different cyclic behaviour due to their unique material composition involved in the electrochemical reaction. The C-SPE exhibits a similar current density when compared to the standard GCE. However, the Ag-SPE current density is 3 times higher than that of the carbon electrodes when comparing the current density for the FeCN oxidation peak ($j_{FeCN}$). Considering the difference in sheet resistance from the I-V sweep measurement (from Figure 3.2a-c) and that silver is generally more conductive than carbon, this is an expected result. Electrode materials require a high electronic conductivity so the rate-limiting process will not the be the electrons moving through the material but the electron movement across the electrode/solution interface [143]. Nonetheless, the electrode intrinsic conductivity can be one of the factors that affects the current performance. As the electrodes have different electrical resistances which in turns affects the $j_{FeCN}$, each printed electrode $j_{FeCN}$ was adjusted to that of the standard GCE for a better comparison between the voltammograms. The current densities before the correction were calculated by their active area, which is 1 x 0.3 cm for the printed electrodes and the circular area for the 3 mm diameter GCE. The correction factor was calculated by dividing the printed electrode FeCN oxidation peak current densities, PE-$j_{FeCN}$, by the respective GCE oxidation peak current densities, GCE-$j_{FeCN}$. Therefore, the Ag-SPEs had their current densities divided by a correction factor of 3.40, the C-SPEs by 0.90 and the G-PEs by 0.14 which was later used for the CVs and DPVs unless stated otherwise.

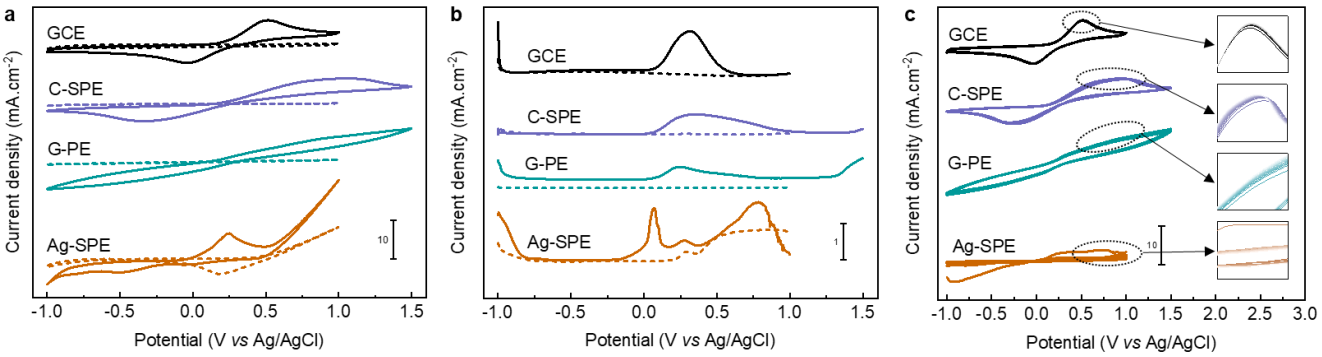


Figure 3.9. GCE, C-SPE, G-PE, and Ag-SPE (top to bottom) CVs (a) and DPVs (b) for 50 mM FeCN in 0.1 M $NaNO_3$ with a scan rate of 100 mV/s (full line) and 0.1 M $NaNO_3$ blank (dashed line) under ambient condition. (c) CVs of 50 mM FeCN in 0.1 M $NaNO_3$ for the different electrodes over 15 continuous cycles under ambient condition and magnified FeCN redox peaks.

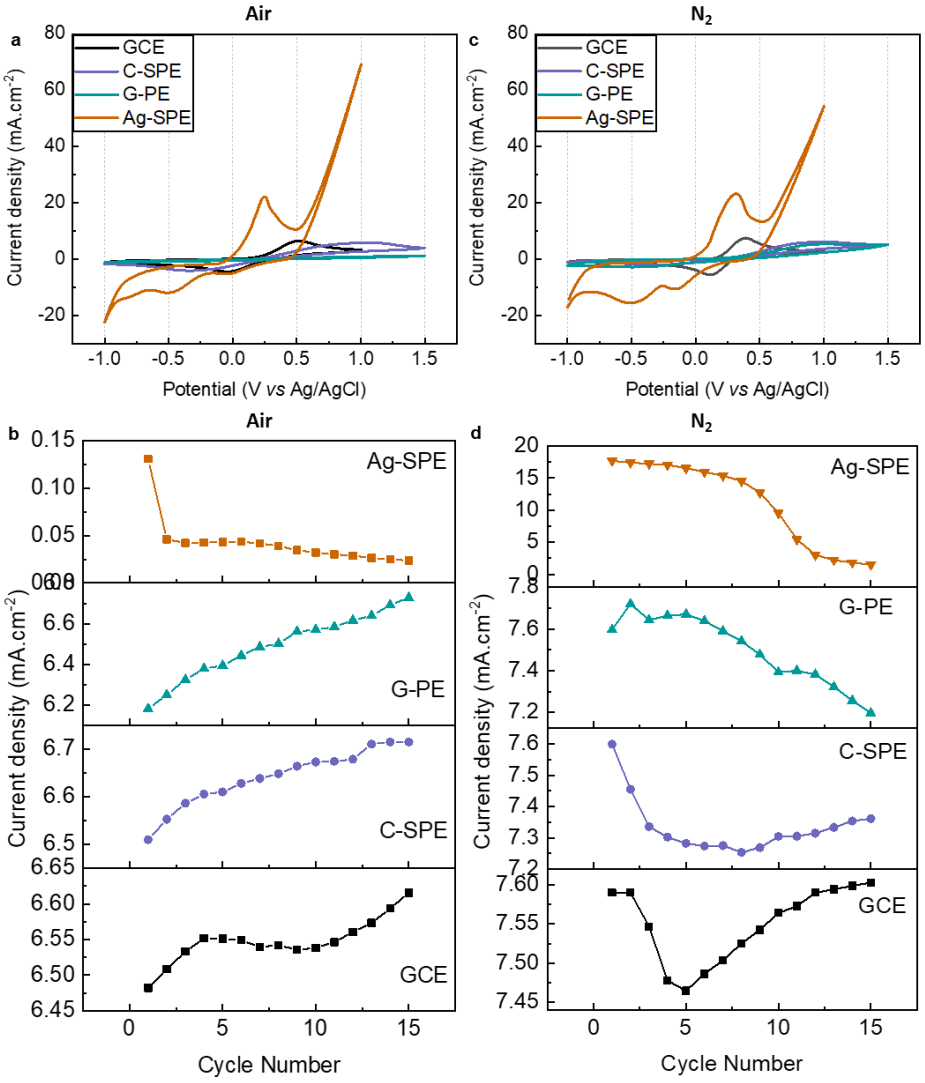


Figure 3.10. (a) Comparison of the CV of the printed electrodes in air atmosphere. (b) The FeCN peak current density variation of individual electrodes during 15 cycles in air atmosphere. (c) Comparison of the CV of the printed electrodes in $N_2$ atmosphere. (d) The FeCN peak current density variation of individual electrodes during 15 cycles in $N_2$ atmosphere.

When correlating with the measured $R_S$ (Table 3-2), the more conductive electrode presented the higher oxidation current but not on the same proportions. This could be due to how the electrodes react with the analyte and the supporting electrolyte solution (such as the oxidation of silver) as electrode conductivity is not the only parameter that affects the electrode performance [61]. The C-SPE showed clear peaks in both voltammograms, although broader than the GCE ones while the G-PE did not present clear peaks in the CV however did have a peak in the DPV. As the G-PE did not show a reliable peak, the correction factor was not used throughout this chapter. The Ag-SPE can react with the FeCN to form a new salt complex which explain the appearance of other peaks in the

Ag-SPE voltammograms [144], explaining why only the first few cycles show a clear oxidation peak. This can be better seen in Figure 3.9c, where the electrodes were cycled 15 times in 50 mM FeCN. While the carbon electrodes appear to be quite stable, the Ag-SPE current density decrease sharply after the first cycle due to the reaction of Ag with FeCN.

The variation of the CV redox peak intensities in air was compared in Figure 3.10a. The current density was not adjusted for Figure 3.10. It was noted that the redox peak intensity changed with the cycles and the change of $j_{FeCN}$ per cycle can be seen in Figure 3.10b. The Ag-SPE presented the expected results of a sharp decreasing trend however the carbon electrodes' current density increased with each cycle. Comparing the first and last cycle, there was an increase of 2.0, 3.1 and 8.8% for the GCE, C-SPE and G-PE respectively and a sharp decrease of -81.8% for the Ag-SPE. This is not what usually happens and to further investigate how the atmosphere affects the electrodes, the CV studies with 50 mM FeCN were repeated under an inert $N_2$ atmosphere (Figure 3.10c and Figure 3.10d). The electrodes were also cycled 15 times and the results can be seen in Figure 3.11.

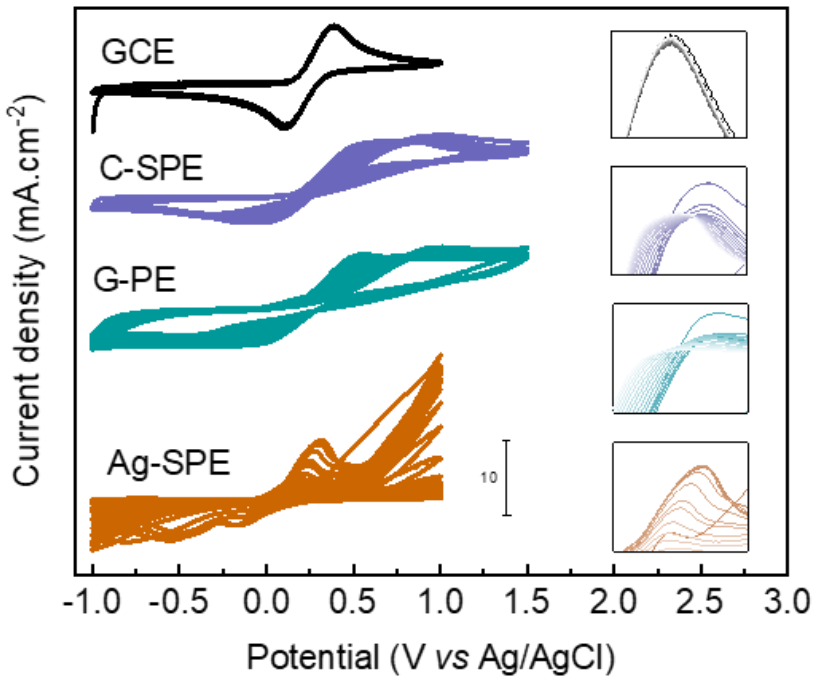


Figure 3.11. CVs of 50 mM FeCN in 0.1 M $NaNO_3$ for the different electrodes over 15 continuous cycles under $N_2$ atmosphere. A zoomed vision of the oxidation peaks is given in the insets.

Interestingly, although there was a clear shift to the left in the peaks for the carbon printed electrodes in Figure 3.10a, the G-PE redox peaks dramatically increased under inert atmosphere, being now comparable to the C-SPE voltammogram, while the C-SPE showed only a slight increase

in current density when compared to the normal atmosphere results. This difference in $j_{FeCN}$ for the G-PEs under different atmospheres could indicate some adjustment issues between the manually printed electrodes, which is to be expected when compared to the SPEs. For example, as the G-PEs presented the largest variation in electrode thickness (Figure 3.3), this could influence the paste properties. A more uniform printing can decrease this difference in Faradaic current. The decrease in the Ag-SPE current density can be seen more clearly in this case. More importantly, the increase in $j_{FeCN}$ with each cycle for the carbon electrodes did not appear to occur under an inert atmosphere (Figure 3.10c,d). This time, when comparing the first and last cycle, the GCE electrode was mostly stable (increase of 0.2%) while the C-SPE, the G-PE and the Ag-SPE presented a decrease of 3.1, 5.3 and 91.5% respectively. This could indicate that gases present in the atmosphere could be reacting with the carbon electrode surface, however further studies are needed to confirm this behaviour. To investigate the electrodes performance in water quality monitoring, further electrochemical studies in artificial seawater and tap water were conducted as discussed below.

### *3.3.4. Interaction with Seawater and Tap Water*

The printed electrodes were also tested in tap water and artificial seawater and compared to the standard GCE (Figure 3.12). In tap water (Figure 3.12a,b), the GCE seems to be the most stable electrode, presenting no redox peaks in the CV and a flat background in the DPV. The printed electrodes instead display some response, with the C-SPE showing a clearer oxidation peak and the Ag-SPE a larger anodic current density. This could once more indicate that the binders used in the C-SPEs influence the voltammogram response. However, the current densities are in the microampere range, which is quite low when compared to the artificial seawater voltammograms (Figure 3.12c,d). When considering the EU's Water Directive 98/83/EC maximum permitted concentration of $Cl^-$ and $SO_4^{2-}$ of 200 mg/L (7.05 mM) and 250 mg/L (2.60 mM) respectively [24], the current density seems reasonable, as the presence of ions is much lower than in other solutions. The G-PE did not display any reaction to the elements present in tap water. As the difference between the silver and carbon electrodes was not as significant, both could be employed as electrodes in mediums with low ionic strength such as tap water. Naturally, it is important to keep in mind silver's tendency to oxidize. In artificial seawater, the electrodes responses were quite different (Figure 3.12c,d) and followed the expected trend as Ag is known to interact with chloride and sulphate ions [99,118]. The Ag-SPE presented a clear redox peak for both CV and DPV while the carbon electrodes showed little to no response. This indicates that the carbon-based electrodes are more suitable for applications in

solutions with high ionic strength, especially when considering the Ag interaction with the halide family.

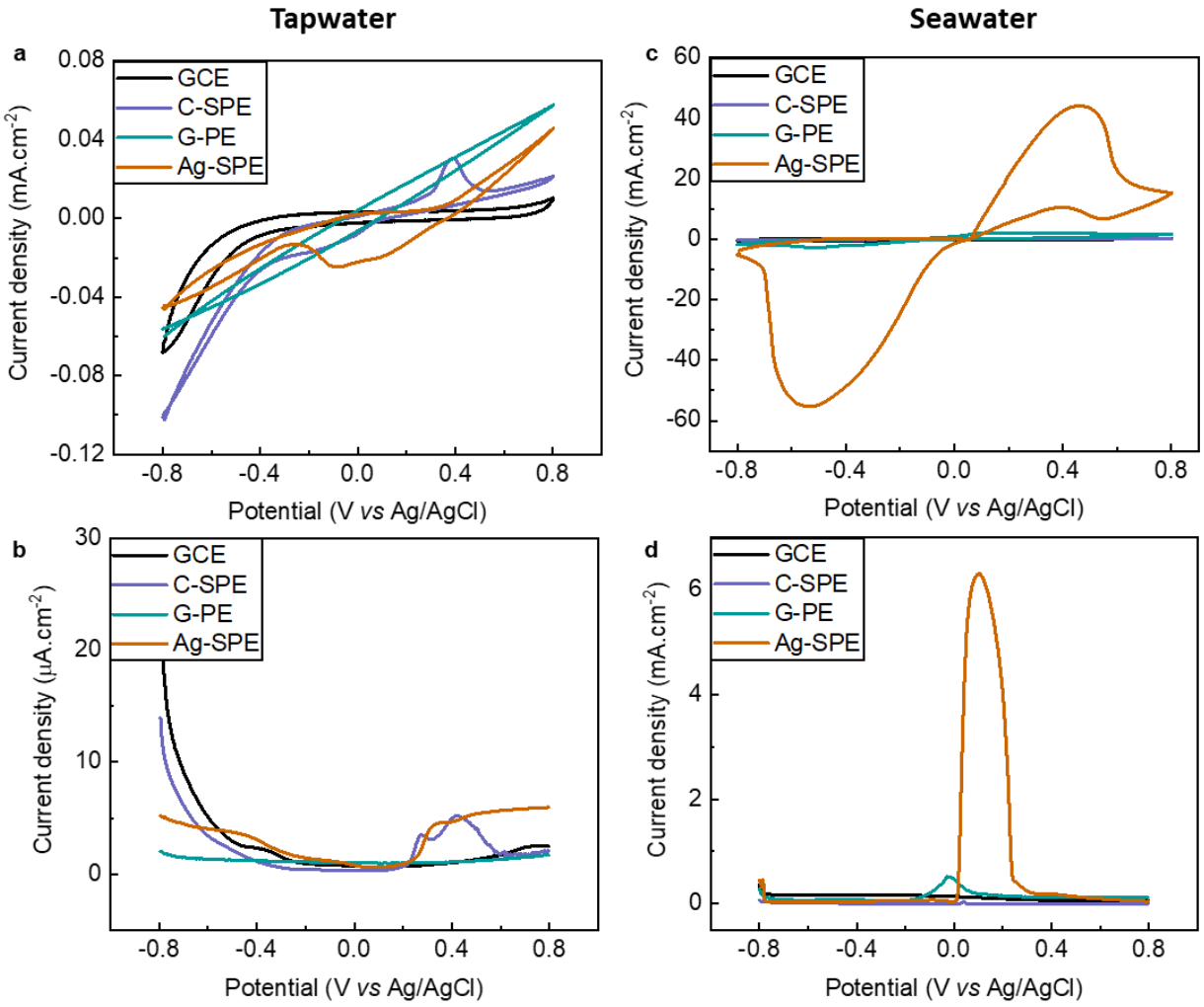


Figure 3.12. (a) and (b) Comparison of CV and DPV curves for the GCE, C-SPE, Ag-SPE and G-PE in tap water. (c) and (d) Comparison of CV and DPV curves for the GCE, C-SPE, Ag-SPE and G-PE in seawater.

### *3.3.5. Static Bending Study*

The printed electrodes were studied under no bending and static bending of 1.60, 1.25, 1.00, and 0.80 cm radius in artificial seawater (Figure 3.13). It is important to notice that these studies are different than the ones performed in Section 3.3.1, as the electrodes are locked at a specific radius. In Figure 3.13a,b, the Ag-SPE presented a slight increase of current density at the first bending radius of 1.60 cm followed by a steady decrease. The conductivity of the Ag-SPE could have decreased due to material deterioration from analyte interaction or introduction of defects from bending conditions,

similar to what was seem in Figure 3.2i. The C-SPE (Figure 3.13c,d) current density increased while the electrodes were bent. From the cyclic bending experiments (Figure 3.1g), the C-SPE presented the most stable response under bending. Bending under normal atmosphere seems to increase the electrode current response likely due to its mechanical stability and surface reaction with atmospheric gases, as seen in Figure 3.10b. The G-PE (Figure 3.13e,f) had a similar trend up until a radius of 1.25 cm, where then the current density started to decrease, possibly due to material degradation or cracking. A table summarizing the CV and DPV current densities peaks according to the no bending state can be seen in Table 3-3.

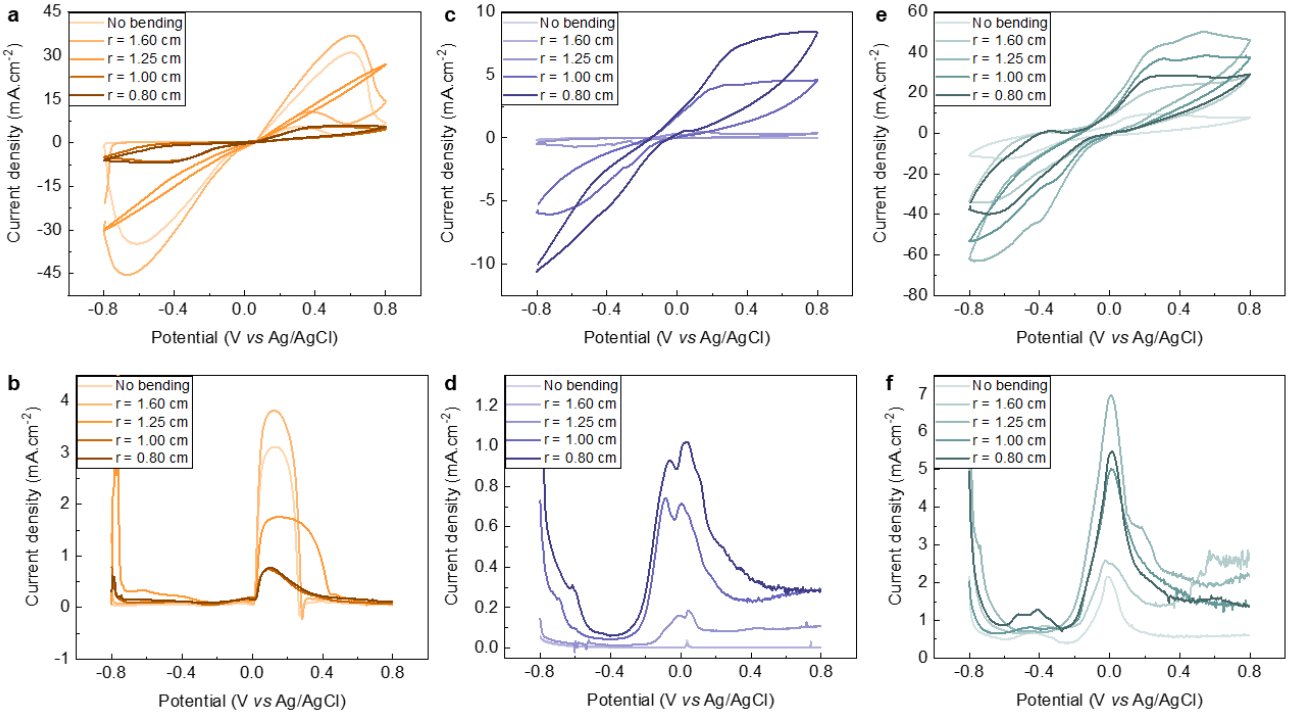


Figure 3.13. Static bending CVs (top) and DPVs (bottom) of Ag-SPE (a and b), C-SPE (c and d), and G-PE (e and f) under no bending, and bending at 1.60, 1.25, 1.00, and 0.80 cm radius in artificial seawater.

Table 3-3. Percentual change in redox peak current density in CV and DPV for various static bending radius in relation to the no bending state.

| | Ag-SPE | | C-SPE | | G-PE | |
|---|---|---|---|---|---|---|
| **Bending radius (cm)** | **CV (%)** | **DPV (%)** | **CV (%)** | **DPV (%)** | **CV (%)** | **DPV (%)** |
| 1.6 | 118 | 122 | 50.7 | 79.4 | 304 | 143 |
| 1.25 | 86.8 | 56.3 | 35.2 | 193 | 518 | 346 |
| 1.00 | 17.9 | 23.7 | 328 | 755 | 398 | 250 |
| 0.80 | 19.2 | 24.6 | 604 | 1015 | 302 | 273 |

### *3.3.6. Long-Term Study*

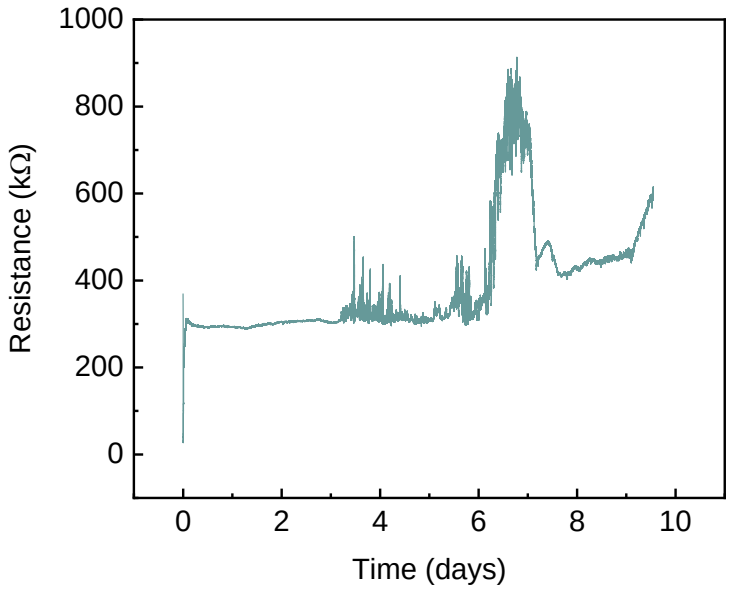


Figure 3.14. 10-day resistance study for the G-PE in artificial seawater.

The G-PE had its resistance monitored over a 10-day period and presented a very high resistance, in the hundreds of kΩ (Figure 3.14). The resistance shifted to almost 1 MΩ around day 7 and then decreased to 400 kΩ. A probable cause for this large resistance peak is a shift in the material position throughout the days, causing the electrode to bend (as seen previously in Figure 3.1h), while other smaller resistance increases could be due to material degradation. The printed electrodes also had their long-term properties studied by analysing their CV and DPV in artificial seawater over a 10-day

period (Figure 3.15). The current density increased over time for all electrodes. This behaviour is similar to what was seen in Figure 3.10a under normal atmosphere, again indicating that gases present in the atmosphere could be reacting with the solution and interfering with the experiment stability.

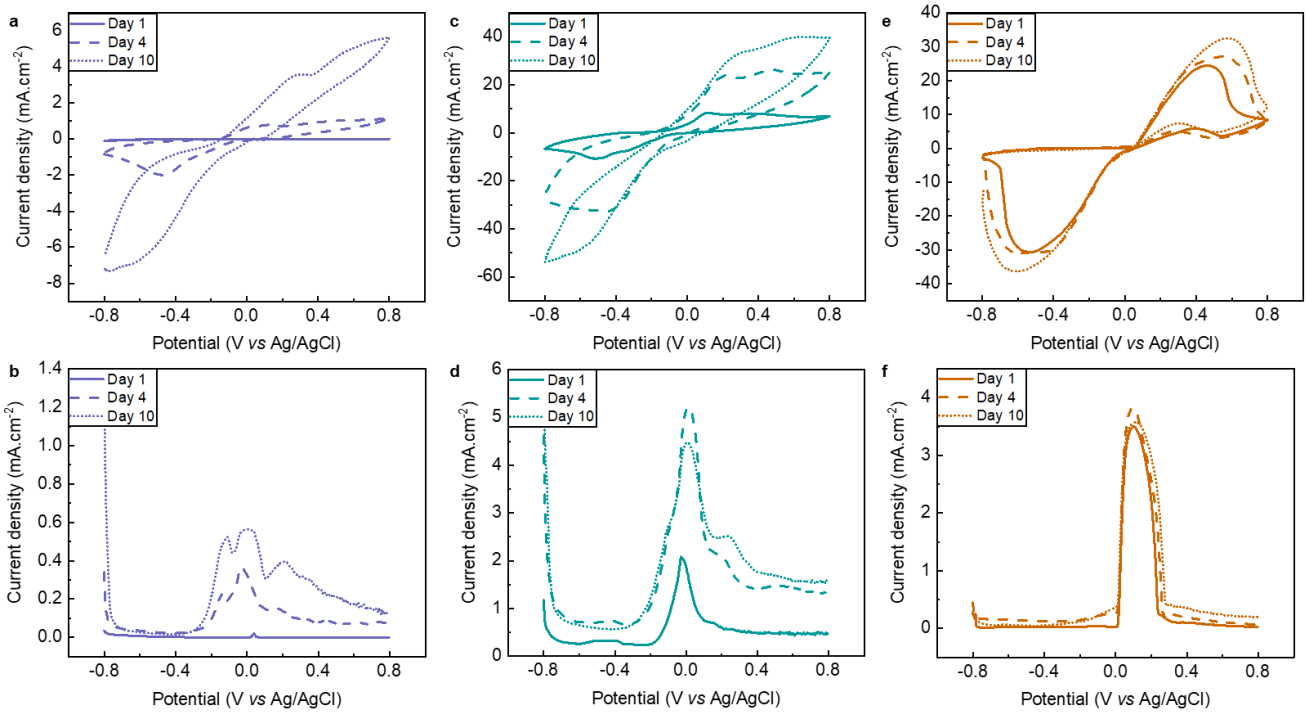


Figure 3.15. 10-day CV (top) and DPV (bottom) long-term study in artificial seawater for the (a,b) C-SPEs, (c,d) G-PE and (e,f) Ag-SPEs.

### *3.3.7. Nitrite Sensing in Artificial Seawater*

To demonstrate the sensing performance of the different pastes, the electrodes were modified with GOx for $NO_2^-$ sensing. GOx and carbon-based materials are known to catalyse $NO_2^-$ into $NO_3^-$, with a faradaic reaction at around +0.8 V, making it a suitable candidate to compare the printed electrodes' performances [81]. Figure 3.16 shows the CV and DPV of the different electrodes with 0 and 3 mM $NaNO_2$. The current densities were not adjusted for the voltammograms in Figure 3.16. The GCE showed the best performance (Figure 3.16a,e), with a sharp redox peak at around +0.8 V. The Ag-SPEs had a carbon-paste layer to mimic what is usually done for the WE. Even though the carbon layer was present, the Ag layer still interfered with the results, presenting a noisy background in the DPV (Figure 3.16b,f). However, overall, the result was similar to the one obtained by the C-SPE (Figure 3.16c,g) and showed a higher current density. The $NO_2^-$ oxidation peak was not as distinguishable for the G-PE (Figure 3.16d,h), although a change in current can be clearly seen when

comparing with no analyte addition. These results are similar to those obtained in Figure 3.9 and indicate that the C-SPE produces similar results to the GCE, while the Ag-SPE is not as suitable for seawater applications. Furthermore, the electron-transfer in the G-PE is not as effective, which compromises the redox peak shape. Further studies are necessary to improve the conductivity so the performance can be increased.

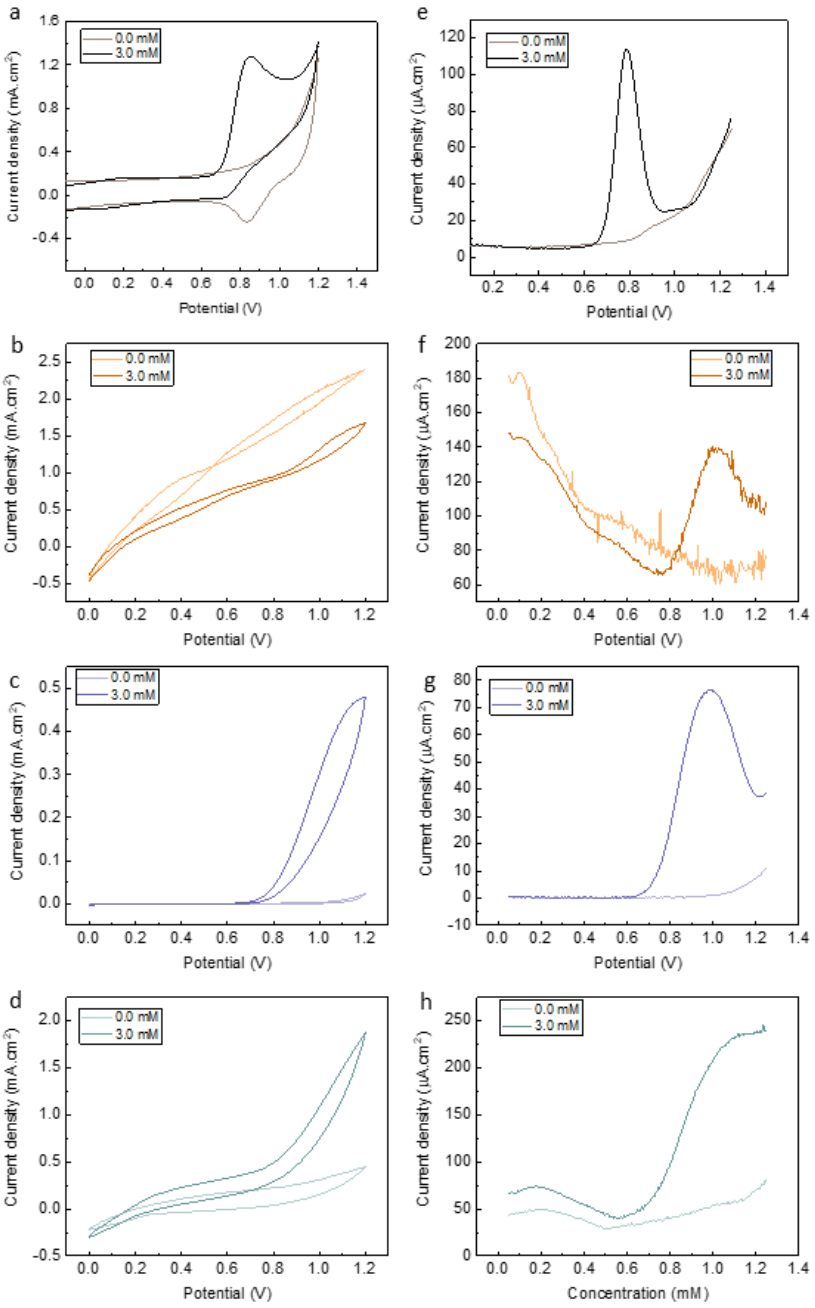


Figure 3.16. CV of the (a) GCE, (b) Ag-SPE, (c) C-SPE, and (d) G-PE with 0 and 3 mM $NaNO_2$ in artificial seawater. DPV of the (e) GCE, (f) Ag-SPE, (g) C-SPE, and (h) G-PE with 0 and 3 mM $NaNO_2$ in artificial seawater.

*3.3.8. Physical and Chemical Degradability Studies*

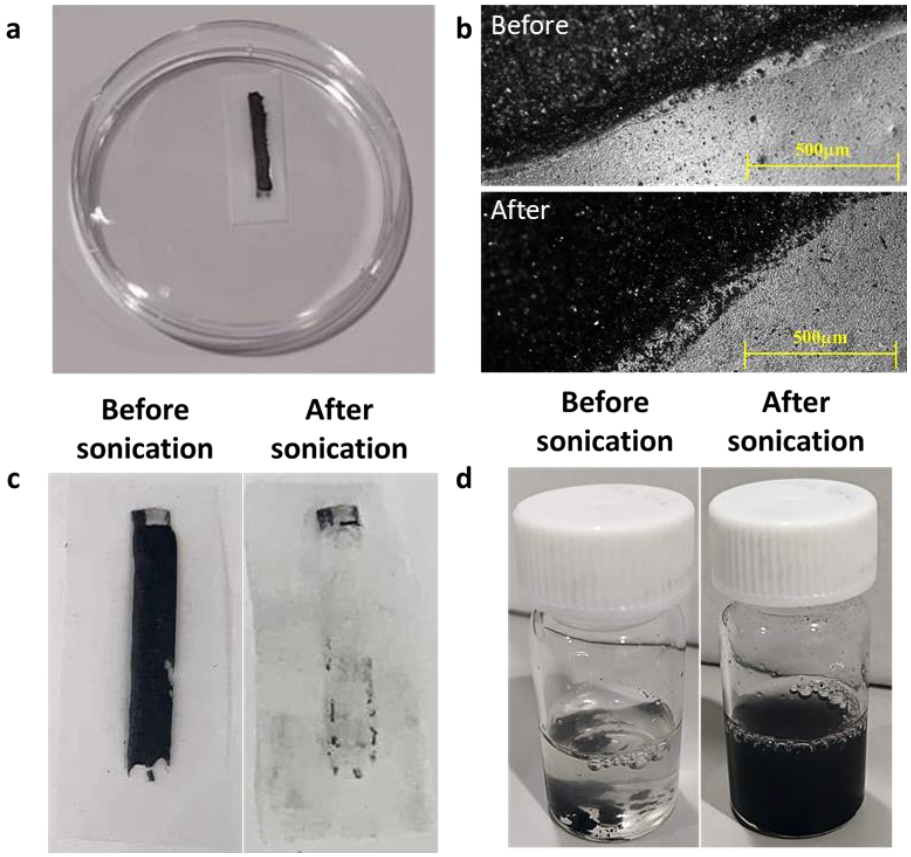


Figure 3.17. (a) G-PE on PHB/PHV substrate after 16 weeks in artificial seawater at 37° C, (b) Optical microscope image of G-PE on PHB/PHV substrate before (top) and after (bottom) 16 weeks in artificial seawater at 37° C, (c) G-PE on PHB/PHV substrate before and after 5 minutes of ultrasound treatment in artificial seawater and (d) Graphite based paste in its cured form, free from substrate before, and after 5 minutes of ultrasound treatment in artificial seawater.

In the current work both a biodegradable PHB/PHV plastic substrate and non-toxic G-PE were used as eco-friendly ingredients for disposable electrochemical electrodes to be used for environmental or water quality monitoring devices. To demonstrate the physical and chemical degradability of the SPEs the disintegration and dissolution of the Ag-SPE and C-SPE on PVC substrates and the G-PE on PHB/PHV substrates in artificial seawater solutions was examined. After being immersed in artificial seawater at 37 °C for 16 weeks, the SPEs retained their original weight, indicating no loss of material when left undisturbed. Furthermore, neither the G-PE, nor the PHB/PHV substrate changed significantly (Figure 3.17a,b), retaining ≈82% of its original weight. This may be explained by the material characteristics of the PHB/PHV substrate. Unlike most other currently available biodegradable plastics or polymer substrate materials, PHB and PHB/PHV

copolymers are generally water-insoluble and thus, relatively resistant to hydrolytic degradation [145]. The degradation of PHB/PHV copolymers therefore depends greatly on their biological environment and can often require a duration of at least a few months, even years [146,147]. For example, a 50 μm thick PHB/PHV film in soil (25 °C) required ten weeks to completely degrade [148]. In seawater (15 °C), the same film required 50 weeks to achieve complete weight loss. Nevertheless, these microbiologically derived synthetic polymers are compostable via anaerobic biodegradation in sediments, non-toxic and have good oxygen permeability, making them ideal material choices for short to medium-term environmental monitoring applications [145].

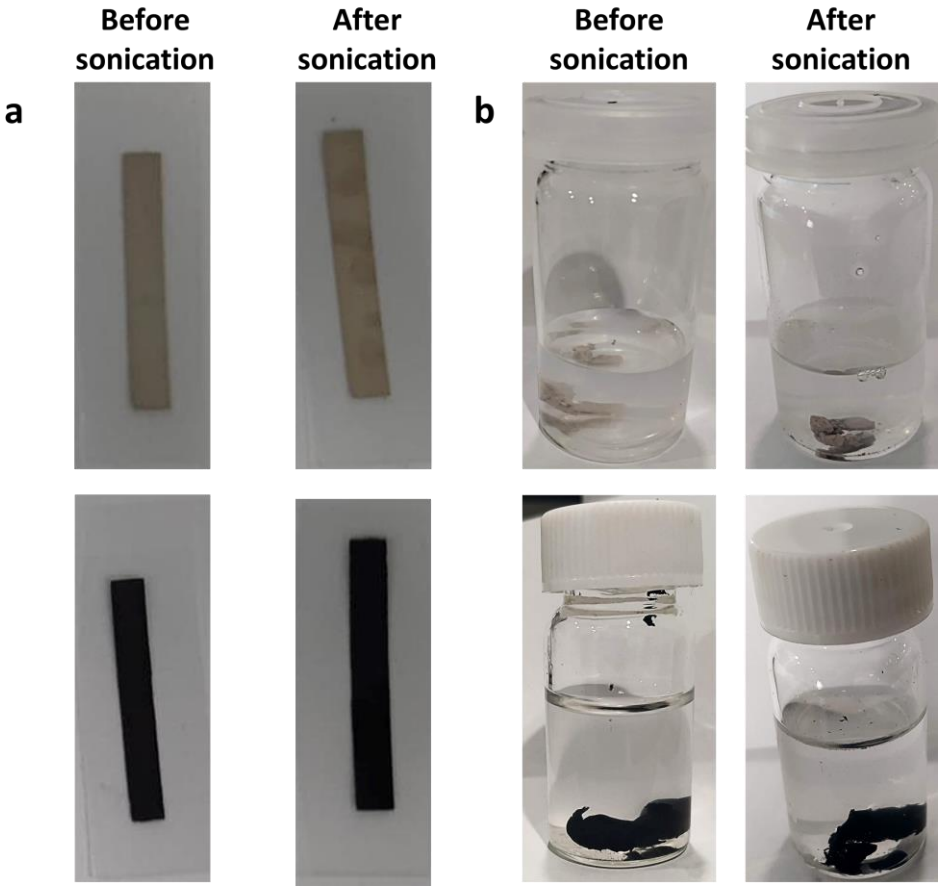


Figure 3.18. (a) Ag-SPE and C-SPE on PVC substrate before and after 5 minutes of ultrasound treatment in artificial seawater solutions and (b) Ag- and C- commercial pastes in their cured form and free from substrate before and after 30 minutes of ultrasound treatment in artificial seawater solutions.

For a timelier disintegration and dissolution of the disposable electrochemical electrode, ultrasound technology, a technique which has proven advantageous in the field of polymer chemistry for yielding degradation, was explored [149]. Despite more than 3 hours of sonication, the PHB/PHV

substrate remained relatively unchanged. The G-PE, on the other hand, began to disperse after less than 1 minute of sonication. As can be seen in Figure 3.17c, after 5 minutes of sonication the G-PE was almost entirely removed from the PHB/PHV substrate. The degeneration, or lack thereof of substrate materials can also significantly influence the dissolution processes of the conducting traces they support, e.g., due to chemical binding between the substrate and the paste. Considering this, the dissolution of the graphite-based paste in its cured form, free from substrate in artificial seawater was also explored using sonication. As can be seen in Figure 3.17d, the G-PE totally dispersed in the solution after 5 minutes of ultrasound treatment. Furthermore, considering the graphite-based paste is composed of only graphite, PVA and water, the byproducts of the degraded species are not as harmful for the environment when comparing with traditional electrodes. It offers advantages over glass and metal-based electrodes particularly if disposable electrodes are needed or when deploying electrodes in areas where there is a risk of breakage or of losing them. However more in-depth and longer studies are still necessary to understand the complete impact of biodegradable substrates and inks, especially when considering the PHA/PHB microplastic byproducts. The degradation and dissolution of the commercial pastes was also examined in artificial seawater. Both the Ag-SPE and C-SPE with (Figure 3.18a) and without the PVC substrate (Figure 3.18b) remained unchanged after 5 (with the PVC) and 30 minutes (without the PVC) of ultrasonication treatment and neither presented any differences before and after 16 weeks in artificial seawater which is in line with the SEM results (Figure 3.5). Therefore, the findings of the current study therefore suggest that the G-PE on PHB/PHV substrate presents a promising platform for eco-friendly electrochemical electrodes that may serve as single use or short-term sensing elements for environmental or water quality monitoring applications.

## 3.4. Conclusion

In the current work a biodegradable PHB/PHV substrate and a more sustainable G-PE were used as eco-friendly ingredients for disposable electrochemical electrodes to be used for environmental or water quality monitoring devices. An in-depth investigation of how different printed conductive pathways would behave under different bending and electrochemical conditions was also conducted. The Ag-SPEs were highly conductive (0.053 Ω/sq) when compared to the C-SPEs (26.9 Ω/sq) and the G-PEs (30.1 Ω/sq), as expected of a metal-based paste. However, under cyclic bending conditions, the Ag-SPE and G-PE $\Delta R/R_0$ varied to more than 60%, while the C-SPE showed a more stable variation of 35.5%. From the electrochemical CV, DPV, and EIS studies, it was observed that the Ag paste easily reacted with the salts present in the solutions while the carbon-based electrodes were mostly inert. The tap water and seawater studies demonstrated that there is almost no difference

between the materials in tap water due to the low concentration of ions but in seawater a clear difference in the faradaic current was observed, supporting the findings from previous electrochemical studies that Ag readily reacts with halides [117]. The electrodes were further modified with GOx and tested for $NO_2^-$ detection. While the C-SPE showed sharp peaks, the electron-transfer of the G-PE needs to be further improved.

To demonstrate the physical and chemical degradability of the SPEs the disintegration and dissolution of the G-PE on PHB/PHV substrates in artificial seawater solutions was examined. After being immersed in artificial seawater for 16 weeks at 37 °C, neither the G-PE, nor the PHB/PHV substrate changed significantly due to the relative resistance of the water insoluble substrate to hydrolytic degradation. This indicates the G-PE can withstand up to a few months before being disposed of. Using ultrasound technology, however, the G-PE dissociated from the PHB/PHV substrate in less than 1 minute, highlighting the suitability of this eco-friendly electrochemical electrode for single use or short-term water quality monitoring sensors that can be reused or naturally discarded. Meanwhile, the Ag-SPEs and the C-SPEs did not show any degradation or dissolution over the course of 16 weeks in seawater or in the ultrasonication studies.

Overall, a higher electrochemical stability for the carbon-based electrodes the fabrication of a new, eco-friendlier G-PE for water quality monitoring were demonstrated. Furthermore, although Ag is still the major component in most screen-printed sensors due to its high conductivity, it was demonstrated that carbon-based electrodes can be suitable, more sustainable alternatives in highly ionic media. As it stands, the G-PE is better suited to be used as a conductive pathway than as a WE due to its high chemical stability and sheet resistance comparable to available commercial carbon pastes, but low faradaic peak separation. In future studies, the aim is to improve the conductivity and charge-transfer capability of the carbon electrodes and perform further studies in the degradability, focusing on the biodegradability aspect and life-cycle studies. In Chapter 4, different techniques were explored to improve the conductivity and overall performance of carbon electrodes.

# Chapter 4

# Influence of Carbon Structures in Printed Voltammetric Sensors for $NO_2^-$ Monitoring

**The laser induced graphene electrodes were fabricated at Silicon Austria Labs, Villach, Austria.*

## 4.1. Introduction

Graphene and graphene-based materials have been incorporated into various areas of technology since their discovery due to their high conductivity, specific surface area, thermal conductivity and tensile strength [150]. In order to be successfully employed in industry, various fabrication routes have been proposed to scale the production of graphene, including chemical-vapor deposition, liquid-phase exfoliation, and reduction to graphene oxide, however they tend to be cumbersome and expensive [150]. Nowadays, graphene-based pastes and inks have been implemented in printed electronics as an alternative to metal-based conductive tracks [113,119]. This allows for a more sustainable approach in printed electronics. In this regard, screen-printing is an established fabrication method due to its scalability, reliability, and usage of inexpensive materials [108]. In screen-printed electrodes (SPEs), carbon is an inexpensive and inert material typically used in the active working electrode (WE) area of electrochemical sensors. It is not usually employed on the conductive tracks because of its lower conductivity, however additives such as carbon nanotubes or graphene flakes have been shown to decrease the SPE resistance [120–122]. In Chapter 3, different carbon-materials were employed to produce printed electrodes, and although they were more stable than the Ag

counterpart, the conductivity and electron transfer capability was severely lacking when compared to metal-based pastes. The problem is binders and solvents are necessary in the paste formulation, therefore the quantity of graphene or other additives is limited.

A new method to engrave three-dimensional graphene-like structures called laser-induced graphene (LIG) was developed by Lin et. al. [151]. The local high temperature combined with a high-pressure environment generated by the $CO_2$ laser allowed the graphitization of the polyamide (PI) substrate. The breakage of C-O, C=O, and C-N bonds of the PI produces high-pressure gas pockets [152]. This facilitates the formation of nanopores, micropores, and other defects, creating a porous 3D graphene-based network that cannot be achieved through other techniques [152,153]. This 3D network is detailed in Figure 4.1b. Although PI is the most used substrate for the formation of LIG, the technique allows the usage of any source of carbon-based feedstock material, e.g., wood, textile, charcoal, and even food items [152,154]. However, since LIG is a new technology, the parameters that affect the formation of high-quality graphene-like structures together with a higher mechanical stability and conductivity are under study. To optimise the LIG, one-factor-at-a-time (OFAT) approaches are usually used, where one parameter, such as laser power or speed, is changed successively until a desired outcome is reached [155]. Although this is a valid technique, utilising other statistical approaches can be advantageous, as they can save time and material resources when compared to OFAT.

Design of experiments (DoE) is a resource-efficient optimisation process that can minimise the cost of experiment by creating models to indicate where the minimum/maximum desired output is [156]. This approach can simplify the optimisation of LIGs, as complex systems can be analysed using less samples than the OFAT alternative as it reduces the number of experiments required [157]. Furthermore, other important aspect of DoE is the ability to highlight parameter interdependency which is unlikely to be determined when using OFAT approaches. This is particularly advantageous for LIG fabrication, as it is a new technique that can benefit from optimisation strategies. When comparing LIGs to SPEs, many factors can be considered. For example, LIGs offer a template-free method to produce highly conductive graphene-based electrodes while SPEs require the use of a mask, which can limit the final pattern resolution [158]. However, screen-printing is a mature, versatile technology, with the possibility of combining various conductive pastes to produce the final product, while LIGs are confined to carbon structures [108,159]. Both techniques have similarities, including a low production cost linked with a high yield. This information is summarised in Table 4-1. LIG and SPEs have been employed in numerous fields, including supercapacitors, solar cells,

fuel cells, and electrochemical sensors [106,108,152,160,161]. LIGs are especially interesting in the field of electrochemical sensors due to their high surface area and high conductivity, as this allows for efficient modification of the working electrode with various materials and faster electron transfer. For example, LIG electrodes could offer advantages in the detection of the $NO_2^-$, as this ion benefits from fast detection techniques due to its short environmental life and it can be detected using unmodified carbon materials [66].

Table 4-1. Comparison of screen-printing and laser engraving techniques for electrode fabrication.

| | **Screen Printing** | **LIG** |
|---|---|---|
| **Pattern** | Requires a mask (e.g., stainless steel) | Mask-free |
| **Resolution** | 40 µm | 12 µm |
| **Sheet Resistance** | < 5 mΩ/sq for Ag paste<br>< 35 Ω/sq for carbon paste | < 10 Ω/sq |
| **Production** | High yield, fast speed | High yield, fast speed |
| **Substrate** | Any compatible with the paste used | Carbon-based precursors |
| **Materials** | Metal, carbon, and insulating pastes | Carbon structures from the substrate |
| **Commercial Cost** | < £1/sensor (e.g., DropSens) | < £2/sensor (e.g., Gii-Sens) |
| **Further modifications** | WE and RE can be screen-printed using different pastes | Requires other techniques to modify WE and RE |
| **Availability** | Commercially available | Mostly research-based |

Increasing levels of nitrite ($NO_2^-$) and nitrate ($NO_3^-$) in ground and surface water have been detected as a result of excessive usage of nitrogen fertilizers, runoff waste from livestock farms and use as a food preservative [30,34]. In the environment, high concentration of nitrogenous compounds can lead to eutrophication of water bodies [34]. In humans, oxygen transportation can be hindered by the $NO_2^-$ ion by the irreversible conversion of haemoglobin to methemoglobin, which is particularly problematic for pregnant women and infants [29,31]. Due to its toxic nature, the recommended levels

of $NO_2^-$ in drinking water are below 3 mg/L [24,29]. As $NO_2^-$ is a reactive ion, the detection techniques need to provide fast, accurate result. However, most of the standard instrumentation involves the use of expensive, time-consuming methods, such as spectrophotometric, chemiluminescence, spectrofluorometric, and ion chromatography detection [31,34,72]. Recently, electrochemical methods have also been employed for the $NO_2^-$ detection, focusing on potentiometric and voltammetric approaches, however they are not as sensitive as standard techniques [34]. The fast analysis time counterbalances the higher detection limit, with voltammetric and amperometric techniques being the fastest electrochemical methods. Considering the $NO_2^-$ ion is highly reactive, a fast technique is very advantageous. Regarding the choice of sensitive material, carbon-based electrodes are widely used for the electrochemical detection of $NO_2^-$ due to its ability to oxidize $NO_2^-$ to $NO_3^-$, but they are usually modified with other metal/metal oxides for higher sensitivity [162]. Common materials include gold, copper, and iron nanoparticles, and the study is mostly done using standard laboratory electrodes, such as the glassy-carbon working electrode [81,162]. Carbon-based printed/engraved sensors, such as carbon-based SPEs and LIGs, can be a good alternative to standard electrodes as they can be readily employed in the field.

In this work, we investigated how the material morphology of carbon-based electrodes affect their electrochemical properties by comparing a standard commercial SPE to optimised LIGs. The aim is to understand if LIGs are a suitable replacement for SPEs, as they provide a low-cost, template-free alternative to carbon SPEs. For this, we used a commercial SPE with graphene/carbon-based tracks and a multilayer graphene sheet on top of the WE (GS-SPE) (Figure 4.1). Meanwhile, the LIGs were engraved on PI and were optimised using a DoE response surface (DoE-RS) approach. By changing different parameters (laser power, speed, and focus) that affect the carbonisation of the PI substrate, two optimised LIGs were chosen to continue the experiments – LIG A and LIG B. Both the GS-SPE and the LIGs were employed without further modification on all studies, simplifying their use. The material characterisation was done by scanning electron microscopy (SEM), Raman spectroscopy, and contact angle analysis. For the electrochemical studies, the oxidation of $NO_2^-$ ion by the graphene-based working electrodes was investigated, as it allowed for the direct comparison of the LIGs to the GS-SPE. The electrochemical investigation was done by cyclic voltammetric (CV) and differential pulsed voltammetry (DPV).

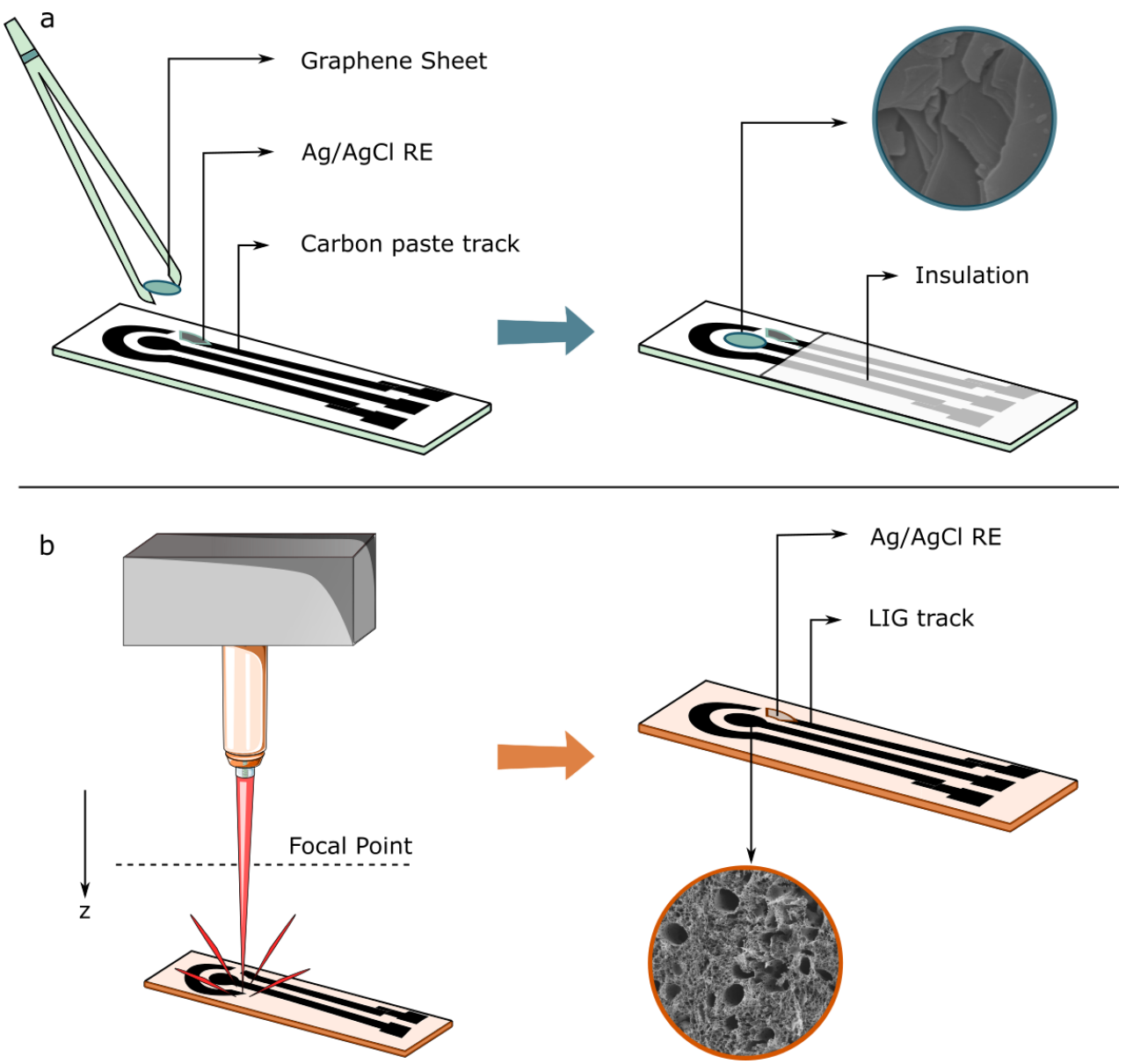


Figure 4.1. a) Fabrication steps of the GS-SPE. The graphene sheet was attached to the commercial carbon WE. An insulation layer protects the screen-printed carbon track. The SEM inset of the graphene sheet shows smooth graphene layers. b) Fabrication steps of the LIG electrodes. Laser engraving on polyamide substrate was done by adjusting from the focal point in the positive z direction and changing the laser power and speed. For the final electrode, Ag/AgCl RE was drop casted on the RE. The SEM inset shows the 3D porous carbon network of the LIG.

## 4.2. Materials and Methods

### *4.2.1. Electrode Fabrication*

#### *4.2.1.1. Screen-Printed Electrode*

In this work, a commercial SPE was acquired from JE Solutions with a 45 mm length by 1.5 mm width conductive tracks and a circular WE of 3 mm diameter. The total size of the SPE was 45 mm length by 6 mm width. The conductive tracks were screen printed using a graphene conductive paste on top of a polyethylene terephthalate (PET) substrate. The RE was screen printed using a silver/silver chloride (Ag/AgCl) paste. The conductive tracks were covered with a white thermoplastic polyurethane insulation ink, leaving only the WE, reference electrode (RE), and counter electrode (CE) exposed. In the laboratory, a commercial pristine multilayer graphene sheet (MGS, Graphene Supermarket, 25 µm thickness) was cut to a 3 mm diameter circle and bonded on top of the WE with graphene paste (JE Solutions). The GS-SPE was then cured at 80 °C for 30 min and used in further experiments. The GS-SPE can be seen in Figure 4.1.

#### *4.2.1.2. Laser Induced Graphene Electrodes*

A Universal Laser Systems PLS6150D $CO_2$ laser engraver with 10.6 µm wavelength, 0-75 W power was used for the LIG engraving. The max speed on the x-axis and y-axis were 1778 mm/s and 508 mm/s, respectively. The electrode pattern was done in Inkscape, with a 20 mm length by 1.5 mm width conductive tracks and a circular WE of 3 mm diameter. The total size of the 3-electrode system was 24 mm length by 9 mm width. For the DoE, only the WE was fabricated and once the system was optimised the 3-electrode LIGs were used for further material and electrochemical characterisation. A polyamide substrate (PI, 500HN Kapton film from Utech Products, 127 µm thickness) was adhered to a plastic substrate using deionised water for a residue-free bond. For the graphitisation of the substrate, the PI was patterned under ambient conditions using the Universal Laser Systems software. The focus was adjusted by first adjusting the laser to the focal point and then using the software to increase or decrease the distance to the substrate. Ag/AgCl paster (JE Solutions) was drop casted on top of the LIG RE, and the final electrode can be seen in Figure 4.1.

### *4.2.2. Design of Experiments*

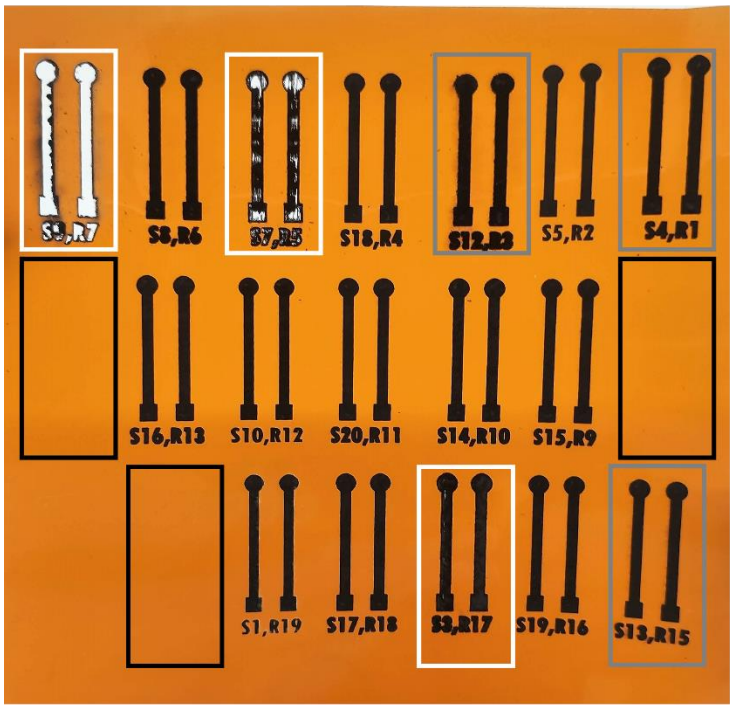


| Sample No. | Run No. | Speed (%) | Power (%) | Focus (mm) | Resistance (Ω) |
|---|---|---|---|---|---|
| 4 | 1 | 30 | 20 | 0.5 | 501 |
| 5 | 2 | 10 | 5 | 1.5 | 507 |
| 12 | 3 | 20 | 25.11 | 1 | 323.5 |
| 18 | 4 | 20 | 12.5 | 1 | 500.5 |
| 7 | 5 | 10 | 20 | 1.5 | 403 |
| 8 | 6 | 30 | 20 | 1.5 | 643 |
| 9 | 7 | 3 | 12.5 | 1 | 10000 |
| 11 | 8 | 20 | -0.11 | 1 | 10000 |
| 15 | 9 | 20 | 12.5 | 1 | 496.5 |
| 14 | 10 | 20 | 12.5 | 1.84 | 438 |
| 20 | 11 | 20 | 12.5 | 1 | 496 |
| 10 | 12 | 37 | 12.5 | 1 | 994 |
| 16 | 13 | 20 | 12.5 | 1 | 492.5 |
| 2 | 14 | 30 | 5 | 0.5 | 10000 |
| 13 | 15 | 20 | 12.5 | 0.16 | 417 |
| 19 | 16 | 20 | 12.5 | 1 | 494.5 |
| 3 | 17 | 10 | 20 | 0.5 | 135.5 |
| 17 | 18 | 20 | 12.5 | 1 | 494 |
| 1 | 19 | 10 | 5 | 0.5 | 374 |
| 6 | 20 | 30 | 5 | 1.5 | 10000 |

Figure 4.2. Photo of the 3-factor (speed, power, and focus) DoE (left). The label corresponds to the sample number and the DoE run number (e.g., sample 4, run 1 corresponds to S4R1). The black rectangles represent the areas where no graphitisation of the substrate occurred; the white rectangles where the substrate was partially/fully cut; the grey rectangles where a more fibrous LIG was produced. Table showing the parameters used for each combination of sample and run number (right). A power of 5 to 20% corresponds to 3.75 to 15 W. Where no graphitisation occurred, a high resistance of 10 kΩ was added to run the DoE-RS.

To optimise the LIGs for resistance and adhesion to the PI substrate, a central-composite DoE-response surface (DoE-RS) was performed iteratively based on both the linear resistance response and the LIG adhesion to the substrate (delamination). DoE-RS is an advanced DoE technique that allows for the optimisation of a response that is influenced by several parameters [156]. In this way, it is a sequential procedure used to determine the optimum operating conditions. For the adhesion response, numbers from 0 to 1 were allocated to each run, with 0 being no material delamination after the bending process and 1 being full delamination after bending. Minitab was used to prepare and analyse all DoE-RS experiments using the central composite design. The linear resistance was taken with a multimeter from the middle of the WE to the middle of the connection pad while the adhesion was visually inspected by bending the electrode at 180° three times. At first, a 3-parameter, 20-point

DoE-RS (speed (10-30% corresponding to 177.8-533.4 mm/s on the x-axis and 50.8-152.4 mm/s on the y-axis), power (5-20% corresponding to 3.75-15 W), and focus (0.5-1.5 mm)) with a pulse density of 1000 pulses per inch (PPI) was performed to select the regions of interest for the next set of DoE-RS (Figure 4.2). The maximum values were based on the reported literature values of power and speed where graphitisation could occur [155]. A negative focus value indicates the substrate is moving closer to the laser. The WE structure was printed twice for each run and the model was based on the mean linear resistance of the electrodes. Many of the parameters did not graphitise the substrate, therefore two new 2-factor DoE-RS were performed around the regions where graphitisation occurred:

i) Focus = -1 mm, 10% < Speed < 20%, and 10% < Power < 20%, PPI = 1000.

ii) Focus = -2 mm, 20% < Speed < 30%, and 20% < Power < 30%, PPI = 1000.

Based on the models, three points of interest were selected to validate each model. The best performing LIG was selected for each DoE-RS, with LIG A consisting of a focus of -1.0 mm, a speed of 20% (355.6 mm/s on the x-axis and 101.6 mm/s on the y-axis), and a power of 10% (7.5 W), and LIG B of a focus of -2.0 mm, a speed of 25% (444.5 mm/s on the x-axis and 127 mm/s on the y-axis), and a power of 17.9% (13.5 W).

### *4.2.3. Material Characterization*

The resistance of the LIG electrodes for the design of experiments was measured using a digital multimeter. The electrodes were characterised by a scanning electron microscope (SEM, FEI QUANTA 200F environmental SEM at 5 kV and aperture size of 30 µm). The ImageJ software was utilised for measuring the height of the cross-section layers and to quantify the LIG pores. For the quantification of the pores, first the threshold was adjusted so the pores were highlighted. To decrease the background noise, both the despeckle and remove outliers (<8px for LIG A and <5px for LIG B) features were used. The highlighted area was then analysed for count and area. The pores were approximated to perfect circles to get the radius. The Raman spectra were obtained using a Renishaw inVia Raman microscope with a 514 nm green Ar laser, a laser power of 10%, an exposure time of 10 s, a grating of 2400 lines/mm, and an accumulation of 1. The middle of the working electrode was selected for all Raman spectra and an extended feature was used to record from 700 to 3200 $cm^{-1}$. After baseline subtraction, the first order (D, G, D') Lorentzian peaks and second order (2D) peaks were fitted to the spectra using Matlab. For the contact angle, the Ossila contact angle goniometer

was used. 20 µL of deionised water were dropped on top the electrodes using a syringe and the process was filmed and analysed by the Ossila contact angle software.

### *4.2.4. Electrochemical Setup*

The cyclic voltammetry (CV) and differential pulsed voltammetry (DPV), and chronoamperometry analysis of the printed electrodes were carried out using the Gamry potentiostat (Interface 1010E). The sensors were attached to an adaptor that is connected to the potentiostat and the solutions were dropped on top of the WE, RE, and CE (Figure 4.1). The sensors were washed with milliQ water between each experiment. All experiments were done under ambient condition. A 50 mM NaCl in milliQ water solution was used for all electrochemical experiments unless otherwise stated. A concentrated sodium nitrite ($NaNO_2$) solution in milliQ water was used to change the concentration of $NO_2^-$. The pH was adjusted to 6, 7 or 8 with diluted sodium hydroxide (NaOH) and hydrochloric acid (HCl). For the ionic compound interference experiment, 50 µM of different ionic compounds in a solution containing 50 µM of $NaNO_2$ pH 7 were tested one at a time. The ionic compounds were calcium carbonate ($CaCO_3$), iron(II) sulphate ($FeSO_4$), magnesium sulphate ($MgSO_4$) or sodium nitrate ($NaNO_3$). Highland spring sparkling water was used for the real water experiment. The GS-SPE and LIG were conditioned by performing 5 CV scans at 100 mV/s in 50 mM NaCl pH 7. The CVs were scanned from 10 mV/s, 50 mV/s and plus 50 mV/s until 250 mV/s with 50 µM $NO_2^-$. The DPVs were run with a step size of 5 mV, a sample period of 0.5 s, a pulse time of 0.2 s, and a pulse size of 50 mV, and the $NO_2^-$ concentration was changed to from 10 to 500 µM.

## 4.3. Results and Discussion

### *4.3.1. Optimisation of the Laser Induced Graphene Electrodes*

The LIGs were fabricated using a laser engraver, in which the user can change the power, speed and the focal distance of the laser to graphitise the PI substrate (Figure 4.1). The combination of these parameters can result in many different possible outputs, making it challenging to obtain a final electrode that is conductive and stable for electrochemical analysis. In this chapter, the optimisation strategy for the LIGs consisted of employing DoE techniques instead of the usual OFAT experimental approach. In this manner, the interaction between different factors can be analysed while greatly reducing the number of experiments needed to achieve the best performing LIG [156]. In the first report of LIG, the authors noted that there was a linear relation of the threshold of the laser power to the scan speed that led to the graphitisation of the substrate [151]. It has also been observed through

other DoE approaches that the power, scan speed, and focus point influence the graphitisation of the PI substrate, while a PPI from 500-1000 and gas flow did not significantly influence the LIG sheet resistance [157]. Therefore, the starting set of parameters for the DoE consisted of a three-factor approach, where the focus, speed, and focal point were changed in each run, with 20 runs in total, with 6 of those corresponding to centre points. Figure 4.2 shows a representation of the DoE-RS results, where the regions in which successful graphitisation of the material occurred can be observed. Some of the power, speed and focus combinations showed no results while others cut through the substrate. By narrowing the second iteration of the DoE-RS to the regions where a lower linear resistance and higher adhesion were found and decreasing the number of factors to the two most significant ones (speed and power), a more controlled optimisation process was attained.

For the second iteration of the DoE-RS, two regions were chosen, with model I corresponding to region (i) (Focus = -1 mm, 10% < Speed < 20%, and 10% < Power < 20%, PPI = 1000) and model II corresponds to region (ii) (Focus = -2 mm, 20% < Speed < 30%, and 20% < Power < 30%, PPI = 1000) in Section 2.1.2.1. Model I (Table 4-2) was built from statistically significant terms, showing a good correlation of the given parameters to the resistance model, with a low *p*-value (less than 0.05) for the lack-of-fit parameter (*p*-value of 0.044). While speed showed a linear response to resistance, power demonstrated a quadratic response (Figure 4.3). Model I presented an overall good fit with a low standard error (Table 4-3). The diagnostic tests for the validation of the ANOVA test (Figure 4.4a-c) showed the data is normally distributed, with random fluctuations of the residuals in the run order. In Figure 4.5a-c, the DoE-RS for the measured two responses are observed, resistance (Figure 4.5a) or delamination (Figure 4.5b), and an overlay of both these responses for the region of interest (Figure 4.5c). Although the delamination model was based on 0 being no delamination and 1 total delamination, the DoE-RS model increased the range of these values to fit the model. The regions with negative values should be understood as no delamination and the regions with value greater than 1 as full delamination. It is important to note that some regions of low resistance showed some cracks on the surface after bending, making the overlay of these two responses of great importance.

Therefore, to obtain a reliable LIG for further characterisation and to validate the model, three regions were chosen for engraving. Table 4-4 includes the selected power and speed percentages chosen alongside their predicted and measured resistance values. The regions corresponding to a higher speed showed a better correlation to the predicted value, but there was overall a good fit to the model. The measured resistances were within the 95% confidence and prediction intervals (CI and PI), with the exception of the measured value of 148 Ω using power 15% and speed 12.5%. The

measured value was lower than the predicted value (187 Ω and 158-270 Ω 95% PI), which also corresponded to the lowest speed used. Although this region presented the lowest linear resistance, it also cracked while bending, so it was not suitable for further experiments. Although the resistance model was not as accurate for these power and speed values, this is a region where delamination is more probable to occur, as can be observed in Figure 4.5c. Therefore, by combining both output models, a better optimisation process can be achieved. After this process, the region highlighted with a red star (Figure 4.5c) was named as LIG A. Various electrodes using the 3-electrode configuration were then printed for further material and electrochemical characterisation.

Table 4-2. Analysis of variance for model I and resistance equation based on the best-fitting model.

| **Analysis of Variance** | | | | | |
|---|---|---|---|---|---|
| **Source** | **DF** | **Adj SS** | **Adj MS** | **F-Value** | **p-Value** |
| **Model** | 4 | 35523.8 | 8881 | 63.32 | 0 |
| **Linear** | 2 | 31364.4 | 15682.2 | 111.82 | 0 |
| **Power** | 1 | 2346.1 | 2346.1 | 16.73 | 0.003 |
| **Speed** | 1 | 29018.2 | 29018.2 | 206.9 | 0 |
| **Square** | 1 | 1428.5 | 1428.5 | 10.19 | 0.013 |
| **Power*Power** | 1 | 1428.5 | 1428.5 | 10.19 | 0.013 |
| **2-Way Interaction** | 1 | 2782.6 | 2782.6 | 19.84 | 0.002 |
| **Power*Speed** | 1 | 2782.6 | 2782.6 | 19.84 | 0.002 |
| **Error** | 8 | 1122 | 140.3 | | |
| **Lack-of-Fit** | 4 | 980.2 | 245.1 | 6.91 | 0.044 |
| **Pure Error** | 4 | 141.8 | 35.5 | | |
| **Total** | 12 | 36645.8 | | | |
| **Resistance (Ω)** | 196.3 - 2.13 Power - 3.72 Speed - 0.571 Power*Power + 1.055 Power*Speed | | | | |

DF = degrees of freedom; SS = sums of squares; MS = mean square.

Table 4-3. Model summary of model I and model II.

| | **Standard Error (Ω)** | **R-squared** | **R-squared (adjusted)** | **R-squared (predicted)** |
|---|---|---|---|---|
| **Model I** | 11.84 | 96.94% | 95.41% | 86.80% |
| **Model II** | 17.92 | 95.73% | 92.68% | 75.89% |

The same procedure was repeated using a more defocused region with a focus of -2 mm. The constructed model II (Table 4-5) showed a *p*-value of 0.075 for the lack-of-fit-parameter. This demonstrated that model II is not as robust as model I and needs further adjustments, either by adjusting the model or performing another iteration of DoE. However, it was sufficient for the aim of this study, as it was still possible to obtain a suitable region through the DoE which would otherwise be difficult to find as the electrodes cracked more often than those from model I. Similarly to model I, power presented a quadratic response to the resistance, while speed is linearly correlated (Figure 4.3). The model summary for model II (Table 4-3) showed a good overall fit, with a slighted higher standard error (+ 6.08 Ω) and lower $R^2$ (- 1.21 %) than model I. The diagnostic tests (Figure 4.4d-f) showed a normally distributed data with higher residual deviation than in model I. The residual *vs* run order graph showed the residuals were mostly randomised. The resistance DoE-RS for model II (Figure 4.5d) also showed a similar trend as model I, where lower speed and higher power resulted in lower resistance. However, by including the delamination of the material from the substrate (Figure 4.5e,f) it can be observed that only a narrow region results in low linear resistance combined with a sturdier LIG. Table 4-4 shows the predicted and measured linear resistance for three combinations of speed and power. The best performing region was selected to continue the experiments, and was denominated LIG B. In the sections below, the LIGs will be compared to the GS-SPE, with further understanding in how the selection of power, speed, and focus affect the carbon composition of the materials.

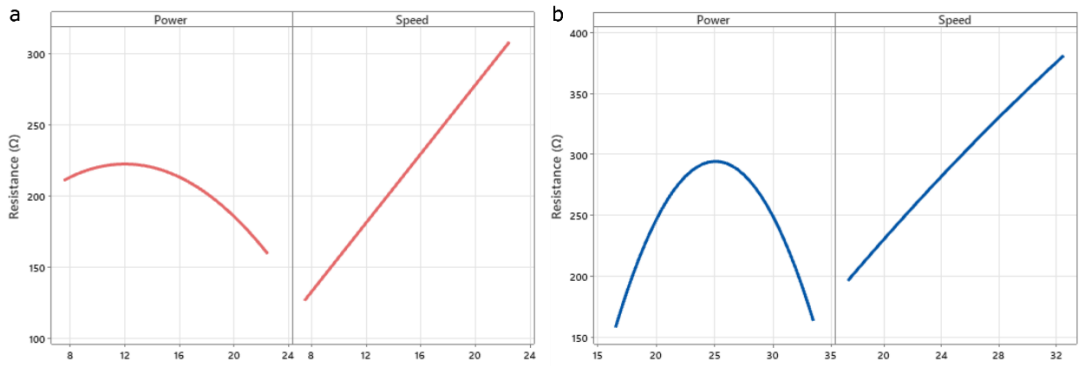


Figure 4.3. Power and speed correlation to resistance for Model I (a) and Model II (b).

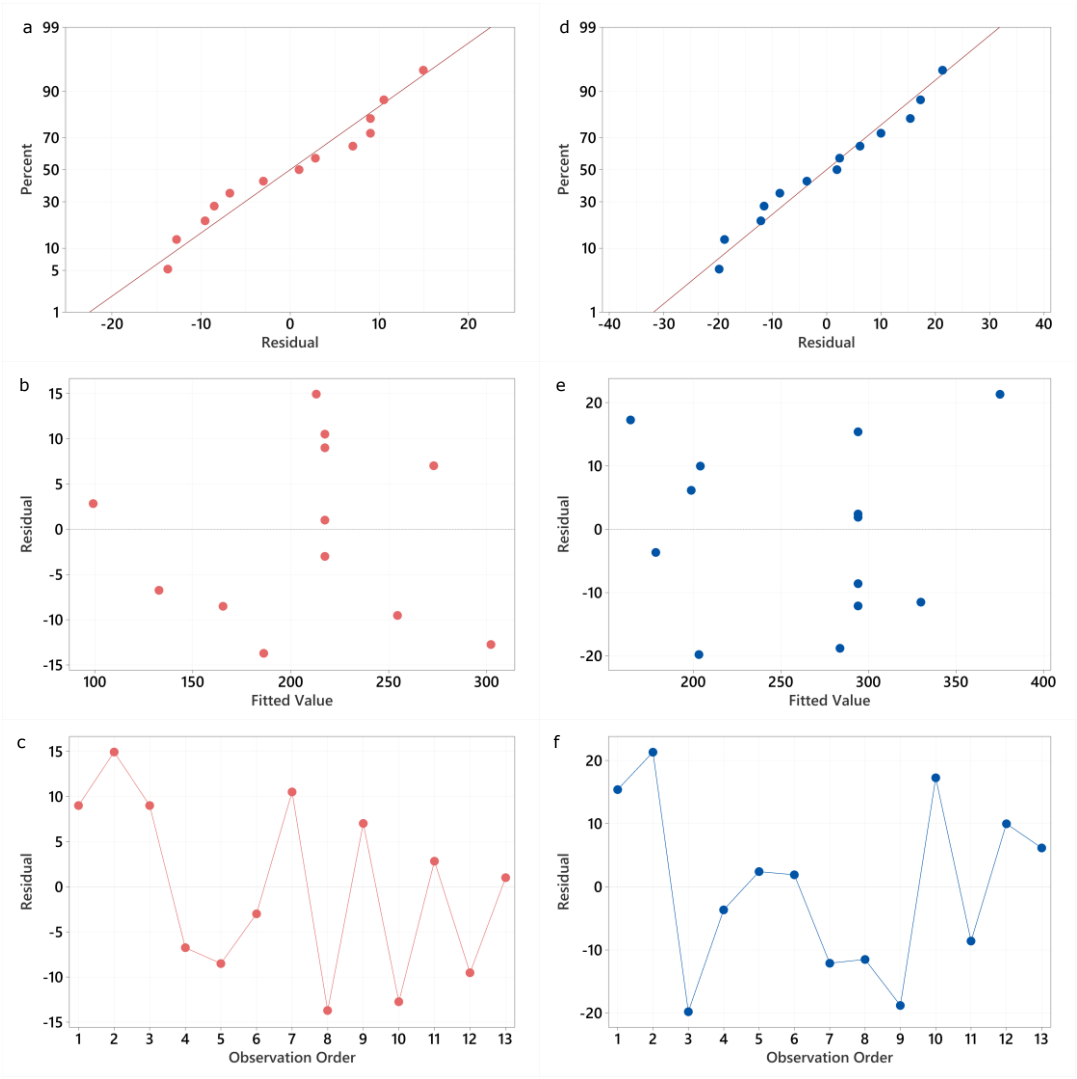


Figure 4.4. Diagnostic tests for the validation of the ANOVA test for the model I (left column) and model II (right column). a and d) Normal % probability against externally studentised residuals. b and e) Externally studentised residuals against predicted values. c and f) Externally studentised residuals against run order.

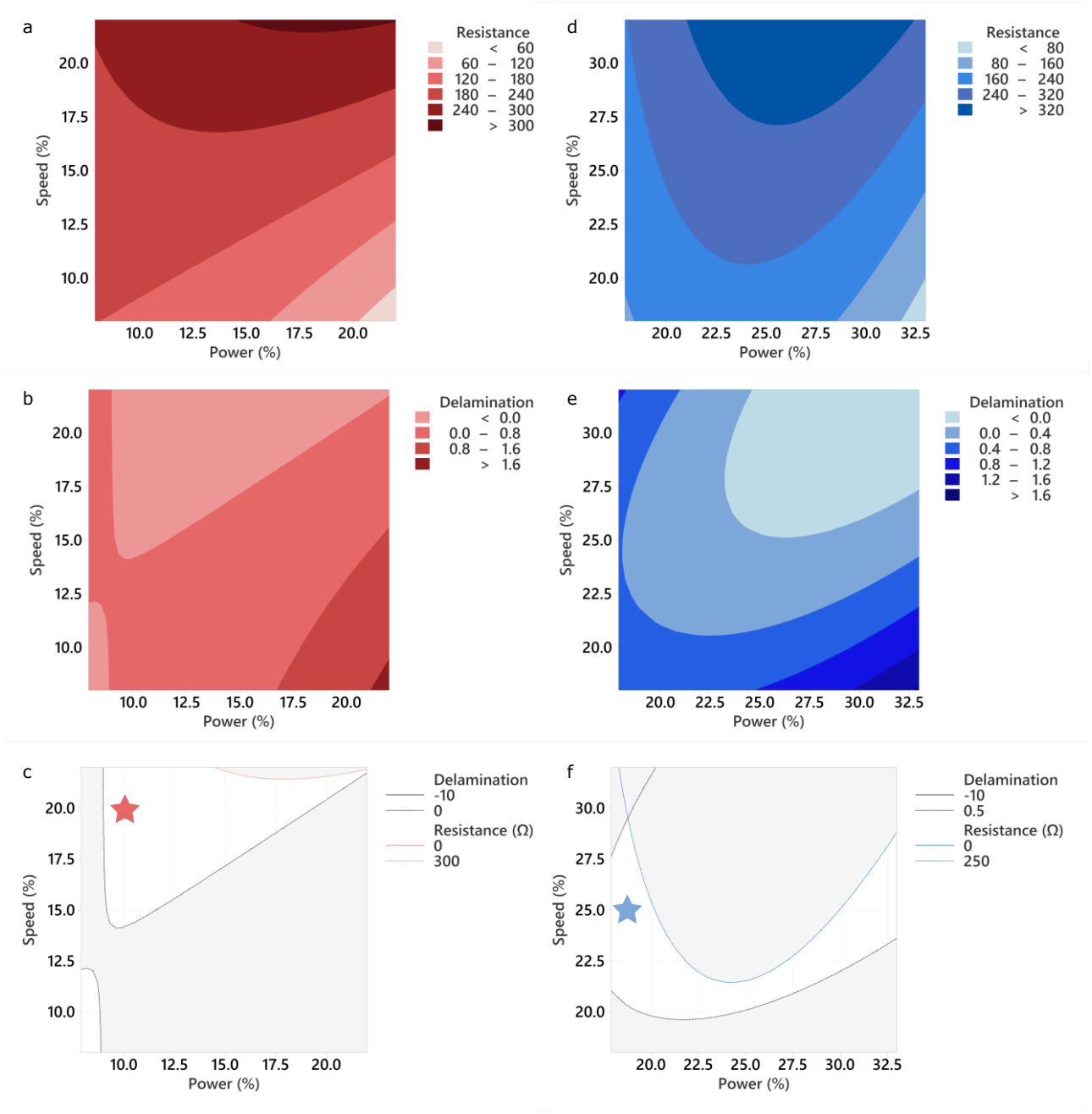


Figure 4.5. DoE-RS contour plots of engraving speed *vs* laser power for the model I (top) and model II (bottom) corresponding to: a and d) the linear resistance in Ω of the LIG; b and e) the coded delamination of the electrode, where 0 is no delamination and 1 is full delamination; c and f) superposition of the regions with delamination < 0 and resistance < 300 Ω for model I and resistance < 250 Ω for model II. The red star represents the region for LIG A and the blue start the region for LIG B.

Table 4-4. Predicted and measured resistance based on model I and model II. Highlighted values correspond to LIG A and LIG B.

| | **Power (%)** | **Speed (%)** | **Fit (Ω)** | **SE (Ω)** | **95% CI (Ω)** | **95% PI (Ω)** | **Measured (Ω)** |
|---|---|---|---|---|---|---|---|
| **Model I** | 10 | 20 | 255 | 9 | 233 - 276 | 220 - 289 | 245 |
| | 15 | 12.5 | 187 | 5 | 176 - 198 | 158 - 217 | 148 |
| | 17.5 | 20 | 279 | 7 | 264 - 294 | 248 - 310 | 283 |
| **Model II** | 17.9 | 25 | 199 | 14 | 166 – 232 | 145 – 253 | 205 |
| | 20 | 22 | 222 | 11 | 196 – 247 | 172 – 271 | 242 |
| | 25 | 27 | 318 | 8 | 300 - 336 | 272 – 365 | 300 |

SE = Standard error; CI = confidence interval; PI = prediction interval.

Table 4-5. Analysis of variance for model II the resistance equation based on the best-fitting model.

| Analysis of Variance | | | | | |
|---|---|---|---|---|---|
| **Source** | **DF** | **Adj SS** | **Adj MS** | **F-Value** | **p-Value** |
| **Model** | 5 | 50362.5 | 10072.5 | 31.37 | 0 |
| **Linear** | 2 | 29869.1 | 14934.5 | 46.51 | 0 |
| **Power (%)** | 1 | 21.8 | 21.8 | 0.07 | 0.802 |
| **Speed (%)** | 1 | 29847.3 | 29847.3 | 92.95 | 0 |
| **Square** | 2 | 18504 | 9252 | 28.81 | 0 |
| **Power (%)*Power (%)** | 1 | 18284.9 | 18284.9 | 56.94 | 0 |
| **Speed (%)*Speed (%)** | 1 | 41.4 | 41.4 | 0.13 | 0.73 |
| **2-Way Interaction** | 1 | 1849 | 1849 | 5.76 | 0.047 |
| **Power (%)*Speed (%)** | 1 | 1849 | 1849 | 5.76 | 0.047 |
| **Error** | 7 | 2247.8 | 321.1 | | |
| **Lack-of-Fit** | 3 | 1781.1 | 593.7 | 5.09 | 0.075 |
| **Pure Error** | 4 | 466.7 | 116.7 | | |
| **Total** | 12 | 52610.3 | | | |
| Resistance (Ω) | -698 + 71.0 Power (%) - 4.2 Speed (%) - 1.844 Power (%)*Power (%) - 0.100 Speed (%)*Speed (%) + 0.860 Power (%)*Speed (%) | | | | |

### *4.3.2. Material Characterization*

An investigation of the GS-SPE and the LIGs morphology was carried out by SEM, Raman, and contact angle analysis. The surface morphology directly affects the sensing properties of the WE, with surface area, hydrophilicity, and material structural being key properties to be analysed. Figure 4.6 shows two magnification settings of the electrodes. The surface graphene sheet of the GS-SPE (Figure 4.6a,d) is smooth and homogeneous, showing a well packed layered structure. The elevation difference in the smooth surface could be attributed to the edge of individual sheets or to folded sheet structures [163]. The smaller fragments on the surface of the graphene sheet (Figure 4.6d) could be derived either from graphite flakes or the graphene sheet breakage [164]. Unlike the graphene sheet, the LIGs structure is very porous and uneven. The surface of LIG A (Figure 4.6b, e) contains both larger outer pores and smaller inner pores inside the cylindrical pores (Figure 4.6e and Figure 4.7e), similar to what can be seen for LIG B in Figure 4.6c,f and Figure 4.7f. LIG A shows defined ablated and non-ablate regions with an increase in pore numbers in the ablated region (Figure 4.6b). LIG B has less defined non-ablated regions, with some over-ablated areas occurring probably due to the high laser power (Figure 4.6c). Non-ablated regions might contribute to the mechanical stability of the carbon film, as LIGs are usually brittle in nature [165]. Overall, LIG A showed a better mechanical stability than LIG B.

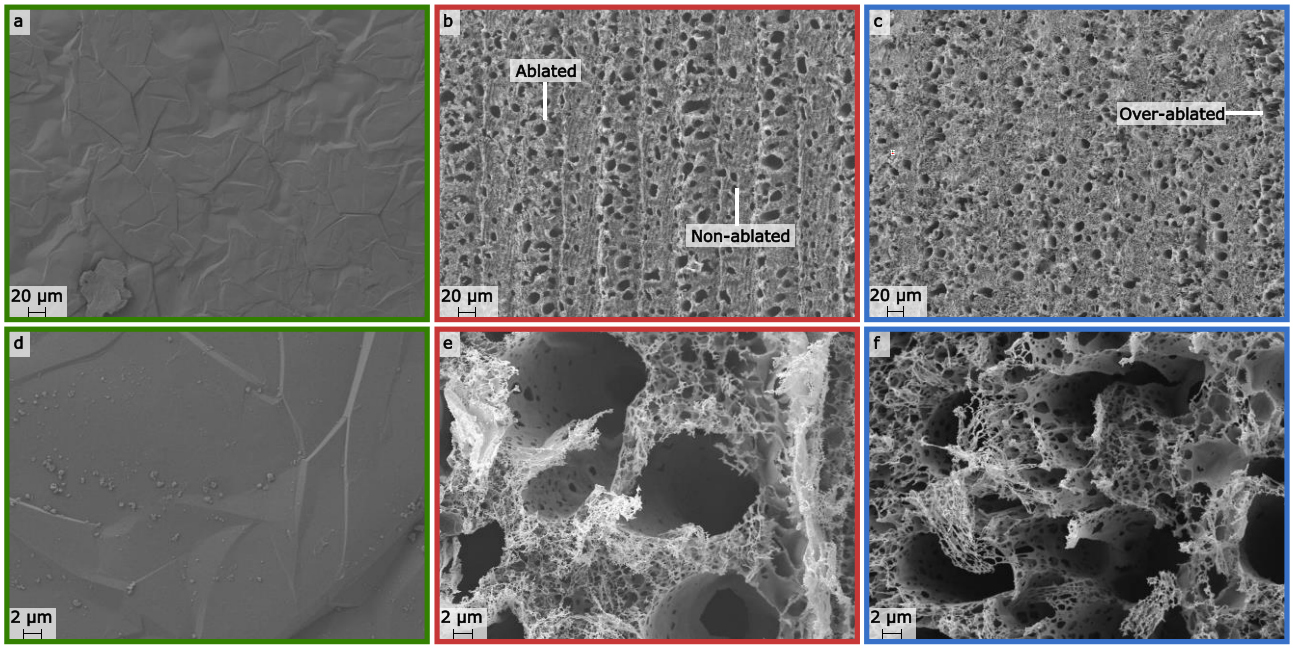


Figure 4.6. Colour coded SEM images of the GS-SPE (green border, a, d), LIG A (red border, b, e, specifying the ablated and non-ablated regions), and LIG B (blue border, c, f, specifying the over-ablated regions). Top row shows a magnification of 600 x and bottom row of 6500 x.

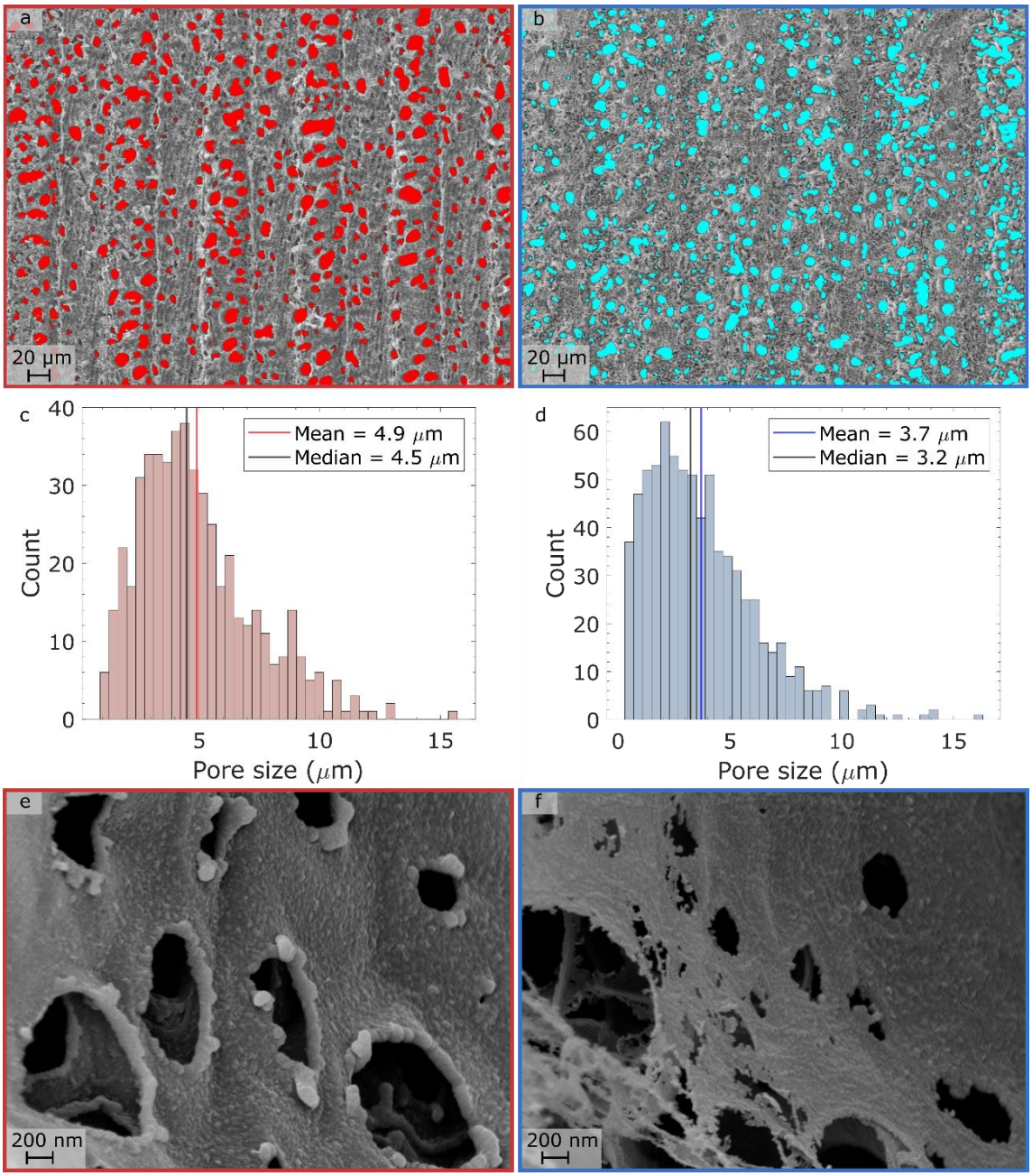


Figure 4.7. Colour coded figures corresponding to LIG A (red) and LIG B (blue). a, b) Coloured distribution of pores on the surface of the LIGs. c, d) Pore size distribution considering the pore radius. e, f) Magnification of 73480 x of the inner pores of the LIGs.

To further investigate the porosity of the LIGs, the pores distribution was processed and analysed (Figure 4.7a,b). It was more difficult to distinguish the pore distribution on LIG B than on LIG A due to the shape and depth of the pores. The distribution of the pore sizes can be seen in Figure 4.7c,d, with LIG A presenting a total of 503 pores and LIG B, 754. Although LIG B had more pores, the size

was overall smaller, with an average radius of 3.7 µm versus 4.9 µm for LIG A. LIG A was fabricated using a 7.5 W laser power, while LIG B used 13.5 W. As previously shown, the LIG porosity increases with laser power [151]. In this case, however, the total area covered by the pores was 13% for both LIGs, indicating that the higher speed used for LIG B might have counterbalanced the laser power effect. Another interesting aspect of the LIGs was the presence of smaller nanopores inside the larger pores (Figure 4.7e,f). The difference in the final structure of the pores is clear, with granular nanoparticles forming on LIG A while LIG B produced a thinner layer. This artifact occurs probably because of the lower engraving speed of LIG A [165]. The cross-section SEM images (Figure 4.8) revealed that both LIGs have similar thickness, with an average of 55 µm. The graphene sheet on the GS-SPE had a thickness ranging from 10 to 70 µm, however that seems to be because it started to peel off from the carbon paste at certain parts. From the magnified cross-section images it can be observed that the LIG B (Figure 4.8f) has many small pores in a honeycomb-like structure while LIG A (Figure 4.8e) has larger cylindrical pores. The graphene sheet layers can be seen in Figure 4.8d.

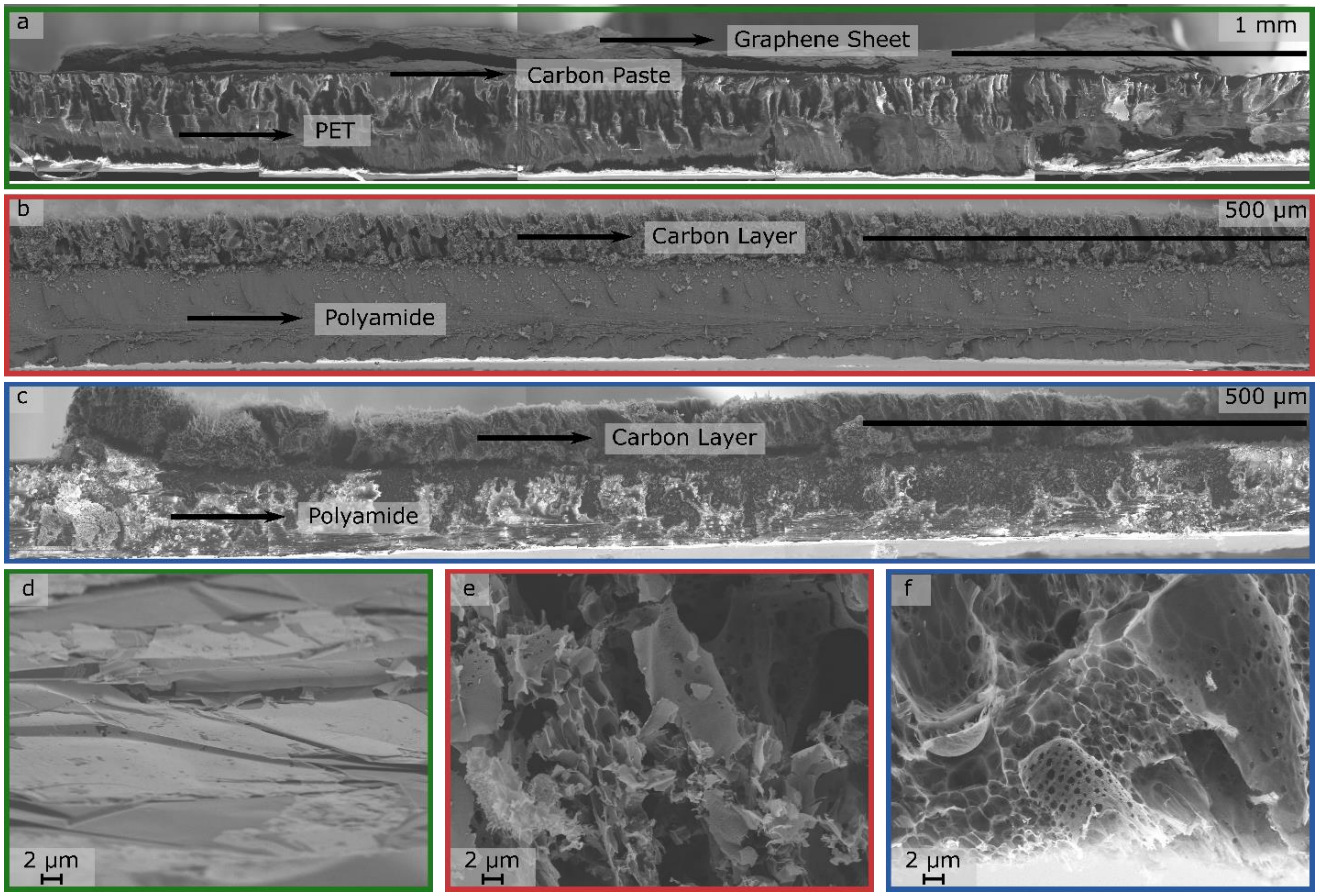


Figure 4.8. Cross-sectional SEM image of the: a) GS-SPE, showing the PET layer, the carbon paste and the graphene sheet. b) LIG A with the PI layer and the carbon layer. c) LIG B with the PI layer and the carbon layer; Magnified carbon layer on the d) GS-SPE, e) LIG A, and f) LIG B.

According to previous studies, the defect density on graphene materials impacts the electrochemical activity of chemical sensors. For example, graphene WEs with disordered materials and more defects can increase the electrochemical performance of the device [166]. Therefore, Raman spectroscopy was conducted to differentiate the carbon composition and crystal order of the fabricated electrodes (Figure 4.9a). The G and 2D peaks were present in all electrodes, while the LIGs also presented the D peak. The D and D' band represents defects in the crystal lattice due to breakage of the sigma bonds [161]. The G and 2D bands are related to highly ordered graphitic structures. The 2D band in specific correlates to the formation of graphene layers, deriving from the stacking of graphene layers on the c-axis [151]. From the Raman spectra, it can be concluded that although LIG A is visually similar to LIG B (Figure 4.6), they have different carbon structures. LIG A is more similar to the highly ordered GS-SPE, while LIG B presents more defects. Table 4-6 summarises the $I_D/I_G$ and $I_{2D}/I_G$ peak ratio for all electrodes. The ratio $I_D/I_G$ can be related to the degree of disorder of the material. LIG B presented the highest ratio of 1.08, indicating it has a highly disordered structure.

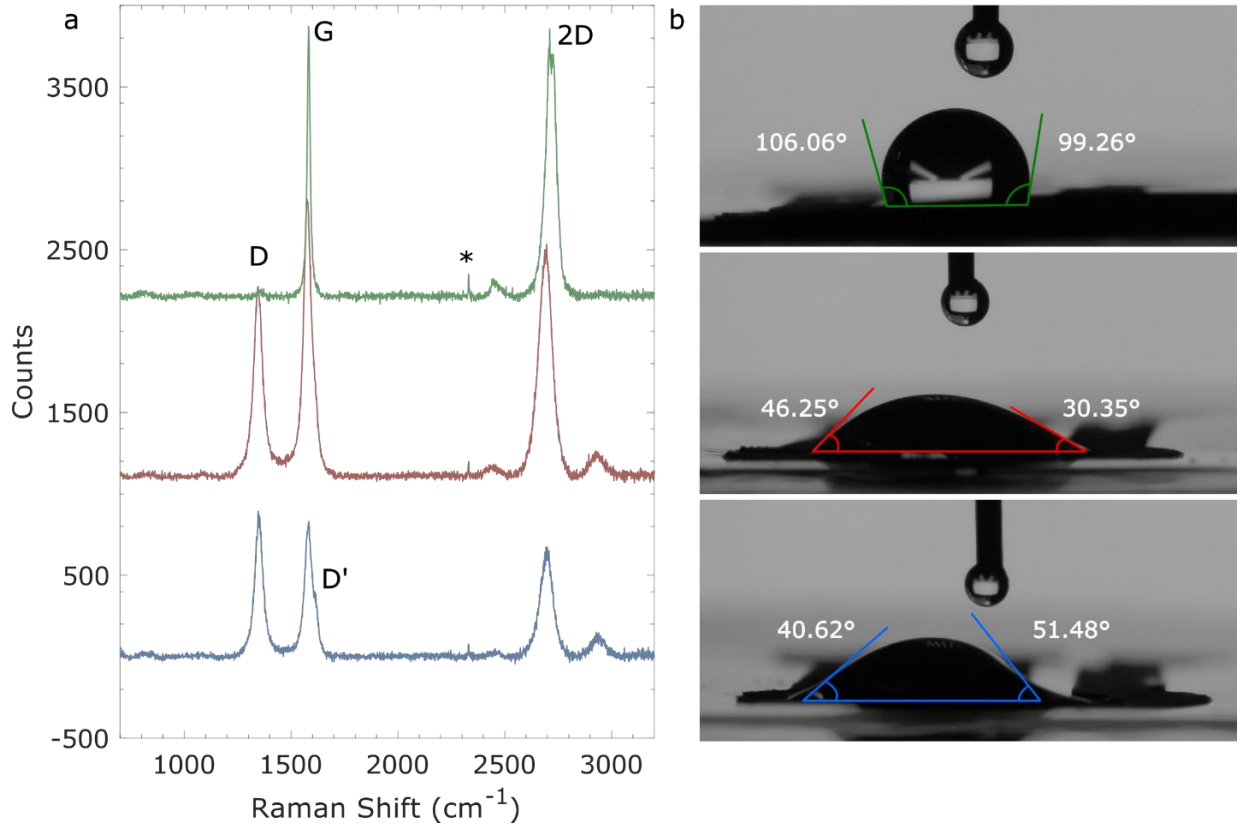


Figure 4.9. a) Raman spectra of the GS-SPE (green), LIG A (red), and LIG B (blue). The D, G, D', and 2D bands are highlighted in the graph. b) Contact angle analysis of the GS-SPE (green), LIG A (red), and LIG B (blue).

To better understand the hydrophilic/hydrophobic behaviour of the electrodes, the surface wettability was studied using the contact angle analysis (Figure 4.9b). This is important because it can affect the sensing properties of the WE. For example, in ion-selective electrodes a hydrophobic WE is desired as it prevents the formation of a water layer between the ion-selective membrane and the WE conductive material, while in this case, since the WE is not treated and is directly oxidising the analyte, a hydrophilic behaviour is more advantageous [161,167]. The GS-SPE has a more hydrophobic surface, with an average contact angle $\theta = 102.66°$. This is likely due to its defect-free, homogeneous surface, which probably decreases the number of oxygen atoms on its surface. On the other hand, both LIGs presented a more hydrophilic surface with $\theta = 38.30°$ for LIG A and $\theta = 46.05°$ for LIG B. This is probably a combination of their high porosity with the presence of heteroatoms on their surface, such as oxygen [161].

Table 4-6. Summary of Raman spectra peaks.

| | **GS-SPE** | **LIG A** | **LIG B** |
|---|---|---|---|
| $\mathbf{I_D/I_G}$ | 0.02 | 0.68 | 1.08 |
| $\mathbf{I_{2D}/I_G}$ | 0.99 | 0.84 | 0.81 |

### *4.3.3. Electrochemical analysis*

Further analysis was performed for all electrodes to investigate how the material composition and surface morphology affected the electrochemical performance. For this, the oxidation of $NO_2^-$ was chosen as it allows the use of the bare carbon WE to be employed as carbon materials have been shown to oxidise $NO_2^-$ into $NO_3^-$ at positive potentials [162]. First, the sensors were tested at pH 6, 7, and 8 in 50 mM NaCl aqueous solution with 50 µM $NO_2^-$ to understand if a change in pH affects the current intensity of the $NO_2^-$ oxidation peak. The pH range was chosen to be within the drinking water pH (6.5 to 9.5 according to the EU Directives) [24]. The DPV can be observed in Figure 4.10a-c, and the difference in peak current ($\Delta i_p$) per pH in Table 4-1. A few observations can be made from this analysis. First is that the LIG B seems to produce a higher peak current ($i_p$) than the other sensors, while also having the largest variation in $\Delta i_p$. LIG A had similar $\Delta i_p$ to the GS-SPE, however it also presented a much higher $i_p$ overall. The higher oxidation current observed for the LIGs is probably due to the higher surface area of the electrodes alongside a more hydrophilic surface, as observed in the SEM images (Figure 4.6 and Figure 4.7) and the contact angle images (Figure 4.9b). This allows

for a better interaction between the analyte and highly porous surface of the LIGs, increasing the active area of the WE. For the rest of the electrochemical experiments, pH 7 was used as it corresponds to a neutral pH.

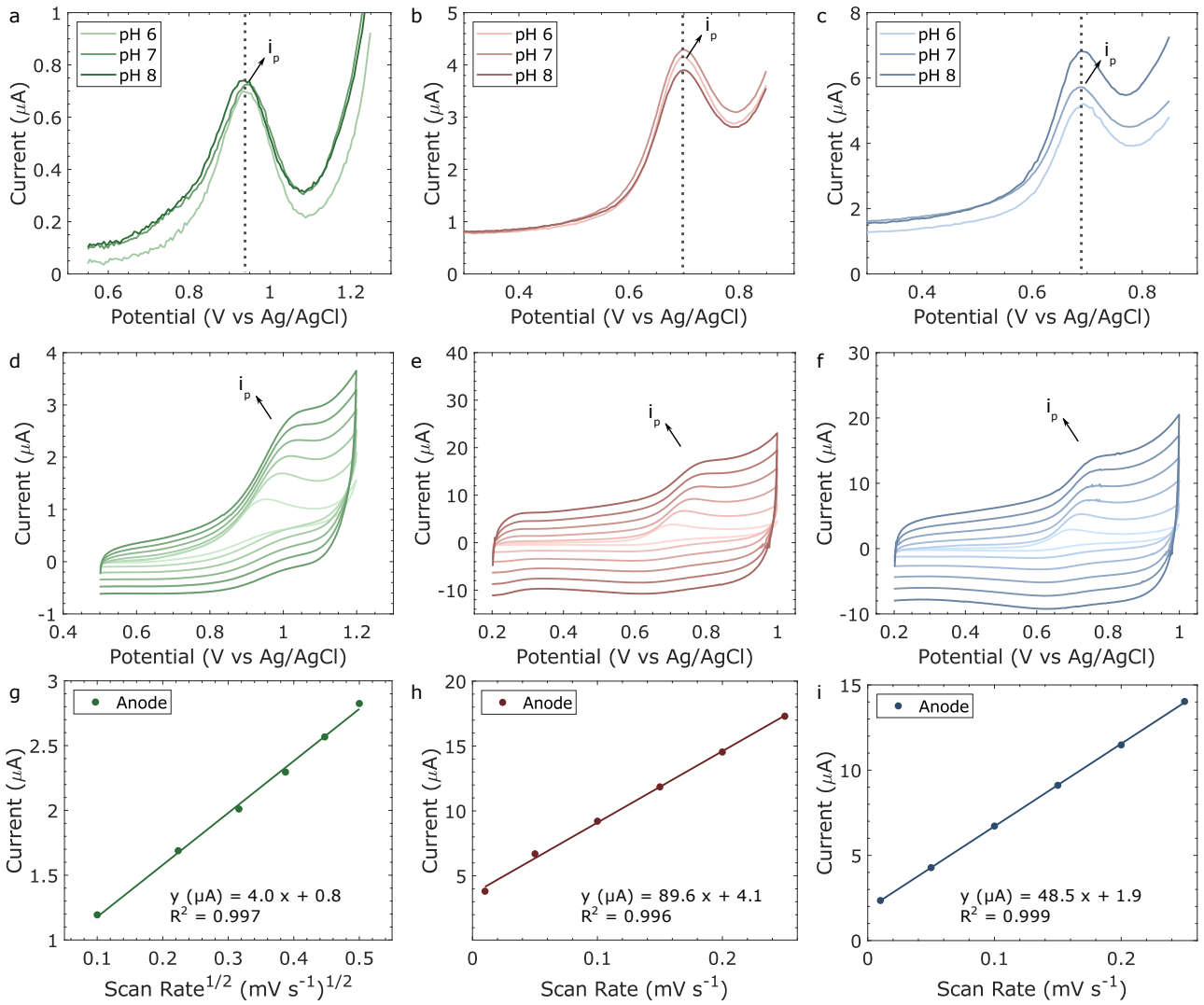


Figure 4.10. 50 µM $NaNO_2$ DPV at pH 6, 7, and 8 with 50 mM NaCl using the: a) GS-SPE, b) LIG A, and c) LIG B. CV scan rate of 10 to 250 mV/s for 100 µM $NaNO_2$ in 50 mM NaCl pH 7 for the: d) GS-SPE, f) LIG A, and g) LIG B. CV scan rate linear fit of the peak current *vs*: g) the square root of the scan rate for the GS-SPE, h) the scan rate for LIG A, and i) the scan rate for LIG B. The $i_p$ current corresponds to the oxidation peak between +0.8 and +1.0 V for the GS-SPE and +0.6 and +0.8 V for the LIGs.

The effect of the scan rate (10 mV/s to 250 mV/s) on the $NO_2^-$ oxidation reaction was investigated in Figure 4.10d-i. The reaction is irreversible and $i_p$ increases with the increase of the scan rate for all

electrodes, however the governing reaction mechanism is different for the GS-SPE and the LIGs. For the GS-SPE, the $i_p$ is linearly proportional to the square root of the scan rate (Figure 4.10g), indicating that the oxidation of nitrite is a diffusion-controlled process [168]. For the LIGs, however, $i_p$ is linearly proportional to the scan rate (Figure 4.10h,i). This could indicate that the reaction is mass-transfer limited in this case due to, for example, adsorption of the ions on the electrode surface [47]. Another reason could be that, unlike the GS-SPE, the LIGs have a high capacitive background current that increases at higher scan rates. Therefore, both faradaic and nonfaradaic currents contribute to the apparent increase of $i_p$.

Table 4-7. Peak oxidation current difference from the peak current at pH 7 for 50 µM $NaNO_2$.

| | **$\Delta i_p$ %** | | |
|---|---|---|---|
| | **GS-SPE** | **LIG A** | **LIG B** |
| **pH 6** | -3.60 | -3.32 | -9.89 |
| **pH 7** | 0.00 | 0.00 | 0.00 |
| **pH 8** | 5.72 | -6.14 | 31.03 |

DPV was employed to investigate the faradaic response of the sensors toward $NO_2^-$, to minimise the capacitive charging of the LIGs that appears in techniques such as the CV. This, in turn, improves the $NO_2^-$ oxidation signal, making it possible to analyse even smaller concentrations of the analyte. The DPV response of the sensors from 10 to 500 µM of $NO_2^-$ and the calibration plot can be observed in Figure 4.11. It can be noticed that the oxidation potential is higher for the GS-SPE than for the LIGs. This suggests that the material composition of the LIGs is more efficient at oxidising the $NO_2^-$ ion as it requires less input energy, possibly because of the structure of the carbon material or the absence of paste binders, making it easier for the electron transfer to occur. Similar to the previous electrochemical results, the GS-SPE had the lowest oxidation current of all electrodes. On average, LIG A had a $i_p$ of 565% higher than the GS-SPE and LIG B, of 729%. The higher electrochemical activity of LIG B could be correlated to its higher disordered structured (Figure 4.9a), as defects and disordered material structure can increase the electrochemical performance of the device [166].

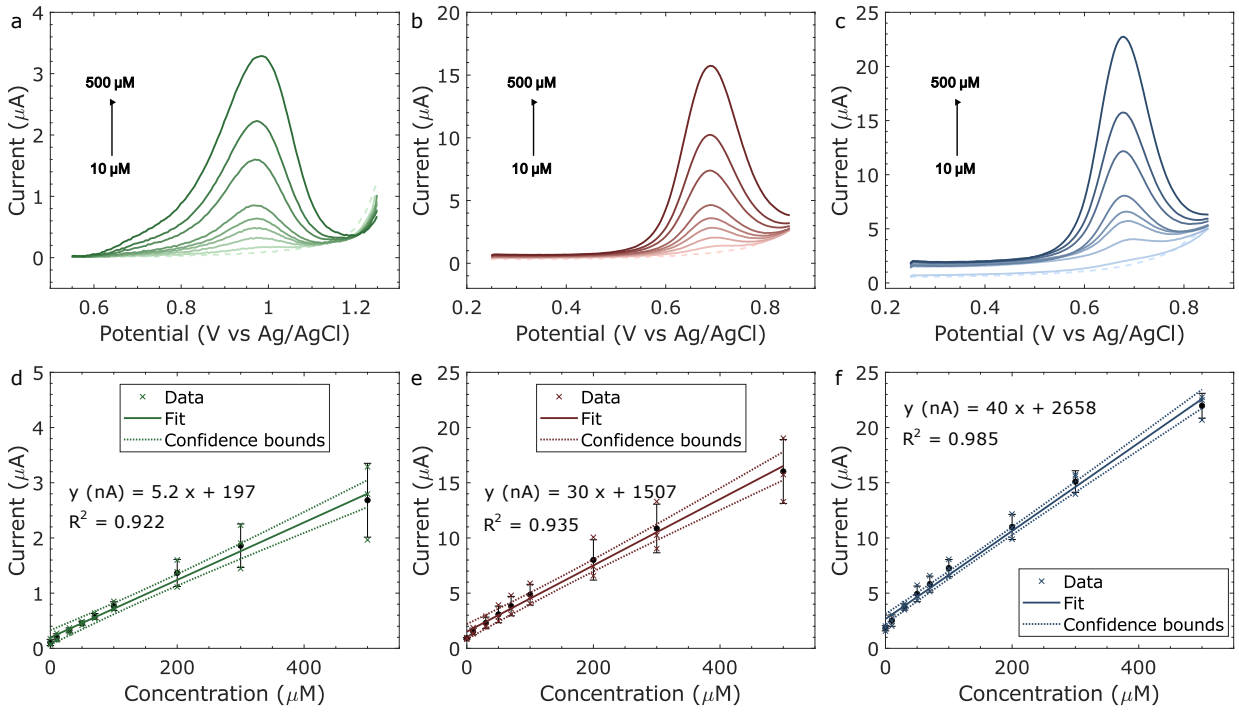


Figure 4.11. DPV of 10 to 500 µM of $NaNO_2$ in 50 mM NaCl pH 7: a) GS-SPE, b) LIG A, and c) LIG B. The baseline is represented by dotted lines. Calibration plot inset for: d) GS-SPE, e) LIG A, and f) LIG B.

Table 4-8. Calibration curve parameters based on the DPV measurements of 10-500 µM $NaNO_2$ in 50 mM NaCl pH 7.

| | **GS-SPE** | **LIG A** | **LIG B** |
|---|---|---|---|
| **Linear range (µM)** | 38-500 | 10-500 | 20-500 |
| **Sensitivity (nA/µM)** | 5.2 ± 0.3 | 30 ± 2 | 40 ± 1 |
| **Intercept (nA)** | 197 ± 64 | 1507 ± 334 | 2658 ± 220 |
| **$R^2$** | 0.922 | 0.935 | 0.985 |
| **RSD (%)** | < 33.6 | < 24.5 | < 20.6 |
| **LOD (µM)** | 37.2 | 8.6 | 19.2 |

Sensor performance was evaluated by measuring the sensitivity, linearity, relative standard deviation (RSD) and limit of detection (LOD). All electrodes presented an increase of $i_p$ with an increase of analyte, presenting a linear correlation with $R^2$ greater than 0.9 throughout the whole $NO_2^-$ concentration range. The summary of the calibration plots can be found at Table 4-8. The RSD was calculated by taking the standard deviation (SD) of each concentration, diving it by its corresponding average $i_p$ and multiplying it by 100 to obtain a percentage, with RSD = 100*SD [concentration]/$i_p$ [concentration]. LIG B presented the best linearity with a RSD < 20.6 %, with LIG A following closely behind. There was a difference of 10 $nA\mu M^{-1}$ in sensitivity between both LIGs, and the GS-SPE displayed the lowest sensitivity of the three, at only 5 ± 0.3 $nA\mu M^{-1}$. LOD was estimated using the IUPAC definition of LOD = 3.3*σ/s, where $\sigma$ is the standard deviation of the background current and *s* is the sensitivity of the calibration plot [169]. The LOD was higher than the lowest tested concentration (10 µM) for both the GS-SPE (LOD of 37.2 µM) and LIG B (LOD of 19.2 µM), while LIG A had a LOD slightly lower than 10 µM (8.6 µM). This could be improved, for example, by fitting two times over the different concentration ranges. For example, one fitting for the lower concentration range and another for higher concentrations, as the slope changes slightly from medium to higher concentrations. For this, further points in between the studied concentrations should be added for more accurate results. Another possibility is to use more sensitive techniques such as chronoamperometry, which allows lower concentrations to be detected.

In comparison to other printed $NO_2^-$ sensors found in literature, the LIGs developed here presented a good performance (Table 4-9). It is especially interesting that the high sensitivity was achieved without the addition of nanoparticles or other carbon additives, as with other $NO_2^-$ LIG sensors [165,168]. By optimizing the laser parameters using the DOE, incredibly sensitive, binder-free $NO_2^-$ sensors were achieved in a single-step process. Furthermore, the fabricated sensors appear to function similarly at different pH (Figure 4.10), making them ideal for quick routine samples, either in the field or in the laboratory.

To investigate the selectivity of these sensors in the field, the $i_p$ signal of 50 µM of the LIGs was compared in the presence of common ionic compounds ($CaCO_3$, $FeSO_4$, $MgSO_4$, $NaNO_3$) present in drinking and river water (Figure 4.12a). As the GS-SPE showed much lower current responses, it was not included in the next experiments. From Figure 4.12a, it can be seen that the $i_p$ of LIG B is highly influenced by the addition of other analytes, specially $NaNO_3$. On the other hand, the $NO_2^-$ oxidation signal is more stable for LIG A even in the presence of other ions. This could be due to the different carbon structure of LIG A compared to LIG B, however further analysis is needed to support this. To

test the sensors' performance in drinking water, a bottled spring water was used without any additional modification. The added $NO_2^-$ concentration was in the range of 10 to 50 µM. Although the same trend of current increase with analyte increase was observed for both electrodes, the $i_p$ found was on average half of that found in the previous DPV studies (Figure 4.11b,c) for LIG A and a third for LIG B. This could be because of the interference of other ions present in the drinking water, which decreased the $i_p$. This indicates that the calibration curve for the LIGs need to be adjusted depending on the medium it is being used.

Table 4-9. Various parameters of printed sensors for the detection of $NO_2^-$.

| **Printing Method** | **Sensing Material** | **Detection Method** | **Linear Range (µM)** | **LOD (µM)** | **Sensitivity ($\mu A \mu M^{-1} cm^{-2}$)** | **Ref** |
|---|---|---|---|---|---|---|
| Screen-printing | Au NPs/ GOx | DPV | 1-6000 | 0.13 | 30.5 | [170] |
| Laser engraving | Chitosan | DPV | 2-1000 | 0.9 | 12.1 | [165] |
| Laser engraving | Au NPs/CNTs | SWV | 10-140 | 0.9 | 18.3 | [168] |
| Laser engraving | Bare LIG | DPV | 10-70 | 0.27 | 58.5 | [171] |
| Laser engraving | Bare LIG | DPV | 10-500 | 8.6 | 42.4 | This work |
| Laser engraving | Bare LIG | DPV | 20-500 | 19.2 | 56.5 | This work |
| Screen-printing | Graphene sheet | DPV | 38-500 | 37.2 | 7 | This work |

CNT = Carbon nanotube; GOx: Graphene oxide; NPs = nanoparticles; SWV = Square wave voltammetry.

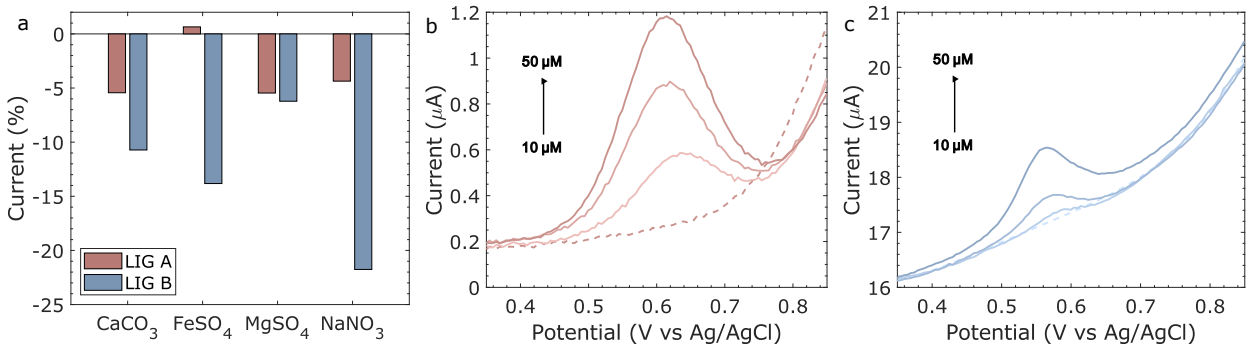


Figure 4.12. a) Peak current difference of 50 µM $NaNO_2$ in the presence of 50 µM of each common interfering ion ($CaCO_3$, $FeSO_4$, $MgSO_4$ or $NaNO_3$) for LIG A and LIG B. DPV of 10 to 50 µM $NaNO_2$ in spring water for the: b) LIG A and c) LIG B. The baseline is represented by dotted lines.

## 4.4. Conclusion

The current work demonstrated that LIGs are a suitable replacement for carbon-based SPEs as electrochemical sensors. In Chapter 3, it was verified that carbon-based SPEs had advantages over Ag paste SPEs, however they had a higher electrical resistance, which lowered the redox peak current. This problem was solved here by using LIGs, which offer the advantages of a graphene-like structure without the need to use binders or solvents. To achieve this, the linear resistance and the carbon adhesion of the LIGs to the PI substrate was improved by using the DoE-RS statistical approach. The instrument parameters that were used to construct the DoE-RS models were the laser power, speed, and focus, as they seem to influence the quality of the LIGs the most. The linear resistance DoE-RS models had a $R^2 > 95\%$, however, only when combined with the delamination models, suitable LIGs could be fabricated. That is because depending on the laser parameters used the LIGs become brittle, even though they had a lower resistance. From the models, two regions with low resistance and good substrate adherence were chosen to fabricate the LIGs, resulting in LIG A and LIG B. It is important to note that although only two responses were employed to construct the models (resistance and delamination), other response variables could be included in future studies, such as Raman spectra or electrode thickness to optimise the LIG to the desired application. To better understand why they showed a better performance, a detailed material and electrochemical characterisation was performed.

The SEM images showed that the LIGs were highly porous, having a higher surface area than the continuous graphene. From the Raman spectroscopy, it was possible to infer that the LIGs showed a disordered graphene structure, while the GS-SPE was constituted of ordered graphene layers. The fabricated LIGs were also more hydrophilic than the GS-SPE, which is advantageous when using the

pristine WE for electrochemical detection in water. These facts combined can increase the electrochemical performance of the device, which was demonstrated by the electrochemical studies on the oxidation of $NO_2^-$ ions. The LIGs were overall more stable and presented a peak current higher than 500% when compared to the GS-SPE. Furthermore, these binder-free, unmodified LIGs exhibited sensitivity comparable to other modified SPEs or LIGs for $NO_2^-$ detection. Although $NO_2^-$ was chosen as the analyte of interest, the LIGs fabricated here can be used as a template to detect other analytes by further modifying the WE with other materials. In this sense, a combination of screen-printing with LIGs could be used to produce sensors for other applications. Overall, the potential of using LIGs as electrochemical sensors was demonstrated, being successfully employed as an alternative to disposable carbon-based SPEs. Further optimisation can be achieved by more iterations of DoE, with lower resistance and more stable LIG electrodes. More importantly, studies on long-term surface degradation of the LIGs are needed, as well as their performance on different water bodies.

# Chapter 5

# Copper-based Dissolved Ammonia Sensors

*Parts of this chapter are adapted with permission from: F. F. Franco, R. A. Hogg, and L. Manjakkal, "$Cu_2O$-Based Electrochemical Biosensor for Non-Invasive and Portable Glucose Detection," Biosensors, 2022, 12(3), doi: 10.3390/bios12030174. The same batch of $Cu_2O$ nanocluster was tested for ammonia sensing and glucose sensing.*

## 5.1. Introduction

From Chapter 2, it was observed that the previously fabricated ZnO dissolved ammonia sensor printed on a silver conductive interdigitated (IDE) electrode showed inadequate performance toward dissolved $NH_3$ after further studies. The electrochemistry analysis showed that the silver conductive track could be influencing the signal response by interacting with the sulphates present in solution. Therefore, new materials need to be investigated to continue the detection studies of dissolved $NH_3$ in water. The development of new materials for $NH_3$ detection plays a major role in sensor selectivity and sensitivity. Synthesizing a material that can detect $NH_3$ at nano and micromolar levels while being stable and cost-effective remains a great challenge [41]. For this, nanostructures and smart material design have been developed, e.g., metal oxides, polymers, and metal organic frameworks. Therefore, a review some of the advances in these materials and what other alternatives have been used for ammonia detection, including how the material size, shape, and composition react with the system is discussed below to select the best material option.

**Metal/Metal oxides.** Metal oxides are a class of material widely studied due to their high surface to volume ratio and excellent electrical and morphological properties, which enhance the sensitivity

and catalytic performance in sensors [64]. For gas sensors, metal oxide-based semiconductors are a popular sensing material, with ZnO, $SnO_2$, and $In_2O_3$ among some of the metal oxides used in $NH_3$ gas sensing [93,101,172]. The sensing mechanism for metal oxides, based on chemiresistance changes, has been thoroughly reported in literature [93,101]. This mechanism is well explained in air, where the surface oxide layer acts as the receptor by interacting with a reducing gas, which in turn alters the resistivity of the metal oxide. [101]. In air, $NH_3$ acts as an electron donor when reacting with the oxygen adsorbed at the metal oxide layer generating free electrons [93]. In wet atmosphere, the mechanism depends on the humidity levels and there is no consensus on how the water layer interacts with the metal oxide. At higher humidity levels the water suffers dissociation into $H^+$ and $OH^-$ and physisorption/chemisorption is observed, but the exact mechanism is dependent on the sensing material [93]. This sensing mechanism is also mentioned in Chapter 2, Figure 2.1.

ZnO appears to be a popular choice for electrochemical $NH_3$ sensing due to its chemical stability, large exciton binding energy and n-type semiconducting properties, which is discussed more in-depth in Chapter 2 [172]. It was proposed that dissolved $NH_3$ reacts with the surface adsorbed superoxides ($O^{2-}$) in an exothermic reaction and the energy released during the decomposition should be sufficient for the electrons to jump to the conduction band, which in turn decreases the resistance of the material [8]. $O^{2-}$ are the most predominant species adsorbed in the metal oxide surface when in presence of a reducing agent, i.e., ammonia [8]. Moreover, a humidity sensor using ZnO nanorods and nanowires showed that at high humidity the water condenses, providing a channel for electrolytic conduction [173]. Another study suggested a model for water interaction with ZnO based on experimental results, where water suffers partial dissociation at the surface, forming an ordered superstructure [104]. By combining the findings of these different studies, it is reasonable to assume that water might dissociate at the surface of the metal oxide into different species and forms an ordered structure, with oxides being the ones that react most strongly with ammonia. This, however, can be an issue for selectivity, as the interaction is not analyte specific.

Other metal oxides used for dissolved $NH_3$ sensing include CuO and $Fe_3O_4$. $Fe_3O_4$ has been implemented in optical and FET-based sensors in the form of nanoparticles and nanotubes [174,175]. A charge transfer study on physiosorbed ammonia on $Fe_3O_4$ described that a thin layer of water was necessary for the activation of the sensor [175]. First, gas $NH_3$ dissolves in the adsorbed water layer. Then dissolved ammonia is adsorbed in the nanotube surface, donating electrons to the material which in turn produces an electrical response that can be used to detect ammonia [175]. This explanation is similar to the one given to the ZnO nanomaterials. For the optical $Fe_3O_4$ sensor, the reducing

absorbance with increasing concentration of ammonia was likely due to the formation of non-absorbing species between ammonia and the $Fe_3O_4$ immobilized nanoparticles [174]. The authors did not comment on what these species were, however, it can be deduced that the same principle of dissolved $NH_3$ adsorbing on the water layer can be applied here. The sensor also had a high tolerance ratio for interfering species including various amines, which was defined as the ratio of the concentration of interfering species over the concentration of ammonia that caused a relative error of 5%, indicating that the detection mode (eg. optical vs electrochemical) is quite important when considering the material selectivity. Cu-based materials have also been used to detect dissolved $NH_3$ [176,177]. The ability of copper to form cupric complexes with ammonia can be used in electrochemical sensors. Cu can be employed in its metallic form or by passivating it with an oxide layer which can increase its sensitivity [178]. Cu oxides present a low net surface charge that prevents the material from being affected by compounds that commonly interfere with other noble metals used as sensing materials [179]. Other metals, such as gold and platinum, have also been employed for the detection of ammonia however they present a higher cost [180,181]. In general, metal oxides are a tested technology specially for $NH_3$ gas sensors and are relatively low cost, although selectivity is often poor.

**Metal Organic Frameworks.** Metal-organic framework (MOF) is a class of materials that exhibits versatile properties due to their unique combination of organic and inorganic units. Due to their adaptable nature, MOFs were successfully employed in a diverse range of applications, including gas storage, catalysis, and energy storage [182,183]. The concept of MOFs was introduced three decades ago, and since then, 1D, 2D, and 3D structures have been designed by exploiting various combinations of organic linkers and metal units [184]. The wide range of molecular building units available allow for a rational design of MOFs by exploiting the strong bonds between the molecules provided by reticular chemistry [183]. MOFs are highly porous, crystalline materials and the development of post-synthetic modifications allow these frameworks to have higher specificity for unique substrates and increased reactivity [183]. By controlling the sterics and the electronics around catalytically active site, excellent performance can be achieved [185]. For ammonia detection, only a few coordination polymers can be found in literature. A AgBr 4-(trimethylammonio)benzenethiol (TabH) 1D coordination polymer was employed for the detection of dissolved $NH_3$, where the acidic sulfihydril groups of the $TabH^+$ react with $NH_3$ through deprotonation [109]. Some MOFs have also been employed to detect gas $NH_3$. A Ba(II) carboxylate MOF was employed as a gas $NH_3$ sensor at high humidity [186]. The carboxylic groups form a hydrogen-bond network which reacts with the gas $NH_3$ to form $NH_4^+$. The MOF is water stable making it a strong contender for dissolved $NH_3$ sensing.

A $SiO_2$-coated Cu-MOF, single layer graphene, and polyaniline composite was used for gas $NH_3$ detection [187]. The increase in resistance with the addition of $NH_3$ was due to the *p*-type behaviour of the composite where a proton was donated to the gas $NH_3$ to form $NH_4^+$ ions. A linear correlation was observed up to 100 ppm where then the composite became proton deficient and lost its ability to interact with the gas $NH_3$. Therefore, MOFs have shown its potential for ammonia sensing but further structures need to be explored for better durability and sensitivity of the material. Scalability is also an issue for MOFs as not all synthesis are compatible with industrial scale and this should be factored in when choosing a suitable MOF.

**Ionophores.** A common material for $NH_4^+$ ion detection are ionophores, which are natural or synthetic compounds that have a high affinity for specific ions and can facilitate their transport across the membrane, with nonactin being the most employed one [77]. They are highly selective to $NH_4^+$ but also to $K^+$ which can be problematic in solution with a high concentration of $K^+$. Nevertheless, commercial ISEs usually employ ionophores making it a robust technology. Several chemical modifications to ionophores have been developed over the years to improve their performance, such as the addition of carbonyl groups and pyrazole rings [77]. For example, a fluoroionophore works by having the ionophore unit bind to the $NH_4^+$ ion while the fluorophore unit is responsible for the optical transduction [188]. Different solvents and cation exchange membranes have been employed together with ionophores to improve their selectivity, such as potassium tetrakis(4-chlorophenyl)-borate and bis-tris methane [80,188]. While the cation exchange membrane is employed for better electrode reproducibility, a buffer solution can be used to maintain a stable pH, fully protonating or deprotonating ammonia. However, sensors that employ ionophores can suffer from long response times, specially at lower analyte concentrations [189]. Commercial ISE sensors can have a response time of up to 600s at low ammonia concentrations and the membrane needs to be rehydrated in an ammonium-free solution for 10 minutes [77,190] .

**Carbon-based materials.** Carbon nanotubes (CNTs) and graphene have been employed to enhance the sensitivity of ammonia sensors. Although they normally are not used to directly detect ammonia, their high conductivity, ability to form composites with other polymers and metals and high chemical stability make carbon allotropes a useful tool in ammonia sensing [191]. For example, CNTs were added to a potentiometric ammonium sensor to improve the electron transfer between the ionophore and the inner electrode, decreasing the data drift [80]. Another sensor used a fluorographene composite to detect changes in impedance in the presence of ammonia [192]. The fluorine is responsible for the selective sensing of ammonia via hydrogen bonding, and the doping of

graphene with fluorine produces a chemically stable, highly conductive compound [192]. Therefore, carbon-based materials can be combined with other materials selective to ammonia to improve its sensitivity by increasing the material electron transfer properties.

Table 5-1. Overview of different material classes used for the electrochemical detection of $NH_3/NH_4^+$.

| Material Type | Advantages | Disadvantages | Examples |
|---|---|---|---|
| **Metal Oxides** | - Low cost<br>- Tested technology | - Selectivity<br>- High working temperature | ZnO, $CuO_2$, $FeO_3$ |
| **Metal Organic Frameworks** | - Selectivity<br>- Many combinations to be explored | - Scalability<br>- Fragile | Sulfihydril groups, Cu metal nodes |
| **Ionophores** | - Commercially available<br>- Low cost | - Interference with $K^+$ and other cations | Nonactin, aza-crown ethers |
| **Carbon-based Materials** | - High conductivity<br>- Chemical stability | - Need to be combined with other materials for selective sensing | CNTs, graphene |

In summary, different classes of materials were investigated for ammonia sensing. By combining it with different detection techniques, particle size, post-synthetic modifications, etc, a higher sensitivity, selectivity and sensitivity can be achieved. A comparison of these materials and the reported sensors are reported in Table 5-1. Most of these materials claim high selectivity, sensitivity, and stability, however except for ionophores, most of these technologies are not commercially available for dissolved $NH_3$ monitoring. Furthermore, it is difficult to find reports relating to the sensor biocompatibility and degradability, a concept particularly important in environmental ammonia monitoring as these materials can adversely affect aquatic life. Therefore, although dissolved $NH_3$ sensing is challenging, there are many opportunities for developing stable and sustainable materials for portable ammonia sensors. MOFs are particularly interesting as they can combine the chemical motifs from other classes of materials that are sensitive to ammonia to design

an improved composite structure. Furthermore, metal oxides have demonstrated a high sensitivity towards dissolved $NH_3$ sensing. In particular, copper-based sensors are a good candidate. They have been successfully used to oxidise ammonia and are relatively cheap as Cu is a low-cost material with a wide crustal abundance [176,193–195].

In this regard, $Cu_2O$ nanoparticles (NPs) and a Cu-MOF were selected here as candidates to compare their performance for dissolved $NH_3$ sensing. The change of oxidation state from Cu(II) to Cu(III) mediates the electrocatalytic activity of copper nanocomposites, with the possibility of tailoring the synthesis to form nanostructures such as nanoflowers, nanowires, and nanocubes [196–198]. To simplify the sensitive material procedure, a straightforward room-temperature reduction synthesis was performed to fabricate the $Cu_2O$ NPs. While $Cu_2O$ NPs are often simple to synthesise, MOF synthesis methods range from simpler procedures as microwave-assisted heating and one pot synthesis, to more complex ones as hydro/solvothermal or electrochemical synthesis [183]. For this work, a Cu node and a 1,4-benzenedicarboxylic acid ($H_2BDC$) organic link were selected to fabricate the MOF using the solvothermal synthesis method. Metal-based MOFs assembled with the 1,4-benzenedicarboxylic acid ($H_2BDC$) ligand are robust and traditional MOFs that during sorption of small molecules can exhibit reversible structural changes [199]. Cu-based BDC MOFs have previously been used for ammonia removal but have not been reported for electrochemical dissolved $NH_3$ sensing, making it an interesting candidate for further studies [199].

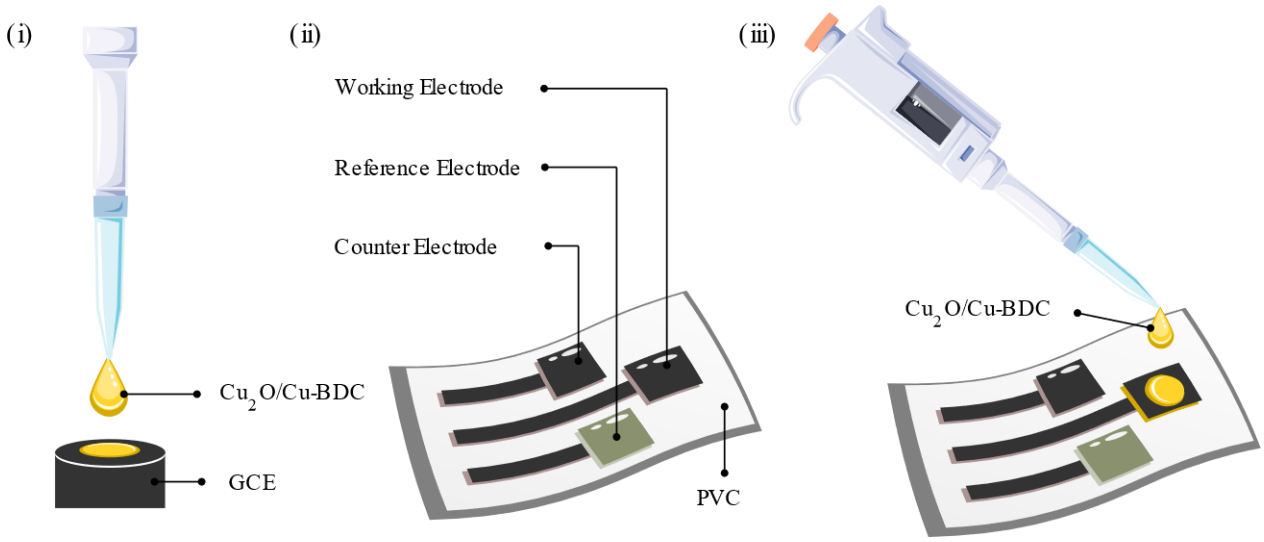


Figure 5.1. Schematic fabrication of the dissolved $NH_3$ sensor. (i) $Cu_2O$ nanoclusters/Cu-BDC MOF drop casted on the GCE for material study. (ii) Printed graphene paste electrodes with a Ag/AgCl RE. (iii) Modified graphene WE with $Cu_2O$ nanoclusters/Cu-BDC MOF.

$Cu_2O$ nanoclusters and Cu-based BDC MOFs (Cu-BDC) were employed as the sensitive material and drop casted on top of the working electrode (WE). To study the feasibility of the Cu-based materials for dissolved $NH_3$ sensing, CV and DPV studies were conducted in basic solutions (0.1 M sodium hydroxide (NaOH), potassium hydroxide (KOH) or carbonate buffer) using glassy carbon electrode (GCE) and graphene paste printed electrodes (PEs). Commercial graphene paste was used for the printed WE, and the top of the WE was further modified with drop casted Cu-based materials. The schematic fabrication is shown in Figure 5.1, with Figure 5.1 (ii) and (iii) showing the visualization of the complete printed sensor, although the Cu-BDC was only tested on the printed WE. As the Cu-BDC had not been yet reported in literature for dissolved $NH_3$ sensing, a more extensive characterisation was carried out, including the redox analysis at different pH for both total ammonia concentration and dissolved $NH_3$. XRD and SEM were employed to study the morphology of the Cu-based materials.

## 5.2. Experimental Section

### *5.2.1. Cu-based Materials Synthesis*

#### *5.2.1.1. $Cu_2O$ Synthesis*

The $Cu_2O$ nanocrystals were synthesized by modifying a previously published work [176]. Briefly, the synthesis consists of an ascorbic acid ($C_6H_8O_6$) and NaOH reduction route at room temperature. The addition of $C_6H_8O$ favours the formation of $Cu_2O$, and the concentration of NaOH dictates the nanoparticle shape [200]. The reaction mechanism is as follows [200]:

$$2Cu(OH)_2 + C_6H_8O_6 \leftrightarrow Cu_2O + C_6H_8O_6 + 3\,H_2O \quad (5.1)$$

Firstly, 0.1 mmol of $CuCl_2$ and 0.1 g of polyvinylpyrrolidone were dissolved in 40 mL. After a dropwise addition of 2.5 mL of 0.2 M NaOH aqueous solution, the mixture was stirred for 5 min. Then, 2.5 mL of 0.1 M aqueous ascorbic acid was added dropwise, and the solution was stirred for further 5 min. The solution changed from pale yellow to light blue. The $Cu_2O$ crystals were recovered by centrifugation and washed two times with ethanol. The crystals were dried and suspended in deionized water (1 mg/mL) to be used for further experiments.

#### *5.2.1.2. Cu-MOF Synthesis*

The Cu-based MOF (Cu-MOF) was synthesised using the solvothermal synthesis method based on a similar reported structure, modified to simplify the synthesis procedure of Cu-BDC MOFs [201]. In a typical synthesis, 3.6 mmol $CuCl.2H_2O$ were dissolved in 12 ml deionized water and mixed with 2.0 mmol of $H_2BDC$ dissolved in 12ml dimethylformamide (DMF). The solution was filled in a 40 ml Teflon liner, placed in an autoclave, and heated to 393 K for 12h. After leaving the autoclave cooling down at room temperature, the solution was centrifuged 3 times and redispersed in deionised water. The product was dried in the oven for 30 min at 90 °C and stored as a powder in a glass vial for further use.

### *5.2.2. Sensor Fabrication*

Unless mentioned otherwise, the sensitive electrode was fabricated on the top of the glassy-carbon electrode (GCE). For this, 5 µL of the $Cu_2O$ aqueous solution (1 mg/mL) or Cu-BDC (1 mg/mL) was drop casted on the GCE and dried at 80 °C for 5 min. In some experiments, the Cu-BDC was further modified with Nafion. 5% w/v of the Cu-BDC was mixed with 0.5% v/v Nafion in deionized water to increase its adherence to the GCE. 5 µL of the mixture was drop casted on a glassy carbon electrode (GCE) with CV and DPV studies subsequently performed.

Screen printing was used to fabricate the carbon electrodes on a flexible polyvinyl chloride (PVC) substrate. A 20 mm by 3 mm strip was used as the WE for the CV and DPV measurements. The carbon SPEs (C-SPEs) were screen printed using the same conductive carbon paste (SunChemical, 21 Ω/sq at 25 µm thickness) employed at Chapter 3. After printing, the pattern was dried at 80°C for 20 min. The Cu-BDC/Nafion solution was directly drop casted on top of the WE and dried at 80 °C for 30 minutes. A paste using the Cu-BDC was also tested. For that, the Cu-BDC powder was mixed with ethyl cellulose (40 wt.%, Sigma Aldrich) binder and terpineol (Sigma Aldrich) solvent using an agate mortar. The paste was then added to the top of the WE and dried at 80 °C for 30 minutes. In The last step, Cu wires were attached on the contact pads using the same carbon paste and a polyurethane layer was cured on the electrodes at 80 °C for 30 minutes.

### *5.2.3. Material Characterization*

The structural characterization of the sensitive electrode was carried out with an X-Ray diffractometer (XRD, P'Analytical X'Pert with Cu Kα ($\lambda$ = 1.541 Å)). The morphological characterization and the atomic composition of the electrodes alongside the energy-dispersive X-ray

spectroscopy (EDS, Oxford Instruments Energy 250) mapping were performed using a scanning electron microscope (SEM, Philips/FEI XL30 ESEM at 20 kV). The SEM images were analysed using the ImageJ software. For the $Cu_2O$ nanoclusters SEM images, a printed electrode was used. The WE electrode layer was hand printed on top of a cellulose substrate using a graphene-carbon paste (JESC-7771G, JE Solutions Consultancy, UK) and heat treated at 80 °C for 1 h in the oven. Then, 20 µL of the $Cu_2O$ was drop casted on top of a printed electrode and dried at 80 °C for a few minutes.

### *5.2.4. Electrochemical Characterisation*

For the electrochemical measurements all reagents were used as received and all solutions were prepared in deionized (DI) water unless otherwise mentioned. The CV, DPV, and EIS analyses of the sensors were carried out using a Gamry potentiostat (Interface 1010E) or the Metrohm Autolab (PGSTAT302N). A three-electrode system, with a commercial glass Ag/AgCl RE, a platinum counter electrode (Pt CE), and a standard GCE, was employed in the initial material studies. The Cu-based solutions were drop casted on top of the GCE and dried at 80 °C for a few minutes. The experiments were performed under normal ambient conditions. To increase its sensitivity, the Cu materials were cycled 15 times in 0.1 M sodium hydroxide (NaOH) from 0.0 to +0.8 V before each experiment [176]. For the $Cu_2O$ nanocluster, the CV and DPV electrochemical measurements were carried out in 0.1 M carbonate buffer (pH 10) aqueous solution with a $NH_4Cl$ concentration varying from 10–3000 µM.

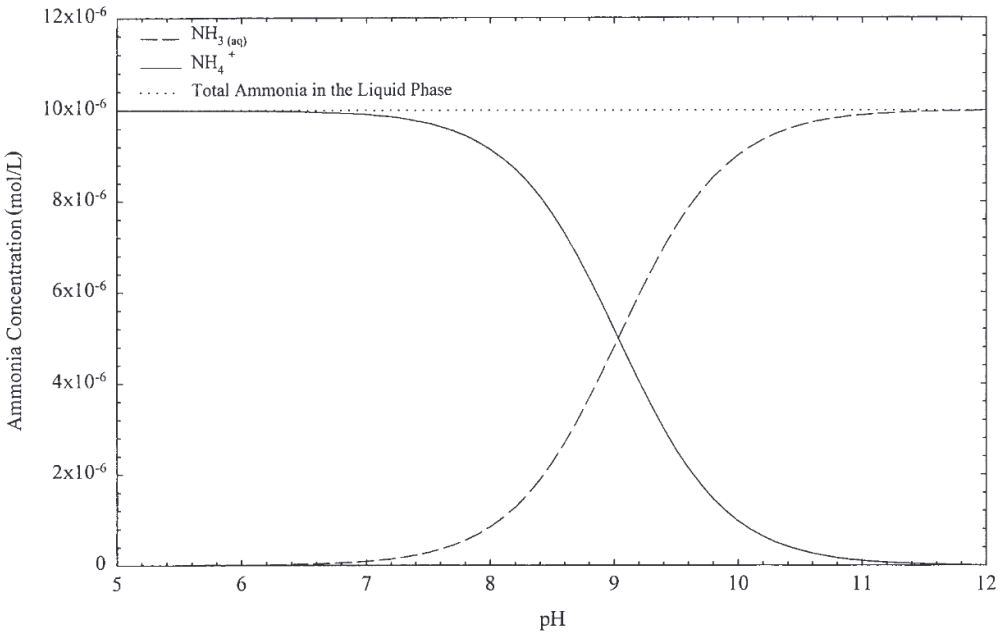


Figure 5.2. Concentration of ammonia species according to pH [202].

For the Cu-MOF, the material was characterised for ammonia sensing using 28-30% ammonium hydroxide solution ($NH_4OH$) in different solutions. For the pH study, 2 mM of $NH_4OH$ was adjusted to pH 5 to 10 using concentrated sodium hydroxide (NaOH) and hydrochloric acid (HCl) solutions. As the available dissolved $NH_3$ percentage changes with pH Figure 5.2, another pH measurement was conducted. To have the same 2mM concentration of dissolved $NH_3$ from pH 7 to 10, different final $NH_4OH$ concentrations were used. The final pH was adjusted using concentrated $NH_4OH$ and HCl solutions. The lower the pH, the higher the needed concentration of $NH_4OH$ for the same dissolved $NH_3$ concentration. The calculations were done using the table in Chapter 1 [10]. The studies on buffer solutions were conducted using phosphate-buffered saline (PBS) pH 7.5 (Sigma Aldrich) and boric acid/sodium hydroxide/hydrogen chloride buffer pH 8 (Centipur Sigma Aldrich). For the sensor performance, the CV and DPV electrochemical measurements were carried out in 0.1 M potassium hydroxide aqueous solution with a $NH_4OH$ concentration varying from 1–2000 µM. The same experiment was repeated by drop casting a 0.5% v/v Nafion membrane (Sigma Aldrich) on top of the Cu-MOF/GCE to improve the material performance. Finally, a set of experiments using the screen printed WE was performed, one using the Cu-MOF paste and one using drop casted Cu-MOF solution with a 0.5% v/v Nafion membrane on top. The CV and DPV electrochemical measurements were carried out in 0.1 M potassium hydroxide aqueous solution with a $NH_4OH$ concentration varying from 100–10000 µM.

## 5.3. Results and Discussion

### *5.3.1. $Cu_2O$ Nanocluster Characterisation*

The XRD spectra for the synthesised and simulated $Cu_2O$ nanoclusters are presented in Figure 5.3. The XRD spectra of the $Cu_2O$ synthesized powder was compared to the simulated $Cu_2O$ spectrum (COD #96-100-0064). The powder $Cu_2O$ peaks matched the simulated cuprite data, indicating a successful synthesis. The morphological structure of the $Cu_2O$ nanoclusters drop casted on the carbon printed electrode can be seen in Figure 5.4. The $Cu_2O$ nanomaterial appears to form clusters on top of the graphene-paste electrode. These clusters are a few micrometres in size and closely dispersed Figure 5.4b. The EDS spectrum (Figure 5.4c) showed the presence of Cl, C, O, and Cu on the drop casted site. This could indicate that not all $CuCl_2$ was washed and remained in the final suspension. Furthermore, both Cu and O are present, with oxygen sites exposed to the surface. This facilitates the formation of hydroxyl groups and the CuOOH configuration, responsible for the catalytic properties of cuprite [198]. The ability of coper to form cupric complexes with ammonia can be explored in

electrochemical sensors. Various copper ammonia complexes can be formed at several redox steps depending on the potential applied, such as the reversible complexes formed in Equations 5.2 and 5.3 [203].

$$Cu^0 + 2\,NH_3 \leftrightarrow Cu(NH_3)_2^{2+} + 2\,e^{-1} \tag{5.2}$$

$$Cu(NH_3)_4^{2+} + 1\,e^{-1} \leftrightarrow Cu(NH_3)_2^{+} + 2\,NH_3 \tag{5.3}$$

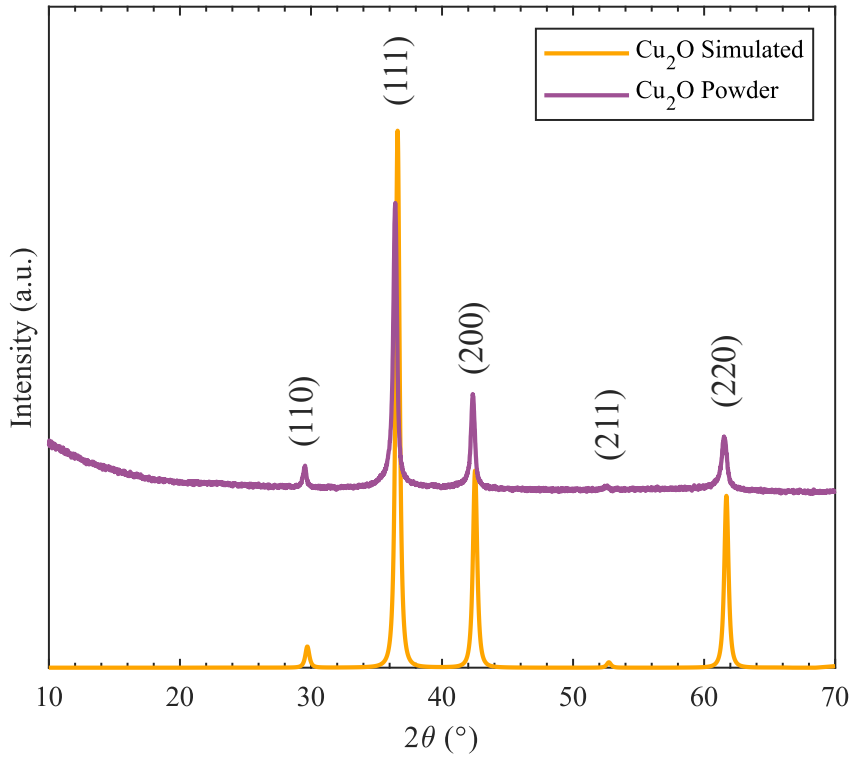


Figure 5.3. XRD spectrum of simulated $Cu_2O$ and synthesized powder $Cu_2O$ nanocluster.

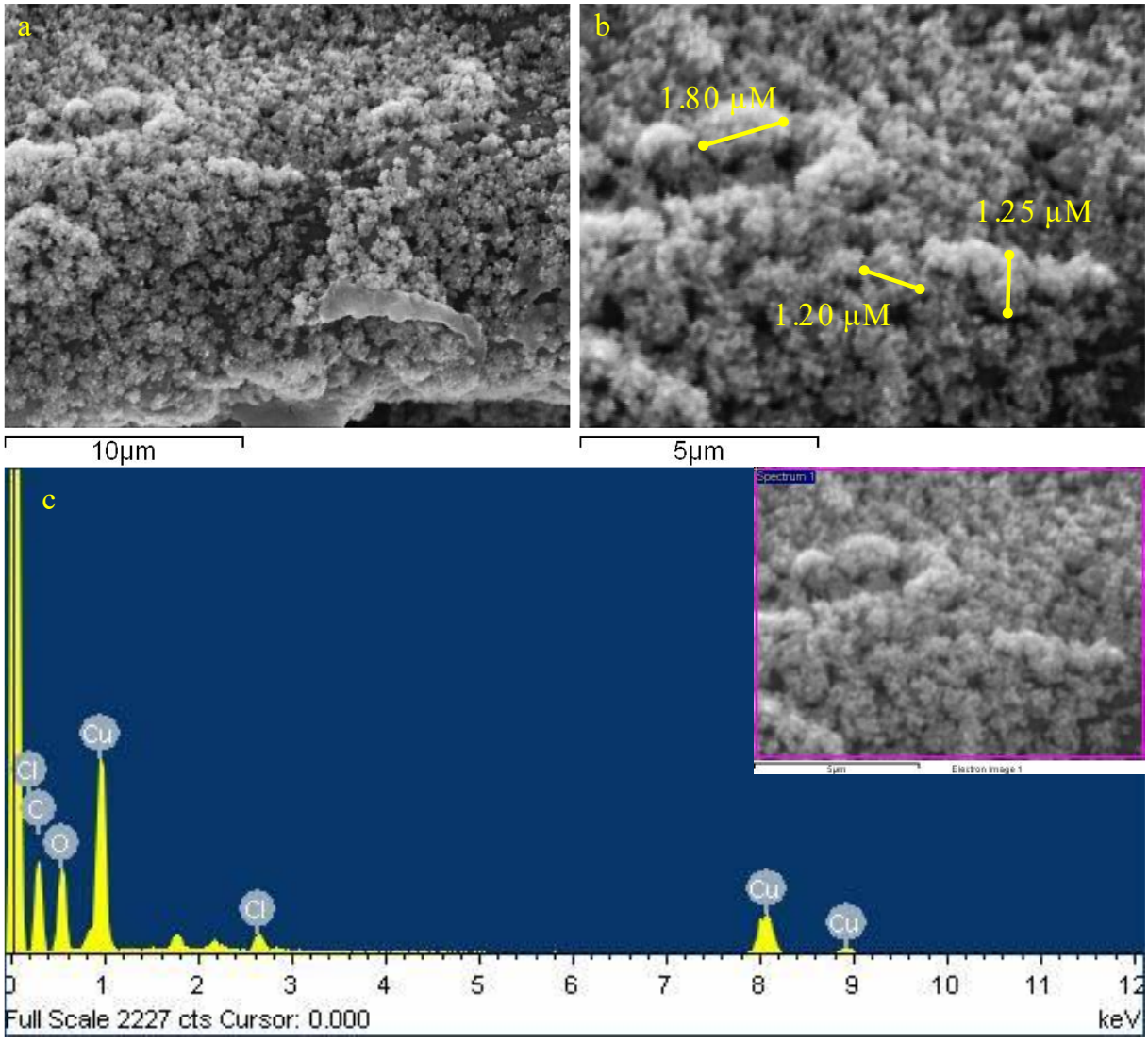


Figure 5.4. SEM images of the $Cu_2O$ drop casted on the carbon paste: a) at. c) EDS spectrum of the $Cu_2O$ drop casted on the carbon paste with the SEM image inset.

To analyse the $Cu_2O$ nanocluster performance on dissolved $NH_3$ detection, an experiment based on a previous work by Valentini *et al.* was carried out [176]. In Valentini *et al.* work's, a Cu/carbon nanotube composite paste electrode was fabricated. In this work, the $Cu_2O$ nanocluster was drop casted directly on the GCE and analysed with CV and DPV on 0.1 M carbonate buffer solution pH 10 (Figure 5.5). The pH 10 carbonate solution was chosen as there is a higher availability of dissolved $NH_3$ in solution for the Cu-$NH_3$ complex to form, as at lower pH the amount of dissolved $NH_3$ is much lower (Figure 5.2). The electrochemical response of the $Cu_2O$ nanocluster to increasing concentrations of $NH_4Cl$ is given Figure 5.5. The CV (Figure 5.5a) shows the most prominent redox reactions occur from -1 to -0.5 V, -0.5 to +0.2 V, and +1.0 to +1.25V, which correlate to the copper oxidation processes or the formation of cupric-ammonia complexes. From the DPV (Figure 5.5b), the

-0.5 to +0.2 V and +1.0 to +1.25V reactions correspond to faradaic processes. Although there seemed to be a response to increasing concentrations of $NH_4Cl$ in both cases, the redox peak signals were decreasing instead of increasing. This is the opposite trend observed in the experiment conducted by Valentini *et al.* (Figure 5.5c) [176].

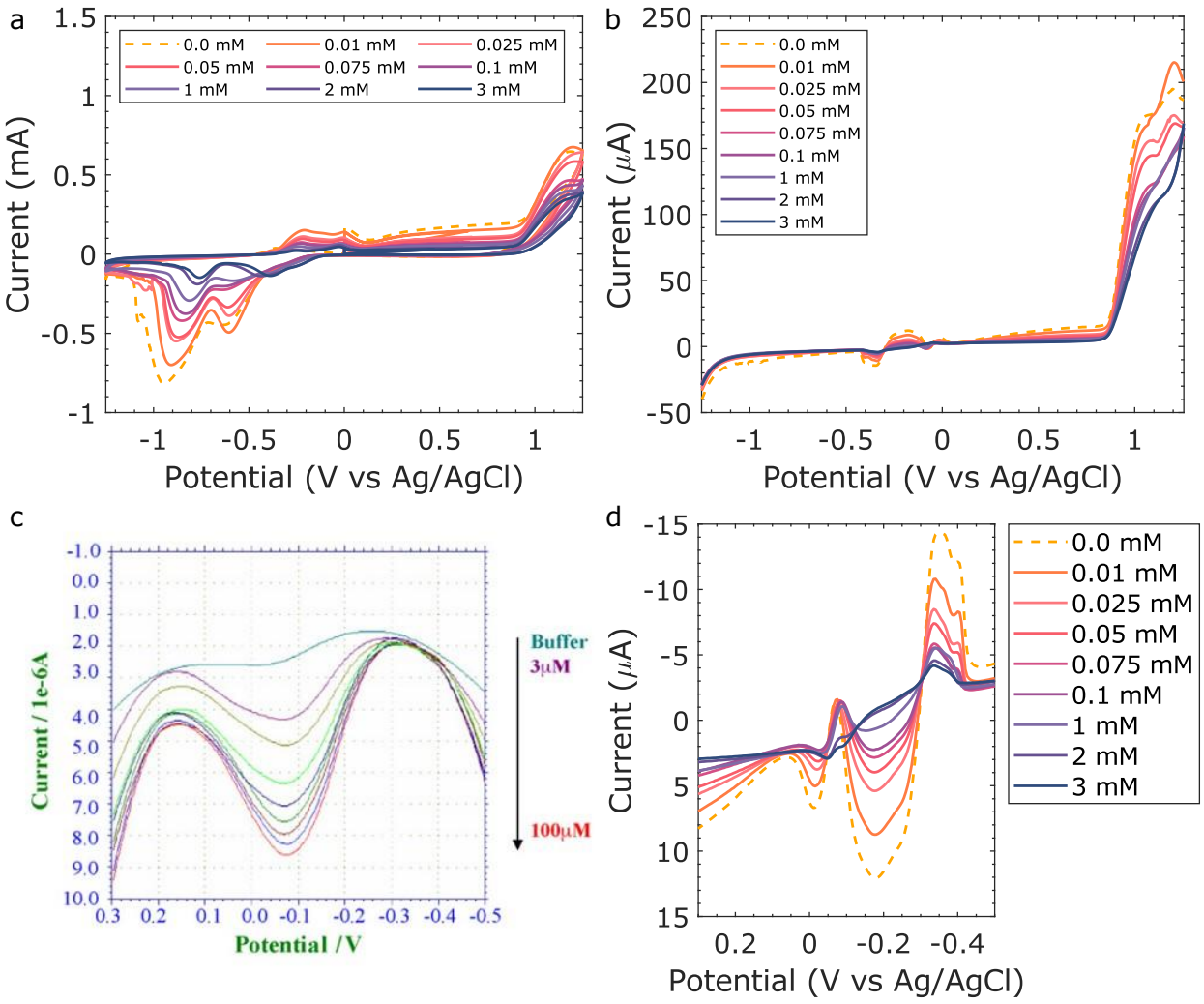


Figure 5.5. (a) CV and (b) DPV of the $Cu_2O$ nanoclusters on GCE with varying $NH_4Cl$ concentrations (0.01 - 3 mM) in 0.1 M carbonate buffer pH 10. DPV comparison of varying $NH_4Cl$ concentrations in 0.1 M carbonate buffer pH 10 for a) the experiment conducted by Valentini *et al.* [176] and b) this work.

This decrease in signal could be due to the degradation of the $Cu_2O$ material over each cycle, as there was no carbon composite to protect the $Cu_2O$ nanocluster. In the same potential range, this work also presented more redox peaks. Once more, this is probably due to the lack of protection and enhanced conductivity properties the carbon nanotube network can offer, changing the electrochemical results obtained. Although the results were not as expected, the $Cu_2O$ did seem to

interact with $NH_3$, however further changes in the synthesis and material preparation are necessary. To protect the Cu site from degradation while maintaining its catalytic properties, a Cu-BDC MOF was synthesised and tested for $NH_3$ sensing. This possible decrease in degradation derives from the porous structure of the Cu-BDC MOF, where the organic ligands can act as a protective shell, shielding the copper node from environmental factors that could cause degradation. Additionally, the porous nature of MOFs allows for selective diffusion of small molecules, which can be used to control the reactivity and stability of the metal node [204].

### *5.3.2. Cu-BDC Characterisation*

A solvothermal synthesis approach was used for the Cu-BDC MOF fabrication, making it feasible to scale up and to have better control of the parameters. The $H_2BDC$ linker can be dissolved in DMF, which participated in the final MOF molecule. The Cu ion is coordinated to two BDC linkers and one DMF molecule [205]. Upon thermal activation, the Cu-BDC MOF loses the reversibly coordinated DMF molecule, leading to an open site for catalysis [206]. The ability of these Cu-BDC MOFs to form 2D structures with square channels can facilitate the diffusion of molecules to the catalyst site [199]. To compare the morphology of the synthesised Cu-BDC with the ones in literature, a XRD was performed (Figure 5.6). The synthesised Cu-BDC did not present the same peaks as the simulated Cu-BDC MOF structure. Without the formation of visible crystals, it is difficult to further explore the atomic structure of the synthesised material, e.g., by single-ray XRD. The differences from the reported Cu-BDC structures to the one synthesised in this thesis could arise from the difference source of Cu used to start the nucleation. For example, $Cu(NO_3)_2$ is commonly employed as the Cu source for the Cu-BDC MOF synthesis, leading to homogeneously distributed sites [206]. For the solvothermal synthesis, a copper chloride salt was used instead, which could have interfered with the final crystal structure. In literature, $Cu_2O$ nanocubes have been used to fabricate nanoparticle shaped Cu-BDC MOF instead of the usual sheet formation [206].

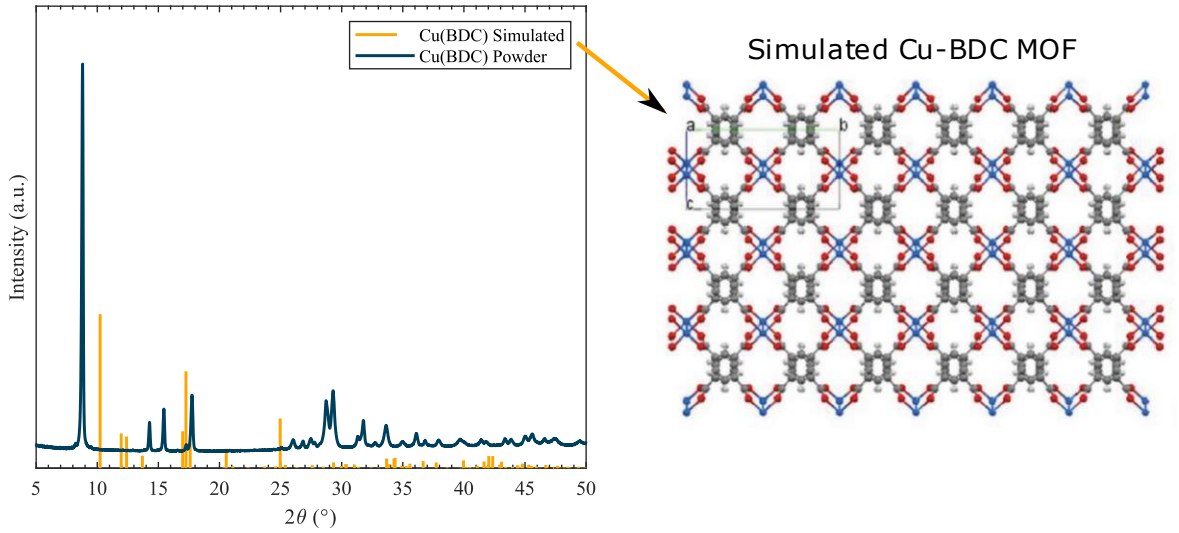


Figure 5.6 XRD from the synthesized powder Cu-BDC MOF and the simulated Cu-BDC MOF. The arrow points to the crystallographic structure of the simulated 2D Cu-BDC MOF without guest molecules (CCDC-687690) [206]. The atoms are C = grey, O = red, H = white, Cu = blue.

Testing the ammonia sensor at different pH is important because the ionization of ammonia changes with pH. The sensitivity and selectivity of the Cu-based $NH_3$ sensor varies depending on the predominant form of ammonia present in the sample solution, therefore it is important to vary the pH to better understand the sensor response. For that, various solutions of hydrochloric acid (HCl) and sodium hydroxide (NaOH) with 2 mM of $NH_4OH$/dissolved $NH_3$ were prepared and the pH was adjusted accordingly. The CV and DPV studies can be observed in Figure 5.7. For the 2 mM $NH_4OH$ pH study, where 2 mM of $NH_4OH$ was adjusted to pH 5 to 10 using concentrated sodium hydroxide (NaOH) and hydrochloric acid (HCl) solutions, the material seems to respond to ammonia only from pH 8 (Figure 5.7a and c), indicating that the Cu-MOF does not interact with the $NH_4^+$ ion since there is less dissolved $NH_3$ at lower pH. Figure 5.2 exemplifies the dependency of ammonia species with pH, while Chapter 1 covers the equations used to calculate the correlation. At 20 ℃ (the temperature used for the experiments here) and pH 7, 0.396% is dissolved $NH_3$, while at pH 8, 9, and 10 it is 3.82%, 28.4%, and 79.9% (Chapter 1, Table 1.2) [10]. At pH 5 and 6, close to 100% of the ammonia dissociates in to $NH_4^+$. The copper-ammonia complexation occurs at various potential steps and is pH dependant. It has been shown that at pH 4, copper is present mostly at its aqueous form, while from pH 6 it starts to react with amines [203]. Most of the studies on copper-ammonia complexes focus on negative potentials up to + 0.5 V. However, in this study, the potential was analysed up to + 1.2 V as the copper is coordinated in a MOF, which can change the electrochemical characteristics of the

material. In Figure 5.7c, from pH 8, the oxidation peak at +1.0 V greatly increased, while the peaks from – 0.5 to + 0.5 V varied.

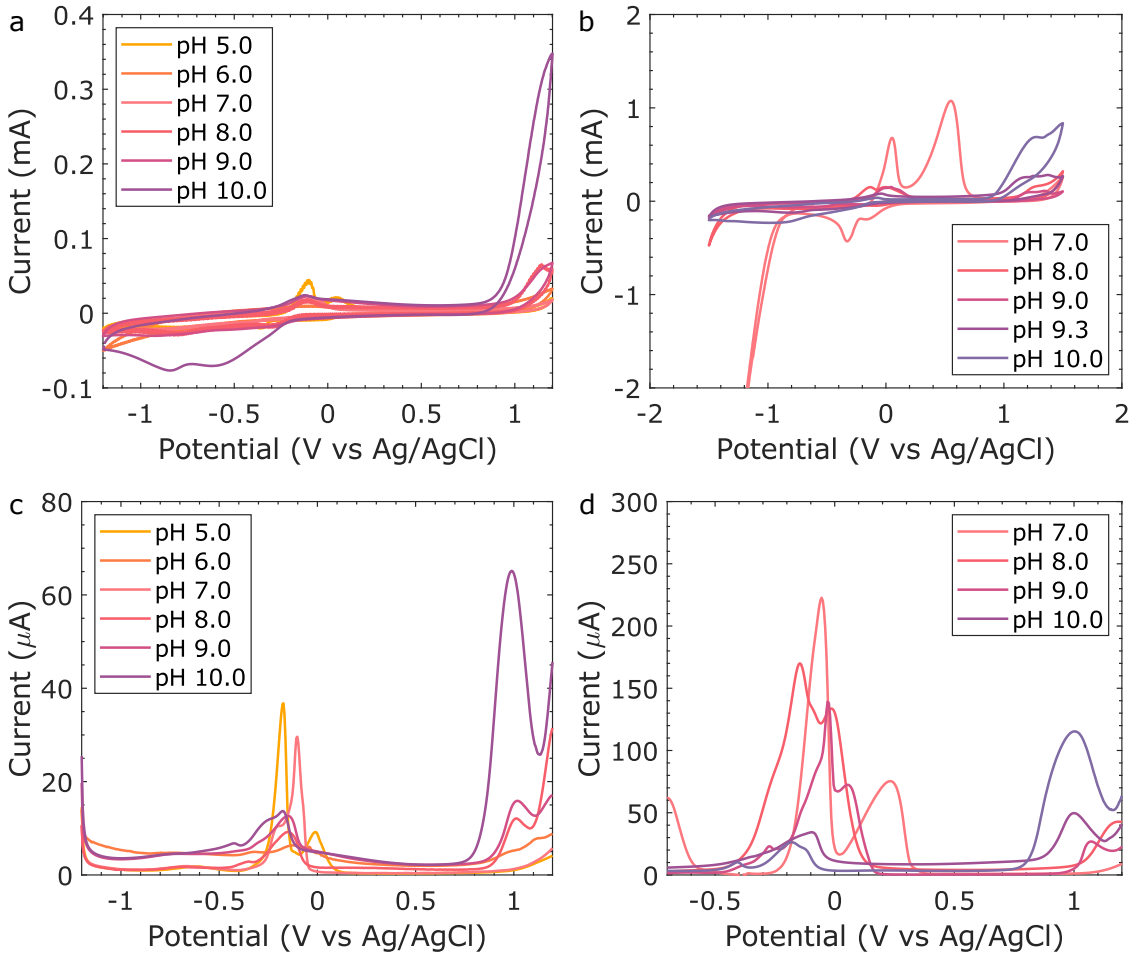


Figure 5.7. a) CV and b) DPV of 2 mM $NH_4OH$ in pH 5 to 10. a) CV and b) DPV of 2 mM dissolved $NH_3$ (varying concentration of $NH_4OH$ depending on the pH) in pH 7 to 10.

To further investigate if the material interacted with dissolved $NH_3$, the same concentration of dissolved $NH_3$ was adjusted to different pH. This involved adding a higher overall concentration of $NH_4OH$ at lower pH. Since almost all the ammonia is present in its $NH_4^+$ form at pH lower than 7, the experiment was conducted from pH 7 to 10. Figure 5.7b,d shows the same trend seen in Figure 5.7a,c, where the oxidation peak at +1.0 V increased at higher pH. However, the peaks were not the same intensity for different pH, indicating that either the Cu-BDC is activated only at higher pH or that the ammonia is reacting with other components at the solution at lower pH, such as $Cl^-$ ions. The next step consisted of exploring if the material interacted with different concentrations of ammonia at lower pH to access its performance at pH ranges closer to those found in natural water bodies. For

that, two buffer solutions were employed, using a PBS pH 7.5 buffer solution and a pH 8 buffer solution (Figure 5.8). A clear difference can be seen when comparing the redox current obtained at buffer pH 8 (Figure 5.8b) to the one obtained at pH 7.5 (Figure 5.8a). At pH 8, the oxidation peak at +1.0 V increases with the addition of $NH_4OH$ while at pH 7.5, there is minimal change in peaks.

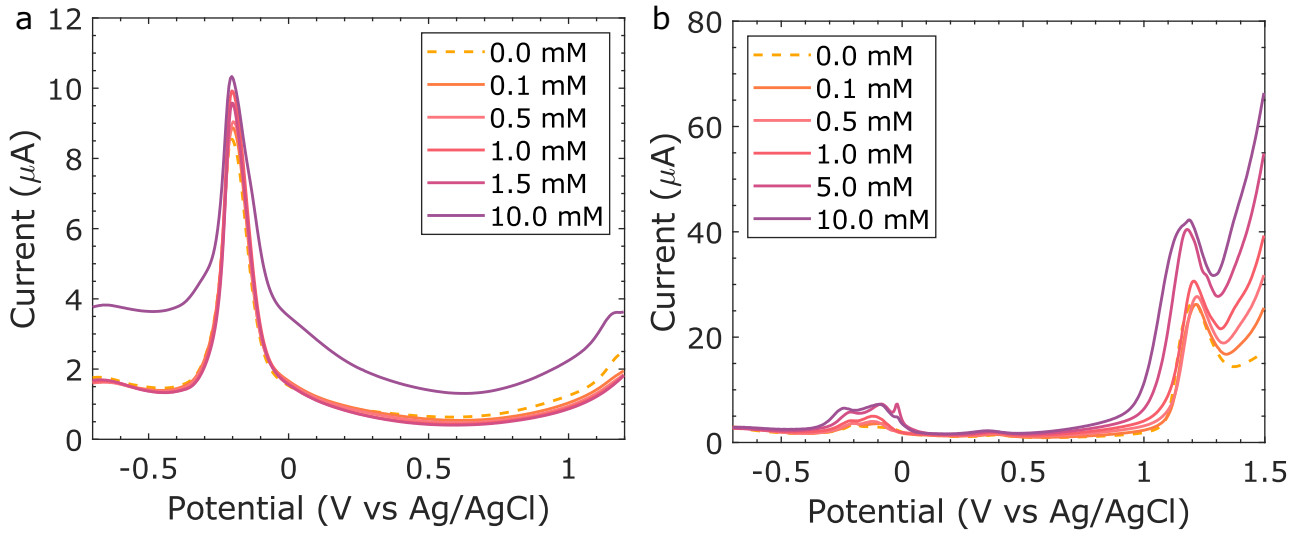


Figure 5.8. DPV with varying concentrations of $NH_4OH$ (0.1 to 10 mM) in a) 0.1 M PBS 7.5, b) pH 8 buffer.

As the Cu-BDC material exhibited better performance at higher pH, the next studies were performed at 0.1 M KOH pH > 13. In this manner, all $NH_4OH$ would be in the form of dissolved $NH_3$. The DPV of the Cu-BDC at varying concentrations of $NH_4OH$ can be seen in Figure 5.9. The first run of the Cu-BDC showed a good performance toward increasing concentrations of $NH_4OH$, in particular the current peak at +1.0 V. However, a second run to test the stability of the Cu-BDC demonstrated that the material was showing signs of degradation. To try to improve the Cu-BDC stability, a Nafion membrane was drop casted on top of the Cu-BDC/GCE. Nafion is a cationic exchange polymer with high stability that can prevent anionic molecules from interfering with the sensing material [207]. Moreover, the Nafion sulfonic acid functional group has been used to enhance poly (vinylidene fluoride-co-hexafluoropropene) membranes for ammonia adsorption and recovery due to its acidic nature [208]. Although the DPV (Figure 5.9c) current was overall lower than the ones without the Nafion membrane and less sensitive, the material seemed more stable. The sudden peak increase at very low concentrations was not present with the Nafion membrane. Lastly, the Cu-BDC was tested on a screen-printed carbon WE (Figure 5.10) to simulate the sensing material performance in a configuration closer to the final product. The Cu-BDC/Nafion WE (Figure 5.10a)

showed a worse performance than the Cu-BDC paste (Figure 5.10b). The Cu-BDC/Nafion WE seemed to oxidate after a few minutes in 0.1 M KOH solution, changing from the normal blue colour the Cu-BDC powder presents to a black colour. Although the peak definition is not optimal on the paste Cu-BDC WE, it was more stable and presented a much higher oxidation current. To improve the peak definition and current response, other electrodes can be modified with the Cu-BDC material, such as the LIGs presented in Chapter 4.

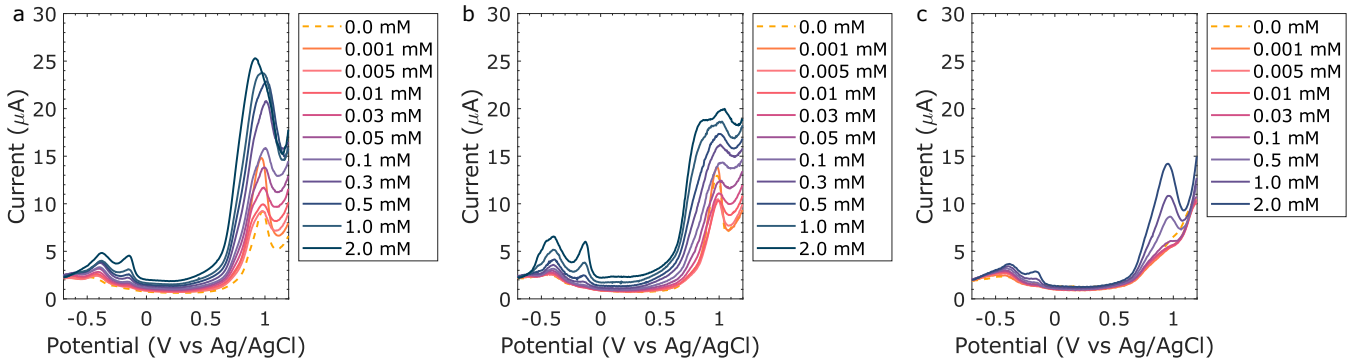


Figure 5.9. DPV of varying $NH_4OH$ concentrations (0.0.1 - 2 mM) in 0.1 M KOH of: a), Cu-BDC on its first use b) Cu-BDC on its second use, c) Cu-BDC with 0.5% Nafion.

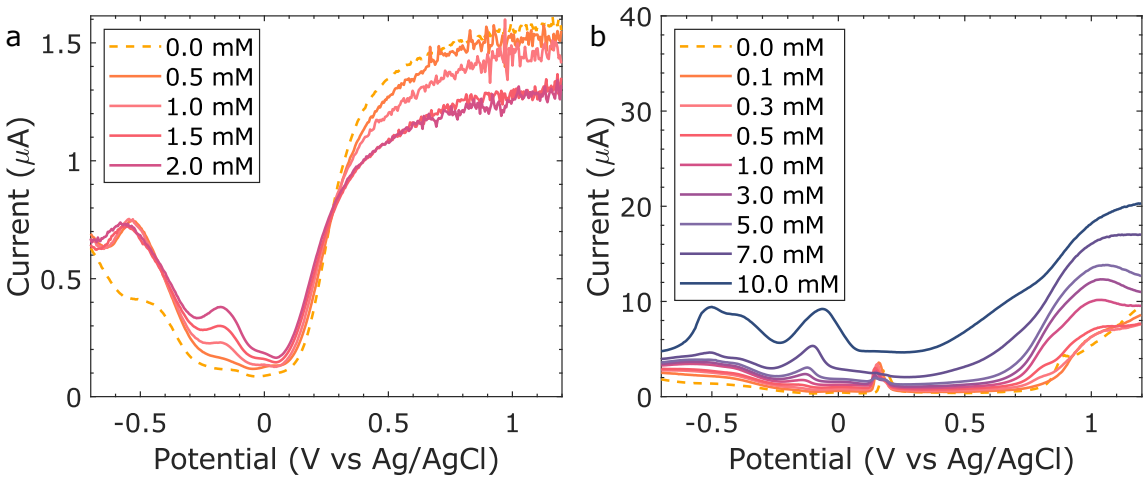


Figure 5.10. DPV of printed carbon WE with: a) Cu-BDC + 0.5% Nafion, b) Cu-BDC paste with terpineol and ethyl cellulose.

## 5.4. Conclusion

The synthesis and characterization of copper materials for ammonia sensing was investigated. The $Cu_2O$ nanocluster did not show the expected response, indicating that the copper material without any further modifications might not be suitable in this instance. Therefore, a new material was synthesised to make a more robust copper complex. In order to facilitate the synthesis for scaling up and to have better control of the parameters, a solvothermal synthesis procedure was modified to recreate the 2D Cu-BDC MOF. However, the XRD result showed that the synthesised material was not the expected 2D Cu-BDC MOF, showing peaks at different angles than the simulated structure. Preliminary studies showed that the Cu-BDC material is sensitive to dissolved $NH_3$ at basic pH, however further experiments are needed to understand its capability. The material response presents a clear correlation with the concentration of dissolved $NH_3$ but a better understanding of the copper-ammonia complexes being formed could improve the sensitivity and robustness of the system.

The reversibility of the Cu-BDC also needs to be studied to understand if the redox reaction changes the material's properties. For this, the material's morphology should be further explored using XRD before and after the measurements, combined with ion chromatography or inductively coupled plasma technique to understand if there is copper leaching into the solution. Overall, considering the aim of applying this sensor for water quality monitoring, copper-based materials could be employed for continuous dissolved $NH_3$ detection if a basic pH buffer is added to the device. Considering the reaction needs a higher pH than what is normally encountered in rivers and other natural water bodies, the use of a microfluidics or disposable buffer cartridges could be used to overcome the pH barrier. Furthermore, it could be a substitute for colorimetric approaches as it requires minimal sample preparation. For that, further studies would be necessary, specifically on how other chemical species present in water react with the Cu-BDC material.

# Chapter 6

# General Conclusion

## 6.1. Main Findings

The aim of this thesis was to develop affordable, convenient water quality monitoring sensors, focusing on the detection of $NO_2^-$ and dissolved $NH_3/NH_4^+$ ions. In this regard, this was accomplished in two concurrent steps:

*i)* *Studies on the materials used in the electrode track and their behaviours in different aqueous media.*

a. SPEs with Ag paste tracks can react to substances present in the solution, altering the electrochemical results (Chapter 1).
b. The Ag paste easily reacted with the salts present in the artificial seawater solution while the carbon-based electrodes were mostly inert (Chapter 2).
c. Carbon-based SPEs are generally not as conductive as Ag-based SPEs, impacting the oxidation current in electrochemical techniques (Chapter 2).
d. A more sustainable G-PE on PHB/PHV substrate was developed, however it did not present a discernible oxidation peak for $NO_2^-$ (Chapter 2).
e. LIGs are a good alternative for carbon-based SPEs, as they presented a much higher $NO_2^-$ oxidation current (Chapter 3).

*ii)* *Development of printed sensors for $NO_2^-$ and dissolved $NH_3/NH_4^+$ ions.*

a. The ZnO paste did not seem to react with the $NH_4^+$ ions as expected (Chapter 2). The ZnO Ag-IDE did not react to the addition of $NH_4OH$, while the ZnO Ag-IDE and bare Ag-IDE reacted to the addition of $(NH_4)_2SO_4$.
b. The GOx drop casted on the C-SPE and the G-PE (Chapter 3) and the GS-SPE (Chapter 4) did not provide a good $NO_2^-$ oxidation current response. The bare LIGs showed the most promising results, with an increase in oxidation current > 500% (Chapter 4).

c. Cu-based sensors were developed for dissolved $NH_3$ sensing (Chapter 5). The Cu-BDC seems to react with dissolved $NH_3$ only at highly basic pH, outside of the pH range found in natural water bodies.

These investigations were connected throughout the chapters presented in this thesis, and the main findings and limitations are detailed below.

### *6.1.1. Material Investigation for the Electrode Track*

Since one of the main objectives was to develop cost-effective, high-performance sensors, SPEs were the straightforward choice to form the backbone of the electrodes. Screen printing is a well-developed field, with some of the key aspects being ease of fabrication, making it possible to fabricate large numbers of electrodes in a short amount of time for a low-cost [107,115]. To achieve this, the materials used for SPEs play a crucial role in determining the properties and performance of the sensors. The most common materials used for SPEs are conductive inks, such as graphite, carbon black, and metal particles, which are screen printed onto a substrate to form the electrode [107,120]. The choice of material depends on the application and the desired electrical and mechanical properties. For example, graphite is often used for its stability, while metal particles are favoured for their high conductivity [91]. Therefore, in Chapter 2 of the thesis, an IDE SPE with Ag paste tracks and a ZnO sensing layer was fabricated to detect $NH_4^+$. ZnO was selected as the sensitive material because of its previous use in detecting ammonia ($NH_4^+$) in literature while the Ag tracks are commonly used in IDEs due to the high conductivity [8,78]. At first, from CV and DPV results, it seemed the ZnO layer was catalysing the $NH_4OH$ analyte, however further investigation revealed that the oxidation peaks were likely due to the formation of $Ag_2SO_4$ from the Ag in the IDE and not the nitrification of $NH_4^+$. This highlights the importance of correctly choosing the electrode material to avoid interaction with the analyte and solution. Overall, in this chapter, the effect that the materials used in printed sensors can produce on the electrochemical measurements was introduced, and this was further investigated throughout the thesis.

Considering the impact the Ag paste had on the electrochemical results in Chapter 2, a more in-depth study of the electrochemical stability of the Ag paste was studied in Chapter 3, as well as investigating carbon-based SPEs as alternative materials. In this chapter, a 3-electrode system was employed instead of the IDE, as it is the standard system used in electrochemical measurements, allowing for more accurate results. Two standard SPEs fabricated using commercial silver and carbon pastes (Ag-SPEs and C-SPEs) printed on a PVC substrate were used for the tap water and seawater

monitoring studies, along with a new sustainable graphite-based paste (G-PE) printed on PHB/PHV substrate. It is important to note that the Ag-SPEs did not have a protective insulation layer commonly used in commercial SPEs. This layer prevents the Ag from interacting with its surrounding, improving the lifetime of the paste. The aim of this study was to show how the bare Ag paste interacts with other analytes. The conductivity and stability of the sensors were studied under different bending and electrochemical conditions. The Ag-SPEs were highly conductive (0.053 Ω/sq) when compared to the C-SPEs (26.9 Ω/sq) and the G-PEs (30.1 Ω/sq), as expected of a metal-based paste, but they easily reacted with the salts in the solution. In particular, the Cl- seemed to strongly react with Ag, while the carbon paste remained electrochemically inert. Overall, the C-SPEs showed a higher electrochemical stability and sharp peaks for $NO_2^-$ detection, indicating it could be used as an alternative material for printed electrode tracks.

An additional aspect of the research was to investigate a more sustainable printed electrode, as the environmental impact of metals and non-degradable plastics in printed electrodes has highlighted the need of employing sustainable materials in environmental monitoring. For that, a biodegradable PHB/PHV substrate and a more sustainable graphite/PVA paste were used as eco-friendly materials for disposable electrochemical sensors for environmental or water quality monitoring. Physical and chemical degradation studies of the sustainable G-PE in seawater demonstrated relatively quick ultrasound induced dissolution (less than 5 min) while the SPEs did not dissolve even after 30 min of sonication. The use of graphite-based paste, made up of only graphite, PVA, and water, presents an environmentally friendly alternative to traditional electrodes. This material is especially beneficial in situations where disposable electrodes are required or in areas where there is a potential risk of loss. Despite these advantages, further extensive and longer-term studies are necessary to fully comprehend the environmental impact of biodegradable substrates and inks, particularly with regards to the PHA/PHB microplastic byproducts produced. Furthermore, the charge-transfer capability of G-PE was much inferior to the Ag- and C-SPEs, and it should be improved before it can replace conventional printed electrodes.

Another electrode fabrication technique was investigated in Chapter 4 as carbon-based pastes showed the potential to substitute metal pates in printed electrodes but lacked the resolution. LIGs were introduced as a substitute for carbon-based SPEs in electrochemical sensors. The investigation in Chapter 3 showed that carbon-based SPEs had better characteristics than Ag paste SPEs, but presented a higher electrical resistance that reduced the redox peak current. By using LIGs, the problem was resolved by offering the benefits of a graphene-like structure without the use of binders

or solvents. The statistical approach of DoE-RS was used to optimize the laser parameters for the fabrication of the LIGs, resulting in two final LIGs with low resistance and good substrate adherence. The SEM images and Raman spectroscopy showed that the LIGs were highly porous and had a disordered graphene structure, making them more hydrophilic and suitable for electrochemical detection in water. The LIGs demonstrated improved stability and sensitivity compared to the GS-SPE in the oxidation of $NO_2^-$ ions, revealing they can be an alternative to disposable carbon-based SPEs. However, further research is needed to evaluate the long-term surface degradation of the LIGs and their performance in different water bodies.

Overall, the main finding in the electrode track aspect was improving new technologies to compete with traditional electrode fabrication techniques while moving towards more sustainable approaches. Particularly by developing LIG electrodes that presented a higher sensitivity when compared to a commercial carbon-based SPEs alternatives. A summary of the evolution of the electrodes used in this thesis can be observed in Figure 6.1, starting with metal-based pastes and substituting them for carbon-based alternatives.

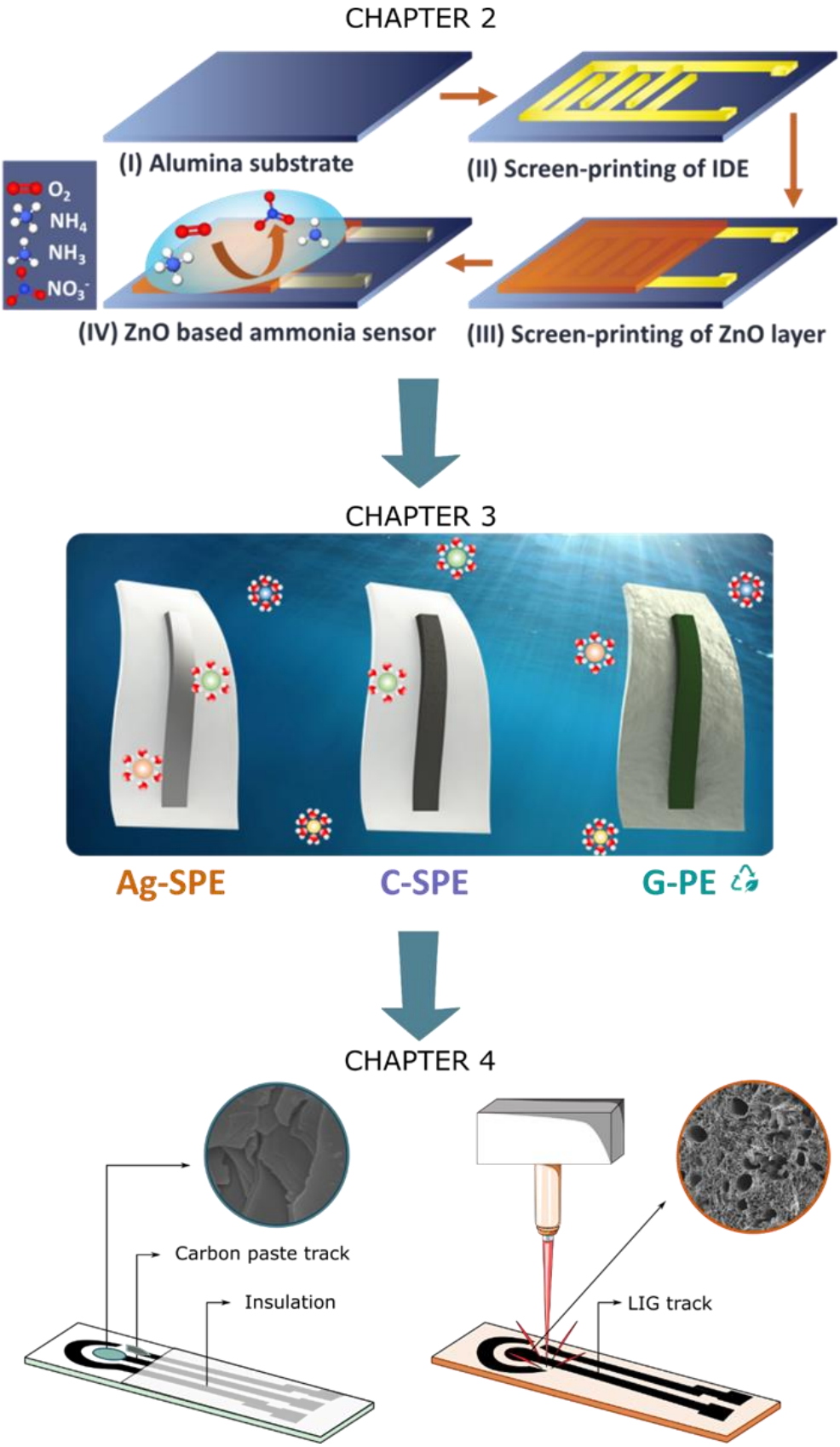


Figure 6.1. Summary of the materials used in the chapter throughout this thesis, evolving towards more sustainable approaches.

### *6.1.2. Sensor Development*

The sensing material is an important but challenging aspect of the sensor development, as it determines the majority of the sensitivity, selectivity and stability characteristics of the device. With the growing demand for portable and low-cost sensors for environmental monitoring, there is a significant push for the development of new and improved sensing materials. Ideally, they should have high conductivity, low electrical resistance, good stability, and be able to selectively detect the target analyte. Synthesising a material that has all these properties is a great challenge, but in addition to the materials themselves, the method of fabrication and the integration with the sensor platform also plays a crucial role in the performance of the sensor. Techniques such as screen-printing, inkjet printing, and laser-induced graphene (LIG) fabrication have been explored for the low-cost and scalable production of electrochemical sensors, and the feasibility of integration is determined by the choice of material employed and how they are synthesised. Therefore, in this thesis, focus was given to sensing materials that are easy to incorporate with current sensor fabrication techniques.

In Chapter 2, ZnO was investigated for $NH_4^+$ sensing. The selection of ZnO as a sensing material was motivated by its high biocompatibility and chemical stability [93,97,98]. ZnO materials have been shown to react to nanomolar amounts of $NH_4^+$ ion, causing alterations in both resistivity and current response that can be measured by electrochemical techniques [8,78]. For environmental deployment, a pH meter and a temperature sensor would need to be integrated to the system as dissolved $NH_3$ is the analyte of concern. The equations to calculate the concentration of $NH_3$ based on the concentration of $NH_4^+$, temperature, and pH can be seen in Chapter 1, Equations 1.1-1.4. The ZnO layer was annealed at a high temperature to produce rectangular nanostructures, increasing the surface area and removing other substances present in the paste. The results of the CV tests indicated the presence of a faradaic peak around +0.4 V, which was initially associated with the conversion of ammonia into nitrate. The Nyquist plot also showed a decrease in the bulk resistance upon addition of the analyte. However, after further experiments, it was possible to infer that the Ag layer was reacting to the $SO_4^-$ ions in the solution. This was tested by testing $NH_4OH$ and $(NH_4)_2SO_4$ on ZnO Ag-IDE and bare Ag-IDE, where no current response was seen when adding $NH_4OH$ but an even stronger response was seen when using the bare Ag-IDE upon the addition of $(NH_4)_2SO_4$. This led to the investigation of the use of other materials for the electrode track, which in turn was used for $NO_2^-$ sensing.

Carbon electrodes, such as graphite and carbon black, are widely used as $NO_2^-$ sensors due to their high electrical conductivity and versatility. The high surface area and good electrical conductivity of

carbon electrodes can enhance the rate of the electrochemical reaction and improve the sensitivity of the sensor [81,162]. Besides, carbon-based materials have a lower environmental impact, as they can be derived from renewable resources and are easy to recycle [91]. Considering this, GOx carbon and carbon/Ag-based electrodes were tested for 3 mM $NO_2^-$ in artificial seawater in Chapter 3. These experiments served only as a base for testing carbon-based sensors for $NO_2^-$, and in Chapter 4 that was explored more in depth. In Chapter 3, the GCE and the C-SPE presented the clearest signals for $NO_2^-$ oxidation, while the Ag-SPE combined with carbon paste presented the highest oxidation peak current. The oxidation peak in the G-PE was not distinguishable, indicating slow electron-charge transfer characteristics. In the case of the Ag-SPE, the signal was noisy, probably because the Ag part of the electrode was unprotected in artificial seawater, and as demonstrated, the Ag paste interacted strongly with the $Cl^-$ and $SO_4^-$ ions. Considering the C-SPE presented the most stable response and is more environmentally friendly than metal pastes, the next studies in Chapter 4 were compared to a commercial C-SPE.

The C-SPE used in Chapter 4 was modified with a graphene sheet to enhance the signal toward $NO_2^-$ detection (GS-SPE). For comparison, a laser engraving technique was employed to produce carbon-based electrodes. LIG is a versatile material that is produced by using a laser to ablate a polymer substrate, in this case, polyamide, resulting in the formation of a graphene-like structure. The process is simple, fast, and scalable, making it an attractive option for the fabrication of various devices, including electrochemical sensors [151,158]. LIGs present unique properties, such as high electrical conductivity, large surface area, and high thermal stability, that make it ideal for use in electrochemical sensors [154,167]. The results showed that the LIGs presented a comparable or higher performance than the GS-SPEs in every aspect tested. For example, the LIGs presented a current peak higher than 500% when compared to the GS-SPE. This was because of a combination of factors, including their higher surface area, disordered graphene structure, and more hydrophilic surface. Furthermore, the graphene-like structure of the LIGs is easy to alter depending on the laser parameters used. In this case, the laser speed, power, and focus were used to construct DOE-RS models to select LIGs with the best characteristics for $NO_2^-$ detection. The studies presented in Chapter 4, although positive, are still far from enabling the production of LIG sensors that can be readily used in environmental analysis. Further testing on sensor stability and selectivity, with possible alterations on the electrodes to make them more suitable for those uses, are still needed.

In Chapter 5, a combination of the previous chapters was used: a carbon paste WE combine with different metal oxide materials. The LIGs were not employed at this stage but would be a great

addition to future studies. As the ZnO nanostructured did not appear to interact with the $NH_4^+$ ions, a different metal oxide was tested after reviewing the literature on what materials had been employed. Copper electrodes are commonly used as dissolved $NH_3$ sensors due to their high sensitivity and selectivity towards $NH_3$ ions [176,177,187]. Dissolved $NH_3$ ions in aqueous solutions can be electrochemically oxidized at a Cu WE to form cupric complexes, which can be detected using different electrochemical techniques. An advantage of the Cu materials is that they are simple to fabricate and integrate to SPEs or other electrodes. Two different Cu materials were tested in Chapter 5, a $Cu_2O$ nanocluster and a Cu-BDC material. The results of the initial CV experiments indicated that the $Cu_2O$ nanocluster did not produce the desired current oxidation profile, suggesting that unmodified copper may not be appropriate for this application. To resolve this, a new material was synthesised to form a more reliable copper complex. To streamline the synthesis process for scaling and to ensure greater control over the parameters, a solvothermal synthesis process was modified from literature to produce the 2D Cu-BDC MOF. However, the synthesised Cu-BDC XRD did not match literature Cu-BDC MOFs XRD spectra, indicating another crystallographic profile. Nevertheless, this new Cu-BDC material presented a clear correlation to the addition of $NH_3$ but needs highly basic pH to show a response. Overall, the Cu materials studied need to be further modified to increase their robustness and detection capabilities. Composite materials could be a solution to decrease the pH needed for the cupric-ammonia complexes.

In general, the main favourable outcome of this part of the thesis was the successful fabrication of LIGs that were highly sensitive toward $NO_2^-$. Furthermore, although experimental confirmation is needed, these LIGs offer the possibility to detect other analytes by further modifying the WE with other sensing materials, providing a more sustainable and conductive backbone for future sensors. Progress was also made toward a simpler $NH_4^+/NH_3$ sensor by using different metal oxides. Although the ZnO and Cu materials did not present the desired sensitivity or stability for $NH_3$ sensing, the Cu materials showed potential for future studies in this area. In specific the Cu-BDC material, which can use different organic linkers and material combinations to produce a more stable compound with higher selectivity. A summary of the sensing materials is presented in Figure 6.2, together with a final vision of a sensor patch that could integrate $NO_2^-$ and $NH_3$ sensing, besides other analytes and parameters depending on the intended purpose.

In conclusion, electrochemical sensing is a vast field with many different fabrication techniques, analytes, and materials that need to be taken into consideration. This thesis investigated different aspects of fabricating affordable, scalable sensors for $NO_2^-$ and $NH_3$ detection but many limitations

were found in the process. Some of the limitations and future research possibilities are discussed below.

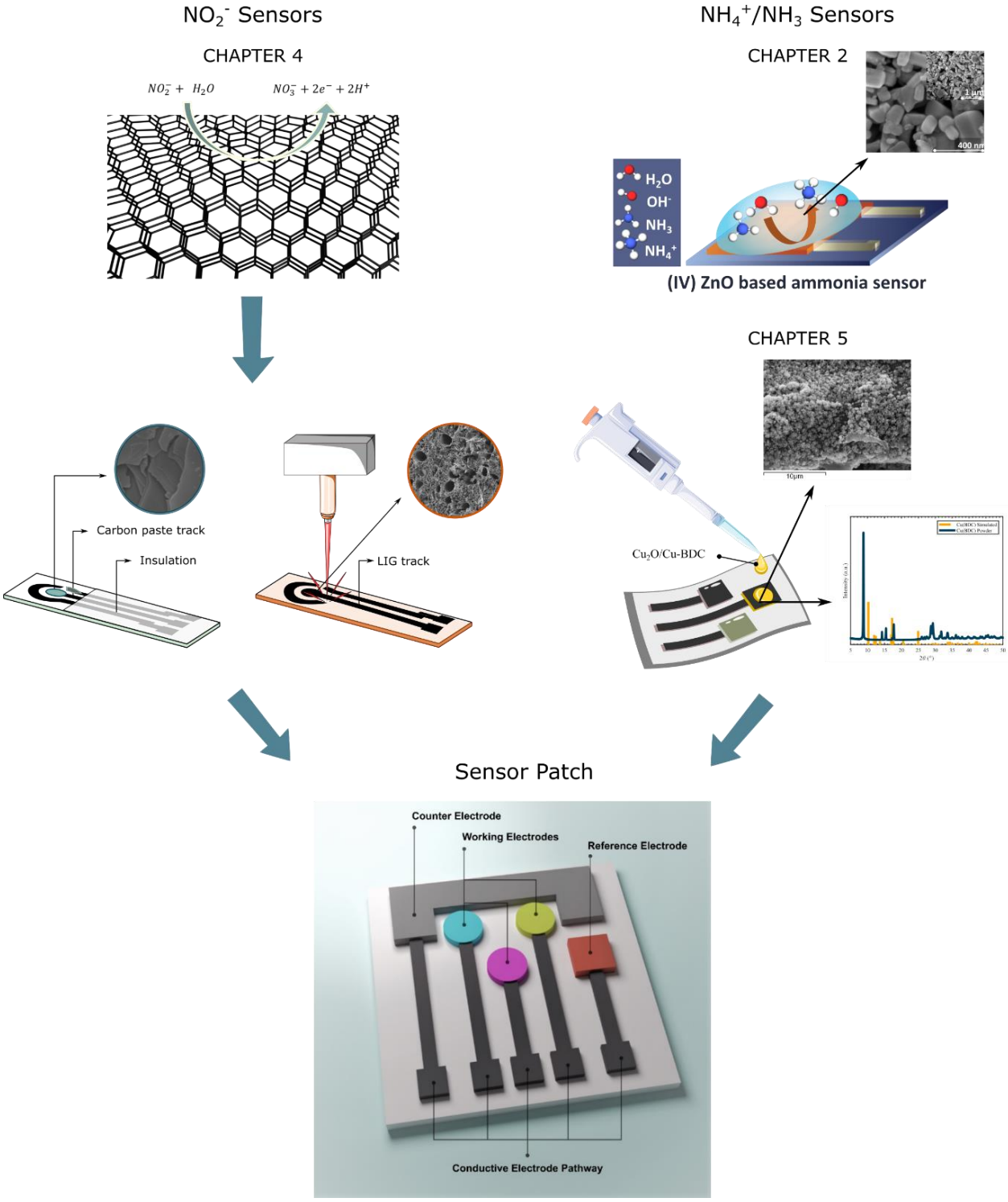


Figure 6.2. Summary of the sensing materials used in the chapter throughout this thesis, together with a vision figure of the final sensor.

## 6.2. Future Research

The research presented in this thesis can be further addressed in many directions. In the electrode track aspect, LIGs showed a superior performance when compared to C-SPEs. However, they are not as versatile as SPEs, which can have a variety of paste formulations to enhance the sensor. To overcome that, LIGs can be functionalized with various chemical groups, such as amino and carboxylic acids, to enhance its selectivity and specificity for certain analytes [154,158]. Otherwise, a combination of LIGs and screen-printing or other techniques can be used to produce a final sensor product. The sustainability aspect of printed electrodes has also been highlighted in the thesis. The use of biodegradable and sustainable materials for printed electrodes is becoming increasingly important as it minimizes the impact on the environment by reducing waste and pollution. This is particularly important for disposable monitoring devices which need to be frequently replaced. The use of biodegradable and sustainable materials such as PHB/PHV as shown in Chapter 3 provides an environmentally friendly alternative to traditional substrates such as PVC or alumina. For the LIGs to become more eco-friendly, alternative substrates should be employed. Laser engraving has been shown to work in a variety of substrates, e.g., cloth, paper, and natural biomasses such as wood, providing suitable alternatives to polyamide substrates [209]. However, the optimisation process would need to be redone for each new substrate, and there could be a trade off in conductivity and/or stability.

The sensing material aspect investigated in this thesis provided a guideline for future research. However, finding a suitable material that is selective to the desired analyte in the selected physical parameters (e.g., temperature, pH, water depth, time-frame) is very challenging. The accurate detection of dissolved $NH_3$ is particularly challenging because it depends on the pH and temperature of the solution, while $NO_2^-$ is an unstable substance and requires instantaneous detection techniques for more accurate results. The materials used throughout the thesis presented some limitations to the precise detection of these analytes, especially regarding the voltammetric detection of dissolved $NH_3$. Furthermore, an important aspect to note is that the sensors developed here were not deployed in the field, which would bring further challenges regarding the material stability and selectivity. Therefore, future studies could include further development of composites or polymeric materials for the selective detection of these analytes or the use of a variety of materials integrated with artificial intelligence (AI). This technique has been increasingly combined with electrochemical sensors to improve their performance and accuracy. AI algorithms such as machine learning and deep learning can be used to analyse and interpret sensor data, leading to more robust and reliable sensor readings

[210]. For example, it can be used to compensate for drift and other sources of error in electrochemical sensors, enabling them to maintain high levels of accuracy over time. Additionally, AI algorithms can be used to optimize sensor parameters, such as sensitivity and selectivity, and to classify different types of electrochemical signals. In this manner, a combination of different materials that suffer interference from different substances could be employed together to monitor one or more analytes of choice, facilitating the search of suitable materials.

# References


[1] L.Y. Stein, M.G. Klotz, The nitrogen cycle, Current Biology. 26 (2016) R94–R98. https://doi.org/https://doi.org/10.1016/j.cub.2015.12.021.

[2] B. Timmer, W. Olthuis, A. van den Berg, Ammonia sensors and their applications—a review, Sens Actuators B Chem. 107 (2005) 666–677.

[3] M. Holmer, K. Black, C.M. Duarte, N. Marbà, I. Karakassis, Aquaculture in the Ecosystem, Springer Science & Business Media, 2007.

[4] T. Li, J. Panther, Y. Qiu, C. Liu, J. Huang, Y. Wu, P.K. Wong, T. An, S. Zhang, H. Zhao, Gas-permeable membrane-based conductivity probe capable of in situ real-time monitoring of ammonia in aquatic environments, Environ Sci Technol. 51 (2017) 13265–13273.

[5] U.S.E.P. Agency, Aquatic life ambient water quality criteria for ammonia - freshwater, 2013.

[6] W.H. Organization, Guidelines for drinking-water quality: Health criteria and other supporting information, 1996.

[7] R.F. Muñoz-Huerta, R.G. Guevara-Gonzalez, L.M. Contreras-Medina, I. Torres-Pacheco, J. Prado-Olivarez, R. v Ocampo-Velazquez, A review of methods for sensing the nitrogen status in plants: advantages, disadvantages and recent advances, Sensors. 13 (2013) 10823–10843.

[8] R. Ahmad, N. Tripathy, M.Y. Khan, K.S. Bhat, M. Ahn, Y.-B. Hahn, Ammonium ion detection in solution using vertically grown ZnO nanorod based field-effect transistor, RSC Adv. 6 (2016) 54836–54840.

[9] S. Körner, S.K. Das, S. Veenstra, J.E. Vermaat, The effect of pH variation at the ammonium/ammonia equilibrium in wastewater and its toxicity to Lemna gibba, Aquat Bot. 71 (2001) 71–78.

[10] K. Emerson, R.C. Russo, R.E. Lund, R. v Thurston, Aqueous ammonia equilibrium calculations: effect of pH and temperature, Journal of the Fisheries Board of Canada. 32 (1975) 2379–2383.

[11] C.E. Bower, J.P. Bidwell, Ionization of ammonia in seawater: effects of temperature, pH, and salinity, Journal of the Fisheries Board of Canada. 35 (1978) 1012–1016.

[12] A.Y.K. Ip, S.F. Chew, Ammonia production, excretion, toxicity, and defense in fish: a review, Front Physiol. 1 (2010) 134.

[13] D.M. Anderson, D.J. Garrison, The ecology and oceanography of harmful algal blooms, (1997).

[14] U.S.E.P. Agency, Ambient Water Quality Criteria for Ammonia (Saltwater), 1989.

[15] M.P. Wilkie, Ammonia excretion and urea handling by fish gills: present understanding and future research challenges, Journal of Experimental Zoology. 293 (2002) 284–301.

[16] M.P. Wilkie, C.M. Wood, The adaptations of fish to extremely alkaline environments, Comp Biochem Physiol B Biochem Mol Biol. 113 (1996) 665–673.

[17] EPA, 2018 Edition of the drinking water standards and health advisories tables, (2018).

[18] V. Walker, Ammonia toxicity and its prevention in inherited defects of the urea cycle, Diabetes Obes Metab. 11 (2009) 823–835. https://doi.org/https://doi.org/10.1111/j.1463-1326.2009.01054.x.

[19] O. Braissant, V.A. McLin, C. Cudalbu, Ammonia toxicity to the brain, J Inherit Metab Dis. 36 (2013) 595–612. https://doi.org/10.1007/s10545-012-9546-2.

[20] L. Cagnon, O. Braissant, Hyperammonemia-induced toxicity for the developing central nervous system, Brain Res Rev. 56 (2007) 183–197.

[21] G.M. Enns, Neurologic damage and neurocognitive dysfunction in urea cycle disorders, in: Semin Pediatr Neurol, Elsevier, 2008: pp. 132–139.

[22] A. Yapicioglu, I. Dincer, A review on clean ammonia as a potential fuel for power generators, Renewable and Sustainable Energy Reviews. 103 (2019) 96–108. https://doi.org/https://doi.org/10.1016/j.rser.2018.12.023.

[23] C. Verma, M.A. Quraishi, E.E. Ebenso, A Review on Ammonia Derivatives as Corrosion Inhibitors for Metals and Alloys BT - Sustainable Ammonia Production, in: Inamuddin, R. Boddula, A.M. Asiri (Eds.), Springer International Publishing, Cham, 2020: pp. 49–67. https://doi.org/10.1007/978-3-030-35106-9_3.

[24] European Comission, Council Directive 98/83/EC of 3 November 1998 on the quality of water intended for human consumption, Official Journal of the European Communities. (1998).

[25] T.W.F. Directive, The Water Framework Directive (Standards and Classification) Directions (England and Wales), 2015.

[26] J.A.T. dos Reis, A.S.F. Mendonça, Análise técnica dos novos padrões brasileiros para amônia em efluentes e corpos d'água, Engenharia Sanitária e Ambiental. 14 (2009) 353–362.

[27] Australia.N.W.Q.M. Strategy, Australian and New Zealand guidelines for fresh and marine water quality, Australian and New Zealand Environment and Conservation Council and …, 2000.

[28] C.N. do M.A. (CONAMA), Resolução CONAMA nº 357/2005, de 17 de março de 2005, Diário Oficial Da União (DOU). (2005).

[29] W.H.O. Nitrate, nitrite in drinking-water. Background document for development of WHO Guidelines for drinking-water quality, Geneva: World Health Organization (WHO/SDE/WSH/07.01/16/Rev/1). (2011).

[30] M.A.P. Mahmud, F. Ejeian, S. Azadi, M. Myers, B. Pejcic, R. Abbassi, A. Razmjou, M. Asadnia, Recent progress in sensing nitrate, nitrite, phosphate, and ammonium in aquatic environment, Chemosphere. 259 (2020) 127492. https://doi.org/https://doi.org/10.1016/j.chemosphere.2020.127492.

[31] P. Singh, M.K. Singh, Y.R. Beg, G.R. Nishad, A review on spectroscopic methods for determination of nitrite and nitrate in environmental samples, Talanta. 191 (2019) 364–381.

[32] W.M. Lewis, D.P. Morris, Toxicity of Nitrite to Fish: A Review, Trans Am Fish Soc. 115 (1986). https://doi.org/10.1577/1548-8659(1986)115<183:tontf>2.0.co;2.

[33] H. Kroupova, J. Machova, Z. Svobodova, Nitrite influence on fish: A review, Vet Med (Praha). 50 (2005). https://doi.org/10.17221/5650-VETMED.

[34] Q.-H. Wang, L.-J. Yu, Y. Liu, L. Lin, R. Lu, J. Zhu, L. He, Z.-L. Lu, Methods for the detection and determination of nitrite and nitrate: A review, Talanta. 165 (2017) 709–720.

[35] F.J. Agardy, P.J. Sullivan, Appendix A: Summary Tables of Drinking Water Standards and Health Advisories, in: Drinking Water Regulation and Health, John Wiley & Sons, Inc., Hoboken, NJ, USA, 2003: pp. 583–619. https://doi.org/10.1002/0471721999.app1.

[36] N.H. and M.R.C. (NHMRC), Australian Drinking Water Guidelines 6 2011, (2011).

[37] B.P. Kafle, Chapter 2 - Theory and instrumentation of absorption spectroscopy: UV–VIS spectrophotometry and colorimetry, in: B.P.B.T.-C.A. and M.C. by S. Kafle (Ed.), Elsevier, 2020: pp. 17–38. https://doi.org/https://doi.org/10.1016/B978-0-12-814866-2.00002-6.

[38] J. Ma, L. Adornato, R.H. Byrne, D. Yuan, Determination of nanomolar levels of nutrients in seawater, TrAC Trends in Analytical Chemistry. 60 (2014) 1–15.

[39] L.I.U. Xia, X.U. Qing, G.U.O. Yafei, Y.U. Xiaoping, D. Tianlong, Ammonia Nitrogen Speciation Analysis in Aquatic Environments, in: International Conference on Biological Engineering and Pharmacy 2016 (BEP 2016), Atlantis Press, 2016.

[40] Y. Zhu, J. Chen, D. Yuan, Z. Yang, X. Shi, H. Li, H. Jin, L. Ran, Development of analytical methods for ammonium determination in seawater over the last two decades, TrAC Trends in Analytical Chemistry. 119 (2019) 115627. https://doi.org/https://doi.org/10.1016/j.trac.2019.115627.

[41] D. Li, X. Xu, Z. Li, T. Wang, C. Wang, Detection Methods of Ammonia Nitrogen in Water: A Review, TrAC Trends in Analytical Chemistry. (2020) 115890.

[42] C. Molins-Legua, S. Meseguer-Lloret, Y. Moliner-Martinez, P. Campíns-Falcó, A guide for selecting the most appropriate method for ammonium determination in water analysis, TrAC Trends in Analytical Chemistry. 25 (2006) 282–290.

[43] K. Lin, Y. Zhu, Y. Zhang, H. Lin, Determination of ammonia nitrogen in natural waters: Recent advances and applications, Trends in Environmental Analytical Chemistry. 24 (2019) e00073.

[44] J.R. Lakowicz, Instrumentation for Fluorescence Spectroscopy BT - Principles of Fluorescence Spectroscopy, in: J.R. Lakowicz (Ed.), Springer US, Boston, MA, 2006: pp. 27–61. https://doi.org/10.1007/978-0-387-46312-4_2.

[45] N. Amornthammarong, J.-Z. Zhang, P.B. Ortner, An autonomous batch analyzer for the determination of trace ammonium in natural waters using fluorometric detection, Analytical Methods. 3 (2011) 1501–1506. https://doi.org/10.1039/C1AY05095H.

[46] A.J. Bard, L.R. Faulkner, Electrochemical Methods Fundamentals and Applications. 2nd Ed., John Wiley&Sons, New Jersey, USA. (2001).

[47] N. Elgrishi, K.J. Rountree, B.D. McCarthy, E.S. Rountree, T.T. Eisenhart, J.L. Dempsey, A Practical Beginner's Guide to Cyclic Voltammetry, J Chem Educ. (2018). https://doi.org/10.1021/acs.jchemed.7b00361.

[48] Subject: A Review of Techniques for Electrochemical Analysis, n.d.

[49] X. Chen, G. Zhou, S. Mao, J. Chen, Rapid detection of nutrients with electronic sensors: a review, Environ Sci Nano. 5 (2018) 837–862. https://doi.org/10.1039/C7EN01160A.

[50] M. Sophocleous, J.K. Atkinson, A review of screen-printed silver/silver chloride (Ag/AgCl) reference electrodes potentially suitable for environmental potentiometric sensors, Sens Actuators A Phys. 267 (2017) 106–120. https://doi.org/https://doi.org/10.1016/j.sna.2017.10.013.

[51] M.W. Shinwari, D. Zhitomirsky, I.A. Deen, P.R. Selvaganapathy, M.J. Deen, D. Landheer, Microfabricated Reference Electrodes and their Biosensing Applications, Sensors . 10 (2010). https://doi.org/10.3390/s100301679.

[52] L. Manjakkal, D. Shakthivel, R. Dahiya, Flexible Printed Reference Electrodes for Electrochemical Applications, Adv Mater Technol. 3 (2018) 1800252. https://doi.org/10.1002/admt.201800252.

[53] M.C. Blanco-López, M.J. Lobo-Castañón, A.J. Miranda-Ordieres, P. Tuñón-Blanco, Electrochemical sensors based on molecularly imprinted polymers, TrAC Trends in Analytical Chemistry. 23 (2004) 36–48. https://doi.org/https://doi.org/10.1016/S0165-9936(04)00102-5.

[54] L. Manjakkal, E. Djurdjic, K. Cvejin, J. Kulawik, K. Zaraska, D. Szwagierczak, Electrochemical impedance spectroscopic analysis of RuO2 based thick film pH sensors, Electrochim Acta. 168 (2015) 246–255.

[55] B.-A. Mei, O. Munteshari, J. Lau, B. Dunn, L. Pilon, Physical interpretations of Nyquist plots for EDLC electrodes and devices, The Journal of Physical Chemistry C. 122 (2018) 194–206.

[56] L. Manjakkal, S. Dervin, R. Dahiya, Flexible potentiometric pH sensors for wearable systems, RSC Adv. 10 (2020) 8594–8617. https://doi.org/10.1039/D0RA00016G.

[57] K. Crowley, E. O'Malley, A. Morrin, M.R. Smyth, A.J. Killard, An aqueous ammonia sensor based on an inkjet-printed polyaniline nanoparticle-modified electrode, Analyst. 133 (2008) 391–399. https://doi.org/10.1039/B716154A.

[58] F.F. Franco, L. Manjakkal, D. Shakthivel, R. Dahiya, ZnO based Screen Printed Aqueous Ammonia Sensor for Water Quality Monitoring, in: 2019 IEEE SENSORS, IEEE, Montreal, Canada, 2019: pp. 1–4. https://doi.org/10.1109/SENSORS43011.2019.8956763.

[59] J.-M. Zen, C.-C. Yang, A.S. Kumar, Voltammetric behavior and trace determination of Pb2+ at a mercury-free screen-printed silver electrode, Anal Chim Acta. 464 (2002) 229–235. https://doi.org/10.1016/S0003-2670(02)00472-5.

[60] C.S. Pundir, S. Jakhar, V. Narwal, Determination of urea with special emphasis on biosensors: A review, Biosens Bioelectron. 123 (2019) 36–50.

[61] F. Scholz, Electroanalytical Methods, Springer Berlin Heidelberg, Berlin, Heidelberg, 2010. https://doi.org/10.1007/978-3-642-02915-8.

[62] F. Scholz, Voltammetric techniques of analysis: the essentials, ChemTexts. 1 (2015) 17. https://doi.org/10.1007/s40828-015-0016-y.

[63] F. Lisdat, D. Schäfer, The use of electrochemical impedance spectroscopy for biosensing, Anal Bioanal Chem. (2008). https://doi.org/10.1007/s00216-008-1970-7.

[64] L. Manjakkal, D. Szwagierczak, R. Dahiya, Metal oxides based electrochemical pH sensors: Current progress and future perspectives, Prog Mater Sci. 109 (2020) 100635. https://doi.org/10.1016/j.pmatsci.2019.100635.

[65] J. Schwarz, K. Trommer, F. Gerlach, M. Mertig, All-Solid-State Screen-Printed Sensors for Potentiometric Calcium(II) Determinations in Environmental Samples, Am J Analyt Chem. 09 (2018). https://doi.org/10.4236/ajac.2018.93010.

[66] Z. Yilong, Z. Dean, L. Daoliang, Electrochemical and other methods for detection and determination of dissolved nitrite: A review, Int. J. Electrochem. Sci. 10 (2015) 1144–1168.

[67] X. Ma, F. Gao, G. Liu, Y. Xie, X. Tu, Y. Li, R. Dai, F. Qu, W. Wang, L. Lu, Sensitive determination of nitrite by using an electrode modified with hierarchical three-dimensional tungsten disulfide and reduced graphene oxide aerogel, Microchimica Acta. 186 (2019). https://doi.org/10.1007/s00604-019-3379-8.

[68] K.V. Singh, A.M. Whited, Y. Ragineni, T.W. Barrett, J. King, R. Solanki, 3D nanogap interdigitated electrode array biosensors, Anal Bioanal Chem. 397 (2010) 1493–1502. https://doi.org/10.1007/s00216-010-3682-z.

[69] S. Smith, P. Madzivhandila, L. Ntuli, P. Bezuidenhout, H. Zheng, K. Land, Printed Paper–Based Electrochemical Sensors for Low-Cost Point-of-Need Applications, Electrocatalysis. 10 (2019). https://doi.org/10.1007/s12678-019-0512-8.

[70] H. Farahani, R. Wagiran, M.N. Hamidon, Humidity sensors principle, mechanism, and fabrication technologies: A comprehensive review, Sensors (Switzerland). 14 (2014). https://doi.org/10.3390/s140507881.

[71] Y. Chen, Y. Zilberman, P. Mostafalu, S.R. Sonkusale, Paper based platform for colorimetric sensing of dissolved NH3 and CO2, Biosens Bioelectron. 67 (2015) 477–484. https://doi.org/10.1016/j.bios.2014.09.010.

[72] E.W. Rice, R.B. Baird, A.D. Eaton, L.S. Clesceri, Standard methods for the examination of water and wastewater, American Public Health Association, Washington, DC. 541 (2012).

[73] J.W. O'Dell, Determination of ammonia nitrogen by semi-automated colorimetry, 1993.

[74] Marc. Roth, Fluorescence reaction for amino acids, Anal Chem. 43 (1971) 880–882. https://doi.org/10.1021/ac60302a020.

[75] H. Hu, Y. Liang, S. Li, Q. Guo, C. Wu, A Modified *o*-Phthalaldehyde Fluorometric Analytical Method for Ultratrace Ammonium in Natural Waters Using EDTA-NaOH as Buffer, J Anal Methods Chem. 2014 (2014) 728068. https://doi.org/10.1155/2014/728068.

[76] Z. Genfa, P.K. Dasgupta, Fluorometric measurement of aqueous ammonium ion in a flow injection system, Anal Chem. 61 (1989) 408–412.

[77] M. Cuartero, N. Colozza, B.M. Fernández-Pérez, G.A. Crespo, Why ammonium detection is particularly challenging but insightful with ionophore-based potentiometric sensors – an overview of the progress in the last 20 years, Analyst. 145 (2020) 3188–3210. https://doi.org/10.1039/D0AN00327A.

[78] G.N. Dar, A. Umar, S.A. Zaidi, S. Baskoutas, S.W. Hwang, M. Abaker, A. Al-Hajry, S.A. Al-Sayari, Ultra-high sensitive ammonia chemical sensor based on ZnO nanopencils, Talanta. 89 (2012) 155–161.

[79] USEPA, Methods for Chemical Analysis of Water and Wastes. EPA/600/4-79/020, 1983.

[80] Y. Huang, T. Wang, Z. Xu, E. Hughes, F. Qian, M. Lee, Y. Fan, Y. Lei, C. Brückner, B. Li, Real-Time in Situ Monitoring of Nitrogen Dynamics in Wastewater Treatment Processes using Wireless, Solid-State, and Ion-Selective Membrane Sensors, Environ Sci Technol. 53 (2019) 3140–3148. https://doi.org/10.1021/acs.est.8b05928.

[81] D. Li, T. Wang, Z. Li, X. Xu, C. Wang, Y. Duan, Application of Graphene-Based Materials for Detection of Nitrate and Nitrite in Water—A Review, Sensors . 20 (2020). https://doi.org/10.3390/s20010054.

[82] G.F. Wang, K. Horita, M. Satake, Simultaneous Spectrophotometric Determination of Nitrate and Nitrite in Water and Some Vegetable Samples by Column Preconcentration, Microchemical Journal. 58 (1998). https://doi.org/10.1006/mchj.1997.1544.

[83] A. Aydin, Ö. Ercan, S. Taşcioğlu, A novel method for the spectrophotometric determination of nitrite in water, Talanta. 66 (2005). https://doi.org/10.1016/j.talanta.2005.01.024.

[84] R. Burakham, M. Oshima, K. Grudpan, S. Motomizu, Simple flow-injection system for the simultaneous determination of nitrite and nitrate in water samples, in: Talanta, 2004. https://doi.org/10.1016/j.talanta.2004.03.059.

[85] A.T. Mubarak, A.A. Mohamed, K.F. Fawy, A.S. Al-Shihry, A novel kinetic determination of nitrite based on the perphenazine-bromate redox reaction, Microchimica Acta. 157 (2007). https://doi.org/10.1007/s00604-006-0661-3.

[86] A.A. Ensafi, M. Amini, A highly selective optical sensor for catalytic determination of ultra-trace amounts of nitrite in water and foods based on brilliant cresyl blue as a sensing reagent, Sens Actuators B Chem. 147 (2010). https://doi.org/10.1016/j.snb.2010.03.014.

[87] T.S. Liu, T.F. Kang, L.P. Lu, Y. Zhang, S.Y. Cheng, Au-Fe(III) nanoparticle modified glassy carbon electrode for electrochemical nitrite sensor, Journal of Electroanalytical Chemistry. 632 (2009). https://doi.org/10.1016/j.jelechem.2009.04.023.

[88] S. Wang, Y. Yin, X. Lin, Cooperative effect of Pt nanoparticles and Fe(III) in the electrocatalytic oxidation of nitrite, Electrochem Commun. 6 (2004). https://doi.org/10.1016/j.elecom.2003.12.008.

[89] A. Gholizadeh, D. Voiry, C. Weisel, A. Gow, R. Laumbach, H. Kipen, M. Chhowalla, M. Javanmard, Toward point-of-care management of chronic respiratory conditions: Electrochemical sensing of nitrite content in exhaled breath condensate using reduced graphene oxide, Microsyst Nanoeng. 3 (2017). https://doi.org/10.1038/micronano.2017.22.

[90] B. Patella, R.R. Russo, A. O'Riordan, G. Aiello, C. Sunseri, R. Inguanta, Copper nanowire array as highly selective electrochemical sensor of nitrate ions in water, Talanta. 221 (2021). https://doi.org/10.1016/j.talanta.2020.121643.

[91] A. Ahamed, L. Ge, K. Zhao, A. Veksha, J. Bobacka, G. Lisak, Environmental footprint of voltammetric sensors based on screen-printed electrodes: An assessment towards "green" sensor manufacturing, Chemosphere. 278 (2021) 130462. https://doi.org/10.1016/j.chemosphere.2021.130462.

[92] N.R. Tanguy, M. Thompson, N. Yan, A review on advances in application of polyaniline for ammonia detection, Sens Actuators B Chem. 257 (2018) 1044–1064.

[93] P. Shankar, J.B.B. Rayappan, Gas sensing mechanism of metal oxides: The role of ambient atmosphere, type of semiconductor and gases-A review, Sci. Lett. J. 4 (2015) 126.

[94] S. Sawan, R. Maalouf, A. Errachid, N. Jaffrezic-Renault, Metal and metal oxide nanoparticles in the voltammetric detection of heavy metals: A review, TrAC - Trends in Analytical Chemistry. 131 (2020). https://doi.org/10.1016/j.trac.2020.116014.

[95] A. Dizon, M.E. Orazem, On the impedance response of interdigitated electrodes, Electrochim Acta. 327 (2019). https://doi.org/10.1016/j.electacta.2019.135000.

[96] A.U. Sardesai, V.N. Dhamu, A. Paul, S. Muthukumar, S. Prasad, Design and Electrochemical Characterization of Spiral Electrochemical Notification Coupled Electrode (SENCE) Platform for Biosensing Application, Micromachines . 11 (2020). https://doi.org/10.3390/mi11030333.

[97] L. Schmidt-Mende, J.L. MacManus-Driscoll, ZnO–nanostructures, defects, and devices, Materials Today. 10 (2007) 40–48.

[98] J.X. Wang, X.W. Sun, A. Wei, Y. Lei, X.P. Cai, C.M. Li, Z.L. Dong, Zinc oxide nanocomb biosensor for glucose detection, Appl Phys Lett. 88 (2006) 233106.

[99] M. Komoda, I. Shitanda, Y. Hoshi, M. Itagaki, Instantaneously usable screen-printed silver/silver sulfate reference electrode with long-term stability, Electrochem Commun. 103 (2019) 133–137. https://doi.org/10.1016/j.elecom.2019.05.019.

[100] D.G. Gromadskyi, Characterization of Ag/Ag2SO4 system as reference electrode for in-situ electrochemical studies of advanced aqueous supercapacitors, Journal of Chemical Sciences. 128 (2016) 1011–1017. https://doi.org/10.1007/s12039-016-1084-2.

[101] A. Dey, Semiconductor metal oxide gas sensors: A review, Materials Science and Engineering: B. 229 (2018) 206–217.

[102] S. Ichikawa, L. Mahardiani, Y. Kamiya, Catalytic oxidation of ammonium ion in water with ozone over metal oxide catalysts, Catal Today. 232 (2014) 192–197.

[103] A. Mulder, A.A. van de Graaf, L.A. Robertson, J.G. Kuenen, Anaerobic ammonium oxidation discovered in a denitrifying fluidized bed reactor, FEMS Microbiol Ecol. 16 (1995) 177–183.

[104] B. Meyer, D. Marx, O. Dulub, U. Diebold, M. Kunat, D. Langenberg, C. Wöll, Partial dissociation of water leads to stable superstructures on the surface of zinc oxide, Angewandte Chemie International Edition. 43 (2004) 6641–6645.

[105] I.H. Cho, D.H. Kim, S. Park, Electrochemical biosensors: Perspective on functional nanomaterials for on-site analysis, Biomater Res. 24 (2020). https://doi.org/10.1186/s40824-019-0181-y.

[106] L. Manjakkal, C.G. Núñez, W. Dang, R. Dahiya, Flexible self-charging supercapacitor based on graphene-Ag-3D graphene foam electrodes, Nano Energy. 51 (2018) 604–612. https://doi.org/10.1016/j.nanoen.2018.06.072.

[107] H. Beitollahi, S.Z. Mohammadi, M. Safaei, S. Tajik, Applications of electrochemical sensors and biosensors based on modified screen-printed electrodes: a review, Analytical Methods. 12 (2020) 1547–1560. https://doi.org/10.1039/C9AY02598G.

[108] M. Li, D.-W. Li, G. Xiu, Y.-T. Long, Applications of screen-printed electrodes in current environmental analysis, Curr Opin Electrochem. 3 (2017) 137–143. https://doi.org/10.1016/j.coelec.2017.08.016.

[109] F. Wang, Y.-T. Wang, H. Yu, J.-X. Chen, B.-B. Gao, J.-P. Lang, One Unique 1D Silver(I)-Bromide-Thiol Coordination Polymer Used for Highly Efficient Chemiresistive Sensing of Ammonia and Amines in Water, Inorg Chem. 55 (2016) 9417–9423. https://doi.org/10.1021/acs.inorgchem.6b01688.

[110] J. Kim, R. Kumar, A.J. Bandodkar, J. Wang, Advanced Materials for Printed Wearable Electrochemical Devices: A Review, Adv Electron Mater. 3 (2017) 1600260. https://doi.org/10.1002/aelm.201600260.

[111] Y. Li, W. Chen, L. Lu, Wearable and Biodegradable Sensors for Human Health Monitoring, ACS Appl Bio Mater. 4 (2021) 122–139. https://doi.org/10.1021/acsabm.0c00859.

[112] E.S. Hosseini, S. Dervin, P. Ganguly, R. Dahiya, Biodegradable Materials for Sustainable Health Monitoring Devices, ACS Appl Bio Mater. 4 (2021) 163–194. https://doi.org/10.1021/acsabm.0c01139.

[113] S. Tajik, H. Beitollahi, F.G. Nejad, M. Safaei, K. Zhang, Q. van Le, R.S. Varma, H.W. Jang, M. Shokouhimehr, Developments and applications of nanomaterial-based carbon paste electrodes, RSC Adv. 10 (2020) 21561–21581. https://doi.org/10.1039/D0RA03672B.

[114] W. Wu, Inorganic nanomaterials for printed electronics: a review, Nanoscale. 9 (2017) 7342–7372. https://doi.org/10.1039/C7NR01604B.

[115] M. Li, Y.-T. Li, D.-W. Li, Y.-T. Long, Recent developments and applications of screen-printed electrodes in environmental assays—A review, Anal Chim Acta. 734 (2012) 31–44. https://doi.org/10.1016/j.aca.2012.05.018.

[116] R. Zhang, S. Xu, Y. Zhu, J. Luo, X. Liu, D. Tang, One-pot facile preparation of Ag nanoparticles for chloride ion sensing, Colloid Polym Sci. 294 (2016) 1643–1649. https://doi.org/10.1007/s00396-016-3928-1.

[117] J. Bujes-Garrido, D. Izquierdo-Bote, A. Heras, A. Colina, M.J. Arcos-Martínez, Determination of halides using Ag nanoparticles-modified disposable electrodes. A first approach to a wearable sensor for quantification of chloride ions, Anal Chim Acta. 1012 (2018) 42–48. https://doi.org/10.1016/j.aca.2018.01.063.

[118] H.S. Toh, C. Batchelor-McAuley, K. Tschulik, R.G. Compton, Electrochemical detection of chloride levels in sweat using silver nanoparticles: a basis for the preliminary screening for cystic fibrosis, Analyst. 138 (2013) 4292–4297. https://doi.org/10.1039/C3AN00843F.

[119] J. Wang, B. Tian, V.B. Nascimento, L. Angnes, Performance of screen-printed carbon electrodes fabricated from different carbon inks, Electrochim Acta. 43 (1998) 3459–3465. https://doi.org/10.1016/S0013-4686(98)00092-9.

[120] J. Wang, M. Musameh, Carbon nanotube screen-printed electrochemical sensors, Analyst. 129 (2004) 1–2. https://doi.org/10.1039/B313431H.

[121] A. Abdelhalim, A. Abdellah, G. Scarpa, P. Lugli, Fabrication of carbon nanotube thin films on flexible substrates by spray deposition and transfer printing, Carbon N Y. 61 (2013) 72–79. https://doi.org/10.1016/j.carbon.2013.04.069.

[122] R.L. McCreery, Advanced Carbon Electrode Materials for Molecular Electrochemistry, Chem Rev. 108 (2008) 2646–2687. https://doi.org/10.1021/cr068076m.

[123] P. He, J. Cao, H. Ding, C. Liu, J. Neilson, Z. Li, I.A. Kinloch, B. Derby, Screen-Printing of a Highly Conductive Graphene Ink for Flexible Printed Electronics, ACS Appl Mater Interfaces. 11 (2019). https://doi.org/10.1021/acsami.9b04589.

[124] Y.H. Hou, M.Q. Zhang, M.Z. Rong, G. Yu, H.M. Zeng, Improvement of conductive network quality in carbon black-filled polymer blends, J Appl Polym Sci. 84 (2002). https://doi.org/10.1002/app.10574.

[125] B. Molinero-Abad, D. Izquierdo, L. Pérez, I. Escudero, M.J. Arcos-Martínez, Comparison of backing materials of screen printed electrochemical sensors for direct determination of the sub-nanomolar concentration of lead in seawater, Talanta. 182 (2018) 549–557. https://doi.org/10.1016/j.talanta.2018.02.005.

[126] A. Chałupniak, A. Merkoçi, Toward integrated detection and graphene-based removal of contaminants in a lab-on-a-chip platform, Nano Res. 10 (2017) 2296–2310. https://doi.org/10.1007/s12274-016-1420-3.

[127] A. Chałupniak, A. Merkoçi, Graphene Oxide–Poly(dimethylsiloxane)-Based Lab-on-a-Chip Platform for Heavy-Metals Preconcentration and Electrochemical Detection, ACS Appl Mater Interfaces. 9 (2017) 44766–44775. https://doi.org/10.1021/acsami.7b12368.

[128] D. Li, H. Duan, Y. Wang, Q. Zhang, H. Cao, W. Deng, D. Li, On-site preconcentration of pesticide residues in a drop of seawater by using electrokinetic trapping, and their determination by surface-enhanced Raman scattering, Microchimica Acta. 185 (2018) 10. https://doi.org/10.1007/s00604-017-2580-x.

[129] W. Tang, Z. Wang, J. Yu, F. Zhang, P. He, Internal Calibration Potentiometric Aptasensors for Simultaneous Detection of Hg 2+ , Cd 2+ , and As 3+ Based on a Screen-Printed Carbon Electrodes Array, Anal Chem. 90 (2018) 8337–8344. https://doi.org/10.1021/acs.analchem.7b04150.

[130] K. Uppuluri, M. Lazouskaya, D. Szwagierczak, K. Zaraska, M. Tamm, Fabrication, Potentiometric Characterization, and Application of Screen-Printed RuO2 pH Electrodes for Water Quality Testing, Sensors. 21 (2021) 5399. https://doi.org/10.3390/s21165399.

[131] A. Kaidarova, M. Marengo, G. Marinaro, N. Geraldi, C.M. Duarte, J. Kosel, Flexible and Biofouling Independent Salinity Sensor, Adv Mater Interfaces. 5 (2018) 1801110. https://doi.org/10.1002/admi.201801110.

[132] A. Kaidaorva, M. Marengo, G. Marinaro, N.R. Geraldi, R. Wilson, C.M. Duarte, J. Kosel, Flexible, four-electrode conductivity cell for biologging applications, Results in Materials. 1 (2019) 100009. https://doi.org/10.1016/j.rinma.2019.100009.

[133] K.W. Meereboer, M. Misra, A.K. Mohanty, Review of recent advances in the biodegradability of polyhydroxyalkanoate (PHA) bioplastics and their composites, Green Chemistry. 22 (2020) 5519–5558. https://doi.org/10.1039/D0GC01647K.

[134] L. Manjakkal, W.T. Navaraj, C.G. Núñez, R. Dahiya, Graphene–Graphite Polyurethane Composite Based High-Energy Density Flexible Supercapacitors, Advanced Science. 6 (2019) 1802251. https://doi.org/10.1002/advs.201802251.

[135] S. Goodwin, Z. Coldrick, S. Heeg, B. Grieve, A. Vijayaraghavan, E.W. Hill, Fabrication and electrochemical response of pristine graphene ultramicroelectrodes, Carbon N Y. 177 (2021) 207–215. https://doi.org/https://doi.org/10.1016/j.carbon.2021.02.078.

[136] J. Kim, W.J. da Silva, Abd.R. bin Mohd Yusoff, J. Jang, Organic devices based on nickel nanowires transparent electrode, Sci Rep. 6 (2016) 19813. https://doi.org/10.1038/srep19813.

[137] Q. Zhang, T. Li, J. Liang, N. Wang, X. Kong, J. Wang, H. Qian, Y. Zhou, F. Liu, C. Wei, Y. Zhao, X. Zhang, Highly wettable and metallic NiFe-phosphate/phosphide catalyst synthesized by plasma for highly efficient oxygen evolution reaction, J Mater Chem A Mater. 6 (2018) 7509–7516. https://doi.org/10.1039/C8TA01334A.

[138] D. Huang, Z.-D. Hu, Y. Ding, Z.-C. Zhen, B. Lu, J.-H. Ji, G.-X. Wang, Seawater degradable PVA/PCL blends with water-soluble polyvinyl alcohol as degradation accelerator, Polym Degrad Stab. 163 (2019) 195–205. https://doi.org/10.1016/j.polymdegradstab.2019.03.011.

[139] A.G. Dickson, C. Goyet, Handbook of methods for the analysis of the various parameters of the carbon dioxide system in sea water. Version 2, Oak Ridge National Lab., TN (United States), 1994.

[140] F.F. Franco, L. Manjakkal, R. Dahiya, Screen-Printed Flexible Carbon versus Silver Electrodes for Electrochemical Sensors, in: 2020 IEEE FLEPS, IEEE, 2020: pp. 1–4. https://doi.org/10.1109/FLEPS49123.2020.9239549.

[141] W.M. Haynes, CRC handbook of chemistry and physics, CRC press, 2014.

[142] L. Meites, Handbook of analytical chemistry, Soil Sci. 96 (1963) 358.

[143] P.M.S. Monk, Fundamentals of electroanalytical chemistry, John Wiley & Sons, 2008.

[144] K.Z. Brainina, A. V Tarasov, M.B. Vidrevich, Silver chloride/ferricyanide-based quasi-reference electrode for potentiometric sensing applications, Chemosensors. 8 (2020) 15.

[145] M.Y. Kariduraganavar, A.A. Kittur, R.R. Kamble, Chapter 1 - Polymer Synthesis and Processing, in: S.G. Kumbar, C.T. Laurencin, M.B.T.-N. and S.B.P. Deng (Eds.), Elsevier, Oxford, 2014: pp. 1–31. https://doi.org/https://doi.org/10.1016/B978-0-12-396983-5.00001-6.

[146] M. Avella, E. Martuscelli, M. Raimo, Review Properties of blends and composites based on poly(3-hydroxy)butyrate (PHB) and poly(3-hydroxybutyrate-hydroxyvalerate) (PHBV) copolymers, J Mater Sci. 35 (2000) 523–545. https://doi.org/10.1023/A:1004740522751.

[147] A.R. Bagheri, C. Laforsch, A. Greiner, S. Agarwal, Fate of So-Called Biodegradable Polymers in Seawater and Freshwater, Global Challenges. 1 (2017) 1700048. https://doi.org/10.1002/gch2.201700048.

[148] C.W. Pouton, S. Akhtar, Biosynthetic polyhydroxyalkanoates and their potential in drug delivery, Adv Drug Deliv Rev. 18 (1996) 133–162. https://doi.org/10.1016/0169-409X(95)00092-L.

[149] E. von der Esch, M. Lanzinger, A.J. Kohles, C. Schwaferts, J. Weisser, T. Hofmann, K. Glas, M. Elsner, N.P. Ivleva, Simple Generation of Suspensible Secondary Microplastic Reference Particles via Ultrasound Treatment, Front Chem. 8 (2020) 169. https://doi.org/10.3389/fchem.2020.00169.

[150] D. Chen, L. Tang, J. Li, Graphene-based materials in electrochemistry, Chem Soc Rev. 39 (2010). https://doi.org/10.1039/b923596e.

[151] J. Lin, Z. Peng, Y. Liu, F. Ruiz-Zepeda, R. Ye, E.L.G. Samuel, M.J. Yacaman, B.I. Yakobson, J.M. Tour, Laser-induced porous graphene films from commercial polymers, Nat Commun. 5 (2014) 5714. https://doi.org/10.1038/ncomms6714.

[152] R. Ye, D.K. James, J.M. Tour, Laser-Induced Graphene: From Discovery to Translation, Advanced Materials. 31 (2019) 1803621. https://doi.org/10.1002/adma.201803621.

[153] Y. Dong, S.C. Rismiller, J. Lin, Molecular dynamic simulation of layered graphene clusters formation from polyimides under extreme conditions, Carbon N Y. 104 (2016). https://doi.org/10.1016/j.carbon.2016.03.050.

[154] Y. Chyan, R. Ye, Y. Li, S.P. Singh, C.J. Arnusch, J.M. Tour, Laser-Induced Graphene by Multiple Lasing: Toward Electronics on Cloth, Paper, and Food, ACS Nano. 12 (2018). https://doi.org/10.1021/acsnano.7b08539.

[155] A. Behrent, C. Griesche, P. Sippel, A.J. Baeumner, Process-property correlations in laser-induced graphene electrodes for electrochemical sensing, Microchimica Acta. 188 (2021). https://doi.org/10.1007/s00604-021-04792-3.

[156] D.C. Mongomery, Montgomery: Design and Analysis of Experiments, John Willy & Sons. (2017).

[157] R. Murray, M. Burke, D. Iacopino, A.J. Quinn, Design of Experiments and Optimization of Laser-Induced Graphene, ACS Omega. 6 (2021). https://doi.org/10.1021/acsomega.1c00309.

[158] L. Huang, J. Su, Y. Song, R. Ye, Laser-Induced Graphene: En Route to Smart Sensing, Nanomicro Lett. 12 (2020). https://doi.org/10.1007/s40820-020-00496-0.

[159] N. Kurra, Q. Jiang, P. Nayak, H.N. Alshareef, Laser-derived graphene: A three-dimensional printed graphene electrode and its emerging applications, Nano Today. 24 (2019). https://doi.org/10.1016/j.nantod.2018.12.003.

[160] L. Manjakkal, W. Dang, N. Yogeswaran, R. Dahiya, Textile-based potentiometric electrochemical pH sensor for wearable applications, Biosensors (Basel). 9 (2019) 14.

[161] F. Vivaldi, A. Dallinger, N. Poma, A. Bonini, D. Biagini, P. Salvo, F. Borghi, A. Tavanti, F. Greco, F. di Francesco, Sweat analysis with a wearable sensing platform based on laser-induced graphene, APL Bioeng. 6 (2022) 036104. https://doi.org/10.1063/5.0093301.

[162] G. Li, Y. Xia, Y. Tian, Y. Wu, J. Liu, Q. He, D. Chen, Review—Recent Developments on Graphene-Based Electrochemical Sensors toward Nitrite, J Electrochem Soc. 166 (2019). https://doi.org/10.1149/2.0171912jes.

[163] L. Tang, Y. Wang, Y. Li, H. Feng, J. Lu, J. Li, Preparation, structure, and electrochemical properties of reduced graphene sheet films, Adv Funct Mater. 19 (2009). https://doi.org/10.1002/adfm.200900377.

[164] X. Zhou, Z. Liu, A scalable, solution-phase processing route to graphene oxide and graphene ultralarge sheets, Chemical Communications. 46 (2010). https://doi.org/10.1039/b914412a.

[165] N. Zhang, J. Yang, C. Hu, Laser-scribed graphene sensors on nail polish with tunable composition for electrochemical detection of nitrite and glucose, Sens Actuators B Chem. 357 (2022). https://doi.org/10.1016/j.snb.2022.131394.

[166] L.F. Mendes, A. de Siervo, W. Reis de Araujo, T.R. Longo Cesar Paixão, Reagentless fabrication of a porous graphene-like electrochemical device from phenolic paper using laser-scribing, Carbon N Y. 159 (2020). https://doi.org/10.1016/j.carbon.2019.12.016.

[167] N.T. Garland, E.S. McLamore, N.D. Cavallaro, D. Mendivelso-Perez, E.A. Smith, D. Jing, J.C. Claussen, Flexible Laser-Induced Graphene for Nitrogen Sensing in Soil, ACS Appl Mater Interfaces. 10 (2018). https://doi.org/10.1021/acsami.8b10991.

[168] S. Nasraoui, A. Al-Hamry, P.R. Teixeira, S. Ameur, L.G. Paterno, M. ben Ali, O. Kanoun, Electrochemical sensor for nitrite detection in water samples using flexible laser-induced graphene electrodes functionalized by CNT decorated by Au nanoparticles, Journal of Electroanalytical Chemistry. 880 (2021). https://doi.org/10.1016/j.jelechem.2020.114893.

[169] J. Mocak, A.M. Bond, S. Mitchell, G. Scollary, A.M. Bond, A statistical overview of standard (IUPAC and ACS) and new procedures for determining the limits of detection and quantification: Application to voltammetric and stripping techniques, Pure and Applied Chemistry. 69 (1997). https://doi.org/10.1351/pac199769020297.

[170] J.M. Jian, L. Fu, J. Ji, L. Lin, X. Guo, T.L. Ren, Electrochemically reduced graphene oxide/gold nanoparticles composite modified screen-printed carbon electrode for effective electrocatalytic analysis of nitrite in foods, Sens Actuators B Chem. 262 (2018). https://doi.org/10.1016/j.snb.2018.01.164.

[171] W.R.P. Costa, R.G. Rocha, L. v de Faria, T.A. Matias, D.L.O. Ramos, A.G.C. Dias, G.L. Fernandes, E.M. Richter, R.A.A. Muñoz, Affordable equipment to fabricate laser-induced

graphene electrodes for portable electrochemical sensing, Microchimica Acta. 189 (2022) 185. https://doi.org/10.1007/s00604-022-05294-6.

[172] S. Aarya, Y. Kumar, R.K. Chahota, Recent Advances in Materials, Parameters, Performance and Technology in Ammonia Sensors: A Review, J Inorg Organomet Polym Mater. 30 (2020) 269–290.

[173] Y. Zhang, K. Yu, D. Jiang, Z. Zhu, H. Geng, L. Luo, Zinc oxide nanorod and nanowire for humidity sensor, Appl Surf Sci. 242 (2005) 212–217.

[174] K. Zargoosh, F. Farhadian Babadi, M. Hosseini, A.H. Kianfar, Fast and selective determination of ammonia in aqueous solutions using immobilized iron(III) oxide nanoparticles on the agarose membrane, Desalination Water Treat. 57 (2016) 11133–11142. https://doi.org/10.1080/19443994.2015.1042057.

[175] K. Bradley, J.-C.P. Gabriel, M. Briman, A. Star, G. Grüner, Charge Transfer from Ammonia Physisorbed on Nanotubes, Phys Rev Lett. 91 (2003) 218301. https://doi.org/10.1103/PhysRevLett.91.218301.

[176] F. Valentini, V. Biagiotti, C. Lete, G. Palleschi, J. Wang, The electrochemical detection of ammonia in drinking water based on multi-walled carbon nanotube/copper nanoparticle composite paste electrodes, Sens Actuators B Chem. 128 (2007) 326–333. https://doi.org/https://doi.org/10.1016/j.snb.2007.06.010.

[177] M.T. Zhybak, M.Y. Vagin, V. Beni, X. Liu, E. Dempsey, A.P.F. Turner, Y.I. Korpan, Direct detection of ammonium ion by means of oxygen electrocatalysis at a copper-polyaniline composite on a screen-printed electrode, Microchimica Acta. 183 (2016) 1981–1987.

[178] A. Darchen, R. Drissi-Daoudi, A. Irzho, Electrochemical investigations of copper etching by Cu (NH3) 4Cl2 in ammoniacal solutions, J Appl Electrochem. 27 (1997) 448–454.

[179] D. Thatikayala, D. Ponnamma, K. Sadasivuni, J.-J. Cabibihan, A. Al-Ali, R. Malik, B. Min, Progress of Advanced Nanomaterials in the Non-Enzymatic Electrochemical Sensing of Glucose and H2O2, Biosensors (Basel). 10 (2020) 151. https://doi.org/10.3390/bios10110151.

[180] Y.-F. Ning, P. Yan, Y.-P. Chen, J.-S. Guo, Y. Shen, F. Fang, Y. Tang, X. Gao, Development of a Pt modified microelectrode aimed for the monitoring of ammonium in solution, Int J Environ Anal Chem. 97 (2017) 85–98. https://doi.org/10.1080/03067319.2016.1277994.

[181] S. Pandey, K.K. Nanda, Au nanocomposite based chemiresistive ammonia sensor for health monitoring, ACS Sens. 1 (2016) 55–62.

[182] H. bin Wu, X.W.D. Lou, Metal-organic frameworks and their derived materials for electrochemical energy storage and conversion: Promises and challenges, Sci Adv. 3 (2017) eaap9252.

[183] H. Furukawa, K.E. Cordova, M. O'Keeffe, O.M. Yaghi, The chemistry and applications of metal-organic frameworks, Science (1979). 341 (2013).

[184] P. Silva, S.M.F. Vilela, J.P.C. Tomé, F.A.A. Paz, Multifunctional metal–organic frameworks: from academia to industrial applications, Chem Soc Rev. 44 (2015) 6774–6803.

[185] S. Wuttke, Introduction to Reticular Chemistry. Metal–Organic Frameworks and Covalent Organic Frameworks Von Omar M. Yaghi, Markus J. Kalmutzki und Christian S. Diercks., Angewandte Chemie. 131 (2019). https://doi.org/10.1002/ange.201906230.

[186] K. Guo, L. Zhao, S. Yu, W. Zhou, Z. Li, G. Li, A water-stable proton-conductive barium (II)-organic framework for ammonia sensing at high humidity, Inorg Chem. 57 (2018) 7104–7112.

[187] S.K. Bhardwaj, G.C. Mohanta, A.L. Sharma, K.-H. Kim, A. Deep, A three-phase copper MOF-graphene-polyaniline composite for effective sensing of ammonia, Anal Chim Acta. 1043 (2018) 89–97.

[188] B.J. Müller, N. Steinmann, S.M. Borisov, I. Klimant, Ammonia sensing with fluoroionophores–A promising way to minimize interferences caused by volatile amines, Sens Actuators B Chem. 255 (2018) 1897–1901.

[189] M.R. Huang, X.G. Li, Highly sensing and transducing materials for potentiometric ion sensors with versatile applicability, Prog Mater Sci. 125 (2022). https://doi.org/10.1016/j.pmatsci.2021.100885.

[190] Methrom Ammonia Ion-selective Electrode, (n.d.). https://www.metrohm.com/en_gb/applications/ab-application-bulletins/ab-133.html (accessed November 3, 2022).

[191] D. Tyagi, H. Wang, W. Huang, L. Hu, Y. Tang, Z. Guo, Z. Ouyang, H. Zhang, Recent advances in two-dimensional-material-based sensing technology toward health and environmental monitoring applications, Nanoscale. 12 (2020) 3535–3559.

[192] K.K. Tadi, S. Pal, T.N. Narayanan, Fluorographene based ultrasensitive ammonia sensor, Sci Rep. 6 (2016) 1–9.

[193] Z. Luo, L. Fu, J. Zhu, W. Yang, D. Li, L. Zhou, Cu2O as a promising cathode with high specific capacity for thermal battery, J Power Sources. 448 (2020) 227569. https://doi.org/10.1016/j.jpowsour.2019.227569.

[194] L. Zhang, Q. Li, H. Xue, H. Pang, Fabrication of Cu 2 O-based Materials for Lithium-Ion Batteries, ChemSusChem. 11 (2018) 1581–1599. https://doi.org/10.1002/cssc.201702325.

[195] S. Chatterjee, A.J. Pal, Introducing Cu 2 O Thin Films as a Hole-Transport Layer in Efficient Planar Perovskite Solar Cell Structures, The Journal of Physical Chemistry C. 120 (2016) 1428–1437. https://doi.org/10.1021/acs.jpcc.5b11540.

[196] C. Espro, S. Marini, D. Giusi, C. Ampelli, G. Neri, Non-enzymatic screen printed sensor based on Cu2O nanocubes for glucose determination in bio-fermentation processes, Journal of Electroanalytical Chemistry. 873 (2020) 114354. https://doi.org/https://doi.org/10.1016/j.jelechem.2020.114354.

[197] G. Zhan, H.C. Zeng, Topological Transformations of Core–Shell Precursors to Hierarchically Hollow Assemblages of Copper Silicate Nanotubes, ACS Appl Mater Interfaces. 9 (2017) 37210–37218. https://doi.org/10.1021/acsami.7b11808.

[198] P. van Dat, N.X. Viet, Facile synthesis of novel areca flower like Cu2O nanowire on copper foil for a highly sensitive enzyme-free glucose sensor, Materials Science and Engineering: C. 103 (2019) 109758. https://doi.org/10.1016/j.msec.2019.109758.

[199] Y. Chen, Y. Du, P. Liu, J. Yang, L. Li, J. Li, Removal of Ammonia Emissions via Reversible Structural Transformation in M (BDC)(M= Cu, Zn, Cd) Metal–Organic Frameworks, Environ Sci Technol. 54 (2020) 3636–3642.

[200] L. Vivas, I. Chi-Duran, J. Enríquez, N. Barraza, D.P. Singh, Ascorbic acid based controlled growth of various Cu and Cu 2 O nanostructures, Mater Res Express. 6 (2019) 065033. https://doi.org/10.1088/2053-1591/ab0dd2.

[201] K. Schlichte, T. Kratzke, S. Kaskel, Improved synthesis, thermal stability and catalytic properties of the metal-organic framework compound Cu3(BTC)2, Microporous and Mesoporous Materials. 73 (2004) 81–88. https://doi.org/https://doi.org/10.1016/j.micromeso.2003.12.027.

[202] G.A. Sorial, F.L. Smith, M.T. Suidan, R.C. Brenner, Removal of ammonia from contaminated air by trickle bed air biofilters, J Air Waste Manage Assoc. 51 (2001). https://doi.org/10.1080/10473289.2001.10464307.

[203] D. Grujicic, B. Pesic, Reaction and nucleation mechanisms of copper electrodeposition from ammoniacal solutions on vitreous carbon, Electrochim Acta. 50 (2005). https://doi.org/10.1016/j.electacta.2005.02.012.

[204] S. Yuan, L. Feng, K. Wang, J. Pang, M. Bosch, C. Lollar, Y. Sun, J. Qin, X. Yang, P. Zhang, Q. Wang, L. Zou, Y. Zhang, L. Zhang, Y. Fang, J. Li, H.C. Zhou, Stable Metal–Organic Frameworks: Design, Synthesis, and Applications, Advanced Materials. 30 (2018). https://doi.org/10.1002/adma.201704303.

[205] A. Corma, H. García, F.X. Llabrés I Xamena, Engineering metal organic frameworks for heterogeneous catalysis, Chem Rev. 110 (2010). https://doi.org/10.1021/cr9003924.

[206] G. Zhan, L. Fan, F. Zhao, Z. Huang, B. Chen, X. Yang, S. feng Zhou, Fabrication of Ultrathin 2D Cu-BDC Nanosheets and the Derived Integrated MOF Nanocomposites, Adv Funct Mater. 29 (2019). https://doi.org/10.1002/adfm.201806720.

[207] R. García-González, M.T. Fernández-Abedul, A. Costa-García, Nafion® modified-screen printed gold electrodes and their carbon nanostructuration for electrochemical sensors applications, Talanta. 107 (2013). https://doi.org/10.1016/j.talanta.2013.01.034.

[208] J. Guo, J.G. Lee, T. Tan, J. Yeo, P.W. Wong, N. Ghaffour, A.K. An, Enhanced ammonia recovery from wastewater by Nafion membrane with highly porous honeycomb nanostructure and its mechanism in membrane distillation, J Memb Sci. 590 (2019). https://doi.org/10.1016/j.memsci.2019.117265.

[209] L. Cheng, W. Guo, X. Cao, Y. Dou, L. Huang, Y. Song, J. Su, Z. Zeng, R. Ye, Laser-induced graphene for environmental applications: progress and opportunities, Mater Chem Front. 5 (2021) 4874–4891. https://doi.org/10.1039/D1QM00437A.

[210] W. Zhang, S.P. Wei, M.K.H. Winkler, A. V. Mueller, Design of a Soft Sensor for Monitoring Phosphorous Uptake in an EBPR Process, ACS ES&T Engineering. 2 (2022) 1847–1856. https://doi.org/10.1021/acsestengg.2c00090.